Shells, outflows and star formation in the giant molecular cloud Monoceros R2.

Item Type	Dissertation (Open Access)
Authors	Xie, Taoling
DOI	10.7275/rjx2-0y03
Download date	2025-07-04 11:48:14
Link to Item	https://hdl.handle.net/20.500.14394/11940

SHELLS, OUTFLOWS AND STAR FORMATION IN THE GIANT MOLECULAR CLOUD MONOCEROS R2

A Dissertation Presented

by

TAOLING XIE

Submitted to the Graduate School of the
University of Massachusetts in partial fulfillment
of the requirements for the degree of

DOCTOR OF PHILOSOPHY

September 1992
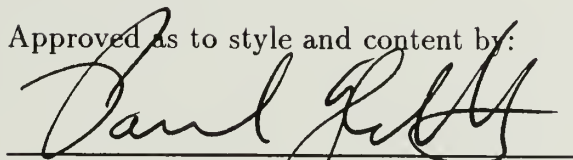
Department of Physics and Astronomy

SHELLS, OUTFLOWS AND STAR FORMATION IN THE GIANT MOLECULAR CLOUD MONOCEROS R2

A Dissertation Presented

by

Taoling Xie
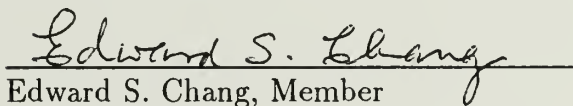
Approved as to style and content by:

_____

Paul F. Goldsmith, Chair

_____

Ronald L. Snell, Member

_____

Robert L. Dickman, Member

_____

Edward S. Chang, Member

_____

Robert B. Hallock, Department Head
Department of Physics and Astronomy

To my beloved grandma and parents

the change of the emphasis of the original thesis proposal from clumpiness to the structure of Mon R2, which is proven to be an essential move. His leaving the department before I finished my thesis has been my loss. Ed's course on atomic physics really entertained my first semester in this country. His giving me an A also added my confidence to adapt to the new environment. His kindness, smiling as well as chatting with me about his solar spectra will be a valuable memory.

Dr. John Bally, now at the University of Colorado at Boulder, is greatly appreciated for his sharing with us the BTL ^{13}CO $J = 1 - 0$ data for Mon R2, which is extensively used in this thesis. Dr. William Langer, JPL/Caltech, provided many useful discussions related to this thesis. His constant encouragement and deep insights into many interesting astronomical problems benefited me greatly in the last year or so. I also thank Drs. Dan Jaffe, Neal Evans, John Scalo and Shudong Zhou at the Astronomy Department, University of Texas at Austin, Drs. Margaret Frerking, Sam Gulkis, Tom Kuiper and Gerald Moriarty-Schieven, JPL/Caltech, for useful discussions.

Some professors in the Five College Astronomy Department have also been very supportive. I am grateful to Prof. William Irvine for his granting me the observing time at FCRAO. The computer terminal in my office constantly activates my deep gratitude to Prof. Susan Kleinmann. Prof. William Irvine, Prof. David Van Blerkom and Prof. Ron Snell are also thanked for the prompt and responsible recommendations that they made for my job-hunting. Dr. John Kwan, Karen Strom, Stephen Strom and many others are sincerely appreciated for useful discussions and encouragement on various problems. Dr. Tom Arny and David Van Blerkom are sincerely thanked for their treating me in all nice terms; when I was a TA in particular. A letter from Tom shortly after I received the official admission from UMASS ended my hesitation among offers from several American universities in 1986. The staff of the FCAD, of the FCRAO in particular, are thanked full-heartedly

I remember my dearest grandma, who brought me up in the difficult years and did not live until today to see my achievement (she passed away in 1990). It is to her that this thesis is dedicated.

<div align="center">

ABSTRACT

SHELLS, OUTFLOWS AND STAR FORMATION IN THE GIANT
MOLECULAR CLOUD MONOCEROS R2

SEPTEMBER 1992

TAOLING XIE, B.S., BEIJING UNIVERSITY

M.S., ACADEMIA SINICA

PH.D., UNIVERSITY OF MASSACHUSETTS

Directed by: Professor Paul F. Goldsmith

</div>

To improve our understanding about giant molecular clouds (GMC) associated with R-associations, a ^{12}CO $J = 1 - 0$ map of $167,000$ spectra with 45" resolution and 25" spacing, a ^{13}CO $J = 1 - 0$ map of $\sim 40,000$ spectra with 1.5' resolution and 1' spacing, *IRAS BIGMAP* images, and maps of high density molecular tracers for the dense cores are obtained for the GMC Monoceros R2 ($D = 830 \pm 50$ pc).

These data reveal that the large-scale structure of Mon R2 is dominated by an expanding bubble shell (~ 30 pc) with front side moving towards us at a radial velocity of $\sim 4 - 5$ km s^{-1}. Distortions of this shell are obvious, suggesting of the inhomogeneity of the cloud before the formation of the bubble. There is no evidence for red-shifted shell at the far side of the bubble. There are at least two generations of star formation in Mon R2. The older generation of stars with an age of $6 - 10 \times 10^6$ years are represented mostly by reflection nebulae. The younger generation of stars with an age of $\sim 10^5$ years are represented mostly by *IRAS* point sources. It is proposed that the large-scale expanding bubble shell is the result of combined effects of ionizing flux and stellar winds originating from the older generation of young stellar objects, but perhaps dominated by O type stars which either are obscured or left main sequence. It is suggested that the formation

of the younger generation of stars has been triggered by the older generation of stars.

The main and the GGD12-15 cores are located on the the large-scale expanding shell, and their harboring both generations of stars can be explained were the cores preexisting clumps. Our CO data reveal an eggplant-shaped bipolar outflow shell, whose shape can be satisfactorily modeled with radially directed stellar winds sweeping up ambient material with momentum conservation.

An inversion method is implemented for analyzing dust emission spectra at FIR wavelengths in terms of a continuous dust temperature distribution, and has been applied to *IRAS BIGMAP* images of Mon R2. Computer programs are developed for identifying clumps and determining their properties in molecular emission maps. The results support the reality of size-linewidth and mass-linewidth relations for clumps in individual GMCs.

TABLE OF CONTENTS

LIST OF TABLES

List of Figures

Chapter 1

Introduction

1.1 GMCs and Star Formation

1.1.1 *What and Why*

Although the classification of molecular clouds in the Galaxy has not yet been unambiguous (see e.g. Goldsmith 1987 for an attempt), the fact that giant molecular clouds (GMCs) are sites of formation of large clusters of young stellar objects ranging from low mass T-Tauri (Hereafter TT) stars to high mass OB stars is quite compelling. GMCs, in fact, dominate the molecular content of interstellar medium, which is a significant mass component in the Galaxy, and are believed to be responsible for the formation of majority of the stars visible or invisible in the galaxy. Thus, studying these clouds is a necessity not only for unraveling one of the greatest mysteries—star formation, but also for understanding the evolutionary chemical and physical processes of the interstellar medium as well as of the Galaxy itself.

1.1.2 *Observing Tools*

Unfortunately, the dominant mass component of molecular clouds, hydrogen molecules and helium, are both very elusive in terms of direct observation. The gas temperature in most such clouds is too low to excite significantly any rotational or vibrational energy levels of the hydrogen molecules to emit electromagnetic waves measurable by available techniques. Fortunately, molecular clouds are not free of other components — dust grains, atomic hydrogen and molecules of various species

(cf. Langer 1985; Irvine, Goldsmith & Hjalmarson 1987). These may represent a minor mass fraction of clouds, yet very important in many other aspects, including emitting electromagnetic waves which serve as tracers of clouds. Although many different tracers exist or remain to be found for studying the general structure of a giant molecular cloud as a whole (cf. Dickman 1988; Goldsmith 1988), by far the most powerful, and the most widely used ones are infrared images which trace the thermal emission from dust grains, and ^{12}CO or ^{13}CO mapping which are good tracers by virtue of their moderate abundances relative to hydrogen molecules and their readily excitable rotational levels. These techniques are widely used in part because only these two techniques can currently furnish data with spatial resolution and coverage adequate for many physical analyses. Although the two tracers complement each other in studying different aspects of GMCs, ^{12}CO or ^{13}CO mapping is undoubtedly a better technique for studying the kinematic and dynamic structure of the giant molecular clouds because it provides information about the velocity distribution as well as the spatial distribution for the molecular material in GMCs.

1.1.3 Intertwined Fundamental Issues

Star formation is perhaps the most important and naturally the most approached issue in the research of GMCs. This is so because stars are believed to be born out of gravitationally condensed, relatively cold molecular material in molecular clouds, and the emergence of the young stellar objects has a profound and violent impact on the overall structure and chemical constituents of the maternal molecular environment. These two aspects of star formation have been so intertwined with each other that diffuse material, protostars and newly-born stars essentially form a whole complex system, and attempts to understand any aspect of the system often end up having to address many related fundamental issues such as the trigger of

star formation, the evolution of the young stars, turbulence, clumpiness in clouds as well as the global structure of the molecular cloud as an entity.

While the notion that stars are born out of cold diffuse material no longer seems to be an active controversial issue among astronomers during the last several decades, the way that stars are formed remains at the present time an open issue under active theoretical and observational investigations. Free-fall gravitational collapse (cf. Larson 1972; Goldreich & Kwan 1974) seems to be an inevitable process in the final stages of star formation. But it is often necessary to involve a number of other processes at an earlier point to explain some well-observed properties of star clustering. One of these mechanisms proposed is sequential star formation (or triggered star formation, Blaauw 1964, 1991; Elmegreen & Lada 1977; Herbst & Assousa 1978). This mechanism, providing a rather neat picture for star formation on various size and mass scales, appeared to be consistent with the distribution and kinematics of molecular material in several GMCs, as revealed by existing molecular data (cf. Elmegreen & Lada 1977; Sargent 1977; 1979; Lada, Blitz & Elmegreen 1978; Wilking *et al* 1984; Thronson, Lada & Hewagawa 1985). However, the available data sets on the several GMCs supporting such claims are still inadequate relative to the importance of this issue, and numerous problems remain to be addressed observationally with high quality data sets (cf. Sargent 1985; Blaauw 1991; Elmegreen 1992).

Parallel to the issue of triggered star formation, an equally important question is the fashion in which protostars and newly-formed stars feed energy back to the ambient molecular material. Several forms of energy release known to occur along with star formation could conceivably produce severe effects on the chemical constituents and structure of the material surrounding YSOs. First, the radiation from the stars may pass significant kinetic energy to dust grains and gas, and significantly change their physical and chemical conditions through absorption, photo-electric

effect, ionization, shock compression and so on. These effects are best illustrated by the fascinating HII regions surrounding massive young stellar objects associated with molecular clouds (cf. Spitzer 1978; Mazurek 1982; Goudis 1982). Second, stellar winds are bound to push away the ambient material and punch holes in whatever material (Pikel'ner 1973; Castor, McCray & Weaver 1975; Falle 1975; Dyson 1977; 1989; Weaver *et al* 1977; Shull 1980; Norman & Silk 1980; Koo & McKee 1992a,b). These violent processes and the accompanying shocks will undoubtedly damage the original molecular clouds in many ways (Shull & Draine 1987). The well-known bipolar outflow phenomenon (Snell 1987) observed associated YSOs provides the best evidence for such effects. Large scale CO and ^{13}CO maps of Orion by Bell Laboratories 7m telescope (Bally *et al* 1987) clearly shows the existence of many ring-like structures and holes at different scales possibly blown out by ionizing flux and stellar winds from young stellar objects. But again, research in this direction remains preliminary and the exact mechanisms responsible for this fascinating phenomenon are not known. More high quality observational data are needed before a better understanding can be achieved.

One other closely related fundamental mystery that appeared with the discovery of molecular clouds is that the line widths of molecular tracers range from a few $km \ s^{-1}$ to as large as more than 10 $km \ s^{-1}$ (Penzias 1975) even in regions where the kinetic temperature of the gas estimated from gas "thermometers" (Goldsmith 1988) is as low as $\sim$ 10 K. While pressure broadening of the lines and some other fancy mechanisms can be ruled out (Dickman 1985), the fact that linewidths are typically an order of magnitude larger than what thermal motions can account for clearly indicates the existence of large non-thermal motions — often referred to as "turbulence". Most attempts to resolve the mystery relate to the existence of star forming activity. The first systematic model was free-fall collapse of these clouds (Goldreich & Kwan 1974) since by that time the free-fall collapse picture had been

intensively pursued theoretically (McVittie 1956; Hunter 1962; Layzer 1964; Hayashi 1966; Tayler 1968; Penston 1969; Disney, McNally & Wright 1969; McNally 1971; Bodenheimer 1972; Larson 1972; 1973). However, it did not take long before it was realized that such a model leads to a star formation rate in the Galaxy far larger (by at least an order of magnitude) than a few $M_\odot/yr$ observed (Zuckerman and Palmer 1974). Many phenomenological models invoking mechanisms such as magnetic field, differential rotation, thermal instabilities and Kolmogorov eddy cascades have been proposed to account for the "turbulence" issue (see reviews by Dickman 1985, Myers 1987 and Scalo 1987). This issue is closely related to another related fundamental problem in the study of GMCs — clumpiness and fragmentation (Silk 1978; Scalo 1985). GMCs are found to be very clumpy; the emission intensity of different tracers, such as CO, is very inhomogeneously distributed spatially and kinematically, and GMCs appear to be made up of a large number of smaller individual "contour islands" (so-called fragments, clouds or clumps) of various sizes and masses as revealed by the techniques of spatial and spatial-velocity contour maps. To add more complexity, these "contour islands" often appear nested and form a hierarchy (Scalo 1985; 1988). These clumps or fragments add up to a total mass of $10^4 M_\odot$ to $10^7 M_\odot$ with a very low average H_2 density of about 50 cm^{-3} (see reviews by Blitz 1980, 1987, Solomon & Sanders 1985, Scoville & Sanders 1987 and Goldsmith 1987). Because the lowest hydrogen density to significantly excite these tracers at a temperature typical of these clouds is expected to be of a few hundred molecules per cubic centimeter, the averaged low density implies a very small beam filling factor for the gas. This point is perhaps clarified when considered from a different viewpoint. Kwan and Sanders (1986) show in their modeling that a certain clumpy structure with a small filling factor is required to explain the often observed Gaussian profiles of optically thick CO lines (see also Tauber 1990). The arguments for a clumpy medium to explain the penetration of ultraviolet photons into cloud interior as

revealed by the far-infrared and submillimeter emission of C and C^+ is also quite convincing (Boissé 1990). After all, observed star forming activity in these clouds requires the existence of fragmentation processes (Silk 1978; Scalo 1988).

An important development in quantitatively studying the clump properties as well as turbulence is the discovery of power-law correlations among clump quantities such as velocity dispersion, characteristic radius, density, and mass (Larson 1979; 1981; Snell 1981). These are referred to as Larson's Laws in this thesis. But research in this direction has been encountering remarkable challenges in the last couple of years (cf. Issa, MacLaren & Wolfendale 1990; Scalo 1991; Adler & Roberts 1991). The major conflict seems to lie in the identification of clumps, which could be complicated mainly by distance ambiguities and cloud blending. Under this situation, a close examination of the Larson's laws based on high-quality data sets for an individual GMC with different and improved ways of defining cloud boundaries will help resolving the controversy. First, efforts to study the Larson's laws based on data sets for individual GMCs remain rare, and few examples are Orion (Bally *et al* 1987; Lada, Bally & Stark 1991), Rosette (Blitz 1987; 1991), Cep OB3 (Carr 1987), ρ Oph (Loren 1989), and M17SW (Stutzki & Güsten 1990). Presumably, such efforts would help assess the reality of the Larson's laws because one would expect to find such relations for sub-concentrations within individual GMCs if they indeed represent a real physical nature of molecular clouds. In individual GMCs, the distance ambiguity difficulty is greatly relieved and remaining difficulty is to improve the way to identify clumps and calculate clump quantities.

1.2 Thesis Motivation

From the brief review above, it is clear that although many fundamental problems in the field of molecular clouds are relatively well posed, none of these issues have yet been addressed in proper detail due to insufficient high-quality observa-

tional data (Dickman 1985; Scalo 1985; Shu, Adams & Lizano 1987; Goldsmith 1987; Myers 1987; Stenholm 1987; Scalo 1988; Blaauw 1991; Elmegreen 1991; 1992;). This point is particularly true for GMCs because their large spatial sizes severely limit the proper CO and ^{13}CO mapping coverage, spatial resolution, and sampling needed to reach reliable conclusions. In fact, the only telescope with resolution better than a couple of arcminutes dedicated to large scale mapping projects had been the Bell Laboratories 7 m telescope, and few systematic studies have been published with adequate quality data sets on individual GMCs. The small number of such systematic studies are naturally biased in the sense that so far the GMCs systematically studied are associated either with the destructive OB associations or with low-mass T star associations. While the other type of stellar associations, R associations, is known to have distinctive properties, little is known about the properties of their maternal GMCs. This situation largely precludes reliable theoretical analyses of the clumpy structure, the origin of clumps, star formation, and the evolution of GMCs as a whole. Obtaining good quality data to systematically examine the fundamental issues associated with the overall structure of such GMCs is undoubtedly a meaningful thing to do, and any results of such a research are bound to shed light not only on the structure of such a GMC itself but also on the study of GMCs as a whole.

1.3   Monoceros R2

1.3.1   The R-association

The development of the focal plane array system consisting of 15 heterodyne receivers (QUARRY) at the Five College Radio Astronomy of the University of Massachusetts has the potential to greatly improve the situation. We have decided to take advantage of this instrument to systematically examine the properties of a GMC associated with an association of reflection nebulae.
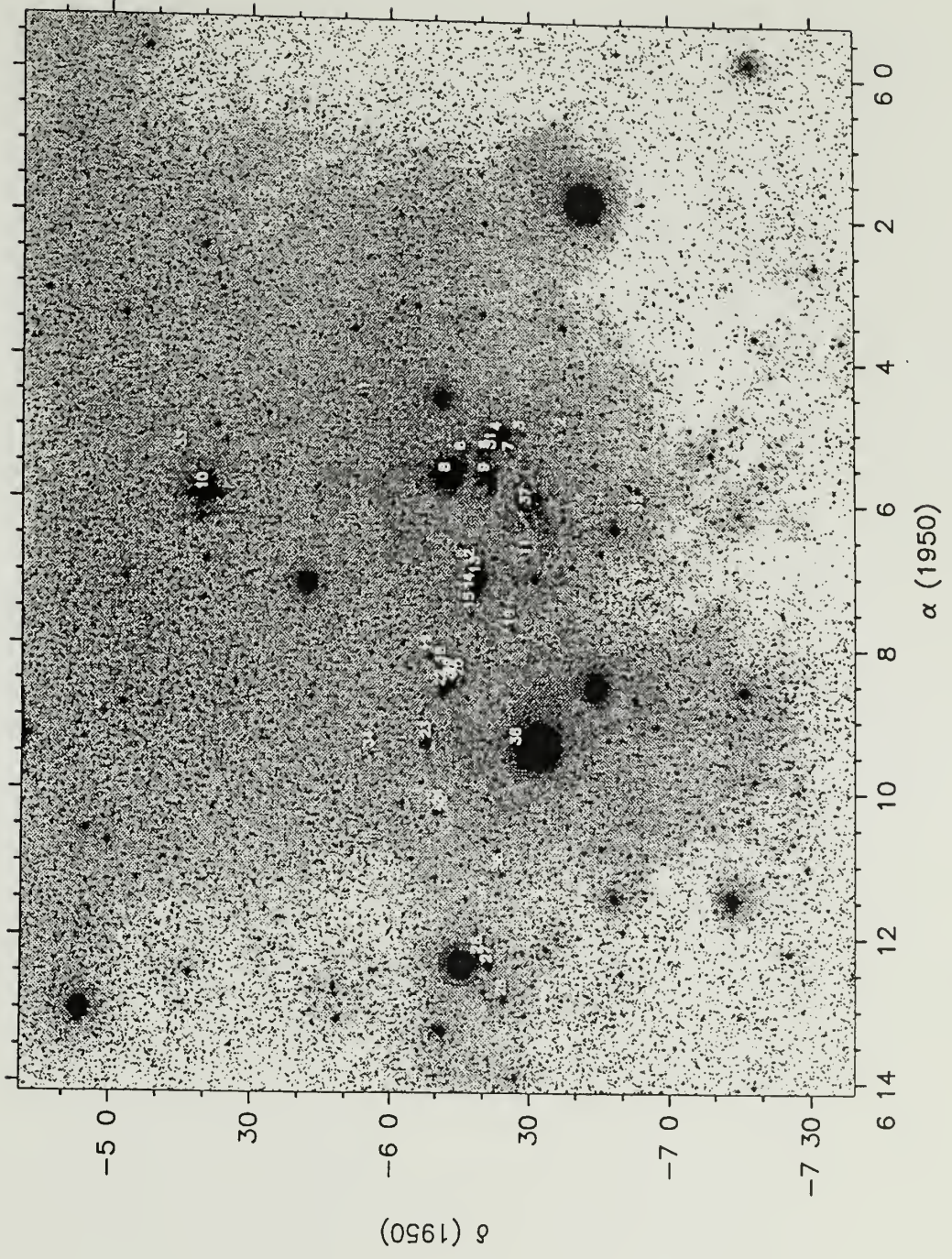
Figure 1.1. POSS blue print with identified reflection nebulae indicated by Arabic numbers
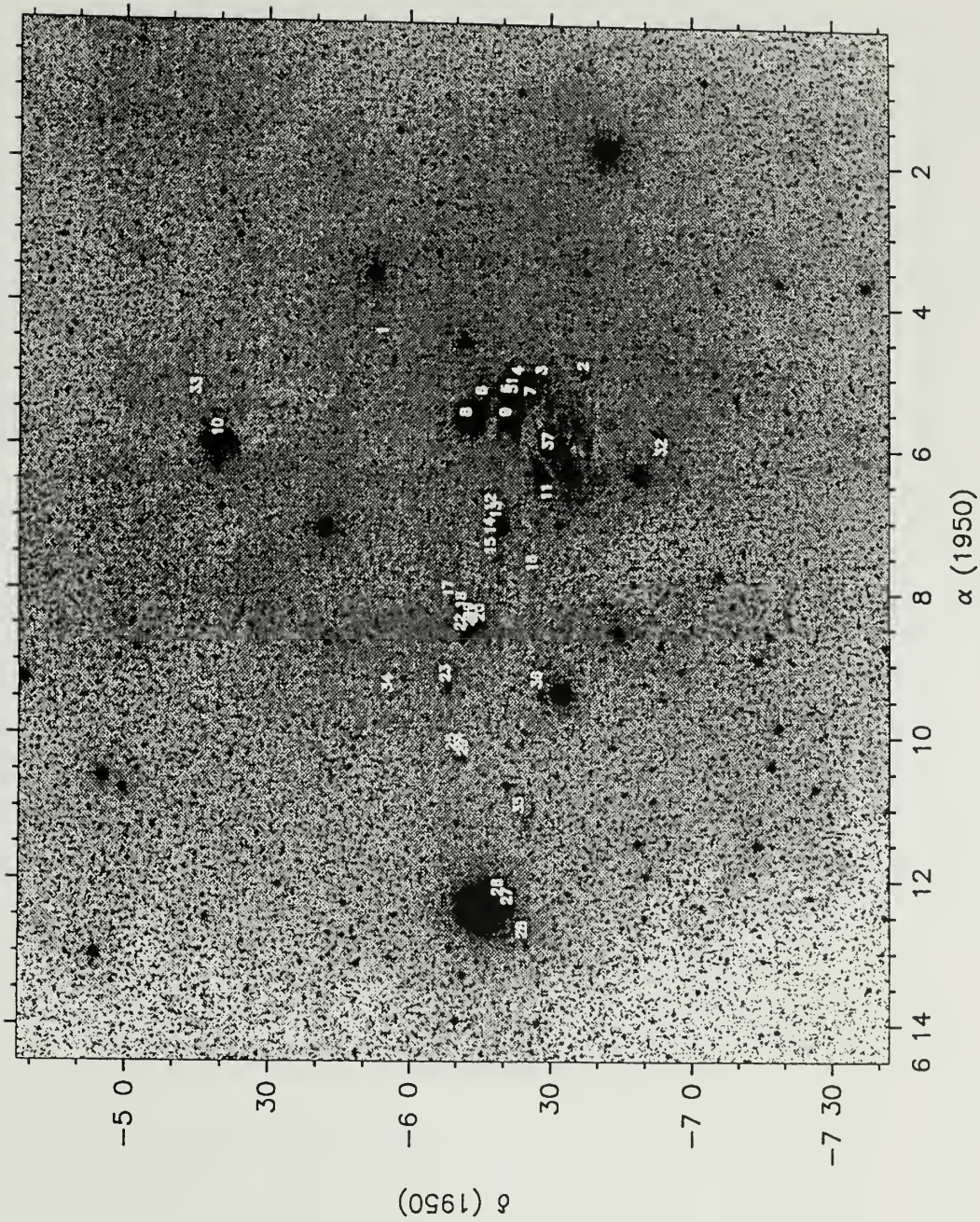
Figure 1.2. POSS red print with identified reflection nebulae indicated by Arabic numbers.

Figures 1.1 and 1.2 show a portion of the sky as revealed by the POSS prints, where an association of reflection nebulae called Mon R2 is located. Attention to this this portion of the sky can be traced back at least to Seares & Hubble (1920) and Hubble (1922). Hubble (1922), in fact, studied a few reflection nebulae in this region along with many others and found the famous Hubble relation for reflection nebulae. Later the reflection nebulae in this region were further studied in the sixties and early seventies by a number of investigators (Dorschner & Gürtler 1964; 1965; van den Bergh 1966, hereafter referred to as vdB; 1968; Racine 1968; Racine & van den Bergh 1970). It is vdB who first coined the name "Mon R2" for the region; it is the second reflection nebula association in the Monoceros constellation in his systematic study of reflection nebulae associations.. The most detailed studies of the Mon R2 association to date are those undertaken by Racine (1968) and Herbst & Racine (1976) (hereafter HR), who did UBV photometry for most of the member reflection nebulae identified from POSS prints and found that majority of them are powered by main sequence B and A type stars, while few of them are TT type, Be and even Orion population (hereafter Op) type stars. Based on these photometric results, the distance of Mon R2 is determined to be 830 ± 50 pc ($m - M = 9.6 \pm 0.1$ $m.e.$). The 30 refection nebulae catalogued by HR are indicated by Arabic numbers 1-30 in Figures 1.1 and 1.2. In Figures 1.1 and 1.2, we have also included some other reflection nebulae identified by different studies; we numbered them from 31 to 37. These numbered reflection nebulae are tabulated in Table 1.1. Positions for these reflection nebulae are determined from our digital images scanned from the POSS prints, as compared with those determined by previous investigators. It must be pointed out that these identified reflection nebulae are almost definitely not all of the reflection nebulae in Mon R2 region. In fact, several candidate Herbig-Haro objects catalogued by Gyulbudagyan, Glushkov & Denisyuk (1978) (hereafter referred to as GGD) and Gyul'budagyan (1982) (Hereafter referred to as G), GGD 11-17 and

G18, are in the Mon R2 region, and some of those (GGD 12-15) studied at 2 μm are suggested to be simply reflection nebulae (Cohen & Schwartz 1980).

This R-association is obviously not associated with any known OB associations (vdB). Several conspicuous features are revealed in Figures 1.1 and 1.2. First, a roughly circular enhanced diffuse emission is clearly visible on the POSS red print surrounding the reflection nebulae on the scale of a few degrees across, with a relatively well defined boundary. But the enhanced emission region on the POSS blue print does not show such roundness. It is not clear the enhancement of the emission is suggestive of the existence of diffuse gas reflecting light from neighborhood stars, or some other emission. Also, towards the NW corner there appears a separate region with similar enhanced background emission, which seems to be extended all the way to the neighboring Orion B region. Second, some reflection nebulae have the tendency to appear in clusters. Third, most of the reflection nebulae are located in a narrow band along the east-west direction (HR; Hughes & Baines 1985).

1.3.2 Mon R2 as a GMC

Not long after the discovery of interstellar CO (Wilson, Jefferts & Penzias 1970), a different aspect of Mon R2 — its association with molecular material — was revealed (Loren, Peters & Vanden Bout 1974), and this molecular cloud was soon found to have an H_2 mass of $> 3.2 \times 10^4$ $M_\odot$ (Kutner & Tucker 1975), which qualifies the cloud as a GMC[1]. This estimate, based on tens of data points of CO $J = 1 - 0$ sampled over a region of 15 square degrees in extent using the University of Texas 5 m telescope, is very close to estimates made later with several other data sets. Specifically, Maddalena et al (1986), who mapped the Mon R2 region with a spacing of 15' or 30' and resolution of 8.7' using the Columbia 1.2 m telescope, estimated a

---

[1] Hereafter when we use Mon R2 without specification, we mean the giant molecular cloud Mon R2.

mass of 9×10^4 $M_\odot$ for the GMC. Loren (1977) mapped the western portion around the central core of the GMC using the University of Texas 5 m telescope with 2' spacing, and gave a rough estimate of 2.3×10^4 $M_\odot$. Jenniskens et al (1986) and Jenniskens & Wouterloot (1990) included a much larger region which they referred to as GMC214-13[2] in their mapping of the OH main lines with a resolution of 30' and a spacing of 20', giving a mass estimate of $3 \pm 1 \times 10^5$ $M_\odot$. Mon R2 was also included in the star counting project of Tomita (1987; 1990), which covers over 2000 square degrees of the sky with resolution ranging from 7' to 20'. This work resulted in a mass estimate of 3.7×10^4 $M_\odot$ for Mon R2. Although these studies do provide valuable information about the structure of the GMC, their poor resolution or inadequate sampling simply does not allow detailed study of the structure and star formation in the cloud. The only one data set in the literature that has reasonably good resolution, sampling, and coverage for Mon R2 is the ^{13}CO $J = 1 - 0$ map obtained using the Bell Lab 7 m telescope (Bally, Langer & Liu 1991). But Bally, Langer & Liu (1991) concentrated on the comparison of the gas emission with dust emission and made no efforts to analyze the detailed structure of the giant molecular cloud.

Relatively better studied is the central core of the GMC, in which a velocity gradient has been found and interpreted as rotation (Loren 1977; 1981; Willson & Folch-Pi 1981; Heyer et al 1986; Richardson et al 1988; Montalbán et al 1990; Wolf, Lada & Bally 1990). But rotational axes determined by these studies differ considerably. This core is definitely a very dense one as indicated by the detection of various high density tracing molecules (Loren, Peters & Vanden Bout 1974; Kutner & Tucker 1975; Sume & Irvine 1977; Linke & Goldsmith 1980; Goldsmith & Linke 1981; Macdonald et al 1981; Torrelles et al 1983). It manifests variety of interesting

---

[2]including Mon R2 and the filamentary clouds to the south of Mon R2. I personally think such a name is confusing given the large size of the region, and thus I will not use this name in this thesis.

phenomena including water masers (Downes *et al* 1975; Morris & Knapp 1976; Knapp & Brown 1976; Rodríguez *et al* 1980), HH objects and even an ultra compact HII region possibly powered by a star with ionizing flux equivalent to B0 type (Valee, Viner, and Hughes 1979; Gilmore 1980; Rodríguez *et al* 1980; Massi, Felli, and Simon 1985). These are strong indicators that it is an active region of massive star formation. The Mon R2 main core was in fact one of the earliest molecular cores found to possess the violent molecular outflow phenomena (Loren 1976; 1977), but the broad linewidth observed was thought to be due to free-fall collapse until the first bipolar outflow was identified in L1551 by Snell, Loren & Plambeck (1980). The Mon R2 bipolar outflow (Loren 1981) is by far one of the largest in size and in mass among the some two hundred outflows identified (Bally and Lada 1983; Lada 1985; Bally and Lane 1991). It is suggested that this outflow consists of possibly two distinct pairs of bipolar outflows with flow axes almost perpendicular to each other (Wolf, Lada & Bally 1990; Meyers-Rice & Lada 1991). Optical and infrared polarimetry studies of this core region reveal a peculiar arc-like magnetic field orientation which is in general coincident with the bipolar outflow direction (Zaritsky *et al* 1987; Hodapp 1987; Novak 1988).

Roughly 45' to the east of the main Mon R2 core, there is another well studied dense core harboring active star formation. This region first received attention because several objects in this region were identified as possible Herbig-Haro objects by Gyulbudaghian, Glushkov & Denisyuk (1978, GGD), and this region is thus referred to as GGD 12-15 region (Cohen & Schwartz 1980). Similar to the main core in Mon R2, this core has a compact HII region powered by a B0 star (Rodríguez *et al* 1980). A bipolar outflow and a number of masing sources are also detected, indicating the youth of this star forming region (Rodríguez *et al* 1982).

As for the stellar content of this GMC on a large scale, the only systematic work in the last 15 years or so after the pioneering works on the R-associations

(HR) is the radio continuum survey by Hughes and Baines (1985). These authors firmly detected three thermal sources, the aforementioned compact HII regions in the GGD11-15 region and the main core. They also found a new radio source with thermal power-law index located roughly at the middle of the line connecting the two cores, which is not associated with any peak in the molecular emission. This research seems to confirm the previous result that star forming activity as indicated by the thermal radio sources and reflection nebulae is mostly along a narrow band across the two dense cores from east to west. Hughes and Baines (1985) suggest that star formation took place or is still taking place in a line or an annular ring in this GMC.

In summary, the GMC Mon R2 seems in many ways to be a promising target of a study designed to fulfill the thesis motivations outlined in the previous section. The relative closeness of Mon R2 ($D \simeq 830 \pm 50$ pc, Racine 1968; HR) and the small uncertainty of this distance determination are very desirable for many aspects of this research. One advantage, for example, is that the error in the determination of the mass of the cloud and of its clumps caused by the uncertainty of distance is relatively small. Also, the fact that this cloud (the central position of the core is $l = 213.0°$, $b = -12.5°$) is located ~ 180 pc below the galactic plane definitely reduces the chance of possible contamination by background and foreground clouds in radio observations, and thus conclusions sensitive to this contamination problem can be drawn with reasonably small risk. In addition, the giant bipolar molecular outflow in the core provides an ideal target to fulfill the author's strong interest in the structure of outflows and their relation to the structure of their parent molecular clouds.

1.4 Thesis Layout

We start by presenting our large data base (for both gas and dust emission) and examining the global spatial and kinematic structure of the giant molecular cloud in Chapters 2 and 3. Chapter 4 examines the structure of the two dense cores, and Chapter 5 presents our discovery of a well-shaped bipolar outflow shell and our modeling of the bipolar outflow. Chapter 6 is devoted to investigations of the distribution of stellar contents of the GMC and the relationship between the stellar objects and the diffuse gas and dust. We discuss the clumpiness of gas in the GMC in Chapter 7. We summarize our main conclusions of the thesis in Chapter 8.

Table 1.1. Reflection nebulae in Mon R2

No.	α(1950)	δ(1950)	V	E(B-V)	Sp.T.	Aliases or associations
1	060431.7	-055439.1	12.49	0.43		HR1,IRAS06045-0554
2	060459.4	-063729.1	12.33	0.70	A0:	HR2
3	060503.2	-062839.2	14.14	0.75:		HR3
4	060503.6	-062337.1	10.31	0.90	B2V	HR4, vdB67,NGC2170
						SAO 132861, REIN2.049
						CED063,DG088, LBN0994
5	060519.2	-062114.7	12.51	0.39:	A5:Op	HR5a,IRAS06053-0622
6	060521.4	-061555.7	13.46	1.22:		HR6,IRAS06053-0614
7	060521.1	-062611.0	14.02	0.93:		HR7
8	060539.3	-061236.1	9.21	0.58	B1V	HR8,vdB68,DG089,NGC2167
						HELW054,CED065,SAO132867
						IRAS06055-0613
9	060538.9	-062058.0	9.67	0.54	B2V	HR9,vdB69,DG090,CED066
						LBN0995,HELW055,SAO132868
						IRAS06056-0621
10	060558.3	-052004.9	8.09	0.33	B1V	HR10,vdB70,DG091,LBN0990
						YM41, IRAS06059-0519, SAO132876
11	060648.1	-062941.8	13.00	0.66		HR11
12	060657.6	-061755.2	12.83	0.92		HR12
13	060703.6	-061903.6	9.22	0.40	B3V	HR13,vdB72,SAO132895,NGC2182
						CED068,LBN0998, REIN2.050
						DG093, IRAS06070-0619
14	060716.9	-061743.8	10.26	0.29	B5V	HR14
15	060733.6	-061749.5	11.40	0.27	B8V	HR15
16	060747.3	-062633.8	13.63	0.58:		HR16
17	060809.7	-060859.6	12.84	0.55		HR17
18	060819.2	-061144.8	15.12		Op	HR18,NGC2183,DG094,CED069
						LkH_α338,IRAS06084-0611,AFGL890
19	060828.4	-061321.7	13.37	1.10		HR19,IRAS06085-0613
20	060829.5	-061532.8	13.39	0.75		HR20
21	060834.0	-061327.4	12.20	0.58		HR21,IRAS06085
22	060838.2	-061133.4	12.23	0.76	B8-A0	HR22,vdB73,NGC2185,DG095
						CED070,IRAS06086-0611
23	060921.2	-060825.4	10.89	0.62	B4V	HR23,vdB74, DG096, CED071
						HELW127,IRAS06093-0608
24	061017.0	-061122.0	13.36	0.42		HR24,IRAS06103-0612
25	061017.8	-060945.2	12.23	0.86		HR25
26	061217.8	-061932.1	12.16	0.40		HR26,IRAS06123-0619
27	061225.0	-062131.8	10.98	0.32	B7V	HR27,DG097,IRAS06124-0621
28	061252.8	-062439.8	10.53	0.48	B5V	HR28,DG098,IRAS06128-0624
29	061021.9	-061207.6	17:		TT	HR29,IRAS06103-0612, Bretz 4
30	060831.4	-061413.0			Be	HR30,IRAS06085-0613
31	060519.6	-062223.1	14.22:	0.78:		HR5b,IRAS06053-0622
32	060610.4	-065400.6				IRAS06062-0655
33	060524.1	-051537.1				IRAS06054-0515
34	060929.9	-055558.9				
35	061109.1	-062359.9				IRAS06111-0624
36	060925.8	-062744.8				IRAS06094-0628
37	060606	-063000				DG092,G213.9-12.5

CHAPTER 2

GAS DISTRIBUTION IN MON R2

2.1 Observations

2.1.1 FCRAO Data

We have made observations of ^{12}CO $J = 1 - 0$ emission from Mon R2 using the QUARRY 15 element focal plane array on the 14 m FCRAO telescope in New Salem, Massachusetts between 1991 April and 1992 January. A detailed description of the system can be found in Erickson et al (1992). The mapping was centered on $\alpha(1950) = 06^h05^m22^s$, $\delta(1950) = -06°22'25''$, the position of the infrared star cluster in the core of Mon R2 (Beckwith et al 1976). The spacing of the data is 25" while the FWHM beam size of the telescope is about 45" at 115 GHz and 47" at 110 GHz. The main beam efficiency was estimated to be 0.45 (Patel 1992). A filterbank with bandwidth 250 kHz (corresponding to a velocity resolution of 0.65 km s^{-1} at 115 GHz) was used as the primary spectrometer with 32 channels for each of the 15 receivers (we centered the filterbank on $V_{LSR} = 9.9$ km s^{-1}), which employed cooled Schottky barrier diode mixers with a common single-sideband filter and cooled image termination. Chopper wheel calibration was used and the data were taken in a position-switching mode with a common reference position at $\alpha(1950) = 06^h11^m00^s$, $\delta(1950) = -04°30'00''$[1]. The single side-band system temperature of the system ranged from ~ 650 K to ~ 1600 K, depending on elevation and weather conditions.

---

[1]This position was verified to be free of ^{12}CO $J = 1-0$ emission down to an rms noise of 0.05 K by positional switching measurements between this position and a second reference position of a couple of degrees away.

Integration times were regulated according to system temperature in order to yield a channel-to-channel rms noise level of $\sim 0.5 K$.

The first photons from Mon R2 for this project were received by the QUARRY focal plane array on the 3rd of April, 1991. When this mapping project was finally ended on the first day of 1992, I had passed > 250 happy hours at the QUABBIN observatory, and obtained about $167,000$ ^{12}CO $J = 1 - 0$ spectra which cover a ~ 8.05 square degrees region. We also mapped two dense cores in ^{13}CO $J = 1 - 0$, CS $J = 2 - 1$, HCO^+ $J = 1 - 0$, HCN $J = 1 - 0$, and $C^{18}O$ $J = 1 - 0$, as will be discussed in Chapter 4. In this chapter, we concentrate on the large scale kinematic structure of the giant molecular cloud.

2.1.2 Bell Labs Data

Observations of ^{13}CO J=1-0 emission for the GMC were made with the AT&T Bell Laboratories 7 m telescope at Crawford Hill in Holmdel, New Jersey. An SIS receiver with a single-sideband receiver temperature ranging from 90 to 200 K was used. A 128 channel filterbank with a 0.25 MHz bandwidth was expanded using a spectrum expander (Henry 1976) to give a 100 kHz resolution. The mapping is centered on $06^h05^m22.0^s$, $DEC = -06°22'25.0"$ and made with a map spacing of 1'. Frequency switching was used for most data with frequency-offsets of ± 3.2 MHz. Integration times were chosen automatically to yield a a channel-to-channel rms noise of 0.3 K. The FWHM beam size is about 90" at 110 GHz, and the main beam efficiency is 0.87.

2.2 Morphology of Gas Emission in Mon R2

Figures 2.1 and 2.2 display the ^{12}CO $J = 1 - 0$ peak antenna temperature and ^{13}CO $J = 1 - 0$ integrated intensity, respectively, overlayed on the POSS red print. Figures 2.3 to 2.10 and 2.11 to 2.18 present the velocity channel maps
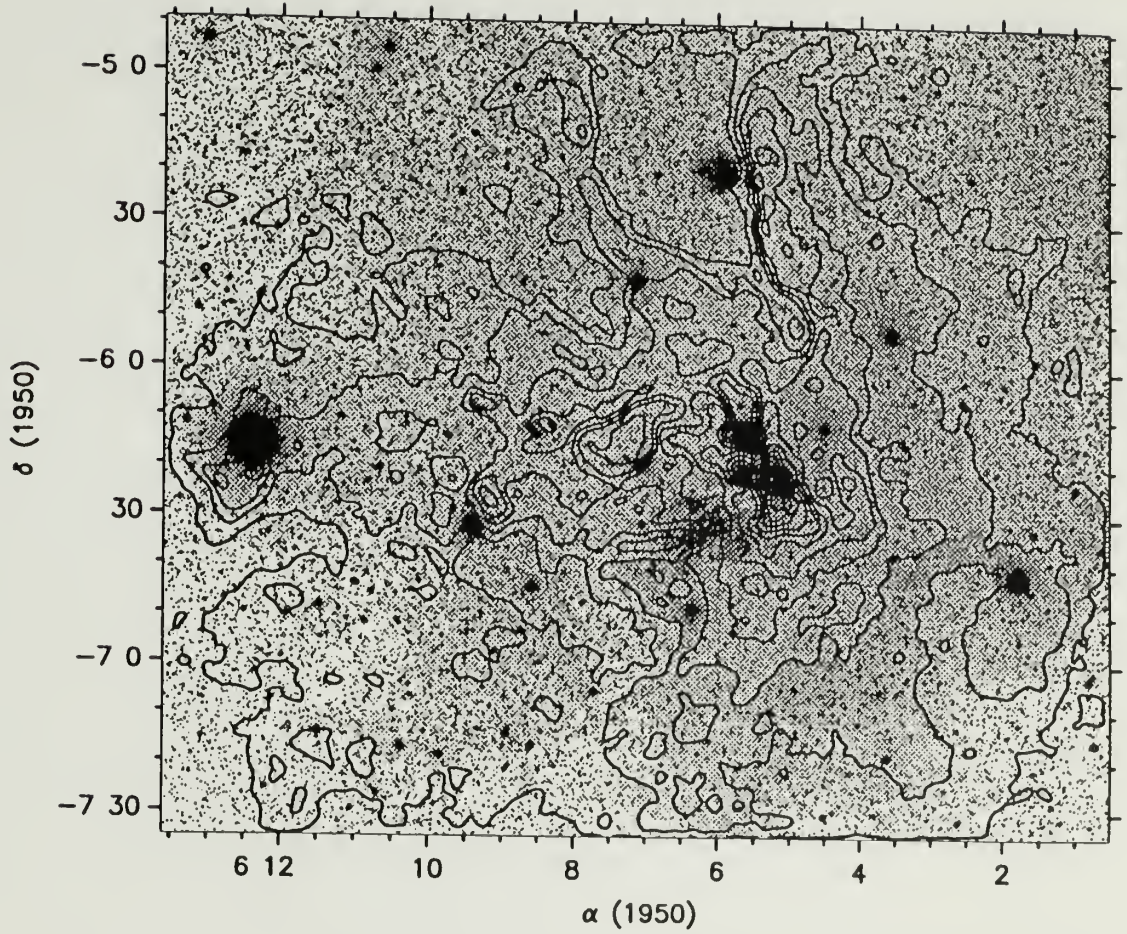
Figure 2.1. Contour Map of the $^{12}CO\ J = 1 - 0$ peak antenna temperature (solid contours) overlayed with POSS red print (halftone). Levels of contours are 1.5, 2.5, ... 14.5 K.
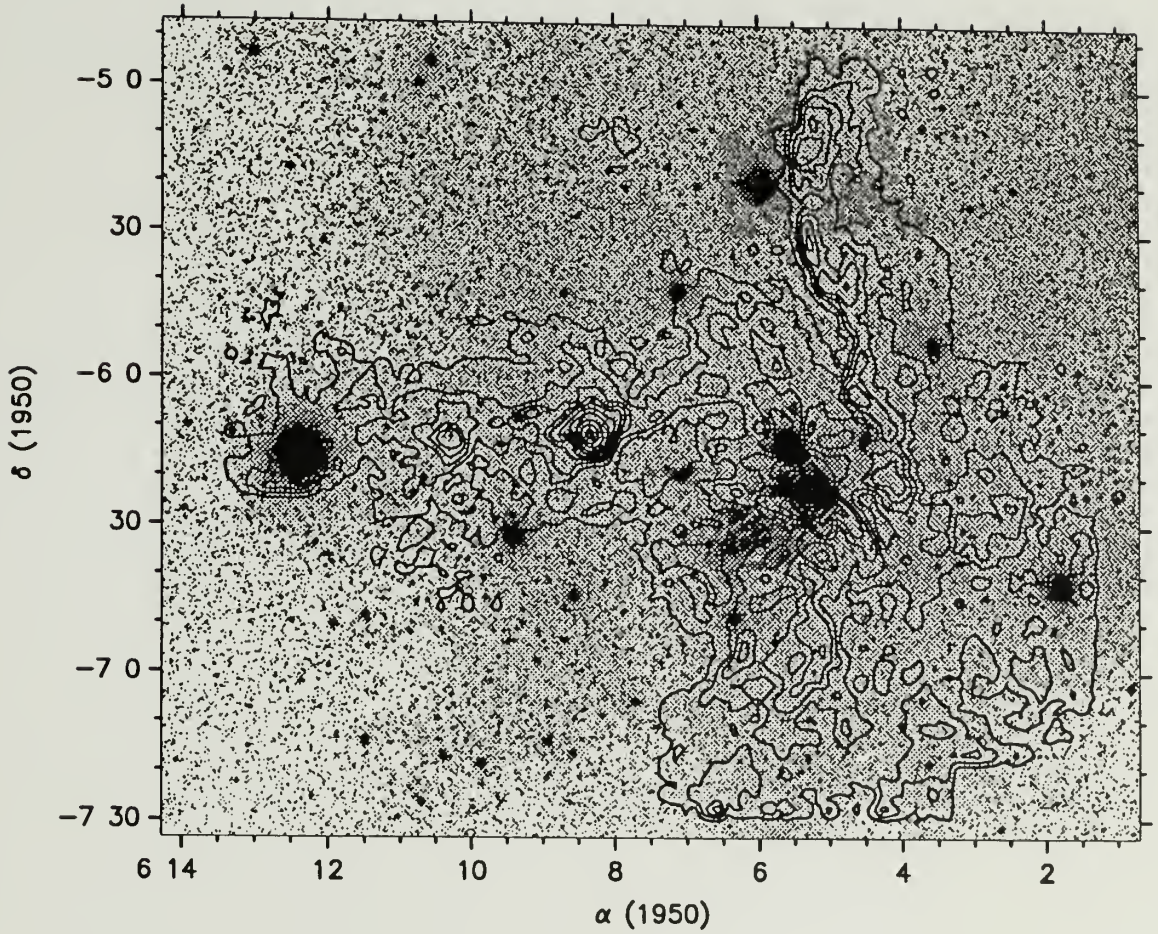
Figure 2.2. Contour Map of the $^{13}CO\ J = 1-0$ integrated intensity (solid contours) overlayed with POSS red print (halftone). Levels of contours are 1, 3, 5, 7, 9, 12, 15, 20, 25, 30, 35, 40 K km/s.

for $^{12}CO\ J = 1-0$ and $^{13}CO\ J = 1-0$ emission, respectively. To facilitate our discussions throughout the thesis from here to there, we have indicated in all these velocity channel maps the positions of reflection nebulae. Although we will not discuss star formation until Chapters 4, 5 and 6, to avoid duplication we have also included in these maps the *IRAS* point sources. These *IRAS* point sources are selected based on simple color criteria (see Chapter 6). Even a quick examination of these images reveals the following main features.

1. $^{12}CO\ J = 1-0$ and $^{13}CO\ J = 1-0$ maps reveal generally the same morphology for the giant molecular cloud, and they all seem to be wispy, filamentary and tenuous, giving the impression of unity and connectedness. But $^{13}CO\ J = 1-0$ appears much more filamentary with more visible individual features, while $^{12}CO\ J = 1-0$ appears to have more connectivity. This is consistent with the large optical depth of $^{12}CO\ J = 1-0$ as a result of the much larger abundance of CO.

2. The outline of the gas emission ($^{12}CO\ J = 1-0$ in particular) is in general consistent with that of the regions with strong extinction (Kutner & Tucker 1975; see also Tomita 1990), which were roughly divided into several dark clouds denoted L1643, L1644, L1645 and L1646 (Lynds 1962; POSS overlay 1979; Dixon & Sonneborn 1980), except the gas emission appears much more wispy and filamentary than the extinction map reveals.

3. The strongest emission of both $^{12}CO\ J = 1-0$ and $^{13}CO\ J = 1-0$ occurs at $\alpha(1950) = 06^h05^m22^s$, $\delta(1950) = -06°22'25"$, where, as pointed out in Chapter 1, active star formation has been taking place in the dense gas traced by millimeter transitions of molecules such as CS, NH_3, HCO^+, HCN, etc. (see Chapter 4 for a detailed discussion). In fact, that is also where a cluster of reflection nebulae, RN3-8, are located (Figure 1.1). Hereafter we will refer
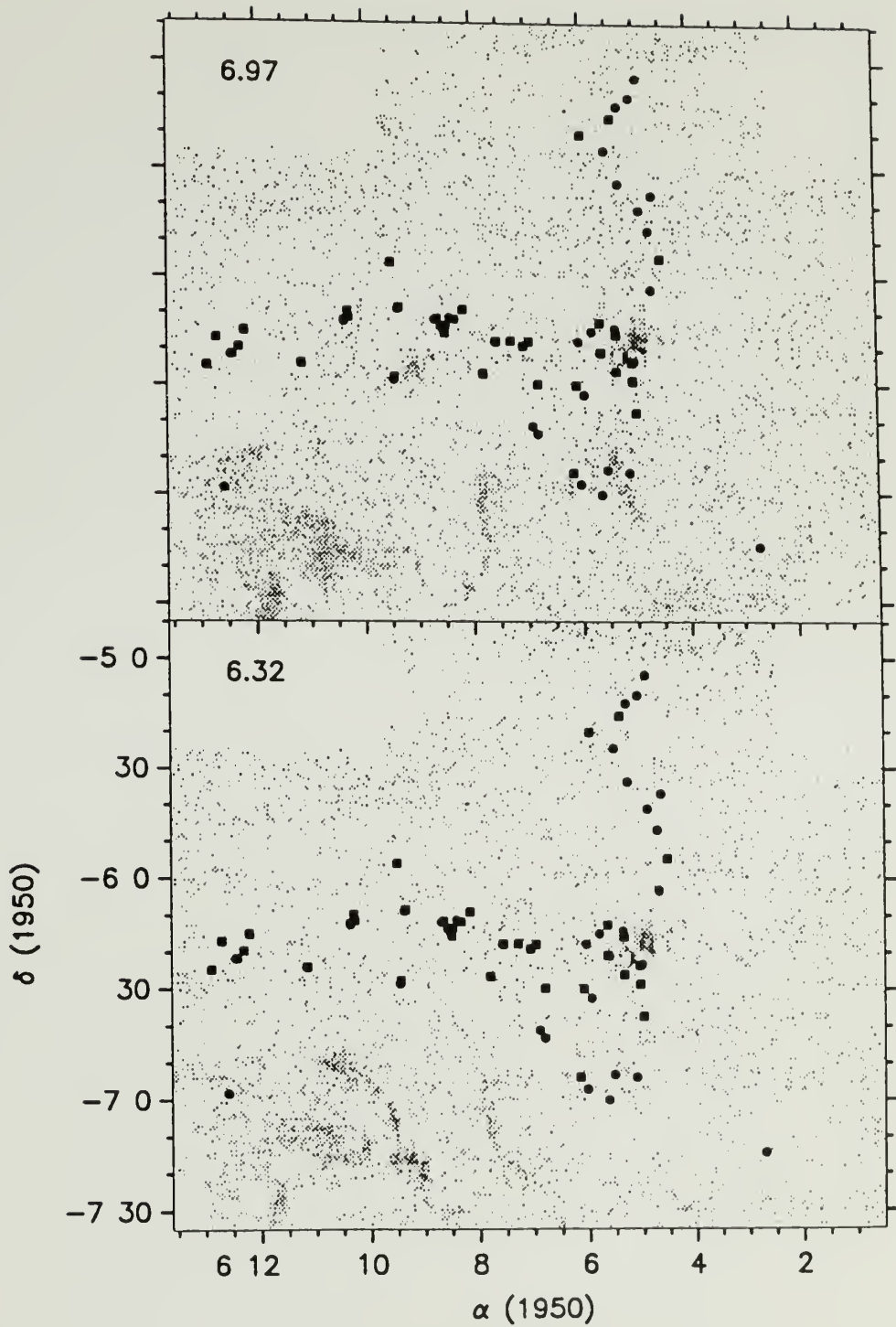
Figure 2.3. ^{12}CO $J = 1 - 0$ emission for two different velocity channels within a bandwith of 0.65 km s^{-1} . The background level is 1 K (white), and the foreground level is 6 K (black). Reflection nebulae are indicated by solid squares, and $IRAS$ point sources are indicated by solid circles.
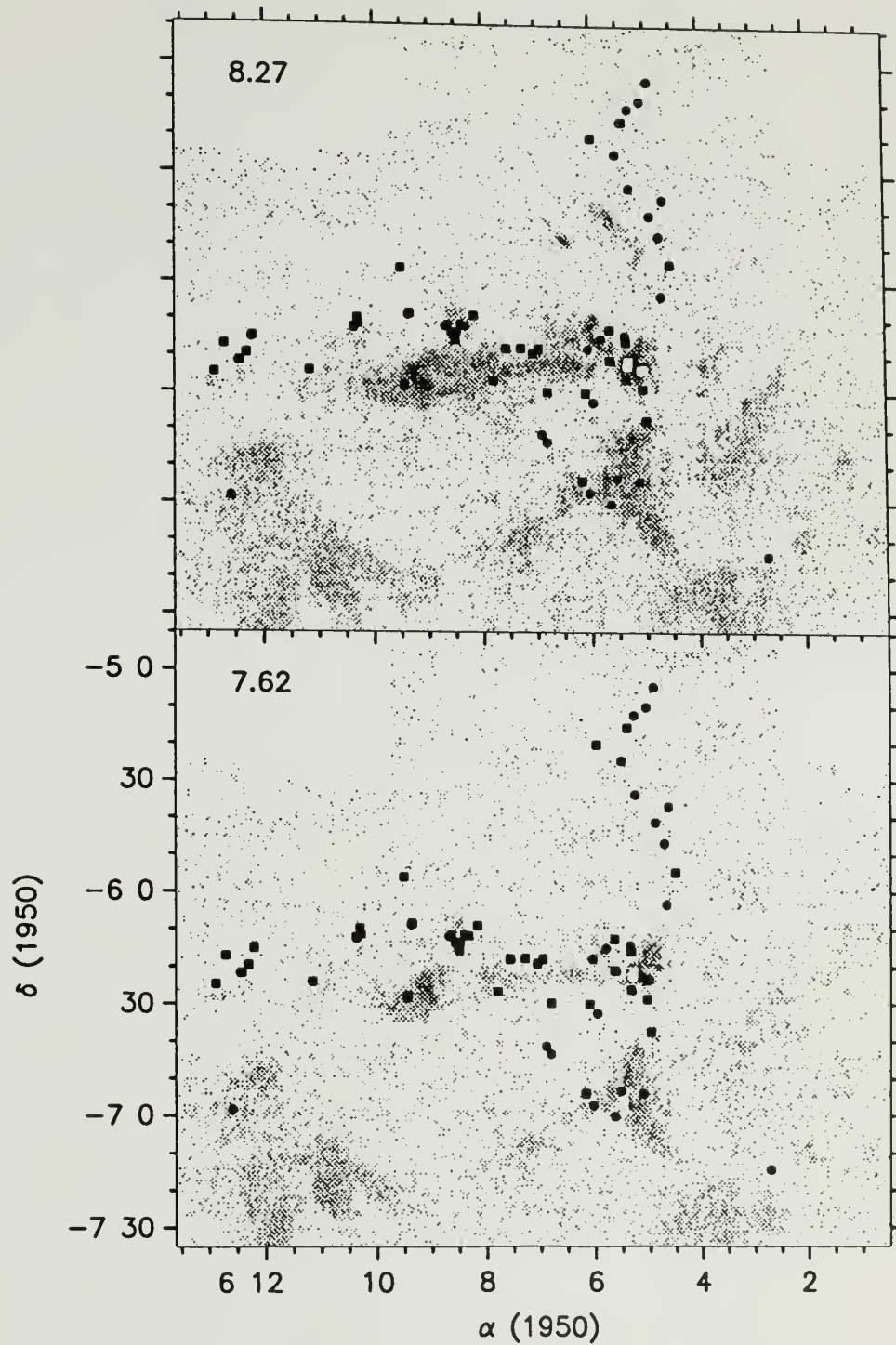
Figure 2.4. Same as Figure 2.3, but for $V_{LSR} = 7.62$ and 8.27 km s^{-1} .
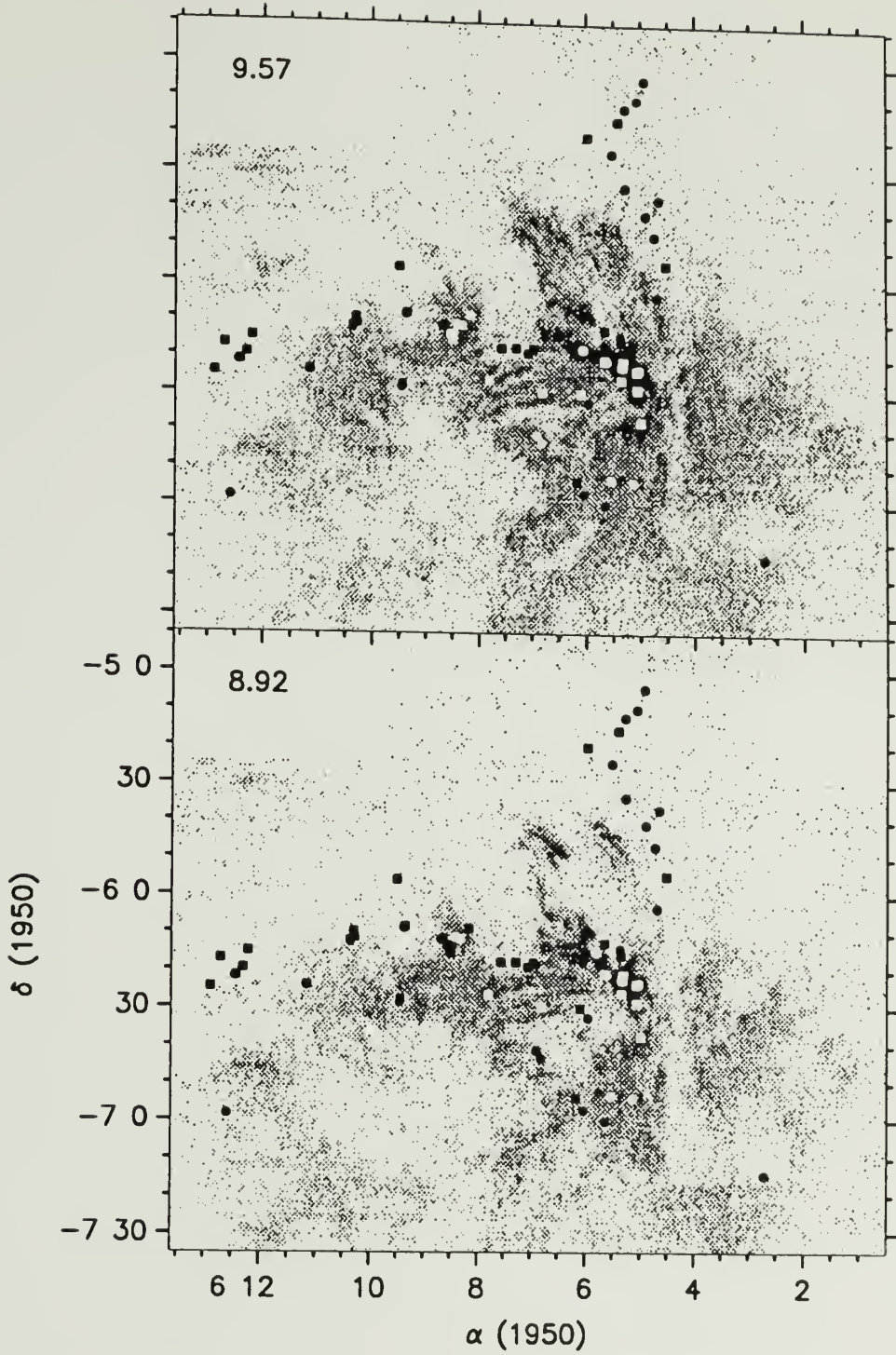
Figure 2.5. Same as Figure 2.3, but for $V_{LSR} = 8.92$ and 9.57 km s^{-1} .
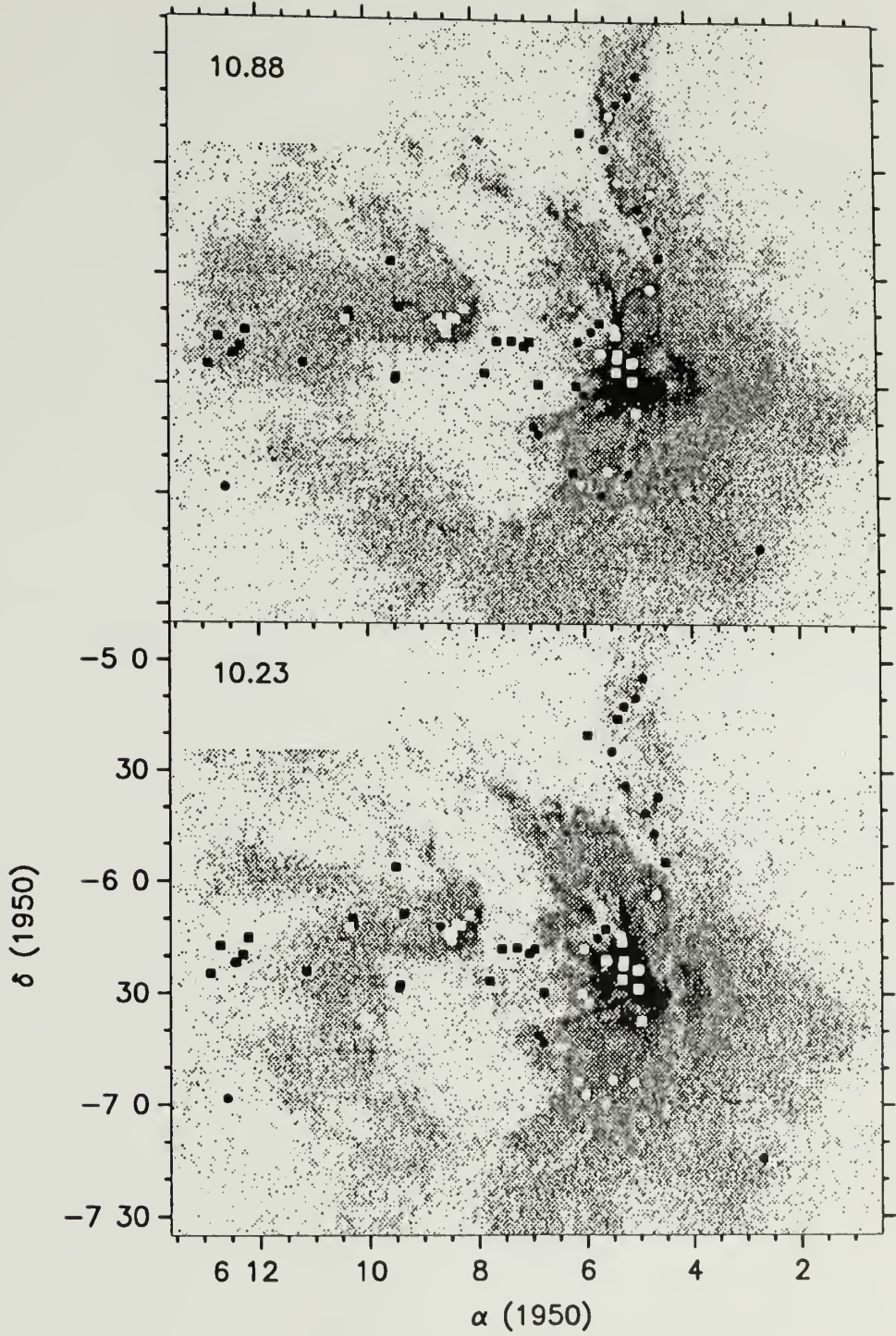
Figure 2.6. Same as Figure 2.3, but for $V_{LSR} = 10.23$ and $10.88\ km\ s^{-1}$.
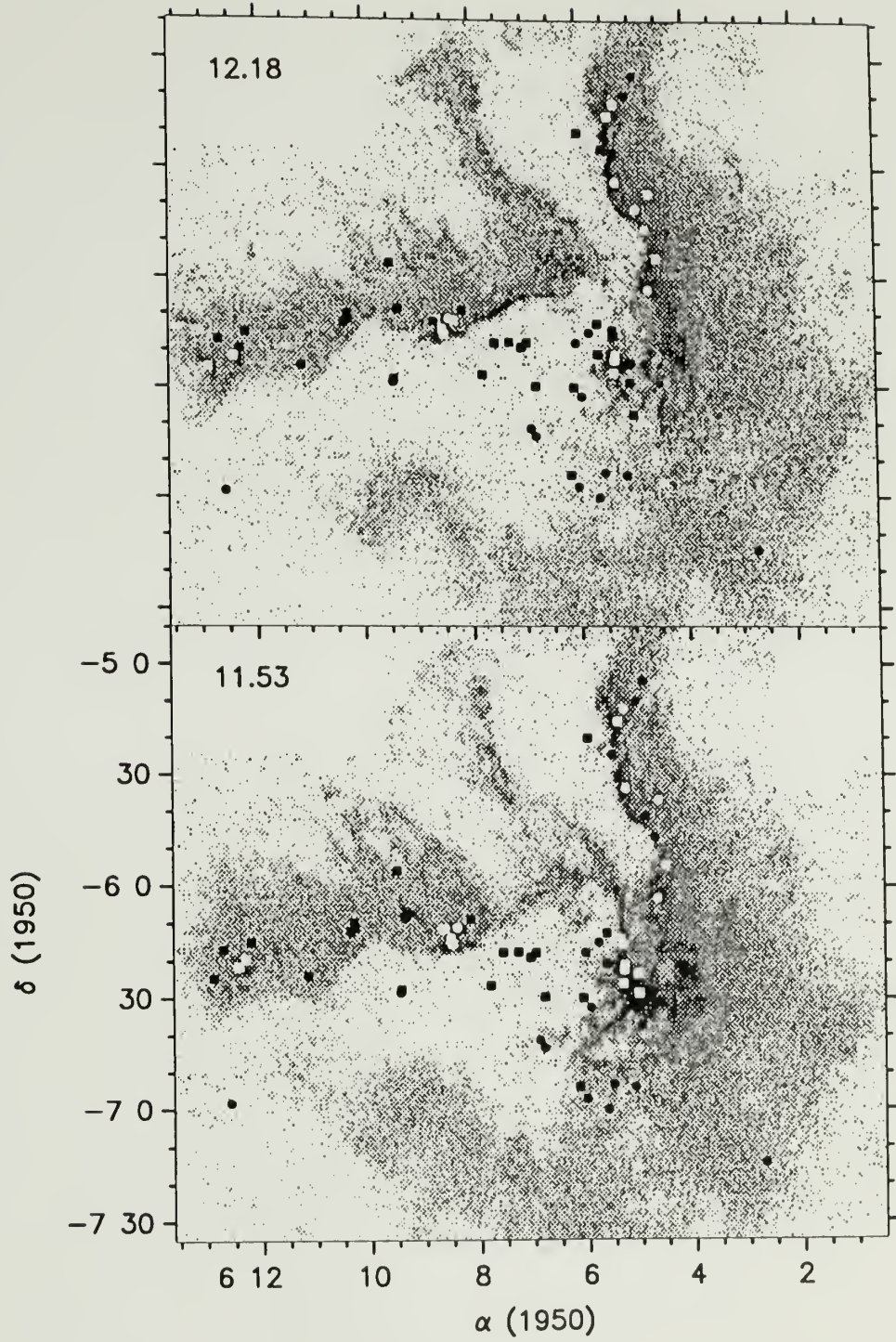
Figure 2.7. Same as Figure 2.3, but for $V_{LSR} = 11.53$ and 12.18 $km\ s^{-1}$.
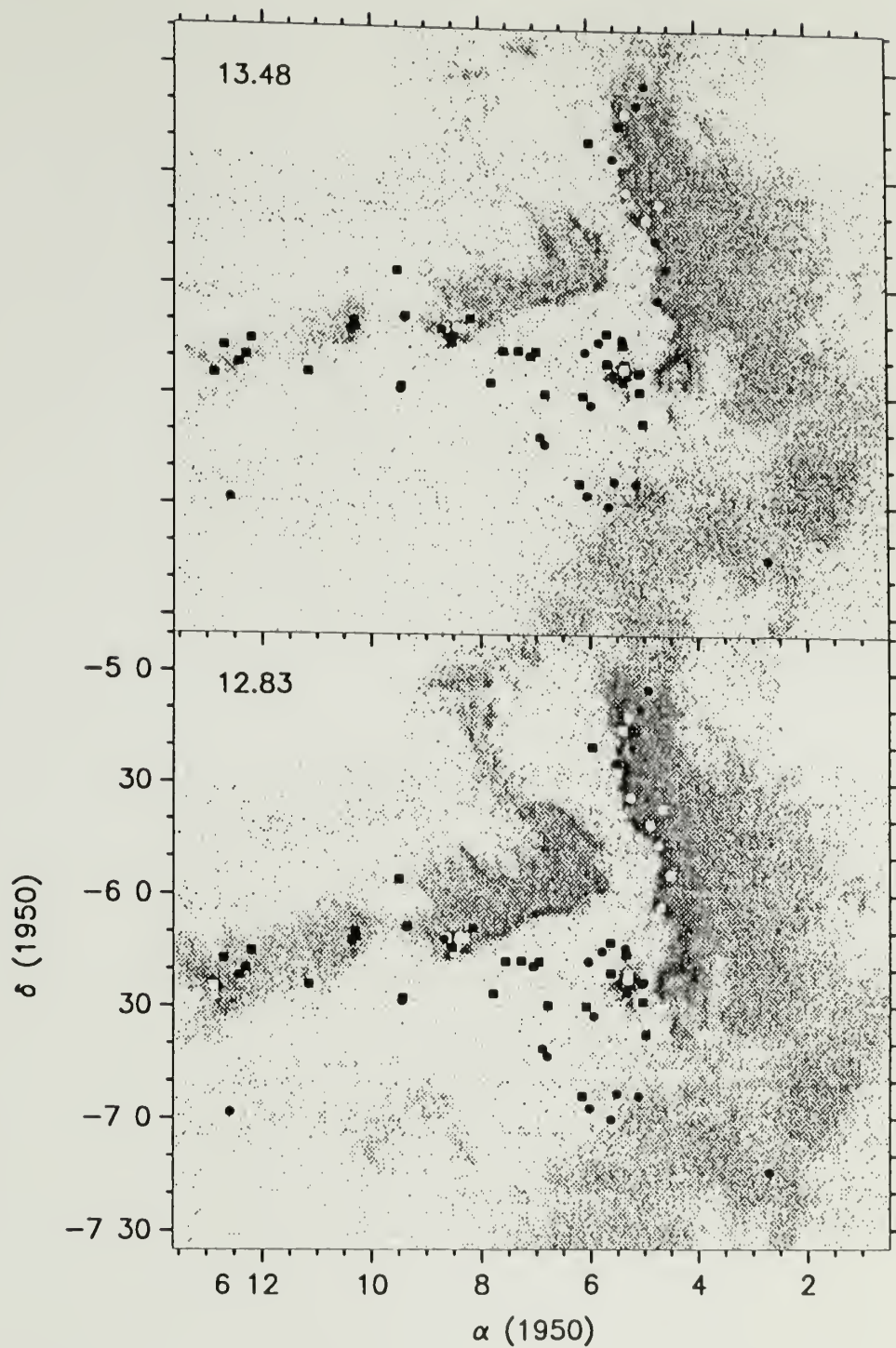
Figure 2.8. Same as Figure 2.3, but for $V_{LSR} = 12.83$ and 13.48 $km\ s^{-1}$.
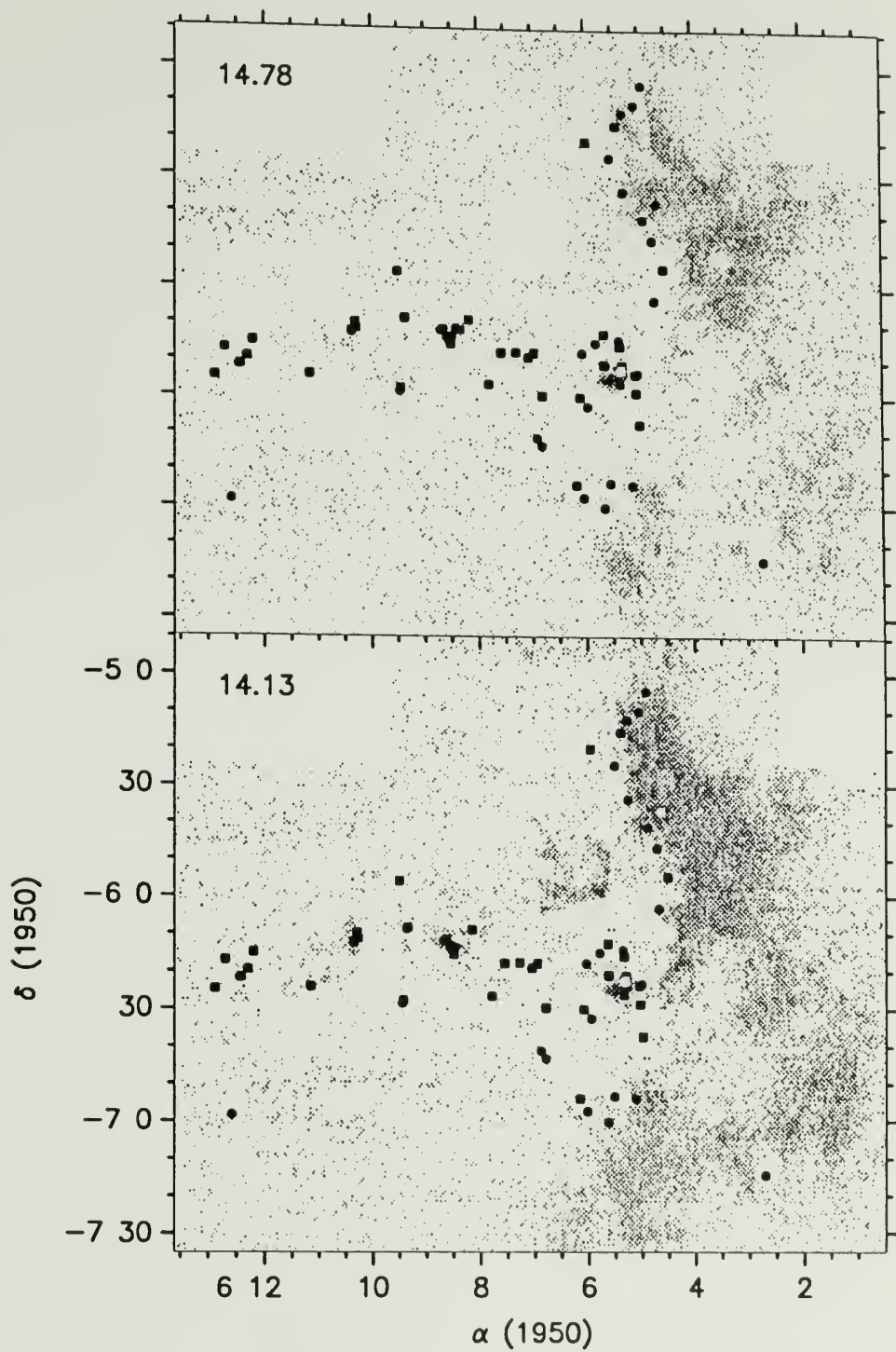
Figure 2.9. Same as Figure 2.3, but for $V_{LSR} = 14.13$ and $14.78 \ km \ s^{-1}$.
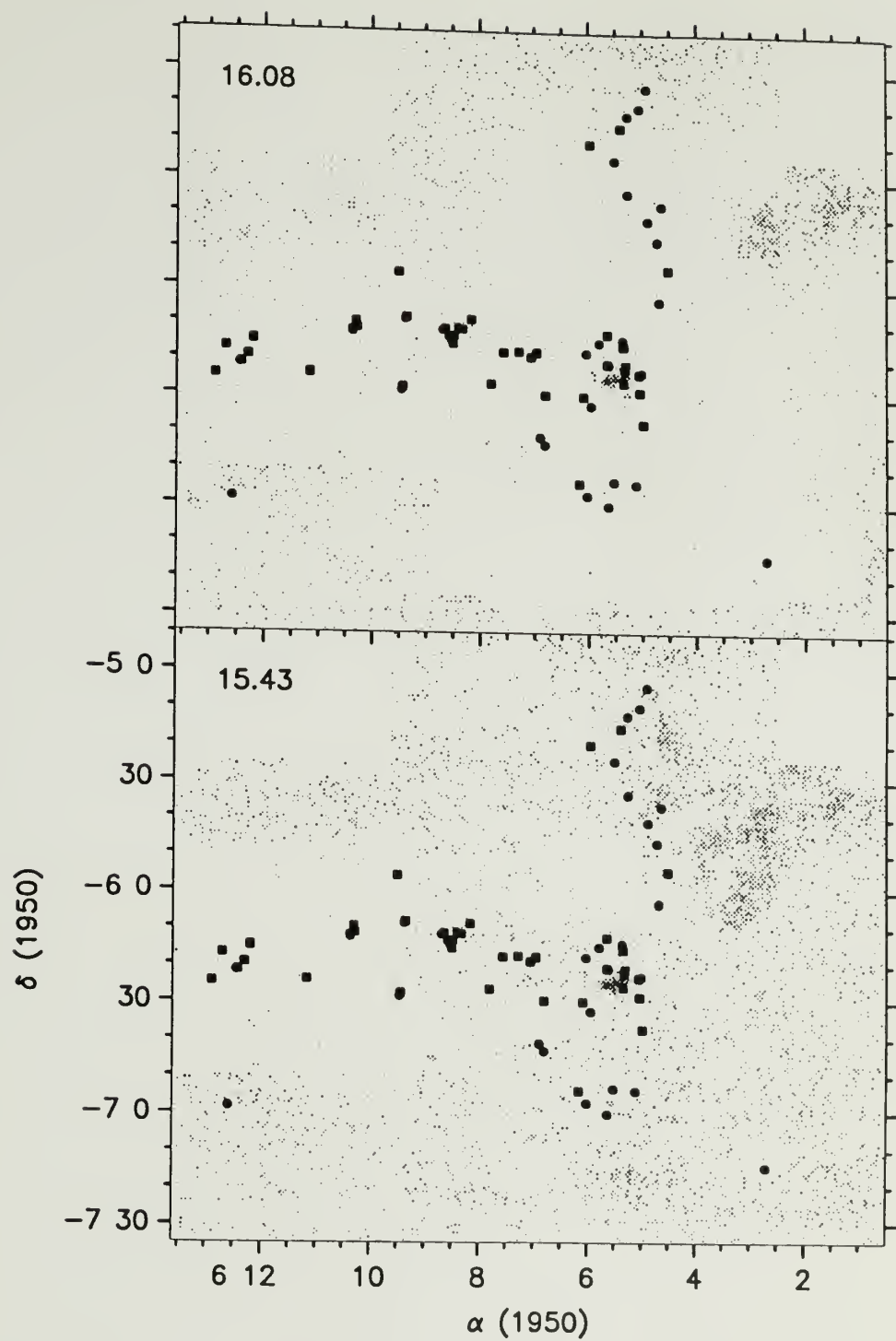
Figure 2.10. Same as Figure 2.3, but for $V_{LSR} = 15.43$ and 16.08 km s^{-1} .

to this peaked emission region as "the main core". Roughly 45' to the east of this core, there appears a second emission peak of $^{12}CO\ J = 1 - 0$ and $^{13}CO\ J = 1 - 0$, which coincides with another small cluster of reflection nebulae, RN17-22 and RN30 (see Figure 1.1) and which is also a site of star formation and strong emission of the aforementioned high density gas tracers (again see Chapter 4 for a detailed discussion). Hereafter we will refer to this core of gas as the GGD12-15 region for historical reasons (e.g., Little, Heaton & Dent 1990). To the east of this core, we find a few more regions of intense emission almost all of which are centered on small groupings of reflection nebulae. We will call these regions according to their association with reflection nebulae. Specifically, they are the RN23 region, the RN24-25/RN29 region, and the RN26-28 region, as labeled in Figures 1.1 and 1.2. Notably, RN24-25/RN29 region is also where GGD16-17 (GGD) are located.

4. One very peculiar fact is that some reflection nebulae, such as RN11-16 region and RN10 region, seem to be coincident with minima of gas emission. These are actually related with HII regions (RN11-16, Hughes & Baines 1985; R10, HR). We will discuss the significance of this fact in Chapter 6.

5. Both the main core and the GGD12-15 core have very low and very high velocity gas emission, which are the known bipolar outflows as mentioned in Chapter 1 (see Chapter 5 for a detailed discussion).

6. In the western portion of the cloud, there appears a strikingly sharp N-S oriented ridge of emission, most conspicuous in high velocity channels. There also appears a roughly East-West oriented emission ridge in the eastern portion of the cloud along the remarkable cometary shape of the GGD12-15 region and a chain of other cores.

7. The sharp emission ridges appear corrugated, suggesting kinematic instability of shock front development (Chevalier & Theys 1975; Vishniac 1983; Hunter *et al* 1986; Kimura & Tosa 1988; Elmegreen 1989; 1992).

8. At low LSR velocities the gas emission shows very wispy features and is concentrated mainly in the central part and at the S-E corner, while at higher LSR velocities the gas emission appears more in the outer part of the mapped region, along the N-S emission ridge, and in the N-W corner in particular. This velocity gradient is along the elongation of the cloud, which in turn is consistent with the direction of the galactic plane and the magnetic field (Dyck & Lonsdale 1979). But the velocity gradient is opposite to that expected from galactic rotation (Hughes & Baines 1985). The $^{12}CO\ J = 1 - 0$ peak antenna temperature map and some velocity channel maps on a large scale are actually suggestive of a circular morphology (conspicuous in the channel map at $V_{LSR} = 10.2km\ s^{-1}$ at the lower-left portion) except in the very north where the roughly vertical emission ridge appears. This large-scale circular feature seems to correspond very well to the enhanced background optical emission (Figure 1.1).

9. Between the adjacent velocity channels (0.65 $km\ s^{-1}$ separation for $^{12}CO\ J = 1 - 0$ and 0.5 $km\ s^{-1}$ for $^{13}CO\ J = 1 - 0$), many small features may appear or disappear or take a rather different shape, indicating the importance of the complex kinematic motions in the cloud.

10. $^{12}CO\ J = 1 - 0$ line profiles all over the cloud are mostly single-peaked, but they do show up as double-peaked features in five regions; the main core, GGD12-15, a small region above NGC2182, south-east corner and south-west corner. $^{13}CO\ J = 1 - 0$ emission agrees with that of $^{12}CO\ J = 1 - 0$ emission except in the main and GGD12-15 cores, indicating that the double-peaked line profiles of $^{12}CO\ J = 1 - 0$ in the two cores are the result of self-reversal.

11. At velocities close to $V_{LSR} = 11\ km\ s^{-1}$ there appears an eggplant-shaped shell feature extending from the main core to the N-W direction to the N-S emission ridge for about 25' or so. This is the limb-brightened shell of the blue-shifted bipolar outflow lobe, as we will further discuss in Chapter 5.

12. Large or small voids or holes, several of which are roundish, are conspicuous on some velocity channel maps.

2.3 Comparison of $^{12}CO\ J = 1 - 0$ and $^{13}CO\ J = 1 - 0$ Emission

Before we go too far in this thesis, let us first examine a "simple" question that most people would ask: is $^{12}CO\ J = 1 - 0$ a good kinematic tracer as $^{13}CO\ J = 1 - 0$ is in Mon R2 ? To answer this question, let us first briefly review the results of previous research concerning $^{12}CO\ J = 1 - 0$ and $^{13}CO\ J = 1 - 0$ emission. Few people would argue against the fact that $^{13}CO\ J = 1 - 0$ integrated intensity can be reliably transformed into the total column density of H_2 along a line of sight[2] since the pioneering works of Dickman (1976, 1978a) (see also later discussions by Frerking, Langer & Wilson 1982; Langer *et al* 1989; Jarrett, Dickman & Herbst 1989; Dickman & Herbst 1990). It is, however, very controversial what $^{12}CO\ J = 1 - 0$ exactly traces. Since the universal abundance of ^{12}C is believed to be 60-89 times that of ^{13}C in nature, it is natural that ^{12}CO emission from molecular clouds is typically found to be stronger than that of ^{13}CO. But the ratio of $^{12}CO\ J = 1-0$ and $^{13}CO\ J = 1 - 0$ peak intensities are generally found to be in the range of a few to ten except for the wings of line profiles, much smaller than the abundance ratio. This can be easily explained in terms of the larger $^{12}CO\ J = 1 - 0$ optical depth and significant saturation. It is based on this knowledge that peak temperature of $^{12}CO\ J = 1 - 0$ is generally used as a gas thermometer (at least for material

---

[2]At least for small to moderate visual extinction A_v.
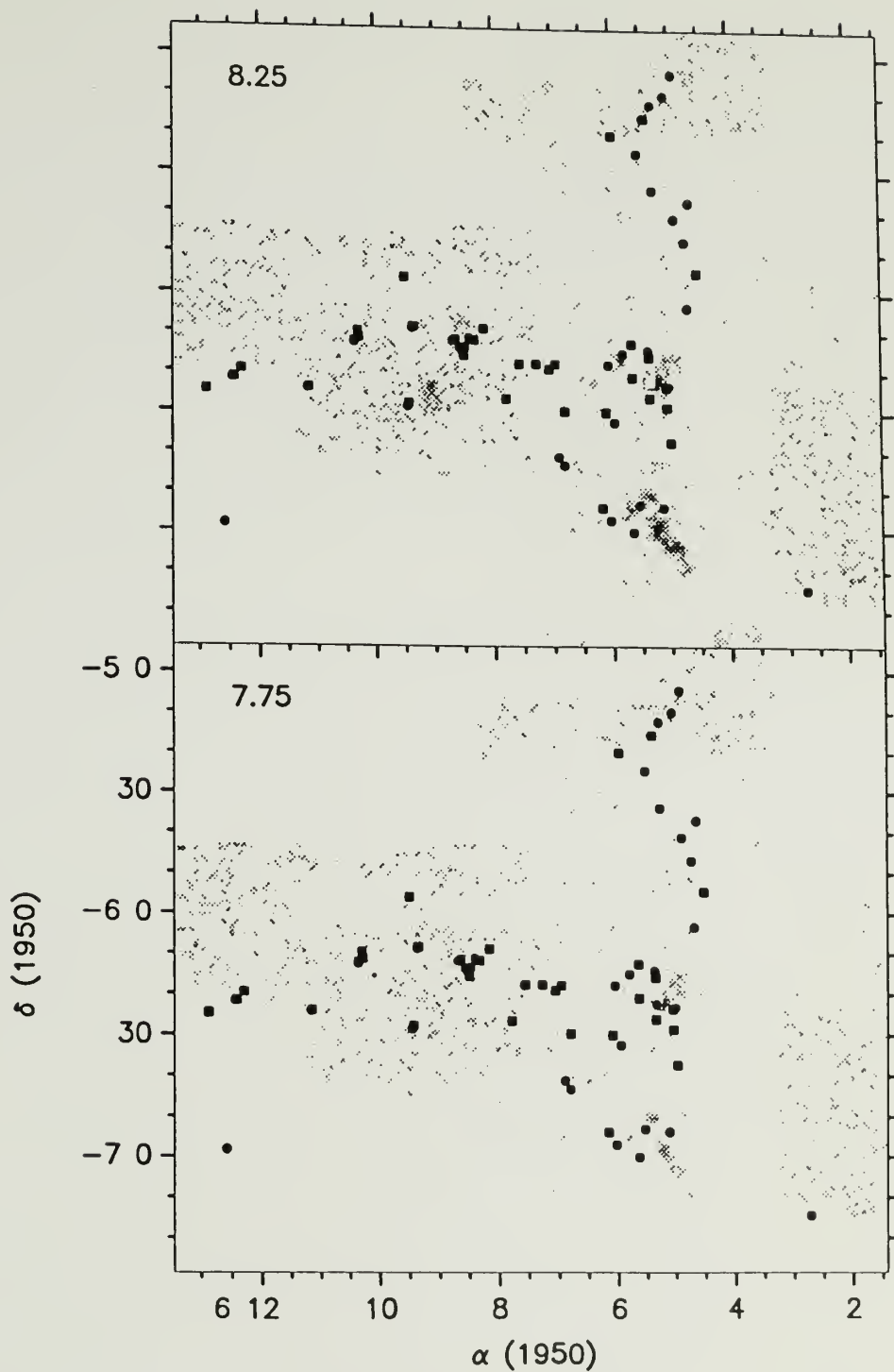
Figure 2.11. ^{13}CO $J = 1 - 0$ emission in two different velocity channels within a bandwidth of $0.5 km$ s^{-1} . The background level is 0.5 K (white), and the foreground level is 4 K (black). Reflection nebulae are indicated by solid squares, and *IRAS* point sources are indicated by solid circles.
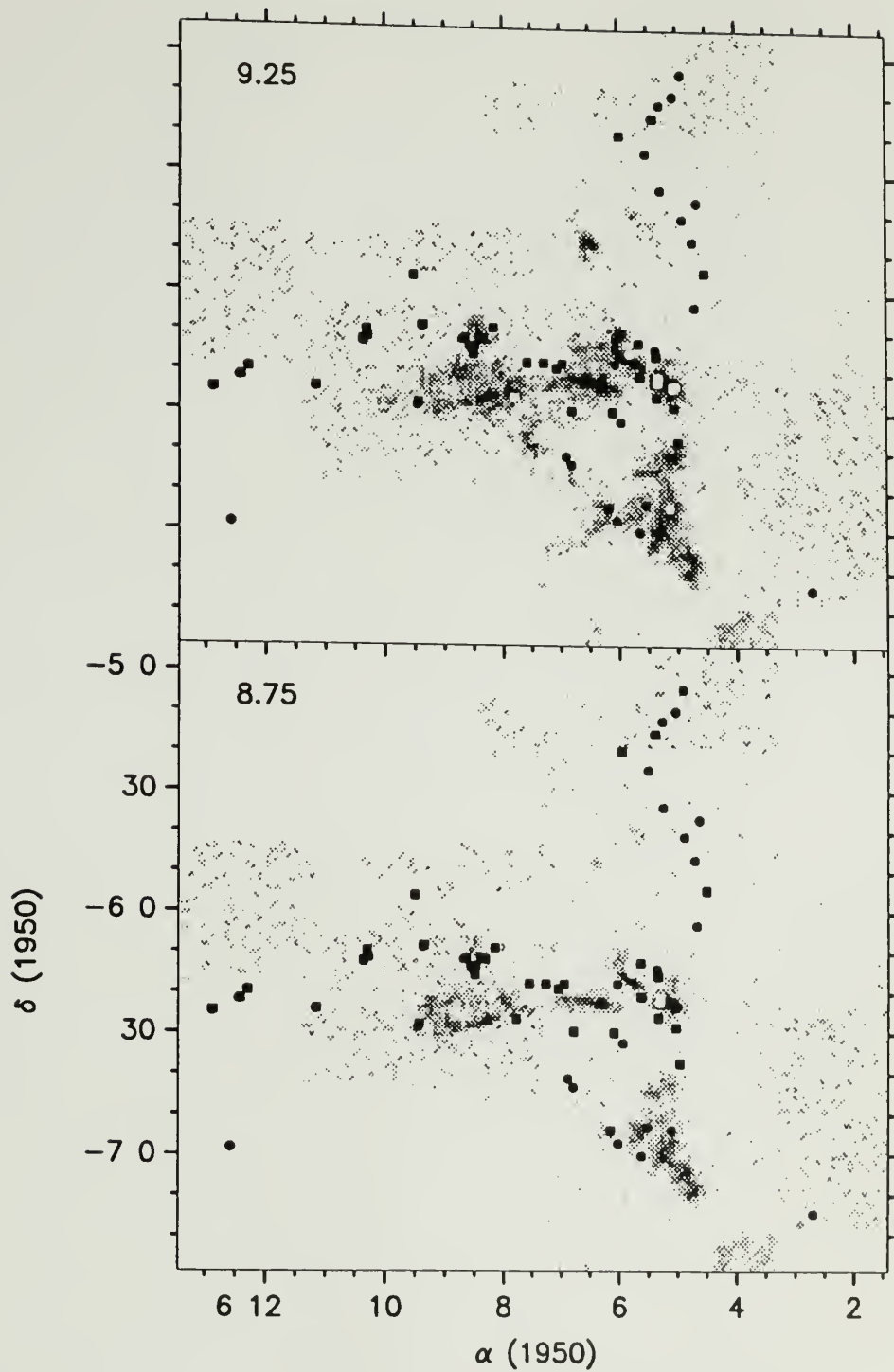
Figure 2.12. Same as Figure 2.11, but for $V_{LSR} = 8.75$ and 9.25 $km\ s^{-1}$.
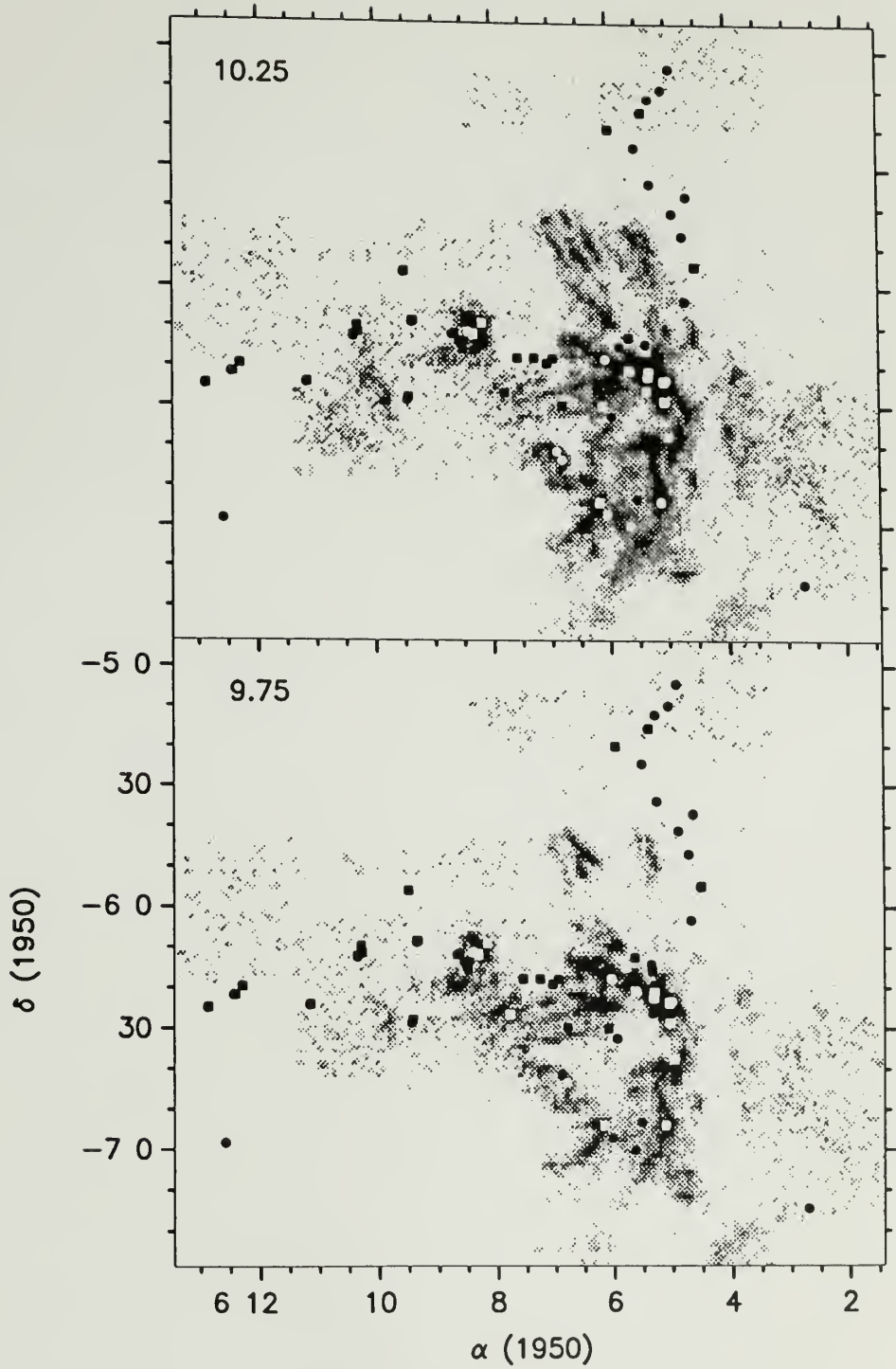
Figure 2.13. Same as Figure 2.11, but for $V_{LSR} = 9.75$ and $10.25\ km\ s^{-1}$.
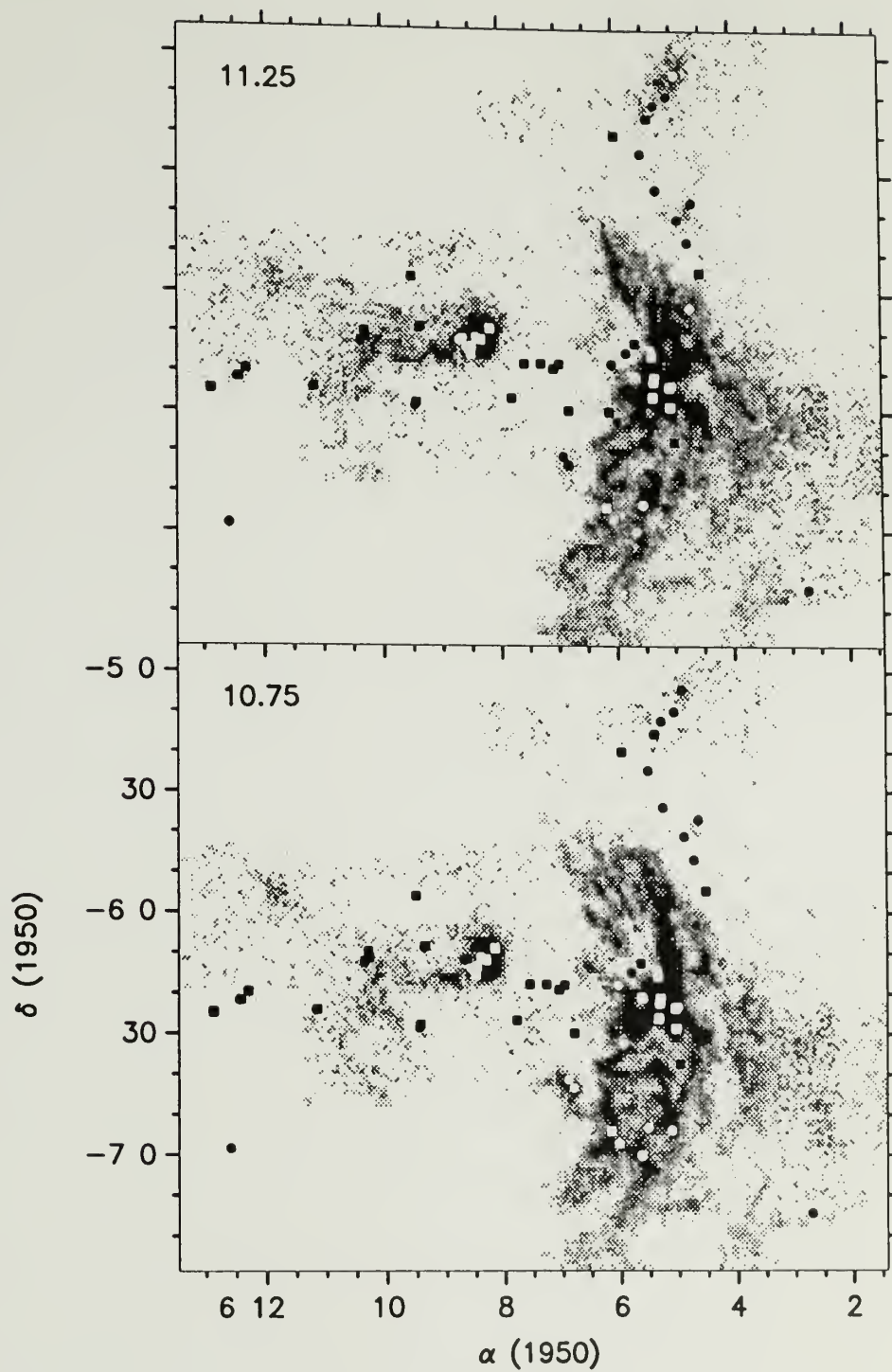
Figure 2.14. Same as Figure 2.11, but for $V_{LSR} = 10.75$ and 11.25 $km\ s^{-1}$.
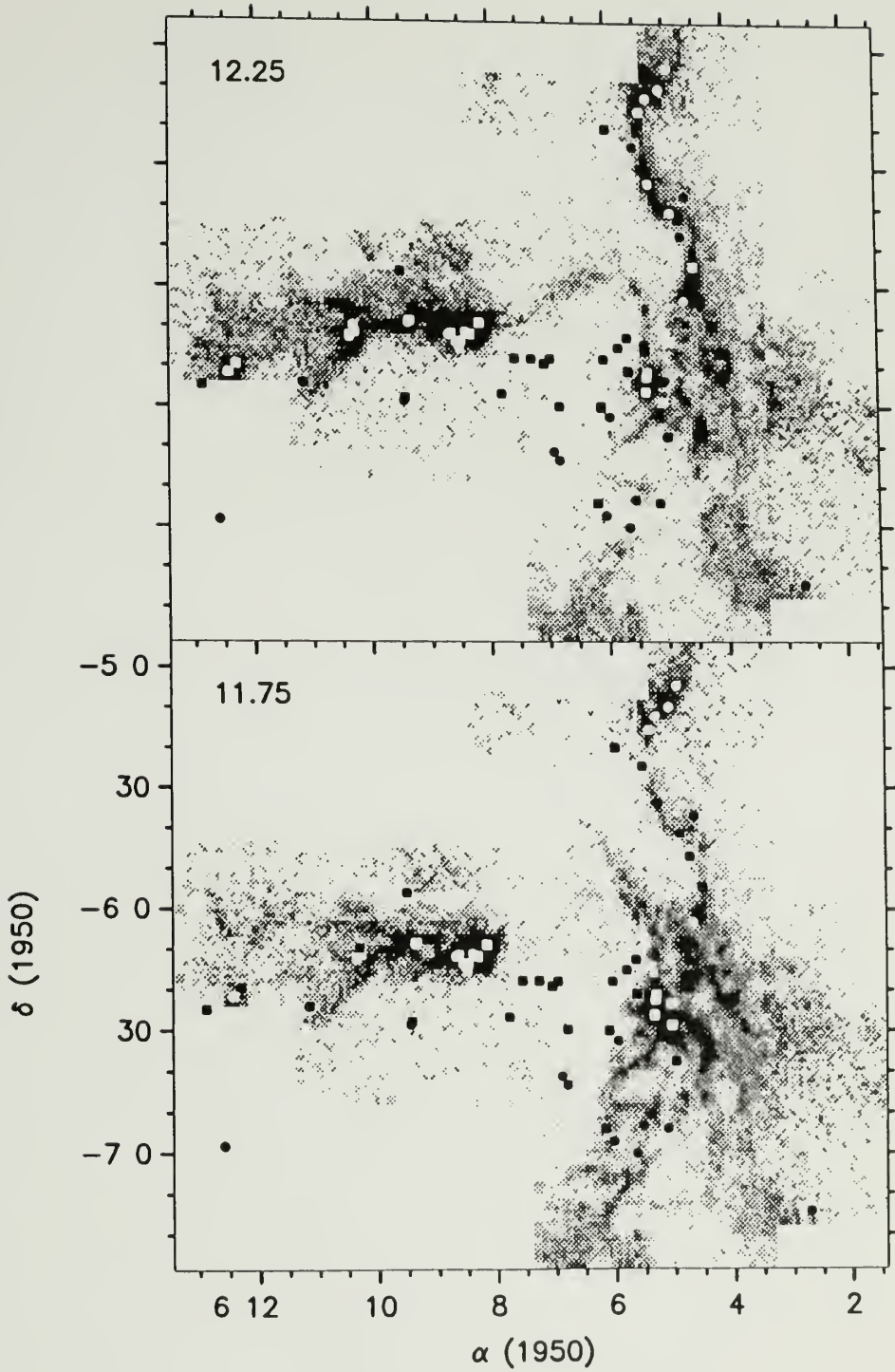
Figure 2.15. Same as Figure 2.11, but for $V_{LSR} = 11.75$ and $12.25\ km\ s^{-1}$.
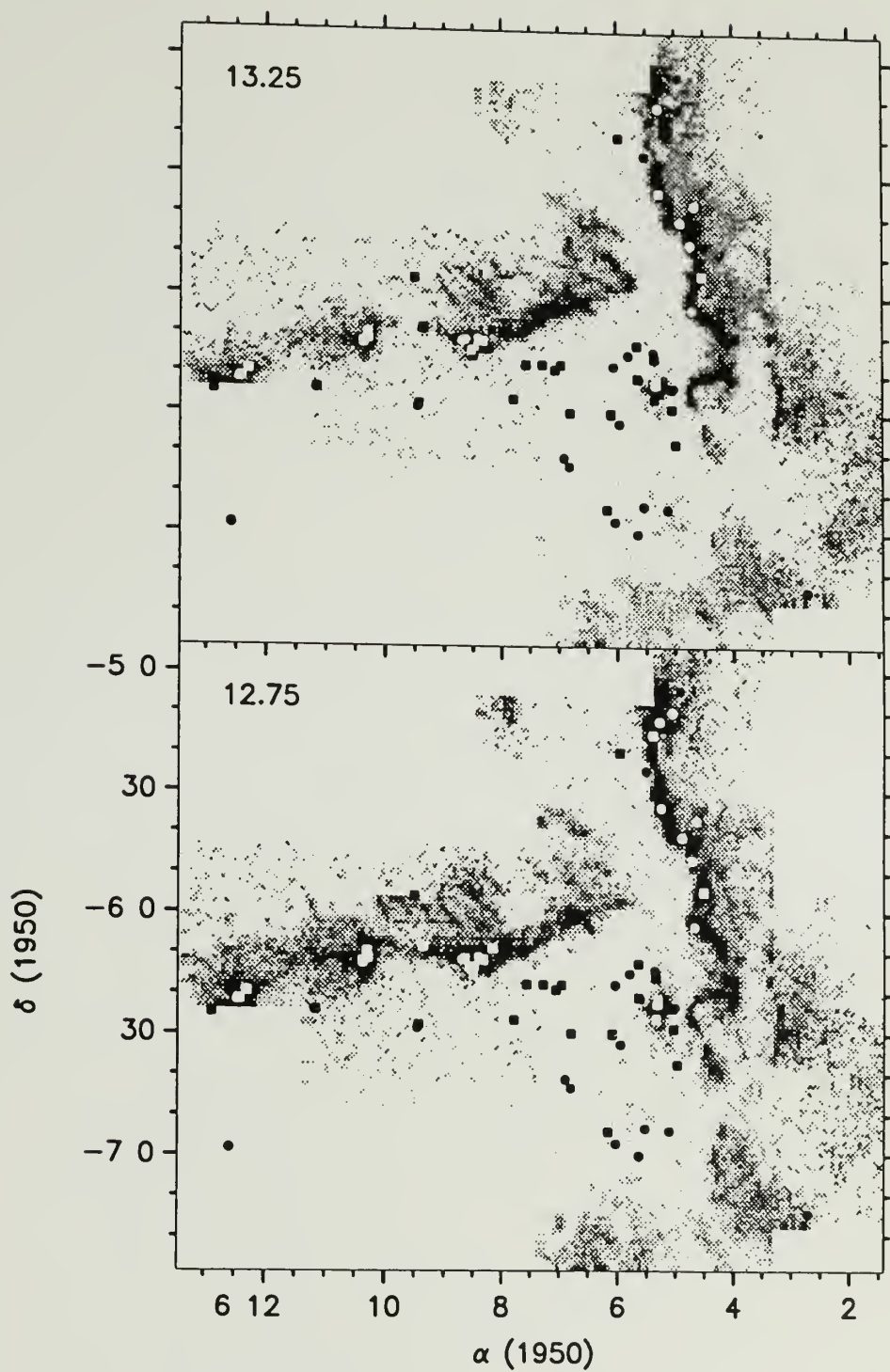
Figure 2.16. Same as Figure 2.11, but for $V_{LSR} = 12.75$ and 13.25 km s^{-1} .
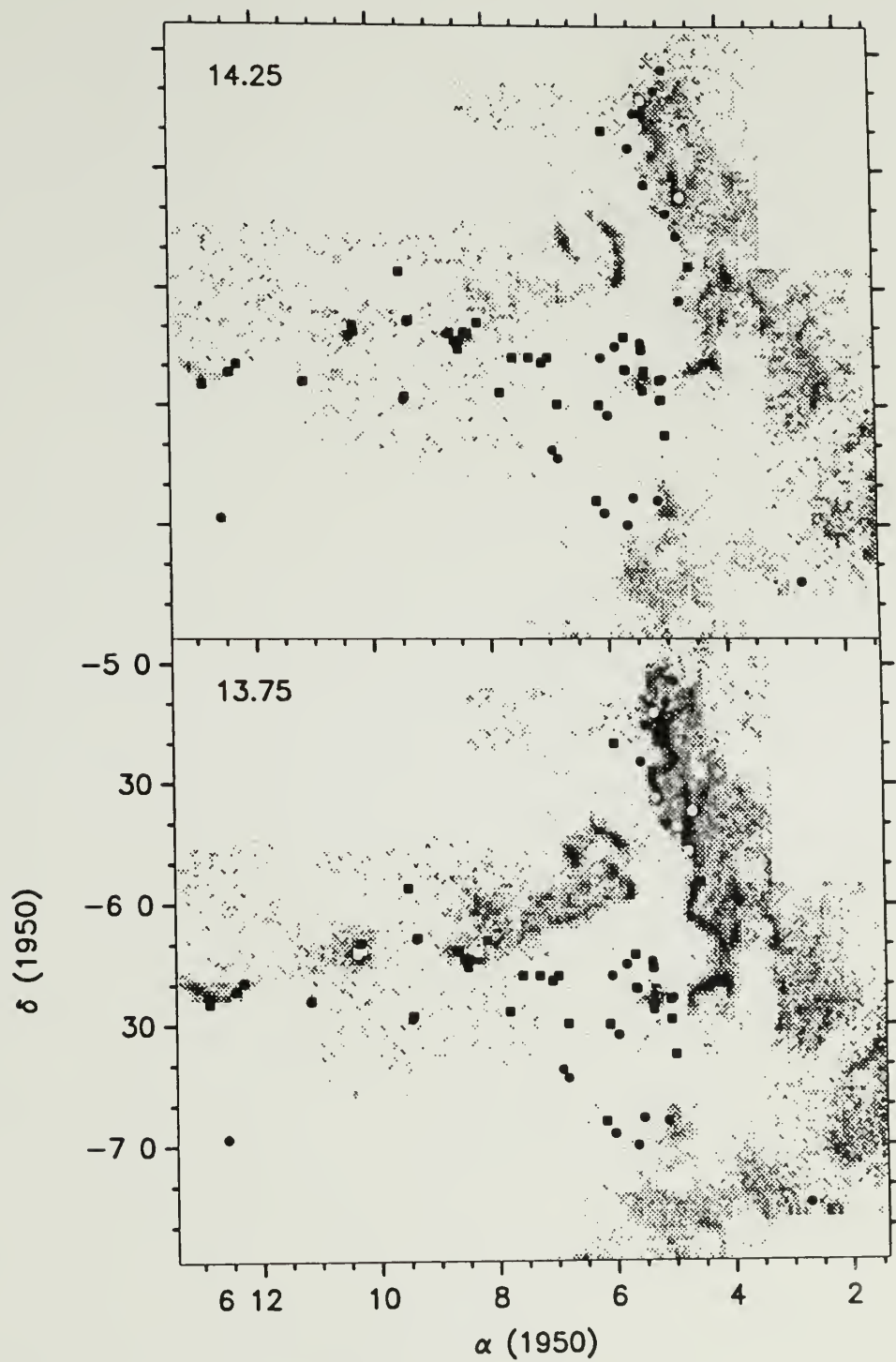
Figure 2.17. Same as Figure 2.11, but for $V_{LSR} = 13.75$ and 14.25 km s^{-1} .
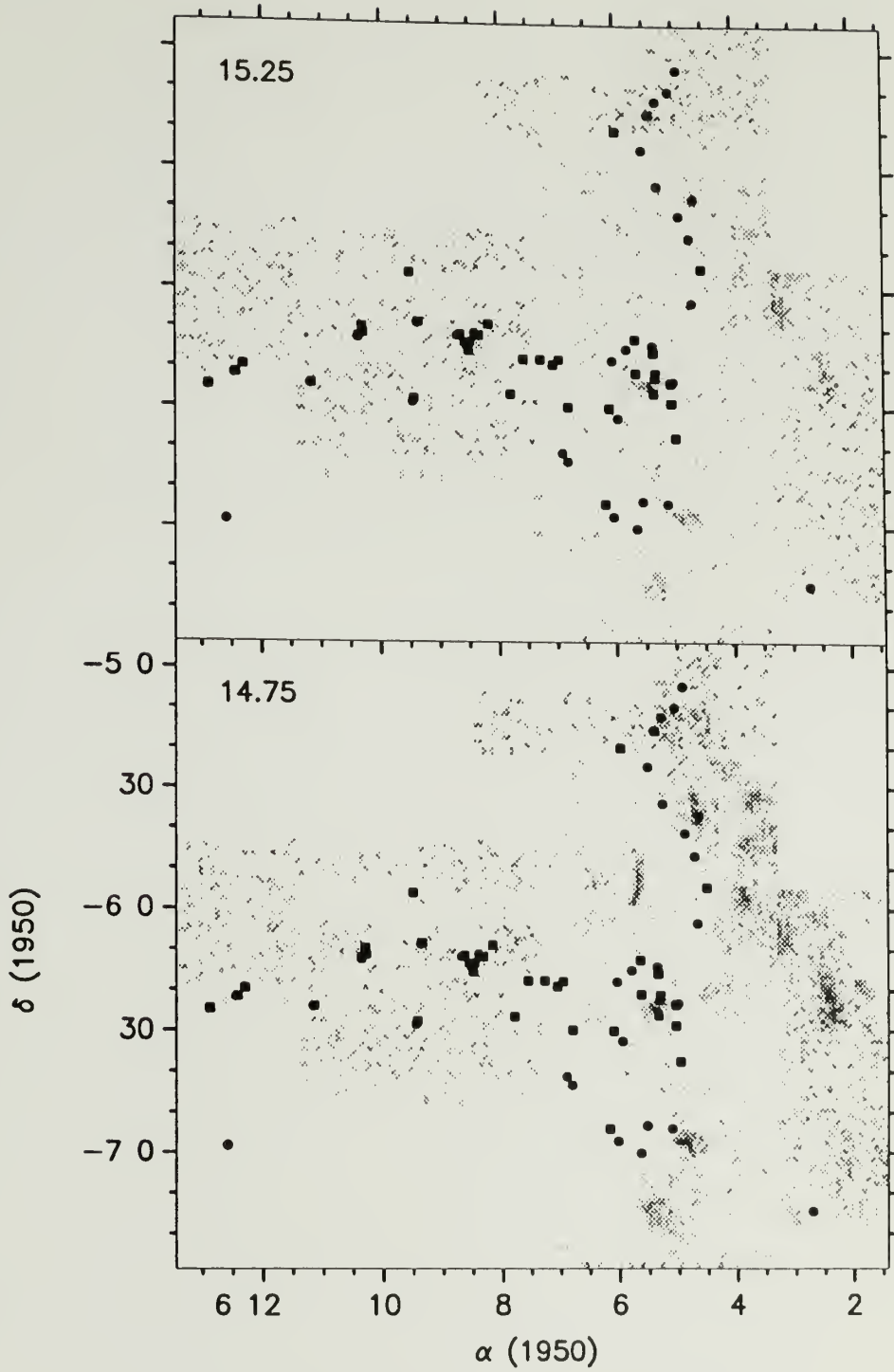
Figure 2.18. Same as Figure 2.11, but for $V_{LSR} = 14.75$ and 15.25 km s^{-1} .

near cloud surface)(cf. Goldsmith 1988). The central issue is what the integrated intensity of $^{12}CO \ J = 1 - 0$ traces. Theoretically, one would not expect that the integrated intensity of an optically thick species to be able to provide any reliable information about the column density because of saturation (see Langer *et al* 1989 for a case), but in case both $^{12}CO \ J = 1 - 0$ and $^{13}CO \ J = 1 - 0$ data are available, the two integrated intensities are found to be correlated (Dickman 1978a; Liszt 1982). It is based on this empirical fact that some authors do believe that $^{12}CO \ J = 1 - 0$ integrated intensity is a linear tracer of column density just as $^{13}CO \ J = 1 - 0$ integrated intensity does (Liszt 1982; Sanders, Solomon & Scoville 1984; Dickman, Snell & Schloerb 1986; Scoville & Sanders 1987; Solomon *et al* 1987). Langer *et al* (1989) studied the dark cloud B5 in Perseus with their data set of CO isotopes and extinction, and found that although $^{12}CO \ J = 1-0$ integrated intensity does show a positive correlation with that of $^{13}CO \ J = 1 - 0$, the relationship is not linear and resembles the growth curve of a saturated line, implying that this positive correlation is the result of saturation broadening effects.

In this section, we wish to examine the relationship of $^{12}CO \ J = 1 - 0$ and $^{13}CO \ J = 1 - 0$ data to see if $^{12}CO \ J = 1 - 0$ can be used as a reliable kinematic tracer. Although we do provide least-squares fits to correlations, a comprehensive approach to what $^{12}CO \ J = 1 - 0$ and $^{13}CO \ J = 1 - 0$ exactly trace quantitatively is beyond the scope of this thesis.

2.3.1 *Pixel-Pixel Correlation*

To compare the $^{12}CO \ J = 1 - 0$ and $^{13}CO \ J = 1 - 0$ emission for the whole GMC, we have smoothed and resampled the FCRAO $^{12}CO \ J = 1 - 0$ data onto the resolution and sampling of the Bell Labs $^{13}CO \ J = 1 - 0$ data. First we notice that the ratio of $^{12}CO \ J = 1 - 0$ and $^{13}CO \ J = 1 - 0$ integrated intensities in the region covered by both tracers ranges from as low as close to 1 in the GGD12-15 region to

about 5 in the weak emission region. Thus under the assumption that the ^{12}C to ^{13}C abundance ratio in the cloud is close to the solar system value of 40-89 (Geiss 1988; Langer & Penzias 1990), $^{12}CO\ J = 1 - 0$ should be generally optically thick while $^{13}CO\ J = 1 - 0$ may be marginally thin.

Figure 2.19 shows the quantitative pixel-pixel comparison of the $^{12}CO\ J = 1 - 0$ and $^{13}CO\ J = 1 - 0$ emission. While the scatter is fairly large, a clear correlation does exist between the two gas tracers. The correlation can be best fit by $\int T_A^\star(^{12}CO)dv = 5.0 + 1.3 \int T_A^\star(^{13}CO)dv$. Notice that $^{12}CO\ J = 1 - 0$ data has a main beam efficiency of 0.5, while $^{13}CO\ J = 1 - 0$ data has a main beam efficiency of 0.9. Also, we smoothed the $^{12}CO\ J = 1 - 0$ data to the resolution of the $^{13}CO\ J = 1 - 0$ data. The peculiar thing is that at higher $^{13}CO\ J = 1 - 0$ integrated intensities, there appear to be two separated branches. The lower branch is very similar to what is found by Langer $et\ al$ (1989) for the dark cloud B5. A closer examination of the data leads to the conclusion that the lower and upper branches correspond to the emission from the GGD12-15 core and the central core region, respectively. In both regions, $^{12}CO\ J = 1 - 0$ emission shows self-reversal absorption, as will be further discussed in Chapter 4. Figures 2.20 and 2.21 show the comparison between $^{12}CO\ J = 1 - 0$ and $^{13}CO\ J = 1 - 0$ emission from the two core regions. Both the $^{12}CO\ J = 1 - 0$ and $^{13}CO\ J = 1 - 0$ data are taken with the FCRAO 14m telescope. Although in both cases $^{12}CO\ J = 1 - 0$ and $^{13}CO\ J = 1 - 0$ integrated intensities demonstrate a remarkably linear correlation, the two cases differ quantitatively. The maximum $^{13}CO\ J = 1 - 0$ integrated intensities are comparable in two cores, but the $^{12}CO\ J = 1 - 0$ intensity of the GGD12-15 region is only about half of that of the main core[3]. The correlation

---

[3]The bad possibility that this lower CO emission for GGD 12-15 is a result of unexpected gain change can be ruled out. First, the telescope gain change was constantly monitored by taking a spectrum every a few minutes at the central position of the main core. Second, that CO antenna temperature of GGD 12-15 region is about only half of that for the main core is consistent with observations carried out almost two decades ago by Kutner and Tucker (1975).

between the integrated intensities of ^{12}CO $J = 1 - 0$ and ^{13}CO $J = 1 - 0$ for the main core and the GGD12-15 core can be best fit by $\int T_A^*(^{12}CO)dv = 4.2 + 3.0 \int T_A^*(^{13}CO)dv$ and $\int T_A^*(^{12}CO)dv = 10.0 + 1.4 \int T_A^*(^{13}CO)dv$, respectively. Notice that both ^{12}CO $J = 1-0$ and ^{13}CO $J = 1-0$ data have a main beam efficiency of 0.5 for the cores. As expected, correlations are also found between ^{12}CO $J = 1-0$ peak antenna temperature and ^{13}CO $J = 1 - 0$ integrated intensity as well as between ^{12}CO $J = 1 - 0$ and ^{13}CO $J = 1 - 0$ peak antenna temperatures for the whole Mon R2 region, as shown in Figures 2.22 and 2.23. Again we see the different behavior of the main core and the GGD12-15 core. Least squares fits are given in the top-left corner of the plots.

2.3.2   Gas Column Density and Mass in Mon R2

If the ^{12}CO $J = 1-0$ peak antenna temperature traces the kinetic temperature which can be approximately taken as the average excitation temperature of the ^{13}CO $J = 1-0$ along the line of sight, then one may obtain the ^{13}CO column density under the assumption of LTE. Figure 2.24 presents the H_2 column density map calculated using the LTE method as described by Dickman (1978b). We assumed a ^{13}CO abundance of 2×10^{-6} relative to H_2 and also corrected for He contribution by a factor of 1.4. The highest column densities are found to be $\sim 80 \times 10^{21}$ H_2 cm^{-2} in the main core and the GGD12-15 region. From this map, we obtain a total mass of 4×10^4 $M_\odot$ for the cloud covered by both our ^{12}CO $J = 1 - 0$ and ^{13}CO $J = 1 - 0$ data. The uncertainty caused by the rms error of the data is small, but given the systematic errors accompanying various assumptions, this value is should only be trusted within a factor of 2.
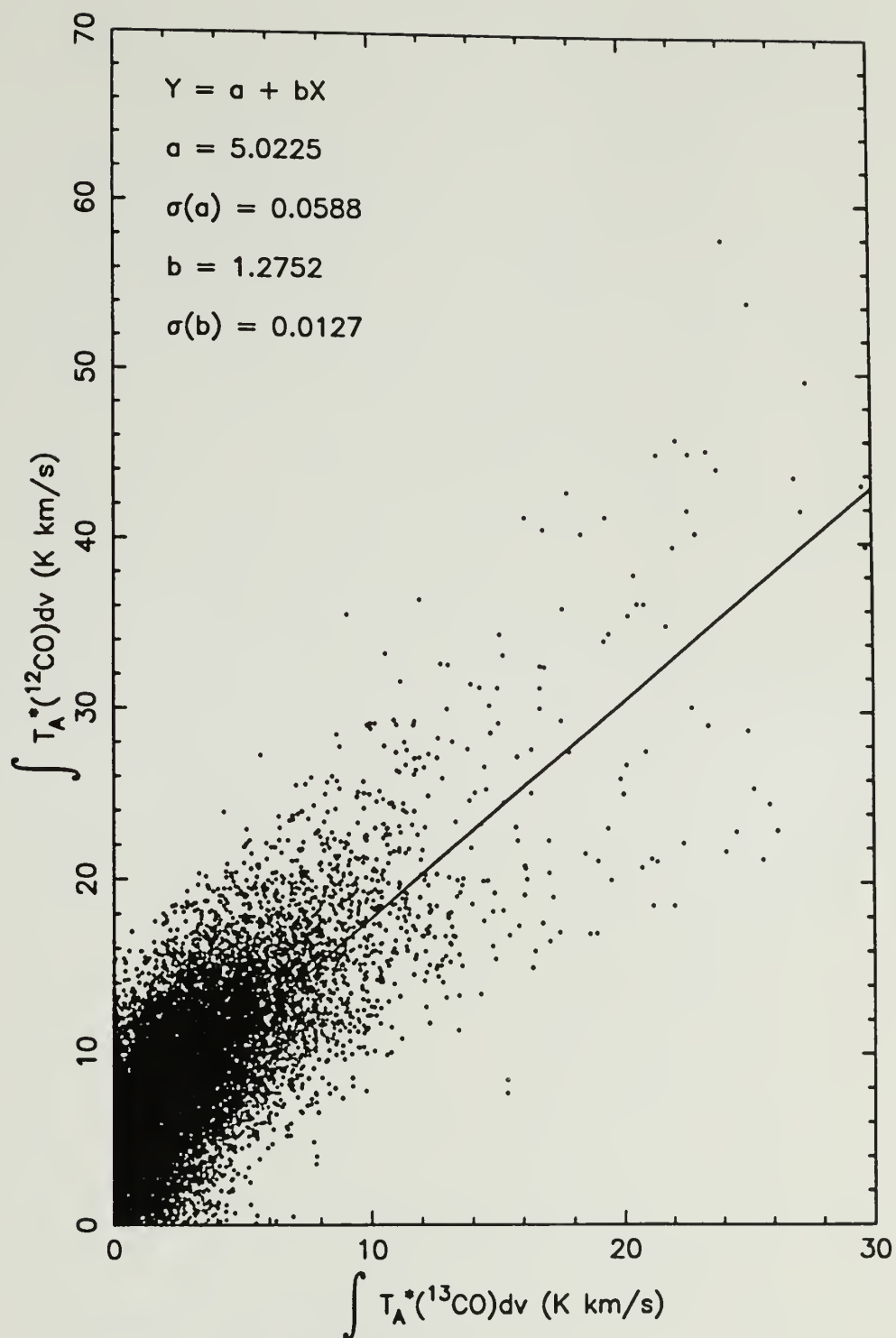
Figure 2.19. Pixel-pixel comparison of ^{12}CO $J = 1-0$ and ^{13}CO $J = 1-0$ integrated intensities for the whole GMC. The solid line is the least-squares fit $\int T_A^*(^{12}CO)dv = 5.0 + 1.3 \int T_A^*(^{13}CO)dv$.
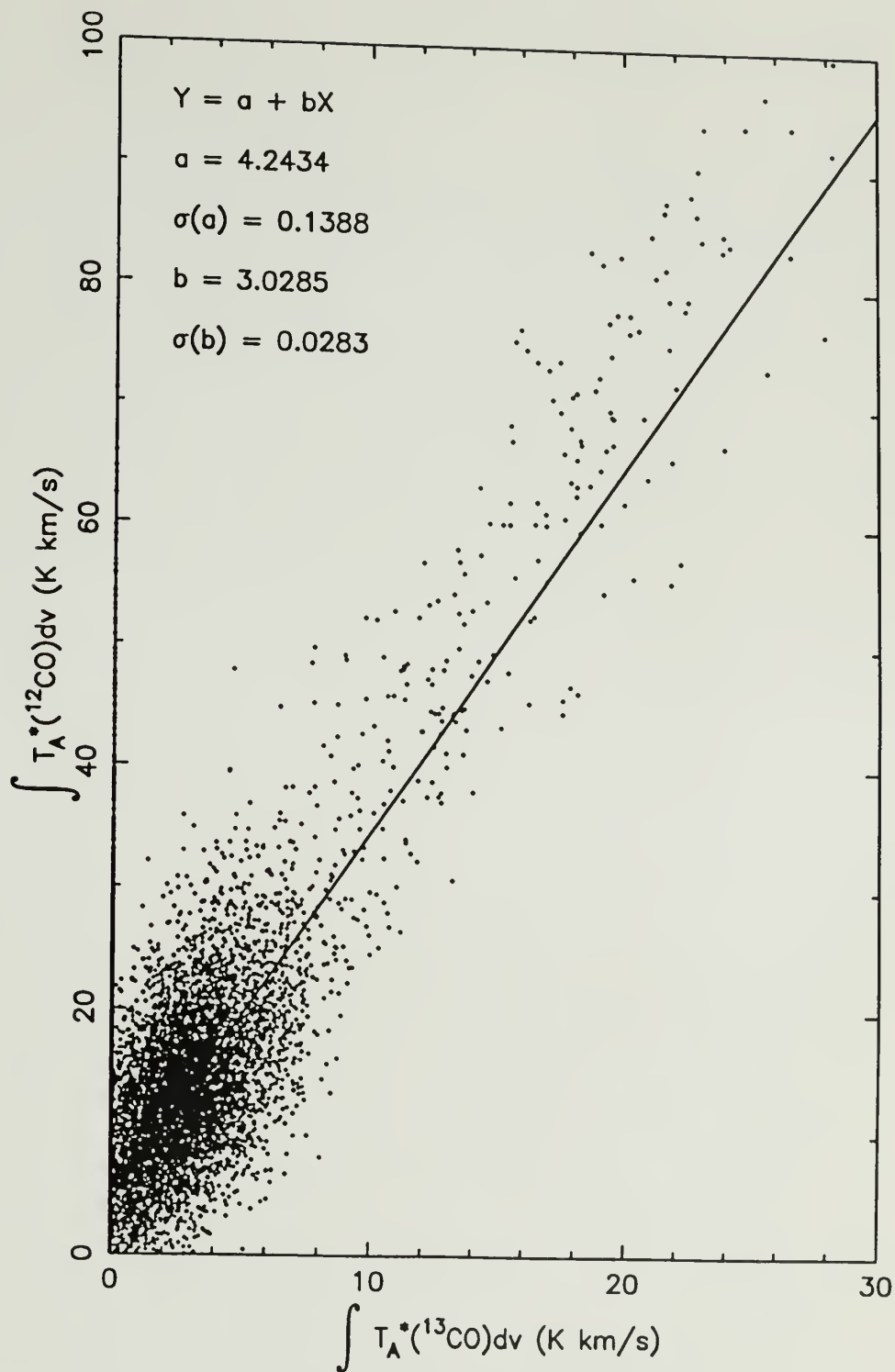
Figure 2.20. Pixel-pixel comparison of ^{12}CO $J = 1-0$ and ^{13}CO $J = 1-0$ integrated intensities for the central core region. The solid line is the least-squares fit $\int T_A^*(^{12}CO)dv = 4.2 + 3.0 \int T_A^*(^{13}CO)dv$.
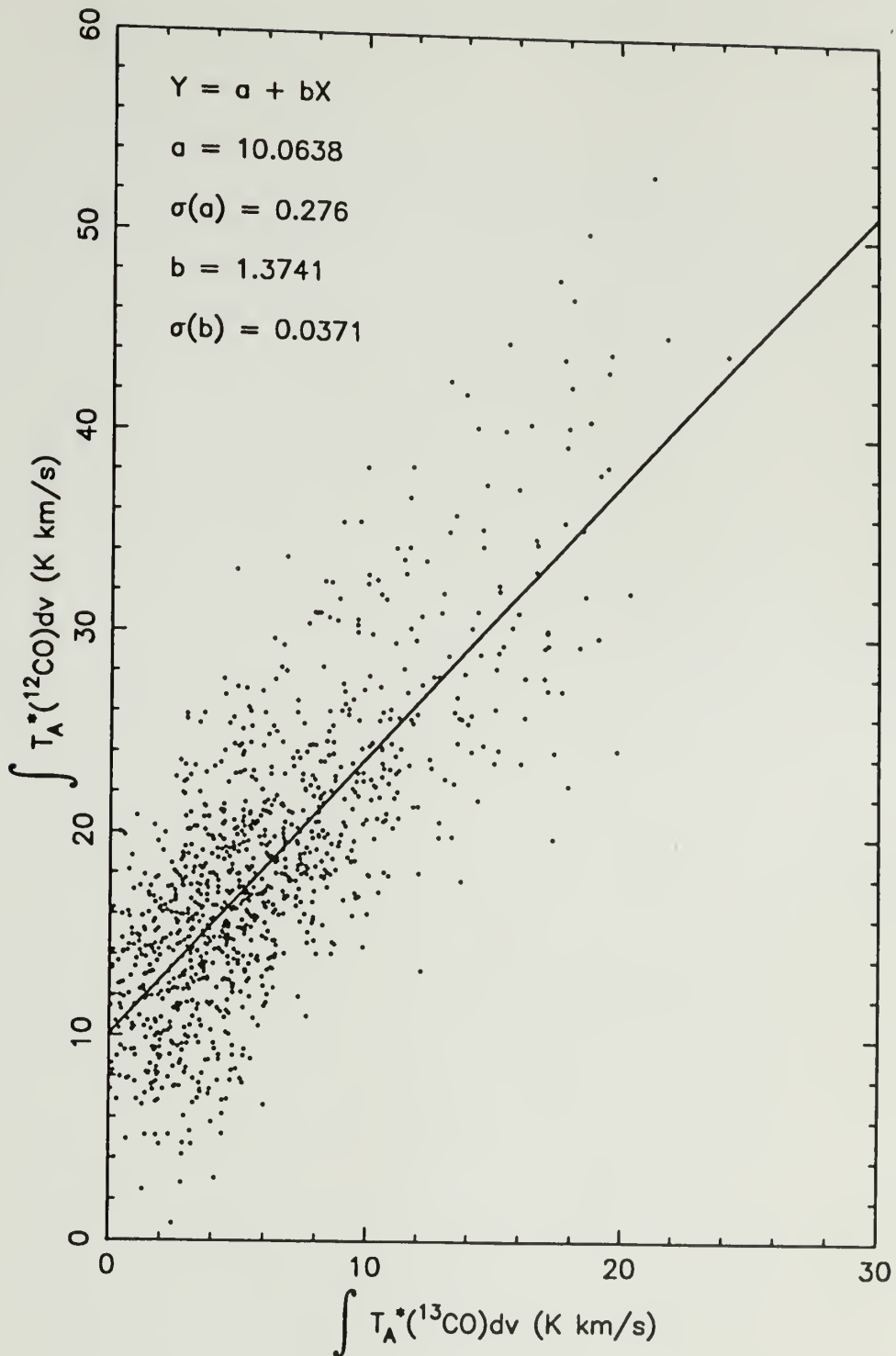
Figure 2.21. Pixel-pixel comparison of ^{12}CO $J = 1-0$ and ^{13}CO $J = 1-0$ integrated intensities for the GGD12-15 core region. The solid line is the least-squares fit $\int T_A^*(^{12}CO)dv = 10.0 + 1.4 \int T_A^*(^{13}CO)dv$.
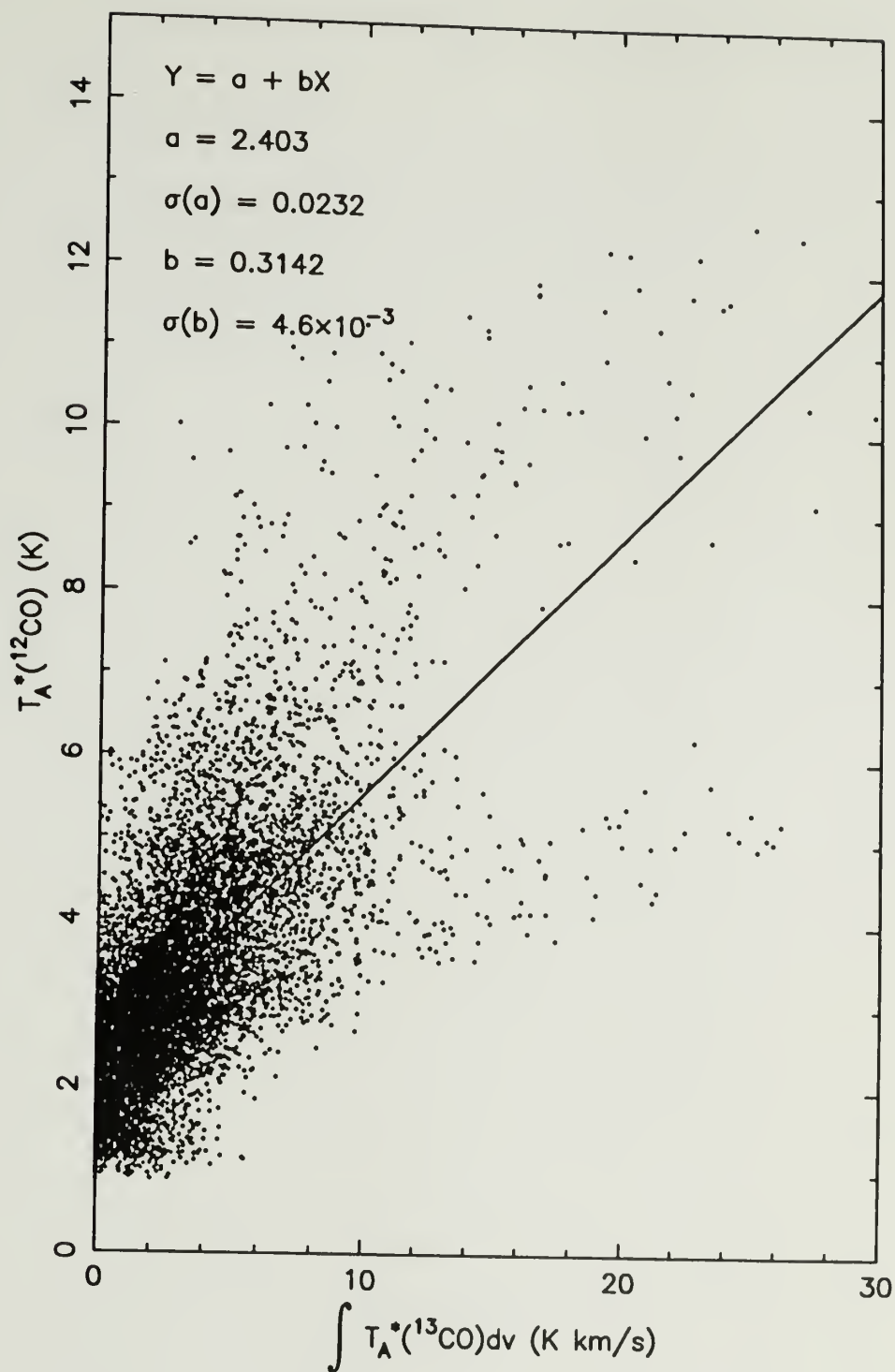
Figure 2.22. Pixel-pixel comparison of ^{12}CO $J = 1 - 0$ peak antenna temperature and ^{13}CO $J = 1 - 0$ integrated intensity for the whole GMC.
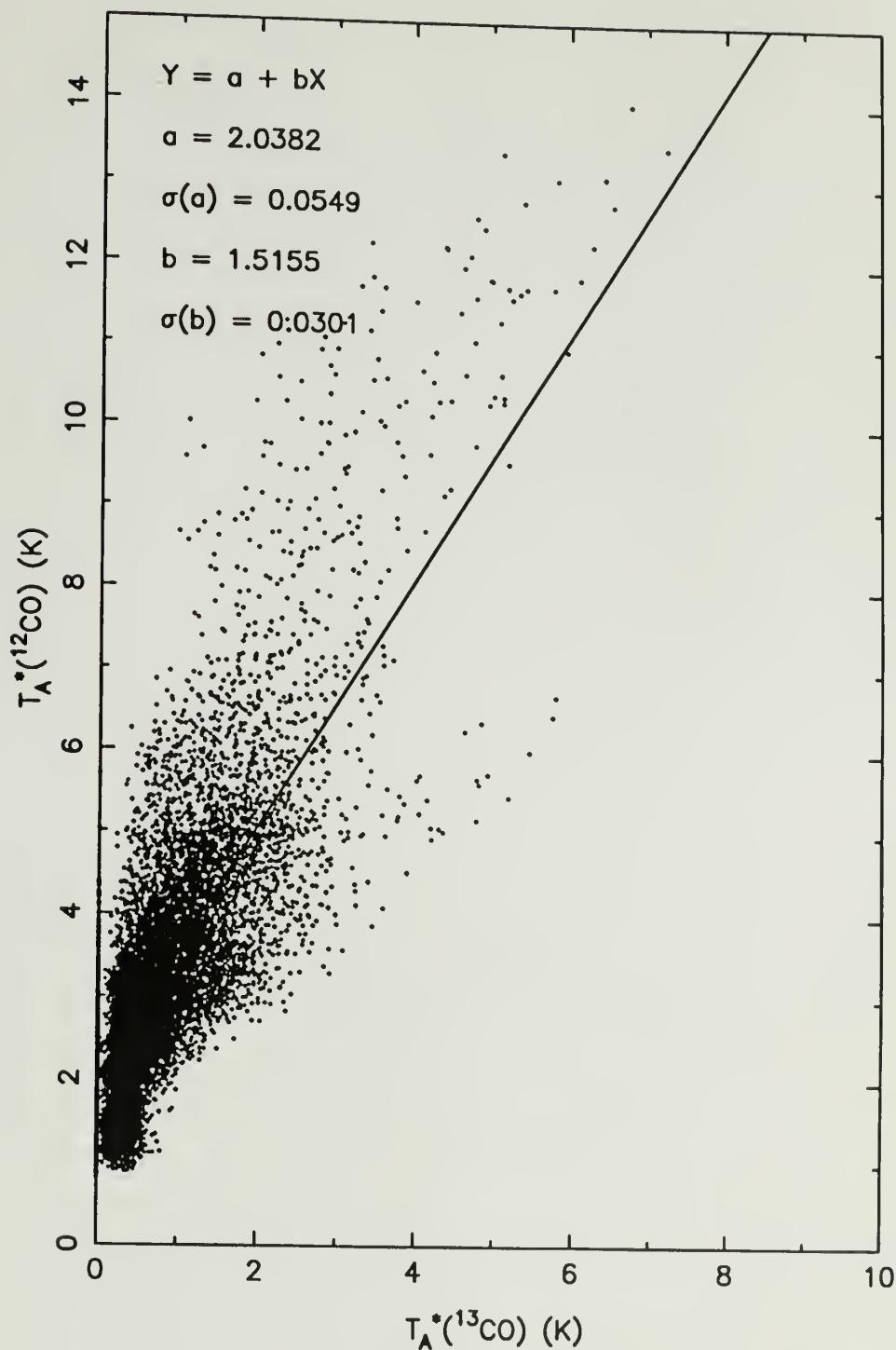
Figure 2.23. Pixel-pixel comparison of ^{12}CO $J = 1 - 0$ and ^{13}CO $J = 1 - 0$ peak antenna temperatures for the whole GMC.
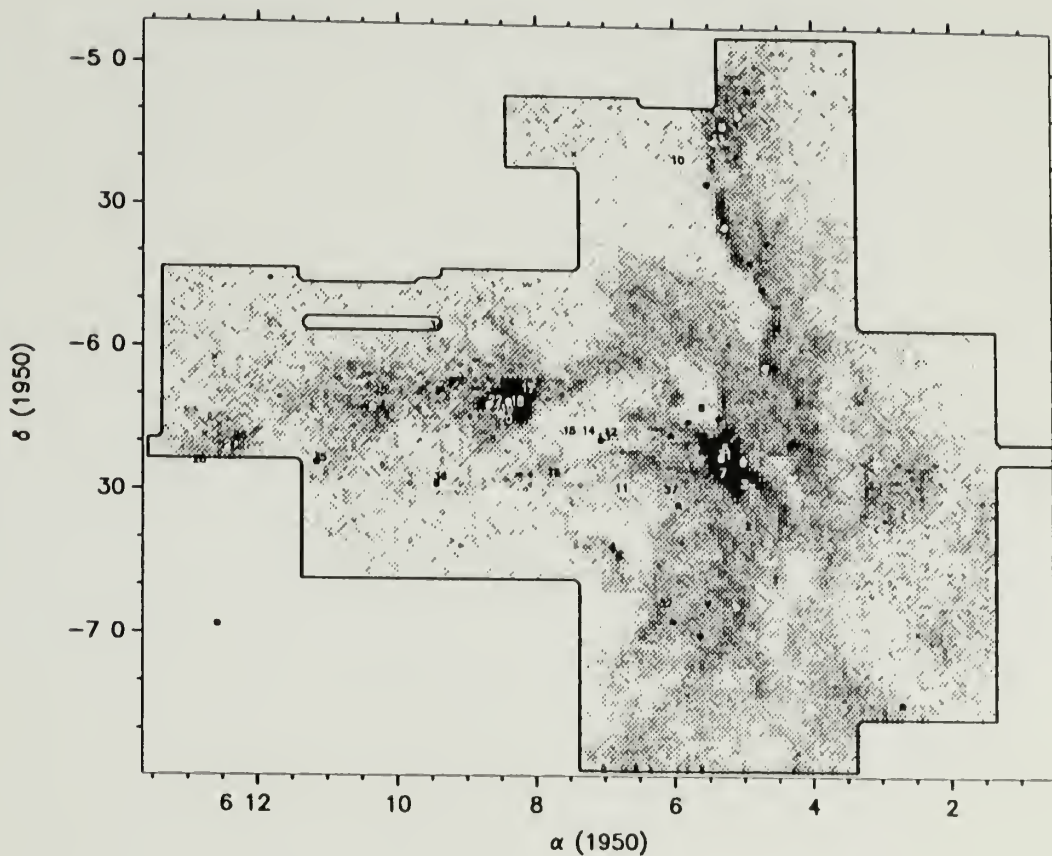
Figure 2.24. H_2 column density of Mon R2 calculated using the LTE method as described by Dickman (1978b). The peak values in this map is $\sim 80 \times 10^{21}$ H_2 cm^{-2}. The positions of the reflection nebulae are indicated by Arabic numbers, and the *IRAS* point sources are labeled by solid circles.

2.3.3 Summary

In summary, we find that ^{12}CO $J = 1 - 0$ and ^{13}CO $J = 1 - 0$ emission in Mon R2 manifests a remarkable correlation, indicating that ^{12}CO $J = 1 - 0$ could in general be as good a morphological tracer as ^{13}CO $J = 1 - 0$. But this correlation may differ from region to region quantitatively, possibly an indication of different physical conditions in different regions, and the fluctuations of the data are large. Thus, caution must be exercised when ^{12}CO $J = 1 - 0$ integrated intensity is used for quantitative purposes on small scales.

2.4 Kinematics in Mon R2

The morphological appearance of a GMC alone can be be misleading. A telescope samples all the material in the beam emitting at the observed wavelength no matter how far away the material is physically in space. Cloud blending in the definition of clouds, GMCs in particular, has never ceased being a controversial problem (cf. Clemens 1985; Blitz 1987; Issa, MacLaren & Wolfendale 1990; see Chapter 7 for more discussion). Fortunately, the Milky Way is a spiral galaxy, and systematic velocity changes of material with galactic radius are expected. This enables the velocity of the material to be used effectively to clarify or relieve ambiguities. For the case of Mon R2, we will see that the kinematics of the molecular material suggests strongly that there is little possibility that all the molecular material observed in Mon R2 region is other than that of a single giant molecular cloud. Based on the results of the previous section, we feel confident using our ^{12}CO $J = 1 - 0$ data set obtained with FCRAO 14m telescope for the following qualitative research on the large scale structure in Mon R2, [4] given its larger coverage, much superior sampling

---

[4] Note the use of ^{12}CO $J = 1 - 0$ lines for the simple kinematical study is problematic in the very small localized regions where ^{12}CO $J = 1 - 0$ lines are double-peaked as a result of self-reversal.

sampling and angular resolution (thus a larger spatial "dynamic range"[5]) as well as its capability of tracing regions where ^{13}CO $J = 1 - 0$ is too weak.

2.4.1   A Large Expanding Bubble Shell

As we have noted in the previous discussion, a conspicuous feature of the cloud on a large scale is the existence of circularly-shaped, diffuse ^{12}CO $J = 1-0$ emission, which is remarkably consistent with the outline of the enhanced diffuse background optical emission visible on the POSS prints. Clarifying the nature of this large scale feature is a critical step for understanding the structure of the GMC.

We find that spatial-velocity (SV) diagrams are extremely informative and useful. Figure 2.25 presents an SV diagram along an east-west cut through the main core. Figure 2.26 shows the SV diagram along a declination cut from south to north at $\alpha = 06^h07^m22^s$. From these figures, several statements can be readily made. **1.** Gas at the inner part of the cloud is blue-shifted relative to the gas in the outer part (eastern and western portion of the cloud) as is indicated by the smooth, blue-shifted bow-shaped feature roughly centered at $\alpha(1950) = 06^h07^m20^s, \delta = -06°22'$, close to a cluster of reflection nebulae, RN11-16 (also referred to as NGC 2182). The maximum velocity displacement of the blue-shifted gas relative to the outer ambient emission is $\sim 4 - 5$ km s^{-1} . **2.** The main core, including the bipolar outflow originating in it, seems to be part of the blue-shifted bow-shaped feature. **3.** The spatial extent of this bow-shaped feature is $\sim 130'$, which corresponds to 31.4 pc at a distance of 830 pc (HR). **4.** Despite the large size, the bow-shaped feature appears impressively continuous and coherently shaped, making other possibilities such as chance superposition of the gas along the line of sight very difficult to accept. **5.** The blue-shifted "bow" has no red-shifted counterpart, and the velocity of the material shows a remarkable symmetry on both ends.

---

[5]Ratio of the number of pixels to the resolution, Scalo 1991.

$T_A^{\bullet}$ (K):   0.7   1.4   2.1   2.8   3.5   4.2   4.9   5.6   6.3   7.0   7.7

A cut from (123.88,   0.00) to (−74.49,   0.00)

($\Delta\alpha$(arcmin), $\Delta\delta$(arcmin))
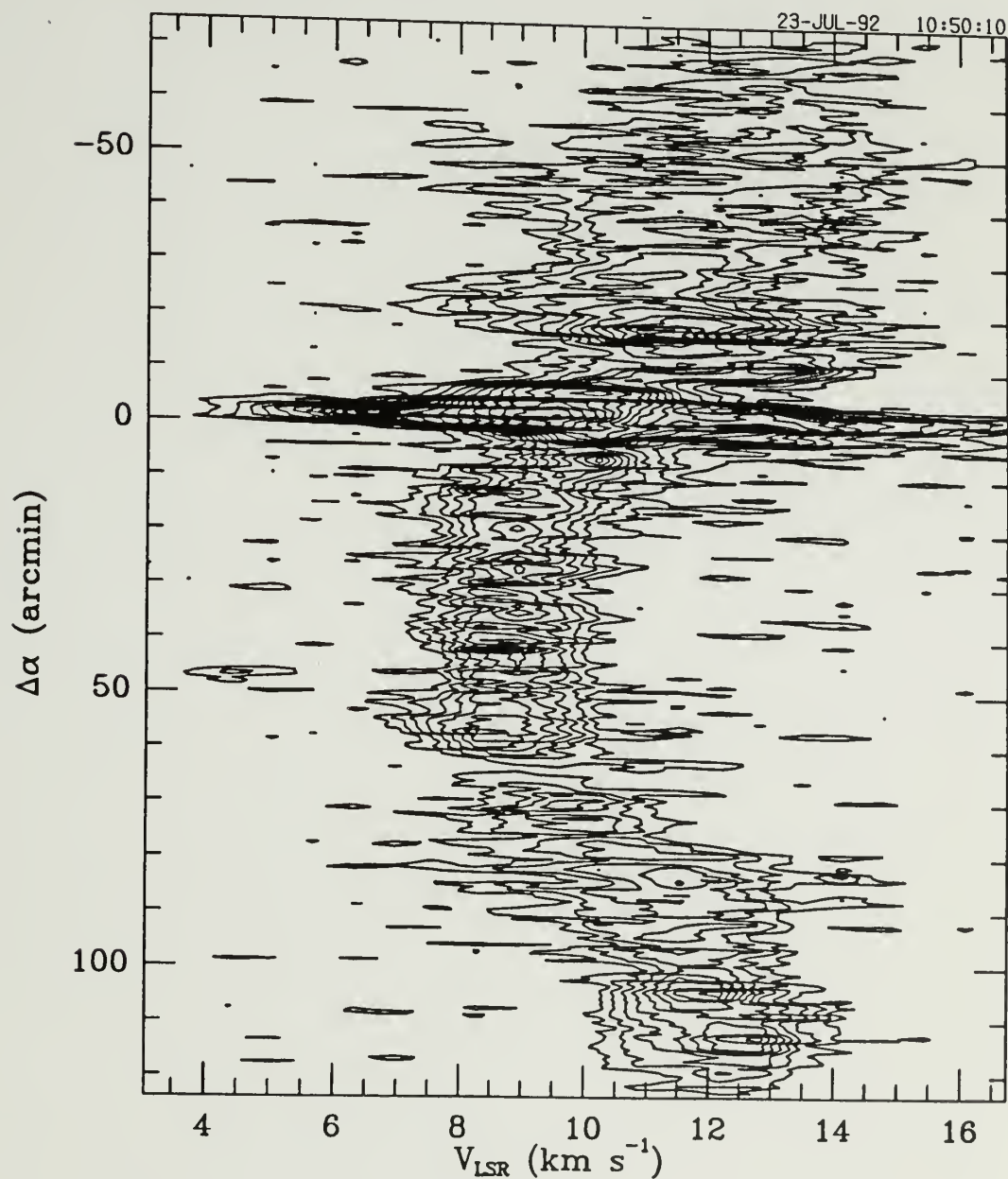
Figure 2.25. An SV diagram along a right ascension cut from east to west going through the center of the main core at $\delta = -06°22'25''$. The contour levels are 0.7, 1.4, ..., 14 K.

$T_A^{\bullet}$ (K):   0.7   1.4   2.1   2.8   3.5   4.2   4.9   5.6   6.3   7.0   7.7
A cut from (25.95, −74.49) to (25.95,   96.67)
($\Delta\alpha$(arcmin), $\Delta\delta$(arcmin))
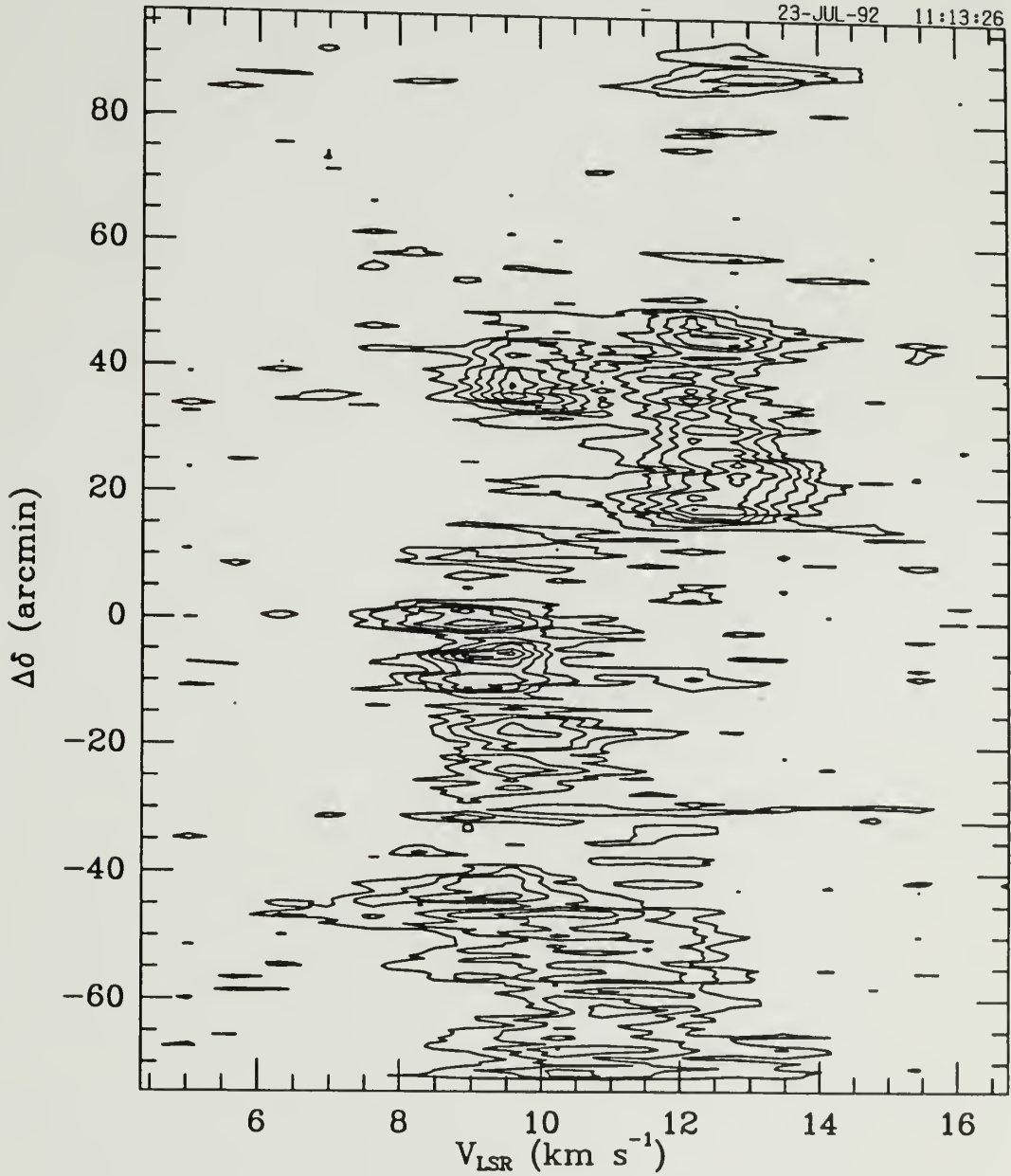
Figure 2.26.   An SV diagram along a declination cut from south to north at $\alpha = 06^h07^m22^s$. The contour levels are 0.7, 1.4, ..., 14 K.

Now the question is: what do these features tell us ? After having done extensive SV examinations along different cuts of our images, we are convinced that the large-scale structure of this giant molecular cloud can be best explained by the existence of an expanding shell with a projected center close to the NGC 2182 region. The front side of the bubble is moving towards us at a radial speed of $\sim 4 - 5$ km s^{-1} , corresponding to the "bow" feature seen in Figure 2.25, while the backside is mostly missing with perhaps only a small quantity of puffy red-shifted material (at ~ 14 km s^{-1}). This judgement is also consistent with the big vertical ridge at those channel maps at velocities higher than 10.23 km s^{-1} and the smaller arc feature to the east of the main core seen in the velocity channels with velocities between 10.23 to 11.53 km s^{-1} ; the large-scale N-S emission ridge (which runs almost all the way from North to South across the image) is likely to be the non-spherical portion of the shell seen edge on, while the smaller arc features are cross-sections of the bubble at blue-shifted velocities. Given the presence of the reflection nebula RN10 close to the northern portion of the N-S ridge, which powers up an optically visible HII region, the non-spherical symmetry of the bubble is not difficult to understand. We will further discuss this point in Chapter 6.[6]

2.4.2 Complexities

It is obvious that a simple large expanding bubble can not provide all the features necessary to explain the morphology of Mon R2. In fact, SV diagrams along different cuts are not always as simple as suggested by Figure 2.25. Figure 2.27, for example, shows an east-west oriented cut at a declination some 16 arcminutes to the north. Although the large "bow" feature again appears, superposed on it is a smaller "bow-like" feature centered at a position close to the GGD12-15 core region, red-shifted

---

[6]For readers who like to jump to conclusions without caring about the details, the cartoon presented in Figure 6.7 may serve the need.

$T_A^{\bullet}$ (K): 0.7 1.4 2.1 2.8 3.5 4.2 4.9 5.6 6.3 7.0 7.7
A cut from (123.88, 16.74) to (−73.66, 16.74)
($\Delta\alpha$(arcmin), $\Delta\delta$(arcmin))
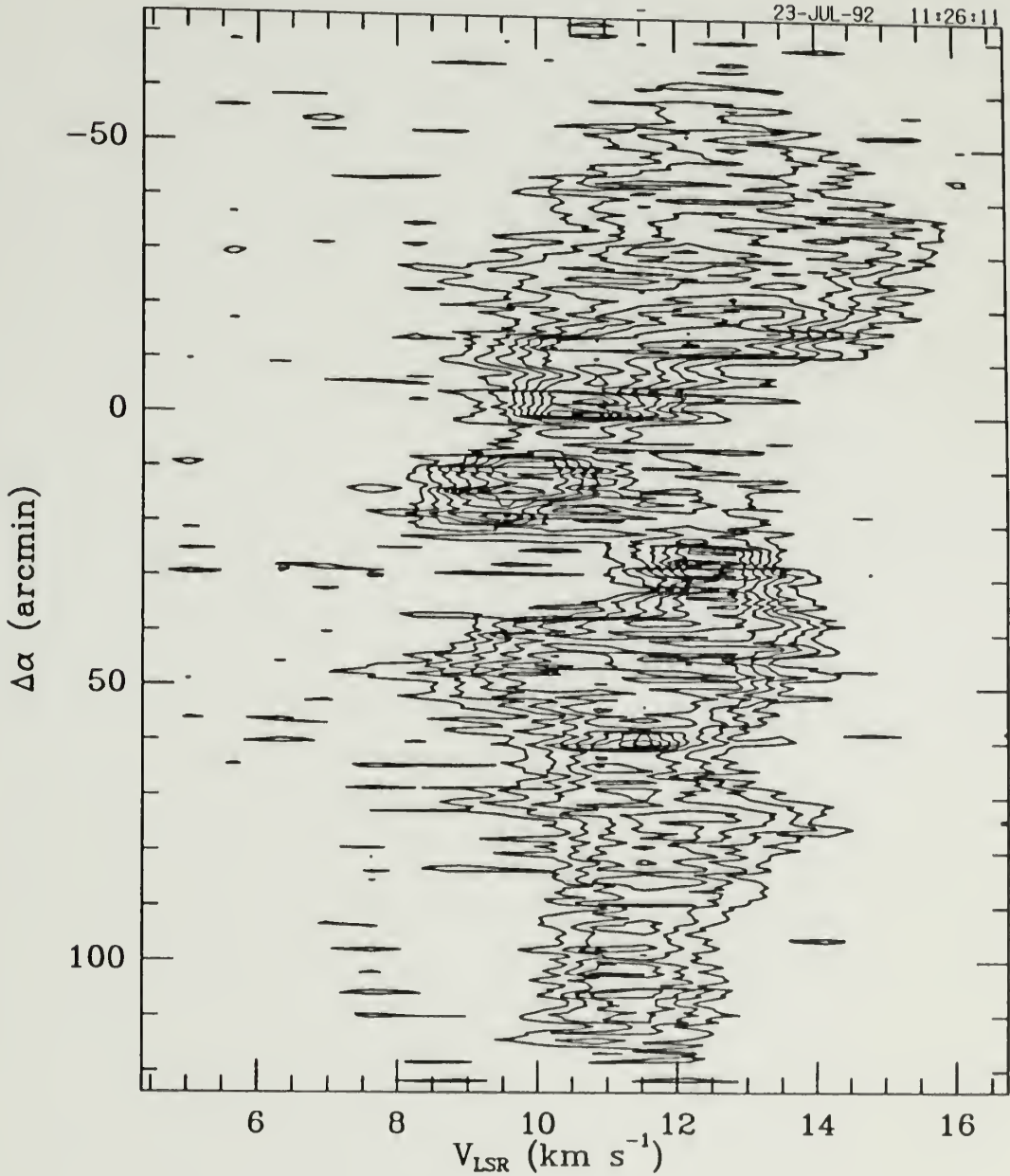
Figure 2.27. An SV diagram along an east-west cut at $\delta(1950) = -06°05'41''$. The contour levels are 0.7, 1.4, ..., 14 K.

relative to the blue-shifted gas. Its existence is noticeable as a "hole" in the velocity channel images of $^{12}CO\ J = 1 - 0$ and $^{13}CO\ J = 1 - 0$ emission, and is also seen on SV diagrams along declination cuts, including the one shown in Figure 2.26. Double line profiles of both $^{12}CO\ J = 1 - 0$ and $^{13}CO\ J = 1 - 0$ in this region provide additional evidence for the reality of this feature. Figures 2.28 and 2.29 show another pair of SV cuts going through a position ($\alpha(1950) = 06^h09^m40^s$, $\delta(1950) = -07°01'15"$) along right ascension and declination, which show also double line profiles with respect to the large blue-shifted "bow", with both red-shifted and blue-shifted emission. The emission through these positional cuts seems to be weak and broken into pieces.

We see three possibilities that may give rise to these distortions. First, the red-shifted material is part of the blue-shifted gas of the large shell slowed down (or retarded). Second, these figures could be a small bubble which occurred on the large blue-shifted shell. Third, these features arise because we are viewing through chords of the large bubble close to the edges.

After careful examination of the features, we feel that its roundish shape and smooth variation with respect to velocity is not likely to be a result of the first process, and instead they are more suggestive of the second or the third possibility. The second possibility is particularly attractive given the star formation on the compressed shell layers (see Chapter 6). In other words, it is possible that we are witnessing small bubbles on large bubbles. As we will see in Chapter 4, the eggplant-shaped bipolar outflow shell conspicuous on the velocity channel map of $^{12}CO\ J = 1 - 0$ at $V_{LSR} = 10.88\ km\ s^{-1}$ provides a convincing example of this assertion. But this does not mean that the first physical process is not a likely physical process in the cloud. Figure 2.30 displays an SV cut going through the main core along declination. Clearly, we see amazingly complicated velocity changes with position. We feel that most of these are the result of retardation in motion of

$T_A^{\bullet}$ (K): 0.7   1.4   2.1   2.8   3.5   4.2   4.9   5.6   6.3   7.0   7.7
A cut from (123.88, −38.50) to (−74.49, −38.50)
($\Delta\alpha$(arcmin), $\Delta\delta$(arcmin))
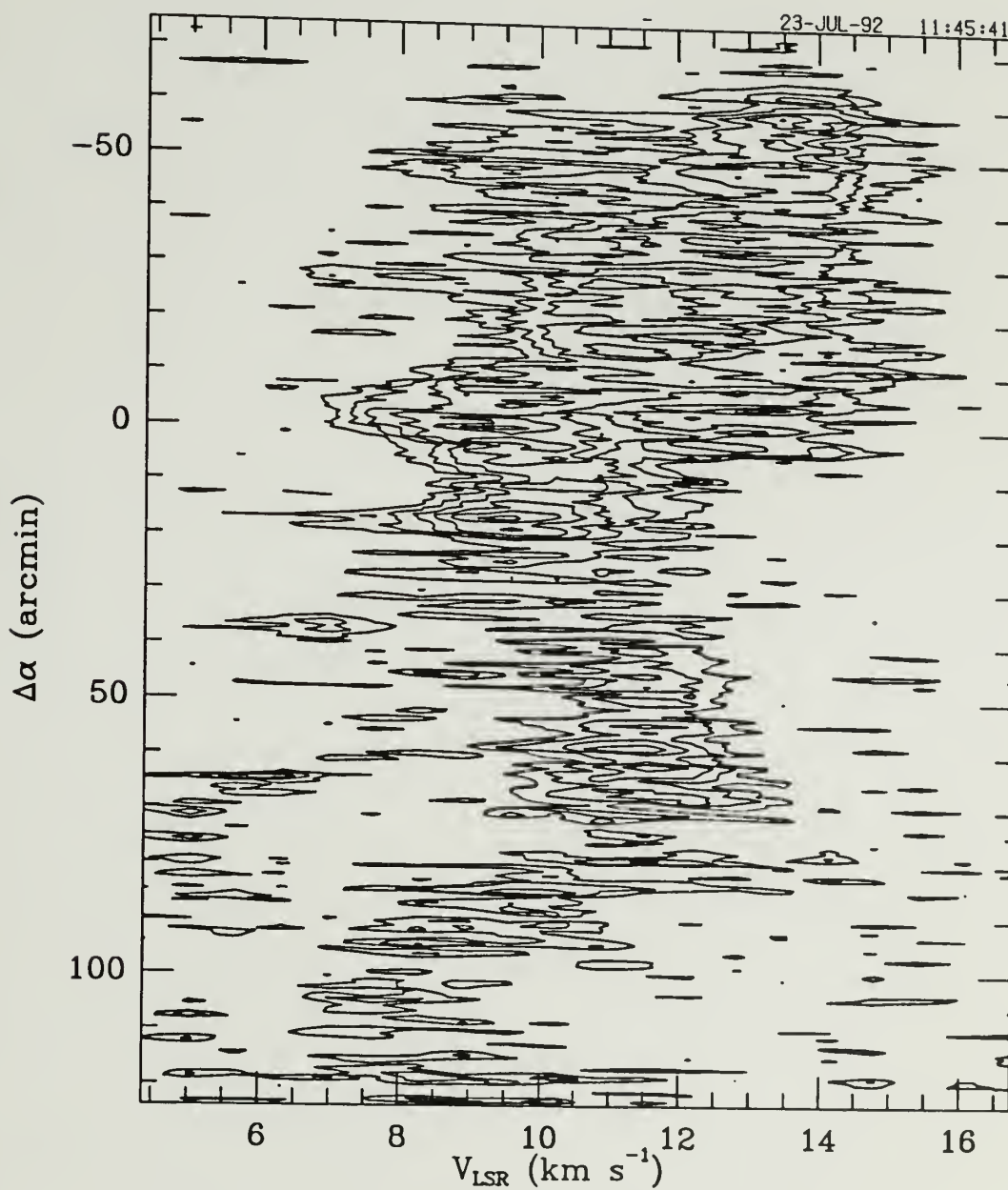
Figure 2.28. An SV diagram along an east-west cut at $\delta(1950) = -07°01'15"$). The contour levels are 0.7, 1.4, ..., 14 K.

$T_A^\bullet$ (K):   0.7   1.4   2.1   2.8   3.5   4.2   4.9   5.6   6.3   7.0   7.7
A cut from (66.96, −74.49) to (66.96, 54.82)
($\Delta\alpha$(arcmin), $\Delta\delta$(arcmin))
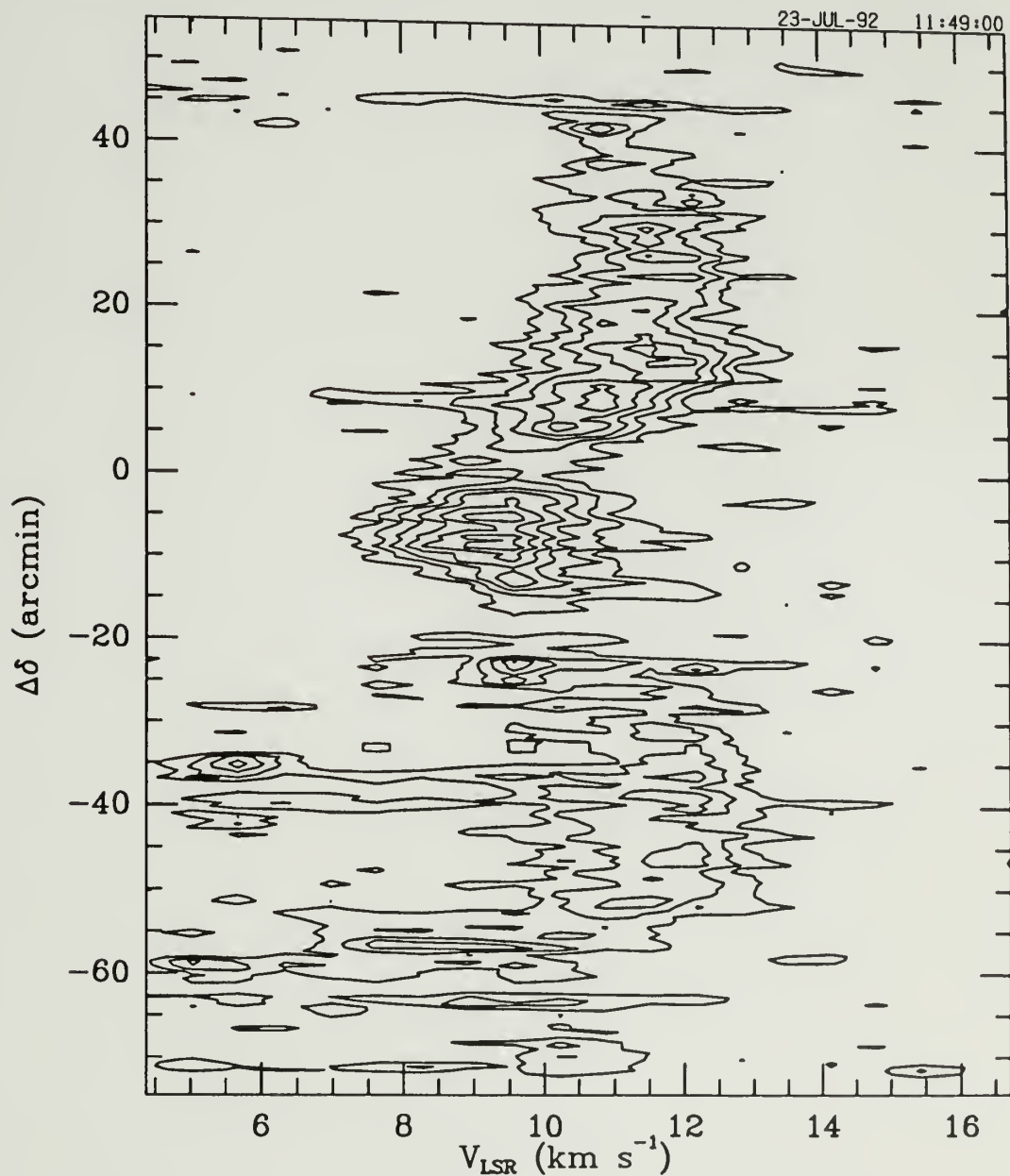
Figure 2.29. An SV diagram along a declination cut at $\alpha(1950) = 06^h09^m40^s$. The contour levels are 0.7, 1.4, ..., 14 K.

$T_A^\bullet$ (K): 0.7 1.4 2.1 2.8 3.5 4.2 4.9 5.6 6.3 7.0 7.7
A cut from (0.00, −71.98) to (0.00, 100.86)
($\Delta\alpha$(arcmin), $\Delta\delta$(arcmin))
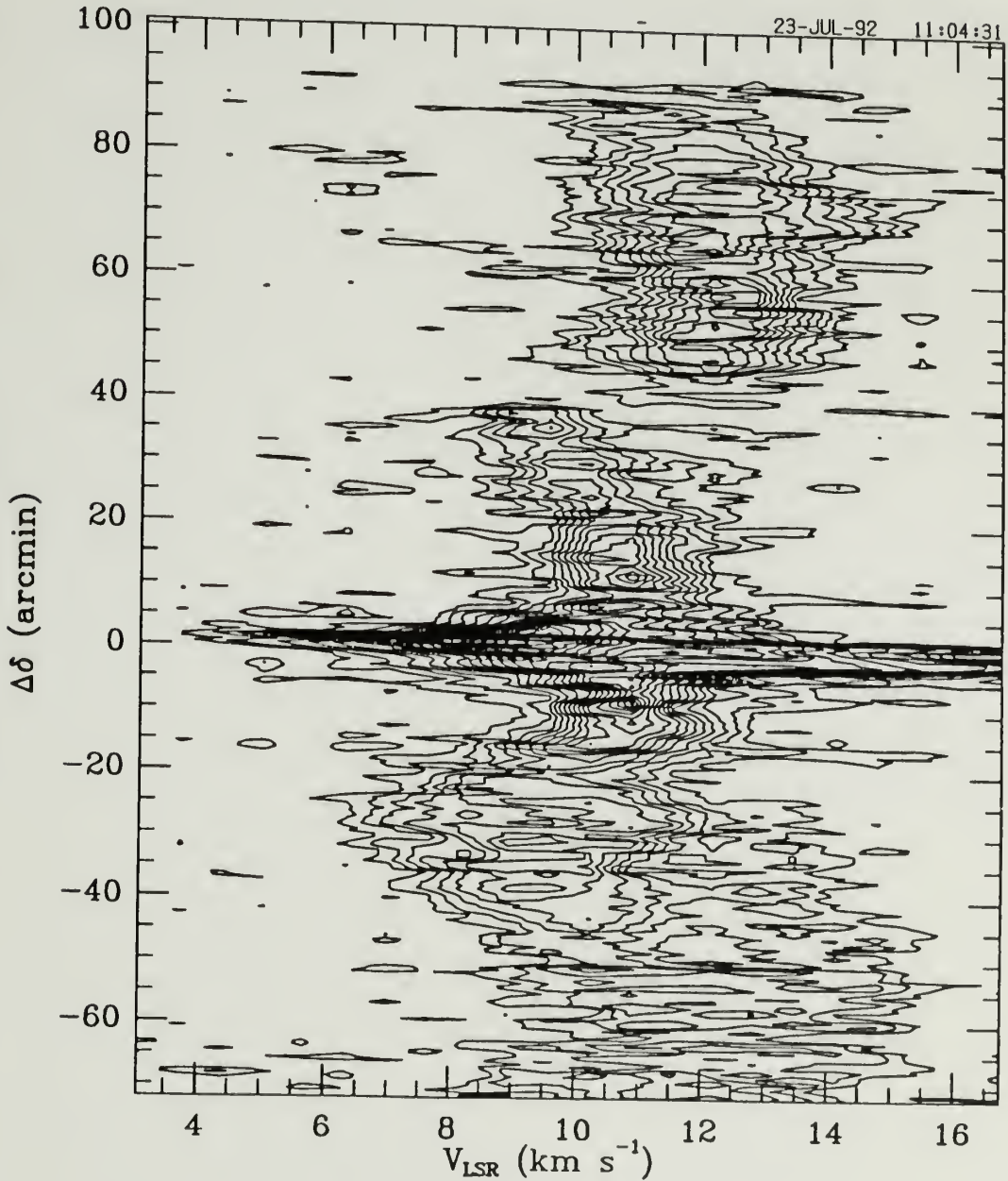
Figure 2.30. An SV diagram along a declination cut at $\alpha(1950) = 06^h05^m22^s$ going through the main core. The contour levels are 0.7, 1.4, ..., 14 K.

the massive and dense clumps of gas relative to the less dense gas exposed to the same pressure from the bubble cavity.

2.4.3 Kinetic Energy

It is not easy to calculate the kinetic energy of the cloud's expanding motions because it requires the determination of a reference velocity relative to which the neutral material moves, which in turn is a model-dependent physical quantity. But if we accept the assumption that majority of the cloud mass is being swept up into shells and the geometry of the shell is semi-spherical, then an order-of-magnitude estimate is $E = 1/2M\Delta V^2 \sim 6 \times 10^{48}$ $ergs$, where the cloud mass M is taken to be the LTE mass of 4×10^4 $M_\odot$, and the shell expansion velocity ΔV is taken to be 4 km s^{-1} . Obviously, this corresponds to the total kinetic energy in all three dimensions. Various possible uncertainties are involved in this estimate. First, it is clear that the real geometry of the large-scale shell cannot be strictly semi-spherical. Second, not all the mass is swept up in the shells. Third, in addition to the large-scale expansion, there are other components of systematic motions, including the bipolar outflows in the cores. Fourth, the mass estimate itself is subject to various uncertainties. It is almost impossible to give a reliable quantitative estimate about the total uncertainty of the given kinetic energy.

One other way to estimate the total kinetic energy of the large bubble is to calculate the kinetic energy for each pixel of the map using the ^{12}CO $J = 1 - 0$ and ^{13}CO $J = 1 - 0$ data under the assumption of LTE, and then sum over the whole cloud. Of course, it is a necessity to presume a reference LSR velocity V_0; we take the V_{LSR} of the N-S emission ridge of 12 km s^{-1} as an approximation. This procedure gives an estimate of 1×10^{49} $ergs$ which includes the "kinetic energy" due to turbulence and should be regarded as overall energy. But it is important to

note that this estimate of kinetic energy is only for one dimension — along the line of sight.

Given the various uncertainties and the difficulties, we feel that the total kinetic energy of the systematic motions of the large-scale expanding bubble is likely to be in the range of $5 - 10 \times 10^{48} \ ergs$.

Chapter 3

Dust Distribution in Mon R2

3.1 Introduction

In Chapter 2, we examined the gas distribution in Mon R2. Starting with this chapter we will examine other important aspects of the GMC — dust distribution, star-formation and clumpiness. We devote this chapter to the dust emission in Mon R2.

Dust presumably comprises only 1% in mass of the interstellar medium, but it is important in many astrophysical situations by virtue of its absorption of short wavelength energy and re-emission at much longer wavelengths. After stars form within interstellar clouds of gas and dust, their emission at short wavelengths is largely absorbed by ambient dust grains and they remain hidden from optical observations for some period of time (cf. Leung 1976; Scoville & Kwan 1976; Scoville 1985; Shu, Adams & Lizano 1987). Observing the emission of dust at much longer wavelengths is a major tool for understanding the star forming processes (cf. Beichman 1987). Since dust thermal emission in the far infrared to millimeter wavelength range (hereafter we refer to this range as FIR) is likely to be optically thin, the surface brightness in this range of a source is a good tracer of the dust distribution (cf. Werner *et al* 1976; Hildebrand 1983; Goldsmith, Snell, & Lis 1987; Draine 1990). The spectral energy distribution provides a measure of the temperature distribution of the dust along a line of sight, which carries valuable information about the central proto- or young stars (cf. Beichman *et al* 1986). Retrieving of this information is a non-trivial problem. Numerical radiative transfer techniques have been developed (cf. Leung 1975; 1976; Scoville & Kwan 1976; Rowan-Robinson

1980; 1986; Dent 1988; Lis & Leung 1991). These techniques, while powerful, require explicit assumptions about the source geometry, homogeneity, density distribution, central star luminosity, and dust thermal equilibrium, in addition to the necessity of explicitly assuming constituents, size distribution and emissivity of the dust. However, it is often the case that we make a few flux measurements towards a position of a cloud at frequencies which are believed to be optically thin, and we do not have detailed data about the source geometry, density distribution, radiation field, etc. The problem is: how do we obtain the maximum amount of meaningful information about the sampled dust column ?

A method widely employed by astronomers is to assume a single- or multi-temperature dust model. This method takes two different forms in the literature depending on the emission source. For star-forming condensations, the typical approach is to treat the exponent of the power-law dust emissivity as a free parameter and use the gray-body emission formula to fit the source spectral distribution (cf. Erickson *et al* 1977; Mundy, Wilking & Myers 1986; Gordon 1987; 1988; Walker, Adams & Lada 1990; Mezger, Wink & Zylka 1990). For diffuse emission in the interstellar medium, such as the abundant data furnished by the *IRAS* satellite, it is more common to obtain two-band intensity ratios, from which dust temperature and column density can be derived under an assumed dust emissivity law by using the gray-body emission formula (Kuiper *et al* 1987; Langer *et al* 1989; Jarrett, Dickman, and Herbst 1989, Bally, Langer & Liu 1991). But dust grains are in reality very likely to be distributed continuously over a broad temperature range at a particular position within a cloud (Panagia 1975). First, interstellar grains of various sizes co-exist (cf. Mathis, Rumpl, & Nordsiek 1977; Mathis 1990) and will attain rather different temperatures even if they are exposed to the same ambient physical conditions (radiation field, etc.). There are also small particles which may be transiently heated (Sellgren 1984; Léger & Puget 1984; Weiland *et al* 1986;

Leene 1986; Puget & Léger 1989; Laureijs *et al* 1989; Désert, Boulanger & Puget 1990; Boulanger *et al* 1990). Second, the ambient physical conditions of dust grains along lines of sight through the cloud and over the extent of telescope beams for observations are likely to be quite different, so that the dust grains are heated and cooled at different rates. Because dust emission is highly sensitive to dust temperature, it is very unlikely that assuming a single average temperature or several temperatures is a satisfactory approximation to the dust emission problem. Bally, Langer & Liu (1992) extensively studied the *IRAS* emission of the Orion-Monoceros molecular complexes with single- and two-component models, and demonstrated the inadequacy of using these models to convert the intensity images into dust column density images. In addition, for the case of star-forming condensations, the current approach of using the single- or multi-temperature model also implies that the average dust emissivity changes significantly from source to source (Walker, Adams & Lada 1986).

In comparison, a more promising approach appears to be the expansion of the original concept of dust temperature distribution (Leung 1975; Scoville & Kwan 1976; de Muizon & Rouan 1985) and to include temperature fluctuations caused by all possible sources considered in theoretical modeling (cf. Draine & Anderson 1985; Pajot *et al* 1986; Dwek 1986; Guhathakurta & Draine 1989; Heyer *et al* 1989; Xie, Goldsmith & Zhou 1991). Xie, Goldsmith & Zhou (1991) developed an inversion technique for obtaining analytical expressions for the temperature distribution of interstellar dust, and thus to determine the total dust column density from an infrared spectrum. In this Chapter, we apply this new method to the large-scale *IRAS* data for Mon R2. The development of the new method has been part of the thesis project, but in order to minimize duplication, we shall try to avoid repeating what we have presented in that publication. Instead we shall try to provide more guidelines concerning the correct use of the method and its limitations. We start

with presenting the observational data in the next section, and we then move to an examination of the widely used color-ratio regime and present a modified Wien displacement law in Section 3.3. We consider the concept of dust temperature distribution in Section 3.4. In Section 3.5, we apply the dust inversion method to *IRAS* images to convert them into dust column density images. We compare the dust emission with the gas emission in Section 3.6. Section 3.7 summarizes this chapter.

3.2 Observations

The *IRAS* satellite was designed to survey the FIR emission presumably from point-like (or small) sources. But it has also produced a wealth of valuable data for the spatially extended emission from dust grains in the interstellar medium, which has been widely used by astronomers to infer information such as the dust temperature, dust distribution and even constituents of interstellar grains in relation to the fascinating phenomenon of star formation. This has been carried out despite the fact that *IRAS* data suffers from calibration uncertainties at low level emission intensities (Langer *et al* 1989).

We have obtained from IPAC/Caltech co-added *IRAS BIGMAP* images of $4° \times 4°$ for all four *IRAS* bands for Mon R2 with a spacing of $1'$. As a standard *BIGMAP* product, the images for all the four bands have a common resolution of $\sim 3' \times 5'$, as determined from the point spread function of point sources within the region. The small and large values correspond to in-scan and cross-scan directions, respectively. In the case of Mon R2, the cross-scan direction is along right ascension. The zodiacal background emission seems to have been effectively removed, and we see no significant gradient[1] across the whole area of the images. The background emission from the galactic plane does not seem to be a problem either, presumably because

---

[1] Mon R2 GMC actually subtends a large portion of the $4° \times 4°$ field provided by the *BIGMAPs*.

Mon R2 is $\sim 13°$ degrees below the galactic plane. But to relieve further possible uncertainties in the relative intensities of four *IRAS* bands caused by the background emission problem, we used the POSS red print as a reference and subtracted a constant from the *IRAS BIGMAP* images so that the intensity values at positions where POSS red print has minimal extinction are essentially zero.

Figures 3.1 to 3.4 presents the *IRAS BIGMAP* images in the four bands overlayed onto the ^{12}CO $J = 1 - 0$ peak antenna temperature image. After comparing with Figures 2.3 to 2.18. we notice the following main characteristics.

1. Some point-like sources are strong at the 12 or/and 25 microns bands, but do not appear in the two longer wavelength bands. For these sources, the fact that the ^{12}CO $J = 1 - 0$ emission at the position does not show any enhancement suggests that they are likely to be stars not related to the molecular cloud.

2. The string of cores along the east-west direction across the cloud identified in Chapter 2 corresponds to a chain of strong infrared emission peaks in all four bands, presumably as a result of both the radiation heating of the dust grains by embedded stars and the enhanced column density. But what appears striking is the exception for the RN11-16 region (also NGC2182), where all the four bands of *IRAS* emission peak but ^{12}CO $J = 1 - 0$ appears weak. Given the reported radio HII region of unknown nature located there (Hughes and Baines 1985) and its near coincidence with the hypothetical center of the large blue-shifted bubble shell (see Chapter 2), this source could be of significance to the structure of the cloud (see Chapter 6).

3. Unlike the gas emission, *IRAS* images do not show any signs for cavities or holes all over the cloud. In addition to the discrepancy between gas and dust emission around the RN11-16 region, the dust emission is also strong close to the RN10, where there is little gas emission to the east of the N-S emission

ridge. The difference in resolution between the gas and the dust images does not explain this discrepancy.

3.3 On the Concept of Color Ratio

Taking the ratios of the intensities at two different wavelengths has been common practice in the use of the *IRAS* data for studying the properties of the dust grains associated with point sources and with diffuse interstellar gas. In the spirit of emphasizing basic understanding of old concepts before trying new things, we contribute this section to examining the physics associated with the color ratio.

The concept of color ratio used in the study of thermal dust emission is possibly borrowed from optical astronomy. In the study of the emission from a star, for example, the emission at the wavelengths generally observed is optically thick and the star's luminosity can be well described by the Planck function multiplied by the star's surface area. Thus the problem has only two parameters; the effective surface temperature and the size of the star, which theoretically can be determined by two flux measurements at the two different wavelengths. Specifically, since the color ratio eliminates the size of the star, it can be used as a direct measure of the star's effective emission temperature.

In the case of thermal FIR emission from dust grains, however, the situation may not be as simple. First, the emission is likely to be optically thin and samples the dust grains at various physical conditions and possibly even different grains as we argued in Section 3.1. Second, both dust emissivity and dust column density enter as multiplicative factors to the Planck function. Under the extreme situation that all dust grains along a line of sight sampled by the two wavelengths have the same temperature, the problem reduces to a two-parameter (dust temperature and dust column density) problem (if the dust emissivity is assumed to be known), which can be solved by use of two flux measurements. But a different problem
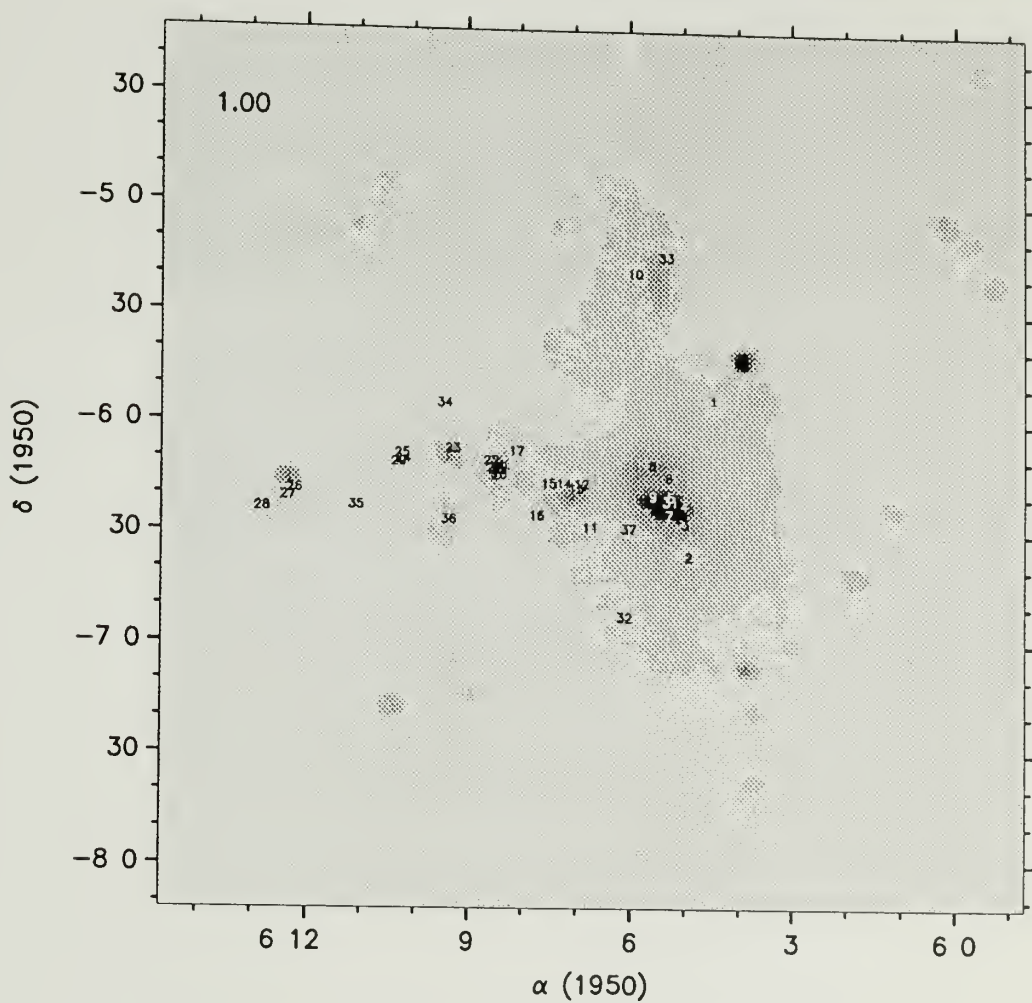
Figure 3.1. The co-added *IRAS BIGMAP* image for 12 μm. Positions of the reflection nebulae are labeled by Arabic numbers.
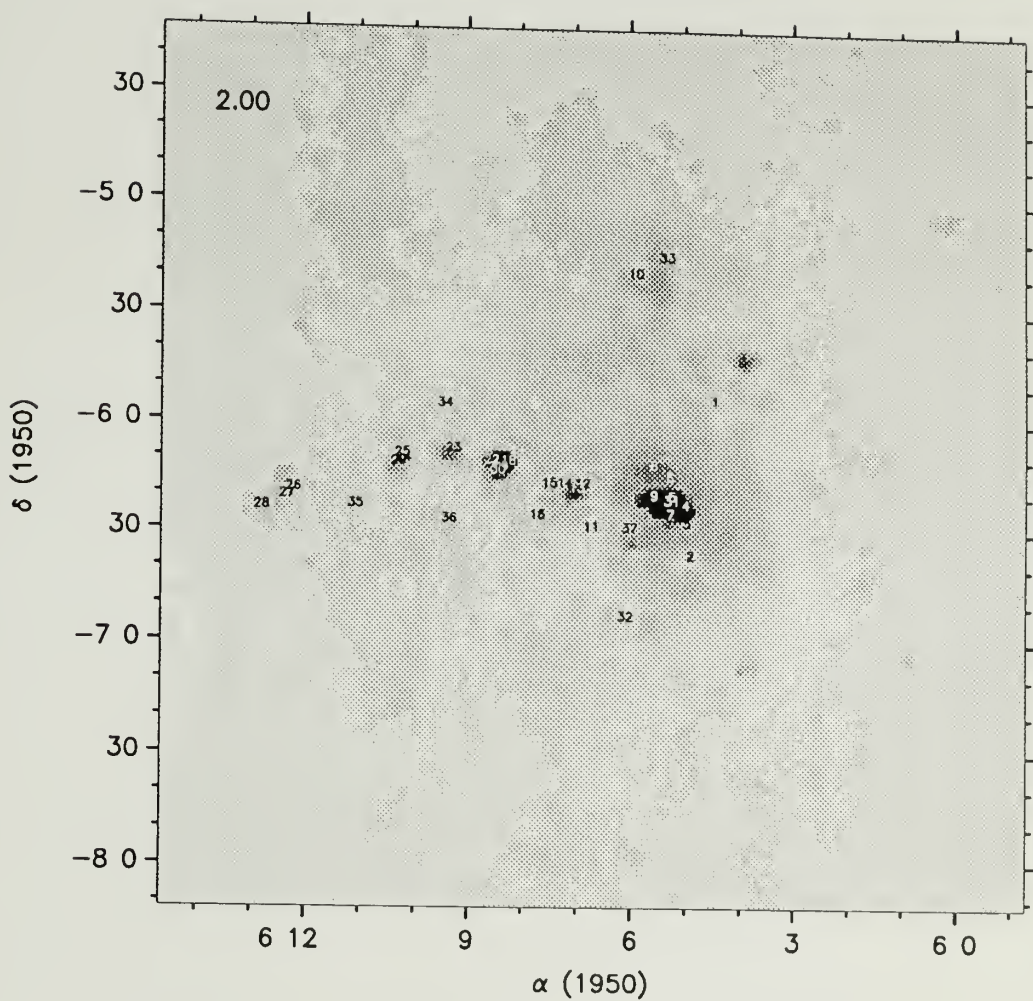
Figure 3.2. The co-added *IRAS BIGMAP* image for 25 μm. Positions of the reflection nebulae are indicated by Arabic numbers.
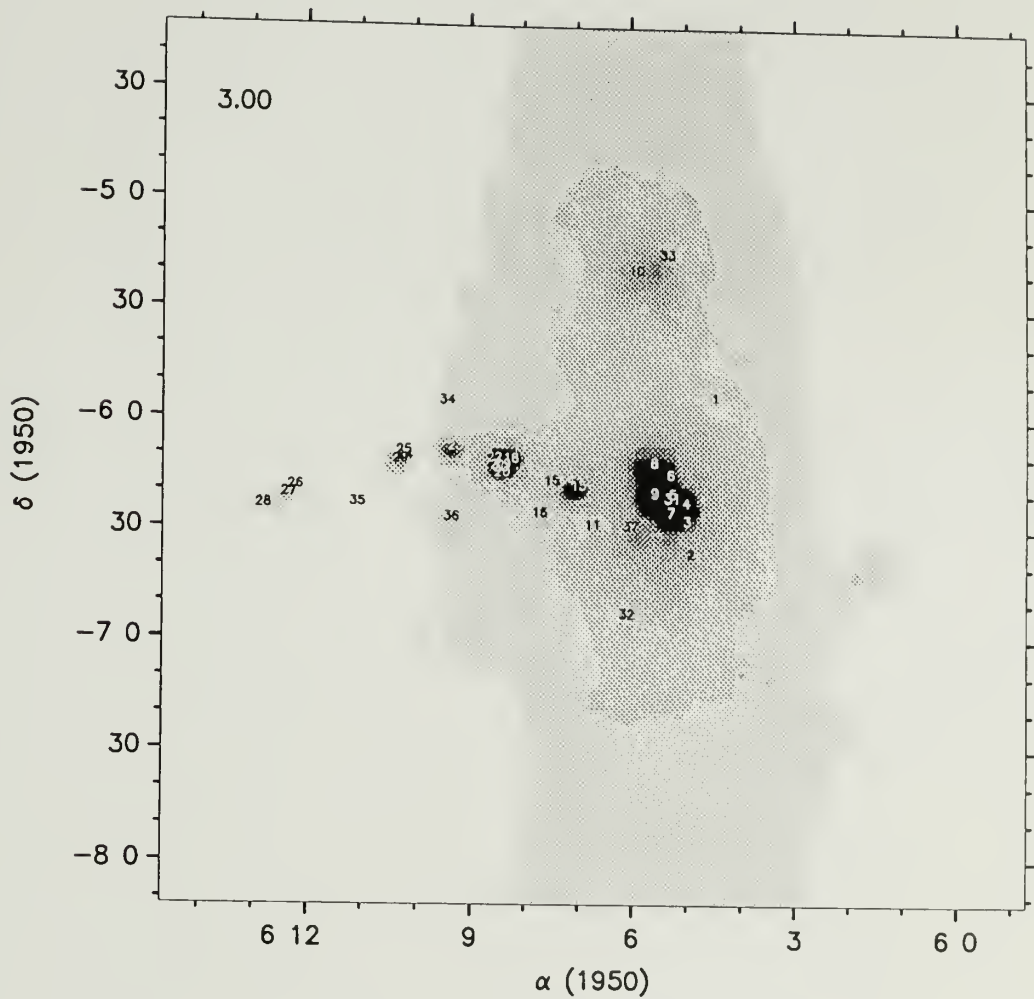
Figure 3.3. The co-added *IRAS BIGMAP* image for 60 μm. The positions of the reflection nebulae are indicated by numbers.
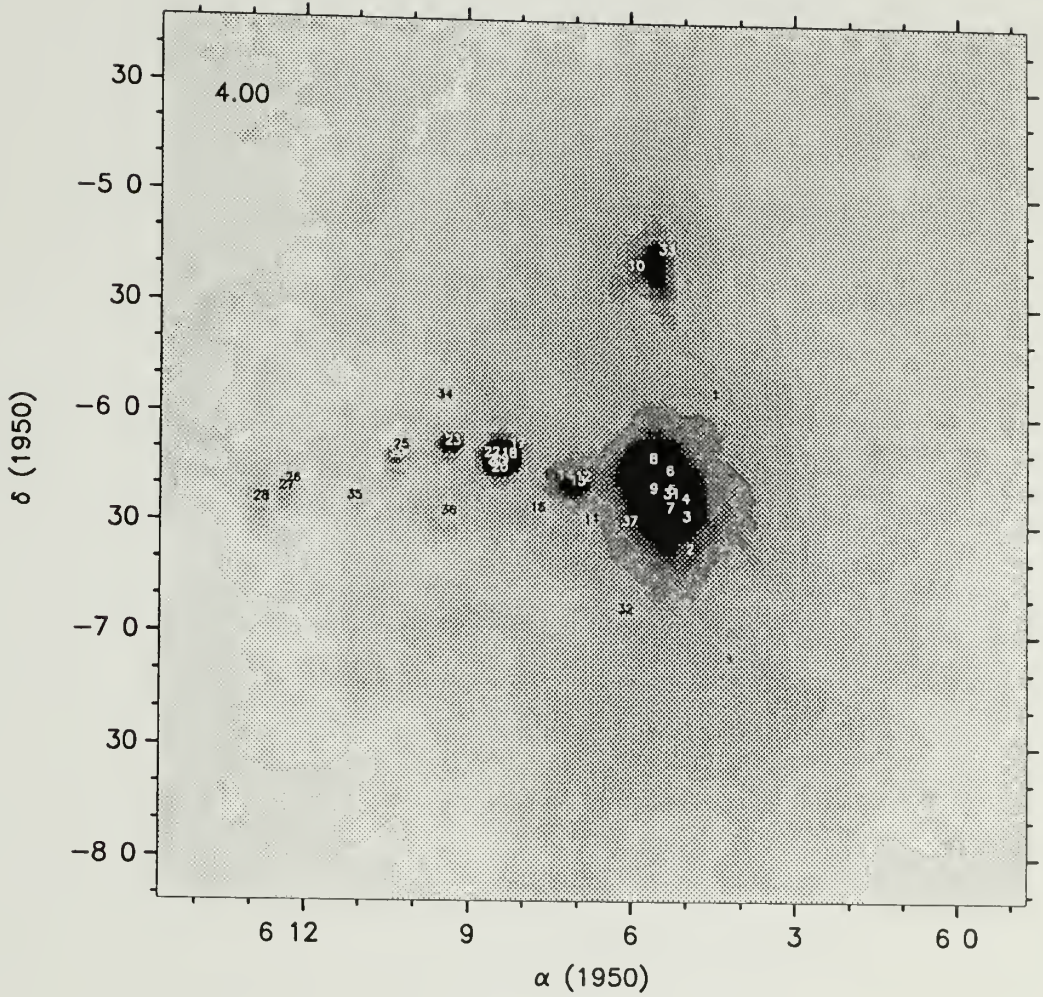
Figure 3.4. The co-added *IRAS BIGMAP* image for 100 μm. Positions of the reflection nebulae are indicated by numbers.

arises when the amount of dust mass is a function of dust temperature, i.e., the dust temperature distribution is not a delta function. This is because emission at different wavelengths is sensitive to grains at different temperatures, and even if one argues that an effective temperature can be defined at each wavelength so that the integral over temperature in the expression of the emission intensity can be eliminated, a color ratio would still not cancel the dust column density term and the problem can not be solved. In fact, in this case, the color ratio along a line of sight is a function of the effective dust temperature and the column densities of all the dust at those temperatures; there are thus four unknowns for any two intensity measurements at two wavelengths. In this case, variation of the color ratio from one line of sight to another cannot easily be interpreted because the effects of dust column density and dust temperature cannot be disentangled. Therefore the difficulty of using color ratio is an intrinsic one. Given the complexity of physical conditions in molecular clouds, we strongly suggest that use of the color ratio technique must be made with extreme caution. If one is to draw conclusions concerning the types of dust grains, their abundances and their temperatures based on color ratios or color-color techniques (cf. Boulanger *et al* 1990; Laureijs, Clark & Prusti 1991), proper decoupling of the dust temperature and the column density should be made.

3.4   Modified Wien Displacement Law

Emission at short wavelengths is sensitive to hot material while emission at longer wavelengths is generally dominated by cold material. For blackbody emission intensity measured with respective to wavelength, this is expressed quantitatively by the famous Wien displacement law, $\lambda_m(\mu m) = 2896/T(K)$. We find that its counterpart for the "grey body" emission of dust grains with emissivity expressed as $Q \propto \lambda^{-\alpha}$ can be written as

$$\lambda_m(\mu m) = \frac{14480}{(5 + \alpha)T(K)}. \qquad (3.1)$$

Assuming $\alpha = 1$, this formula predicts that the four bands of $IRAS$, 12, 25, 60 and 100 microns, should be most sensitive to dust grains at temperatures of 201, 96, 40 and 24 K, respectively.

3.5   Dust Temperature Distribution

3.5.1   Theory

Consider the thermal emission of dust grains in a molecular cloud. Let the specific intensity be denoted by I_ν ($erg\ s^{-1}\ Hz^{-1}\ sr^{-1}\ cm^{-2}$), the mean absorption coefficient (also referred to as dust emissivity in this paper), per gram of dust material, $\kappa_\nu (gm^{-1}\ cm^2)$, and the emission coefficient per unit volume, j_ν ($erg\ s^{-1}\ Hz^{-1}\ sr^{-1}\ cm^{-3}$). For spherical grains of radius a and density ρ, $\kappa_\nu = \frac{3Q}{4a\rho}$, where Q is the often-used dimensionless absorption efficiency or dust emissivity (Hildebrand 1983; Casey 1991). If $dl(cm)$ is the positional displacement along a line of sight, and $\rho_d(r)(gm\ cm^{-3})$ is the mean density of dust material within a volume element whose position is uniquely expressed by $\vec{r}$ in a spherical coordinate system, we may define the optical depth $\tau_\nu(l) = -\int_0^l \rho_d(\vec{r})\kappa_\nu dl$ into the cloud from its surface ($l = 0$) towards us, and we have the emergent intensity (cf. Spitzer 1978)

$$I(\nu) = B_\nu(2.7K)e^{-\tau_\nu(L)} + \int_0^L j_\nu(\vec{r})e^{-\tau_\nu}dl. \qquad (3.2)$$

In the above equation, $B_\nu(2.7K)$ is the cosmic microwave background radiation and L is the extent of the cloud along the line of sight.

A volume element in a molecular cloud may contain dust grains of different sizes, shapes and compositions. As mentioned in the introduction, even if these grains are exposed to the same ambient physical conditions they will attain very different equilibrium temperatures, and smaller grains may even have a time-dependent temperature due to transient heating. Assume that the bulk thermal emission of an ensemble of grains of different sizes, shapes and compositions does not change

significantly with time, despite temperature fluctuations. Since we are considering the far infrared to millimeter range, a single grain i is likely to be optically thin to its own emission. If the grain has a temperature T^i and contributes a mass density ρ_d^i, then the contribution of this grain to the total emission coefficient, according to Kirchhoff's law, is just $j_\nu^i = \rho_d^i \kappa_\nu^i B_\nu(T^i)$, where $B_\nu(T)$ is the Planck function. The total emission coefficient from all grains within a unit volume at a position $\vec{r}$ is $j_\nu(\vec{r}) = \sum_i j_\nu^i$.

If we define $P(\vec{r}, T)(gm\ cm^{-3}\ K^{-1})$ as the mass of dust per unit interval of temperature per unit volume at position $\vec{r}$, and assume the mean absorption coefficient of the ensemble of grains can be meaningfully characterized by a temperature-independent κ_ν (Draine & Lee 1984), we may write $j_\nu(\vec{r}) = \kappa_\nu \int_0^\infty P(\vec{r}, T) B_\nu(T) dT$. Notice that normalization requires $\int_0^\infty P(\vec{r}, T) dT = \rho_d(\vec{r})$. Eq.(1) leads to the emergent flux at the cloud surface ($l = 0$) within a solid angle Ω

$$F(\nu) = \int_0^\Omega B_\nu(2.7K) e^{-\tau_\nu} d\Omega + \kappa_\nu \int_0^\infty dT \int_0^\Omega d\Omega \int_0^L dl P(\vec{r}, T) e^{-\tau_\nu} B_\nu(T). \quad (3.3)$$

We define $W(\nu, T)(gm\ K^{-1}) = D^2 \int_0^\Omega \int_0^L P(\vec{r}, T) e^{-\tau_\nu} dl d\Omega$ to be the dust temperature distribution, where $D(cm)$ is the distance to the cloud. We then have

$$F(\nu) = \int_0^\Omega B_\nu(2.7K) e^{-\tau_\nu(L)} d\Omega + \frac{\kappa_\nu}{D^2} \int_0^\infty W(\nu, T) B_\nu(T) dT. \quad (3.4)$$

In the optically thin case ($\tau_\nu(L) \ll 1$), the exponential terms in the above equation (in both the first term and the expression for $W(\nu, T)$) can be approximated by 1, $W(\nu, T)$ will thus be independent of frequency and can be interpreted as the total mass of dust within the solid angle considered and a unit temperature interval at T ($W(T) = \frac{dM}{dT}$). A position-switched observation subtracting the "off source" signal produced by the background from the "on source" emission gives

$$F(\nu) = \frac{\kappa_\nu}{D^2} \int_0^\infty W(T) B_\nu(T) dT. \quad (3.5)$$

Since this equation does not explicitly contain the source size, it applies to both "resolved" and "unresolved" sources. For the case of diffuse emission, the typical

quantity used is the intensity $I(\nu) = dF(\nu)/d\Omega$ for each line of sight. In this case, the above equation becomes

$$I(\nu) = \kappa_\nu \int_0^\infty G(T) B_\nu(T) dT, \tag{3.6}$$

where $G(T)(gm\ cm^{-2}\ K^{-1}) = \int_0^L P(r, T) dl$ is the dust column density per unit temperature interval.

$I(\nu)$ is determined observationally, and solving for the dust temperature distribution $G(T)$ from Eqs. 3.5 and 3.6 is the first step towards understanding the dust emission. One way to accomplish this is to assume a parameterized functional form for this distribution with parameters being estimated by fitting Eqs. 3.5 and 3.6 to the observed source spectra (Pajot *et al* 1986; Heyer *et al* 1989). There are at least two drawbacks to this approach. First, assuming a form for $G(T)$ is partially assuming a solution. Second, when the spectrum $G(\nu)$ is not simple, finding the appropriate $G(T)$ can be a formidable task.

Xie, Goldsmith & Zhou (1991) have recently used an inversion method for solving for $G(T)$ analytically based on Chen's modified Möbius inversion theorem (Chen 1990). Fitting a function $G(\nu)$ to the observed spectrum, it can be shown that the dust mass distribution as a function of temperature can be expressed as

$$G(T) = \frac{h}{kT^2} \sum_{n=1}^\infty \frac{\mu(n)}{n} f(u/n), \tag{3.7}$$

where $u = \frac{h}{kT}$, $\mu(n)$ is the Möbius function in number theory, and

$$f(u) = L^{-1}[\frac{D^2}{\kappa_\nu} \frac{c^2}{2h\nu^3} I(\nu)], \tag{3.8}$$

where L^{-1} stands for the inverse Laplace transformation, and h, k and c are Planck constant, Boltzmann constant and the speed of light, respectively.

3.5.2 Dust Column Density Distribution

Xie, Goldsmith & Zhou (1991) used a simple power-law form for characterizing the *IRAS* emission and then convert it into the dust temperature distribution

along a line of sight. That work concentrated on the application of the inversion technique, leaving many important issues unaddressed. In this section, we will start with discussing some of those that we deem relevant to this thesis. First, it is worth pointing out that the power-law form used is neither required by the inversion method, nor necessary for fitting the spectra. In principle, one may use any functional forms (e.g., polynomials) to fit the spectra, as long as a reasonably good fit can be achieved and the functional form does not deny the existence of the inverse Laplace transformation. In reality, one may wish to minimize the number of free parameters given the limited number of data points, and one should be careful about the function's behavior outside the frequency range of the available data points because theoretically the dust inversion method uses the entire range of frequencies from zero to infinity. Although the power-law form has a desirable behavior at short wavelength extreme, it predicts far too big an emission intensity at long wavelengths. With this form for the spectrum, the dust temperature distribution, in fact, also takes a power-law form (Xie, Goldsmith & Zhou 1991). The net effect of this undesirable behavior of the spectral fit at long wavelengths is to cause an overestimate of the amount of cold dust and possibly a correspondingly smaller amount of warm dust.

Given the fact that we do not have available data points for longer wavelengths, we see only two ways other than giving up. One is to "overcome" the difficulty by arbitrarily bending down the spectral fit at wavelengths longer than 100 μm, which will lead to a corresponding "bending down" at low temperatures (cf. Xie *et al* 1993). But we feel this is uncertain and correspondingly dangerous. The other way is to try to circumvent the difficulty by restricting the interpretation of the results. We can take two steps in this direction. 1. The modified Wien displacement law provides us a good guideline concerning the temperature range of the dust that *IRAS* data really samples. For $\alpha = 1$, the high and low temperature

limits are 201 and 24 K, respectively. **2.** Given the amount of dust, we notice that increasing the dust emissivity is equivalent to augmenting the dust emission. Within the specified temperature range, our test runs show that the error in the dust temperature distribution caused by the unrealistic rise of the adopted spectral fit at long wavelengths is much smaller than that caused by the order-of-magnitude uncertainty of the emissivity at long wavelengths (Draine 1990). Part of the reason is that the dominant fraction of the amount of overestimated dust mass caused by the power-law spectral fit falls below the low temperature limit set by using the modified Wien displacement law. Realizing this, we decide to use $\kappa_\nu (gm^{-1}\ cm^2) = 2.5 \times 10^{11} \nu(Hz)$, which is roughly the upper limit for the theoretical emissivity (Draine 1990), in order to further compensate the possible overestimate of dust at the lower temperature end.

With these considerations, we adopt a simple power-law form $S(MJy) = a\nu^b$ to fit the four-band *IRAS* data for each pixel of the images. Although the power-law form of the spectral fit itself is less problematic at the short wavelength end, the interpretation of the emission intensity data at this end may be complicated by the possible existence of transiently heated PAHs (Désert, Boulanger & Puget 1990). These very small grains (or large molecules) may make a considerable contribution to the emission spectra at wavelengths from a few microns up to 25 microns (Puget, Léger & Boulanger 1985). While the determination of the dust temperature distribution under the dust inversion method does not specifically involve the types of dust grains, the problem arises because the dust emissivity of PAHs may not be appropriately accounted for by simple power-laws. Forcing grains to take a simple power-law form will certainly cause an error in the dust temperature distribution at the high temperature end. But since our main concern here is the dust column density along each line of sight, which is typically dominated by the amount of cold dust instead of hot dust, it can be hoped that the dust column

density image obtained from the inversion method reflects reliably the change from pixel to pixel.

We present in Figure 3.5 the dust column density image of Mon R2 derived using the dust inversion method. The maximum value of this image is 4×10^{-4} gm cm^{-2}, which is equivalent to the mass column density of 1.2×10^{20} H_2 cm^{-2}. Despite its inability to give definitive information about the total dust column density along each line of sight, the dust inversion method does seem to to be superior in a number of important aspects. First, it takes into account of the dust temperature distribution and avoids the obvious inadequacy of the single-temperature model. Second, it is free of the unphysical abrupt pixel to pixel variations encountered in the attempts to use a two-temperature model (Bally, Langer & Liu 1991). More importantly, except for two of the many point sources which are obviously not related with the molecular clouds, our derived dust column density image is free of the unphysical holes in column density found close to embedded heating sources, which are generally encountered when the traditional single-temperature model is used (Langer *et al* 1989; Snell, Heyer & Schloerb 1989; Jarrett, Dickman & Herbst 1989).

Before concluding this section, we emphasize that *IRAS* data alone, no matter what method one uses, will not lead to any reliable information about the total dust column density along each line of sight. The best that one can hope is that the amount of dust as obtained from *IRAS* data using the dust inversion method may provide a not-so-terribly biased percentage of the total amount of dust, for localized regions at least, in the same sense as the total amount of dust is believed to be a fixed percentage of the total amount of interstellar gas, or the CO or ^{13}CO is believed to be proportional to the total amount of gas. Although all these may be rather "ad hoc", given the lack of better approaches it is reasonable to hope the best. But it is exciting to note that combination of the *COBE* FIR data with IRAS
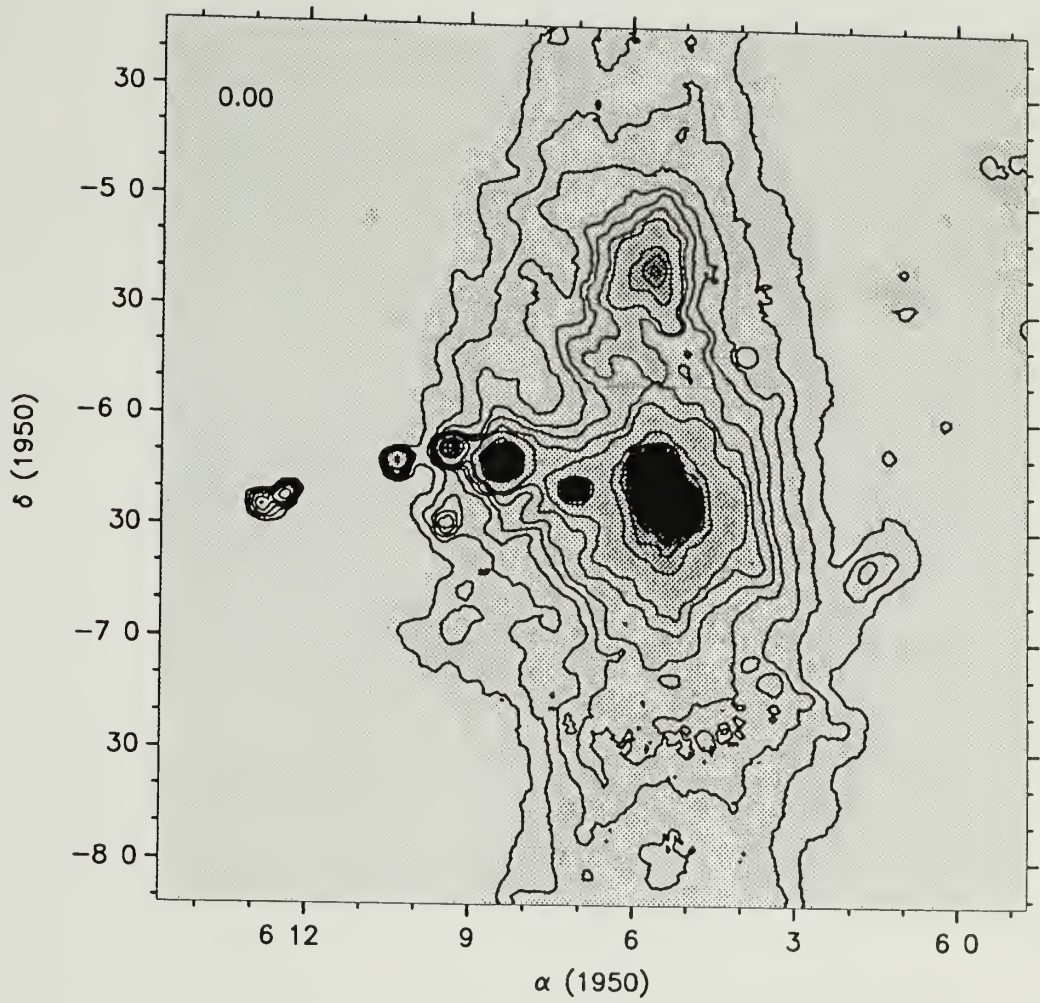
Figure 3.5. Dust column density image. The peak value in this image is $\sim 4 \times 10^{-4}$ gm cm^{-2}. The contour levels are $20, 40, ... 100, 200, ..., 1000 \times 10^{-8}$ g cm^{-2}

data may shed light on the problem (Langer 1992) as for the case of star-forming condensations (Xie *et al* 1993), although the resolution of the resulted images would be much lower than the *IRAS* data can provide alone.

3.6   Pixel by Pixel Comparison of Dust and Gas

Figure 3.6 presents the pixel by pixel correlation between the LTE gas column density and the dust column density obtained using the dust inversion method. A positive correlation trend is clear, but the behavior of this correlation differs significantly at low and high column densities. We have divided the correlation into two parts separated at $N_{LTE} = 10 \times 10^{21} \ H_2 \ cm^{-2}$. For the first part with $N_{LTE} = 1 - 10 \times 10^{21} \ H_2 \ cm^{-2}$, the best least-squares fit achieved is $N_{LTE}(10^{21} \ H_2 \ cm^{-2}) = 0.21 + 1.5 \times 10^6 \sigma_{IRAS}(gm \ cm^{-2})$. For the second part with $N_{LTE} = 10 - 60 \times 10^{21} \ H_2 \ cm^{-2}$, the best fit is $N_{LTE}(10^{21} \ H_2 \ cm^{-2}) = 6.6 + 1.3 \times 10^5 \sigma_{IRAS}(gm \ cm^{-2})$. If the total amount of dust is 1% in mass of the total gas represented by the LTE column density derived from $^{12}CO \ J = 1 - 0$ and $^{13}CO \ J = 1 - 0$ emission, the theoretical relation between gas column density and dust column density is $N_{LTE}(10^{21} \ H_2 \ cm^{-2}) = 2.14 \times 10^4 \sigma(gm \ cm^{-2})$. We have assumed 40% mass contribution from Helium in obtaining the above relationship. Thus, the proportional constant in the best least-squares fit of the LOWER column density region implies that *IRAS* data, under our inversion technique, samples only 1.4% of the total amount of dust. The proportional constant in the best least-squares fit of the HIGHER column density region implies that *IRAS* samples 16% of the total amount of dust. These values are in general agreement with the results of previous studies using single-temperature models (Snell, Heyer & Schloerb 1989; Langer *et al* 1989; Jarret, Dickman & Herbst 1989).

One interesting point of the above results is that *IRAS* seems to sample different fractions of the total amount of gas at low and high column density regions. This
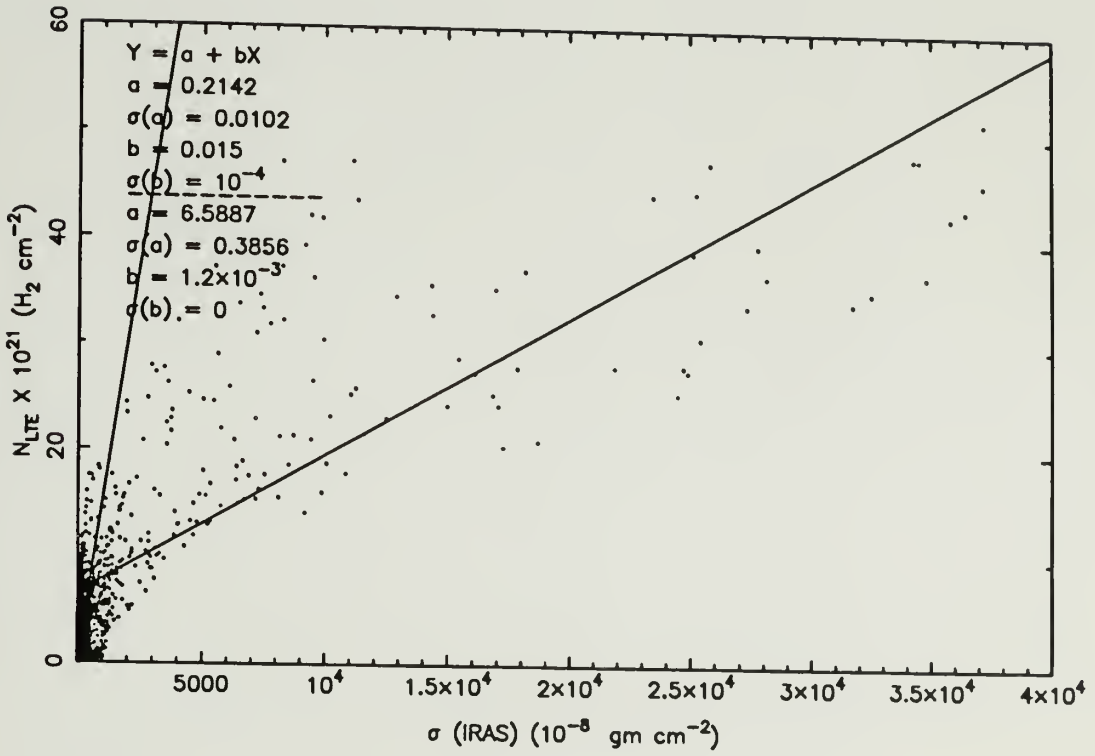
Figure 3.6. Pixel by pixel correlation between the LTE gas column density and the dust column density.

can be understood as follows. In low density regions where there is no significant embedded heating sources, it is possible that only small grains are heated warm enough to emit significantly at *IRAS* bands, while majority of the large dust grains which dominate the dust mass are not warm enough to emit significantly at the *IRAS* bands and thus are under-sampled. In core regions where there is significant internal heating, larger dust grains are warm enough to be sampled by *IRAS* data. In other words, there is serious sampling bias as far as *IRAS* data are concerned regarding regions having significantly different physical conditions. This sampling bias might also explain the large scatter in Figure 3.6. But, the large scatter may result also partly from the fact that in many situations the H_2 column density does not represent the total gas column density, because hydrogen may well be in neutral atomic or even ionized form. This point is supported by the striking discrepancies between the dust column densities and the LTE gas column densities around RN11-16 region and the RN10 region.

3.7 Conclusions

We have discussed difficulties with the use of single- or multi-temperature dust models in deriving dust temperature and column density. An inversion method has been implemented for analyzing dust emission spectra at FIR wavelengths in terms of a continuous dust temperature distribution, and has been applied to *IRAS BIGMAP* images of Mon R2. Although it is impossible to constraint the amount of very cold dust using *IRAS* data alone, we suggest that the column density image obtained with proper care serves a good mapping of the variation of dust column density. We have derived a modified Wien's displacement law to constrain the interpretation of the results concerning the range of dust temperature that the *IRAS* data sensitively samples.

The dust column density image derived using the inversion method has a much better correlation with the gas column density image than any *IRAS* image alone with the gas column density. Even so, the quantitative correlation between the dust and gas column densities has large scatter, and differs at high and low density regions. These results are interpreted in terms of the existence of non-molecular gas, and the insufficient heating of the large dust grains in weak emission regions not associated with active star forming activity.

STAR FORMING CORES IN MON R2

4.1   Introduction

We have shown so far that the basic structure of the entire Monoceros R2 GMC is dominated by a very large half bubble shell (Diameter $\sim$ 32 pc) consisting of mostly blue-shifted gas. As we have summarized in Chapter 2, there appears also a chain of strong emission regions associated mainly with grouping of reflection nebulae. Two of these emission cores, the main core and the GGD12-15 core, which received considerable attention in the past, appear to be interacting with the bubble activity. Although considerable understanding has been achieved of the structure of these two cores, many interesting and important questions remain unaddressed. As anticipated, understanding the overall structure of the GMC has provided quite a few important clues to the structure of the cores. Conceivably, understanding the cores is definitely a necessity for understanding the origin of the huge bubble shell and the nature of the interactions between the cores and the bubble. Studying the structure of these cores is a critical step towards understanding the obviously ongoing star formation in the cores of Mon R2.

Studying these cores is also of great interest, in a general sense, for understanding dense cores as a distinct class of objects. Systematic observational studies of dense cores were first performed in NH_3 emission (Ho & Townes 1983; Myers & Benson 1983; Myers 1983; 1987). For this reason, dense cores are often referred to as ammonia cores. Star formation in these cores was systematically examined by Beichman et al (1986). Several of the main results of these studies are: 1). The average density of these regions is $\sim 10^4$ cm^{-3}. 2). The ammonia emission from

these small dense cores often have subsonic velocity dispersion of $\sim 0.4\ km\ s^{-1}$, which is much smaller than the typical linewidths of molecular clouds. 3). These cores are often sites of star formation as indicated by their association with $IRAS$ point sources, most of which have no optically visible counterparts. Thus these $IRAS$ point sources could be embedded protostars. The CS survey of dense cores carried out by Zhou et al (1989), however, reveals a rather different picture. First, the dense cores appear larger and more extended in CS emission than in ammonia emission. This is obviously not an expected result because CS transitions typically have a larger critical density for collisional excitation and dense cores are believed to be centrally condensed. Second, CS transitions lead to a much larger velocity dispersion (supersonic for the typically assumed kinetic temperatures) for these cores. This complexity of dense cores was further strengthened by the work of Goldsmith et al (1992), who mapped the NGC 2071 core with numerous millimeter molecular tracers and found that each of them revealed a considerably different morphology for the core.

We have made observations of two dense cores in Mon R2, the main core and the GGD12-15 core, in $^{12}CO\ J = 1 - 0$, $^{13}CO\ J = 1 - 0$ and $C^{18}O\ J = 1 - 0$ transitions as well as several high density tracers such as $CS\ J = 2 - 1$, $HCN\ J = 1 - 0$ and $HCO^+\ J = 1 - 0$, using the 15 element QUARRY focal plane array system at FCRAO. The $HIRES$ images of $IRAS$ data produced by IPAC also prove very useful in revealing the morphology of the dust emission from the cores. We will present the results of this research in this chapter. As we realize that the structure of the cores are greatly affected by star formation processes, we concentrate on the interaction of the outflow with the ambient gas.

4.2 Observations

4.2.1 Millimeter Wave Molecular Observations

Before the QUARRY 15 element array (Erickson *et al* 1992) was available at FCRAO, we mapped the main core region in a number of millimeter transitions using the single beam receiver on the FCRAO 14 m telescope, in the period of October 1989 to March 1990. The primary filterbank used had 256 channels each of 100 kHz bandwidth, corresponding to 0.26 km/s resolution at 115 GHz, and the main beam efficiency was estimated to be 0.55, slightly higher than that of the QUARRY array. We first mapped the central $14' \times 14'$ region in ^{12}CO $J = 1-0$ and ^{13}CO $J = 1-0$ with a spacing of 30", and a smaller region of $4' \times 4'$ region in $C^{18}O$ $J = 1-0$. Then we mapped the central $4' \times 4'$ region in high density tracers such as CS $J = 2-1$, HCN $J = 1-0$, HCO^+ $J = 1-0$. These maps were too small to cover the emission region of interest. So when the QUARRY system became available in April 1991, we mapped the main core again in ^{13}CO $J = 1-0$, CS $J = 2-1$ and HCN $J = 1-0$ to achieve a larger coverage, and we have also mapped the GGD12-15 core region in ^{13}CO $J = 1-0$, CS $J = 2-1$, HCN $J = 1-0$ and HCO^+ $J = 1-0$. All these observations were carried out during the period of mapping the whole Mon R2 in ^{12}CO $J = 1-0$ from 1991 April to December. The parameters for the QUARRY mapping of the cores are essentially the same as used for mapping ^{12}CO $J = 1-0$ (Chapter 2), so we will omit any description here.

Although the data sets for the main core taken with the single beam receiver have a smaller spatial coverage than the new QUARRY data, they prove essential for the study of the kinematics of the core because of their much better spectral resolution and coverage. In fact, for quantitative analysis of the high velocity gas in the bipolar outflow of the main core, because the velocity coverage of the filterbank available with QUARRY at the time the data were taken was only about 20 $km\ s^{-1}$,

which can not provide reliable information for the gas at the highest velocities in the bipolar outflow region, we sampled a strip of more than 30 arcminutes long in CO with 30" spacing along the outflow axis, using the single-beam receiver system when the QUARRY system was taken down in April 1992.

4.2.2 IRAS HIRES Images

The resolution of the *IRAS BIGMAP* seems to be inadequate for the study of the cores, and we have therefore obtained the *HIRES* product from IPAC/Caltech for the Mon R2 region. The resolution achieved after 20 iterations is $0.76' \times 0.46'$, $0.80' \times 0.40'$, $1.04' \times 0.60'$ and $1.48' \times 1.11'$ for 12 μm, 25 μm, 60 μm and 100 μm, respectively (IPAC Users' Guide, 1989). The larger and smaller values correspond to the cross-scan and in-scan directions, respectively. For Mon R2, the cross-scan direction is in Right Ascension. The images have dimensions of 481×481 pixels with 15" sampling, covering a $2° \times 2°$ region. Although these images provide no information about the absolute intensity of the emission and thus can not be used for photometric purposes, they appear very useful for revealing the morphological structure, as we will see in this chapter.

4.3 The Main Core

4.3.1 Review

As mentioned in Chapter 1, this core region received considerable research attention from infrared, optical as well as radio astronomers. A radio HII region (also visible on the POSS prints), PKS 0605-06 (G213.7-12.6), was first detected by Shimmins *et al* (1966) and was later studied in radio continuum by Downes *et al* (1975), Gilmore, Brown & Zuckerman (1975) and Vallée, Viner & Hughes (1979). Downes *et al* (1975) pointed out that this HII region has at least two components at 5 GHz; a small, high density one of $\sim$ 15" in size and a large low density envelope

$\sim 2 - 3'$ in size, and that the HII region is powered by an ionizing star of B0 type (ZAMS) or earlier. This result was later confirmed in the observations by Gilmore (1980a,b) and Massi, Felli & Simon (1985). Massi, Felli & Simon (1985) have indicated that the small, high density component is of the "blister" type with a sharp emission edge on the S-E side (see also Torrelles *et al* 1990). Downes *et al* (1975) also reported the detection of type I OH and H_2O masers (Knapp & Brown 1976; Morris & Knapp 1975; Genzel & Downes 1977; Rodríguez *et al* 1980; Rodríguez & Cantó 1983) in the vicinity of the small, high density component of the HII region.

The central $\sim 1' \times 1'$ region was studied intensively in the near and far infrared (Beckwith *et al* 1975; Loren 1977; Cohen & Frogel 1977; Thronson *et al* 1980; Sargent *et al* 1981; Hackwell *et al* 1982; Hodapp 1987; Aspin and Walther 1990). One main result of these studies is the finding of an infrared cluster of more than 10 members (Aspin & Walther 1990) and a shell-like structure with highly polarized NIR emission. The total infrared luminosity is estimated to be $3 \times 10^4 L_\odot$ (Thronson *et al* 1980; Sargent *et al* 1981; Walker, Adams & Lada 1990; Xie *et al* 1993).

Loren, Peters & Vanden Bout (1974), Downes *et al* (1975) and Kutner & Tucker (1975) first detected molecular emission from the core. It is found that the HII region is on the far side of the molecular core since the H_2CO 6 cm line is seen in absorption against the radio continuum (Downes *et al* 1975; Loren 1977). Loren (1977) first suggested that the cloud core is rotating about an NW-SE oriented axis based on his $^{12}CO\ J = 1 - 0$ and $^{13}CO\ J = 1 - 0$ data. This claim of rotation was later supported by the ammonia observations (Willson & Folch-Pi 1981[1]). Loren (1977) first noticed the broad emission wings of the $^{12}CO\ J = 1-0$ emission and concluded that the self-reversal of CO line profile along with the high velocity gas indicates

---

[1] Note the incorrectly labeled orientation of the galactic plane in the figures of this paper. The actual galactic plane is oriented roughly at 90° to what is labeled (e.g., Maddelena *et al* 1986). The conclusions of the paper concerning the galactic plane should thus be changed accordingly.

that the molecular core is undergoing gravitational collapse (see also Snell & Loren 1977). The theoretical work by Leung & Brown (1977) reached a similar conclusion although they argue that expansion must be present to explain the broad emission wing while setting up an upper limit of $\sim 1\ km\ s^{-1}$ to the velocity of collapsing motion based on the analysis of the self-reversal dip of $^{12}CO\ J = 1 - 0$ relative to the $^{13}CO\ J = 1 - 0$ emission peak. Loren (1981) reanalyzed the high velocity emission in Mon R2 region in terms of a bipolar molecular outflow (see also Bally & Lada 1983). The structure of the outflow is studied in detail by Wolf, Lada & Bally (1990) and Meyers-Rice & Lada (1991). Torrelles *et al* (1983), Heyer *et al* (1986), Richardson *et al* (1988), Wolf, Lada & Bally (1990) and Montalbán *et al* (1990) have studied the core region with numerous high density molecular tracers such as CS, HCN, HCO^+ and NH_3. These observations seem to reveal an elongated structure perpendicular to the outflow axis. But the ammonia maps of Montalbán *et al* (1990), which have a resolution of 42", reveal a considerably more complicated structure consisting of as many as 7 clumps distributed around the infrared cluster of stars.

Zaritsky *et al* (1987) have used a CCD imaging technique to study the polarization of background stars in a $9' \times 9'$ region in Mon R2 and have found that the polarization direction is roughly along the galactic plane, which is coincident with the bipolar outflow direction. Jarrett *et al* (1992) studied a number of $20' \times 20'$ fields in Mon R2, and their results confirm the general orientation of the magnetic field in the core region.

4.3.2 Dust Emission

Figure 4.1 presents the *IRAS HIRES* images at the four bands for the core. Reflection nebulae are indicated by numbers and *IRAS* point sources are labeled by

solid circles. These $IRAS$ sources are all the sources listed in the $IRAS$ Point Source Catalog falling in this region.

An elliptical ring-like emission feature is conspicuous in the 60 μm and 100 μm images and visible also on the $12 \mu m$ and $25 \mu m$ images. On the ring-like feature are located the group of reflection nebulae, RN3, RN4 (vdB67), RN6, RN7 and RN 9(vdB69) [2], while the ultra compact HII region appears as a very strong IRAS point source IRAS 06053-0622 in the center of the ring-like feature. It is this unresolved source that contains more than 10 infrared stars along with a shell-like nebulosity (cf. Hodapp 1987; Aspin & Walther 1990). RN 5 & 31 are coincident with IRAS06053-0622. Connected with the ring-like feature, a second ring-like nebulosity visible on the 60 and 100 μm images extends to the NE. RN 8 (vdB68)[3] falls inside this second ring-like feature, on which are found another group of IRAS point sources. In fact, it appears that both ring-like features are clumped into more point-like sources than can be explained by known reflection nebulae and the $IRAS$ point sources catalogued by the IRAS PSC Catalogue. Given the general consistency of the other features in the images with known sources, we feel that the chance that these sources are artificial results of HIRES algorithm is very small. Thus they could be real new young stellar objects.

4.3.3   Gas Emission

Figures 4.2 and 4.3 present velocity channel maps of the main core region for $^{12}CO\ J = 1 - 0$ and $^{13}CO\ J = 1 - 0$, respectively. On the scale of the plots, the two CO isotopes show a similar structure. The eggplant-shaped shell identified in Chapter 2 appears in some velocity channels of both $^{12}CO\ J = 1 - 0$ and $^{13}CO\ J = 1 - 0$ maps. Figure 4.4 presents an overlay of the peak antenna temperature of

---

[2]Note that this source is incorrectly labeled vdB68 in HR.

[3]Note that this source is incorrectly labeled as vdB69 in HR.
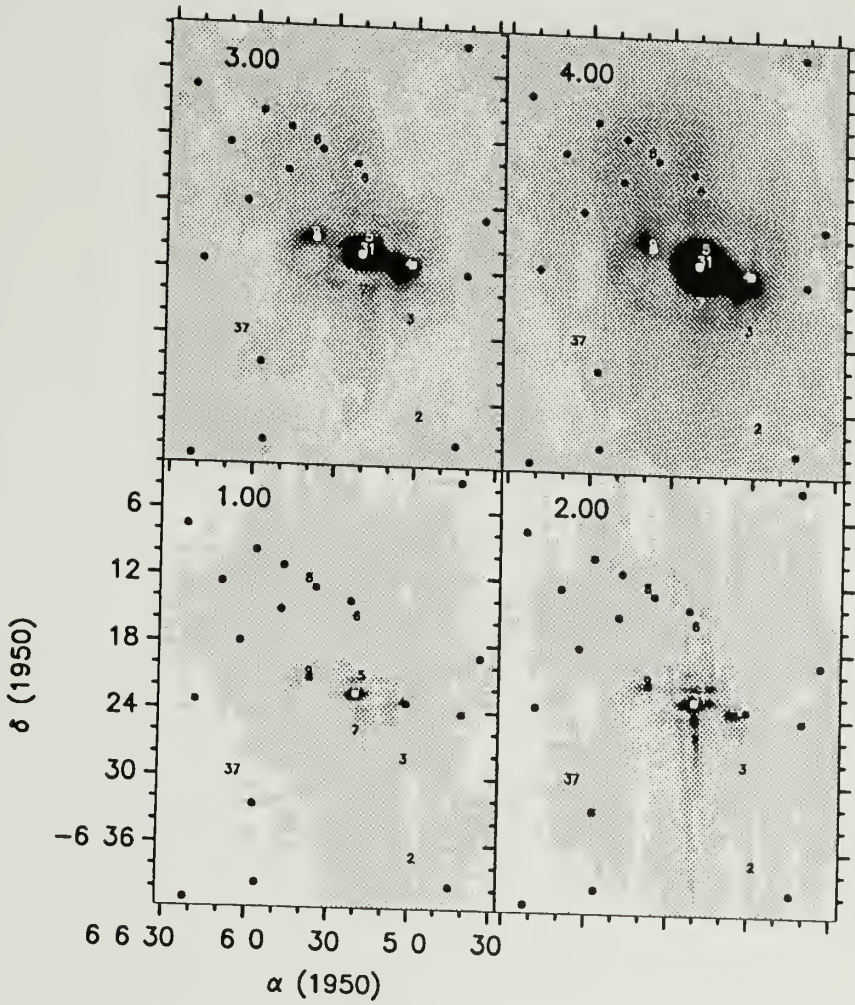
Figure 4.1. *IRAS HIRES* images of the main core region. Reflection nebulae are labeled by numbers and *IRAS* point sources are labeled by solid circles.
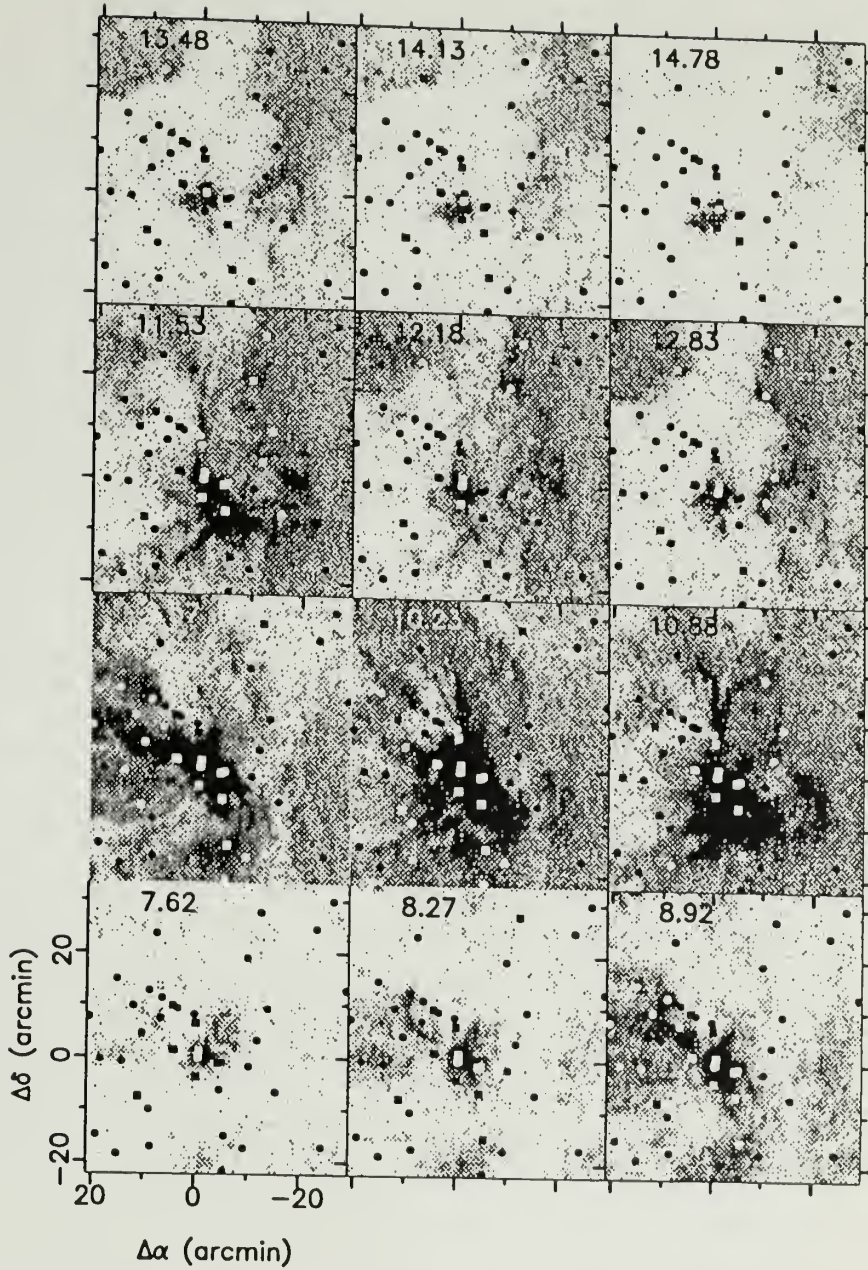
Figure 4.2. ^{12}CO $J = 1 - 0$ emission from the main core region of Mon R2 at different velocity channels. Gray scale ranges from 1 K (white) to 15 K (black). The reflection nebulae and IRAS point sources are labeled by solid squares and circles respectively.
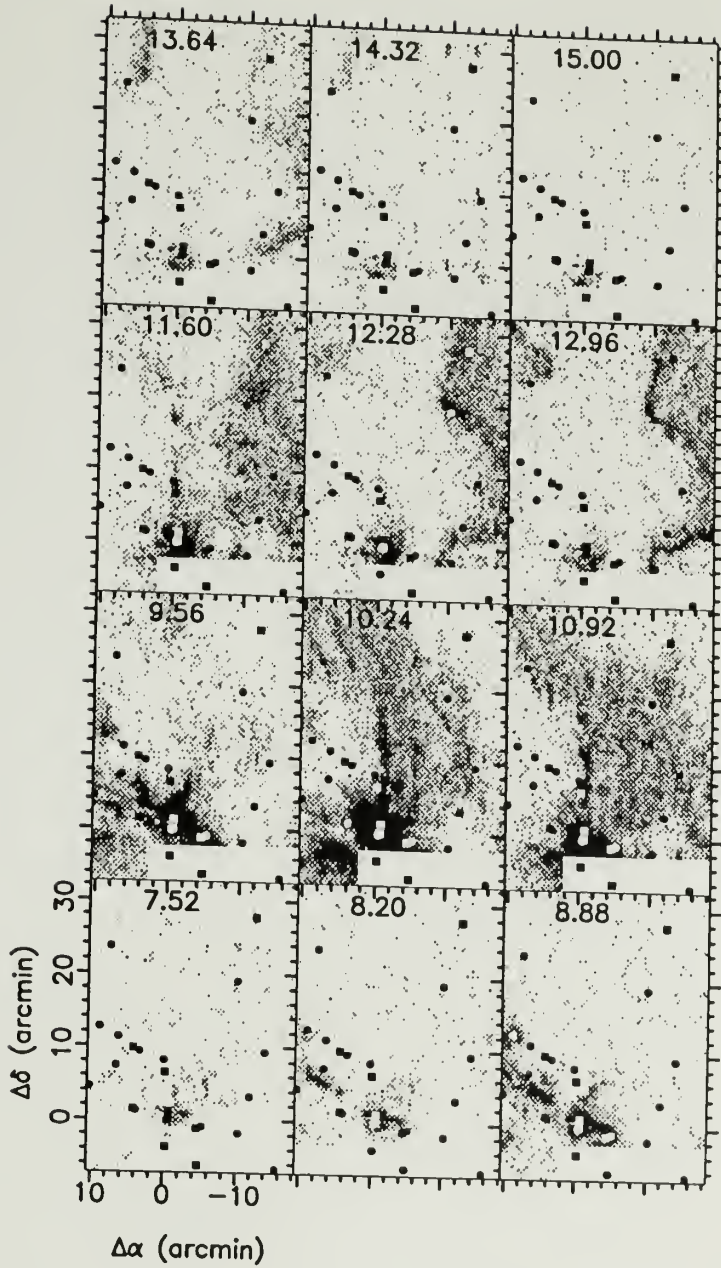
Figure 4.3. ^{13}CO $J = 1 - 0$ emission from the main core region of Mon R2 at different velocity channels. The gray scale ranges from 0.5 K (white) to 7 K (black). The reflection nebulae and IRAS point sources are labeled by solid squares and circles respectively.

^{12}CO $J = 1 - 0$ and the integrated intensity of ^{13}CO $J = 1 - 0$. Figure 4.6 presents an overlay of the CS $J = 2 - 1$ and HCN $J = 1 - 0$ antenna temperature maps [4]. This is consistent with the previous observational results in the same tracers (cf. Richardson *et al* 1988). The interesting point is that these two clumps appear symmetrically displaced with respect to the outflow axis. All these data sets were obtained using the QUARRY system. The emission of the two high density tracers, CS $J = 2 - 1$ and HCN $J = 1 - 0$, seems more spatially confined to the center, and reveals the same feature — two clumps separated by about 0.43 pc; one to the NE and one to the SW relative to the (0, 0) position where an infrared star cluster resides. Figure 4.5 shows the peak antenna temperature map of CS $J = 2 - 1$ emission compared to the POSS red print. Figure 4.7 presents an overlay of the eggplant shaped-outflow shell with the CS $J = 2 - 1$ emission. These two clumps can also be seen in the ^{13}CO $J = 1 - 0$ maps. It is difficult to see this feature in the ^{12}CO $J = 1 - 0$ maps. It is my impression that ^{12}CO $J = 1 - 0$ peak antenna temperature manifests an elongated ridge perpendicular to the outflow axis and displaced a bit to the NW along the outflow axis relative to the clumps in the aforementioned high density tracers. If we take the peak antenna temperature of ^{12}CO $J = 1 - 0$ as tracing the surface kinetic temperature of the gas, then we may interpret this elongated structure as a hot ridge.

We also obtained HCO^+ $J = 1 - 0$ and $C^{18}O$ $J = 1 - 0$ maps using FCRAO 14 m telescope before the QUARRY system was available. These maps cover a smaller area. Figures 4.8 presents integrated intensity map in HCO^+ $J = 1 - 0$ overlayed with the ^{13}CO $J = 1 - 0$ emission. Figure 4.9 presents integrated intensity of $C^{18}O$ $J = 1 - 0$ overlayed with that of CS $J = 2 - 1$ emission. The structure revealed by HCO^+ $J = 1 - 0$ map is clearly different from that revealed by the

---

[4]The integrated intensity maps and the peak antenna temperature maps for these two tracers show essentially the same morphology. We choose to present the peak antenna temperature maps here because they have a smaller noise

coymax—thcoyint
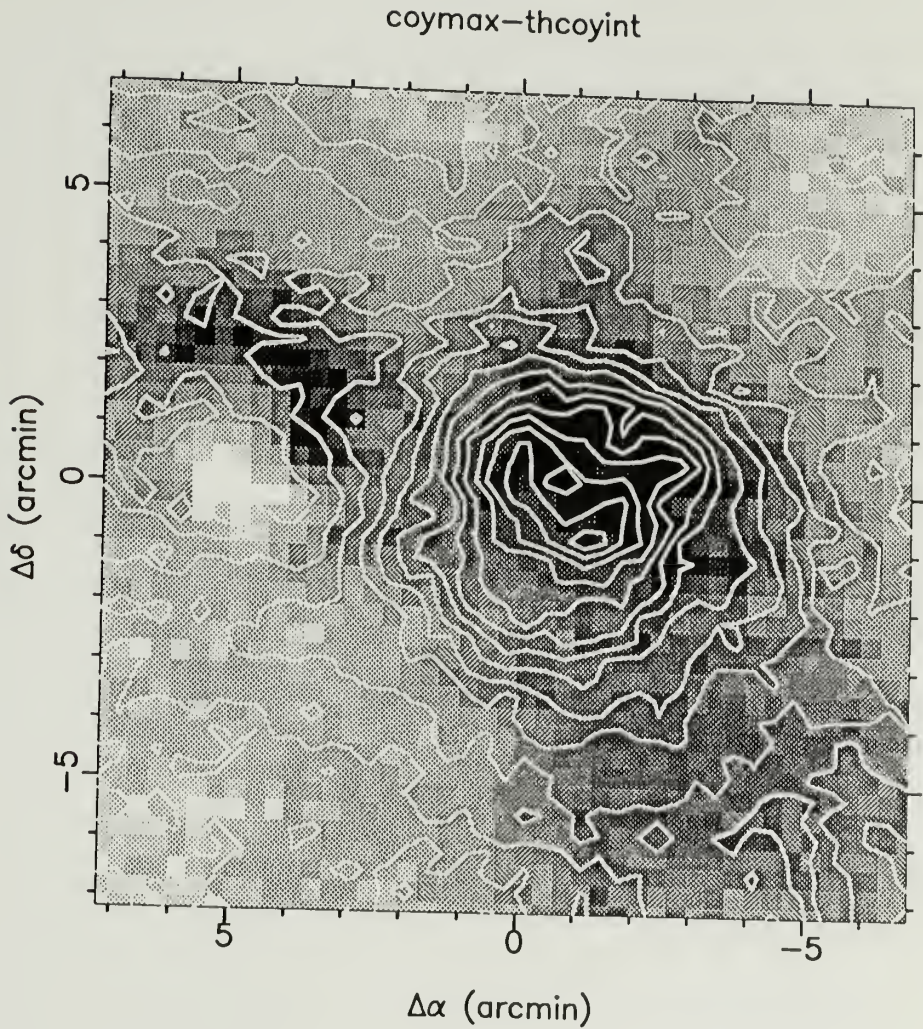
Figure 4.4. An overlay of the peak antenna temperature of ^{12}CO $J = 1 - 0$ emission (halftone) with the integrated intensity of ^{13}CO $J = 1 - 0$ emission (contours) for the main core of Mon R2. The gray scale ranges from 5 K (white) to 17 K (black), and the contour levels are 2.5, 5.0, ..., 37.5 K km s^{-1}.
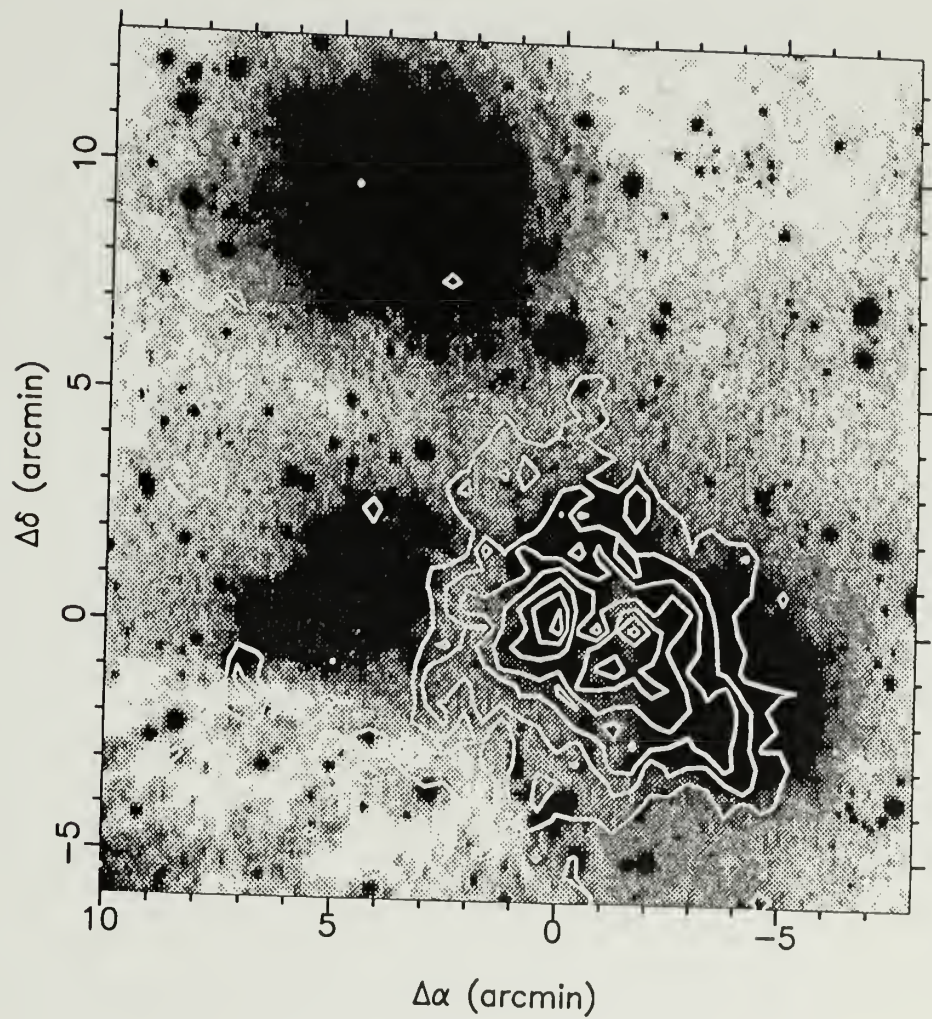
Figure 4.5. An overlay of the antenna temperature map of $CS\ J = 2 - 1$ (contour) on the POSS red print (halftone) for the main core region. Contour levels are 0.8, 1.3, ..., 4.8 K
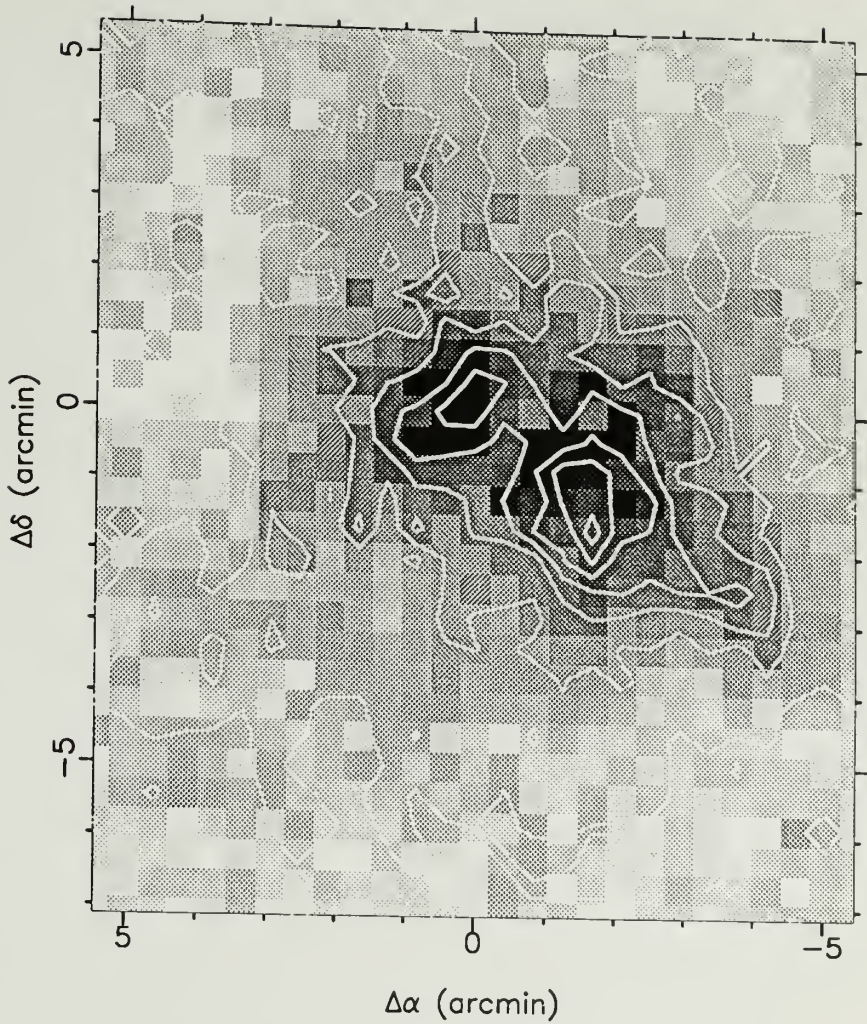
Figure 4.6.   An overlay of the peak antenna temperature map of CS $J = 2 - 1$ (halftone) with that of HCN $J = 1 - 0$ (contours) for the main core of Mon R2. Gray scale ranges from 0.3 K (white) to 4.8 K (black). Contour levels are 0.5, 1.0, ..., 5.5 K.
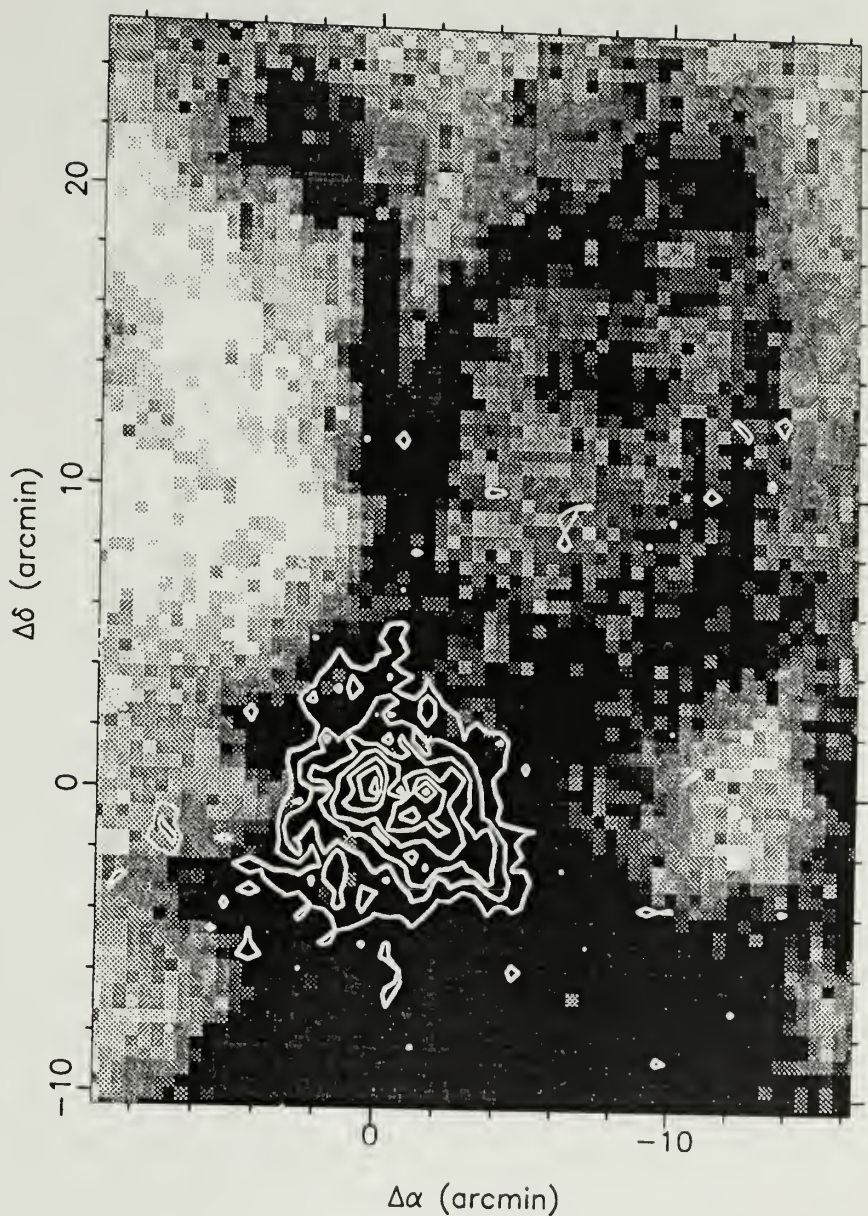
Figure 4.7. An overlay of the ^{12}CO $J = 1 - 0$ emission (halftone) at a velocity of 10.88 km s^{-1} with the peak antenna temperature map of CS $J = 2 - 1$ emission (contours) in the main core. Gray scale ranges from 1 K (white) to 15 K (black). Contour levels are 0.8, 1.3, ..., 4.8 K.

$^{13}CO\ J = 1-0$, $CS\ J = 2-1$ and $HCN\ J = 1-0$ maps, although it also shows two clumps. Because the $C^{18}O\ J = 1-0$ emission is very weak, the signal to noise of our data does not allow a firm assessment of the morphology. But it seems that $C^{18}O\ J = 1-0$ has also a somewhat different distribution from that traced by $CS\ J = 2-1$, and $HCN\ J = 1-0$.

4.3.4   Discussion

The morphology of the core does not appear the same in the various molecular tracers. While the $CS\ J = 2-1$, $^{13}CO\ J = 1-0$, and $HCN\ J = 1-0$ reveal similar structure, $^{12}CO\ J = 1-0$, $C^{18}O\ J = 1-0$, $HCO^+\ J = 1-0$ and NH_3 do not. The ammonia map of Matalbán *et al* (1990) shows a more clumpy structure (consisting of as many as 7 clumps) than our maps presented above, although the spatial resolutions of these maps are comparable. This result is in general agreement with that of Goldsmith *et al* (1992) for the core of NGC2071, which also harbors a bipolar outflow. Goldsmith *et al* (1992) argued that these differences can not be explained in terms of radiative transfer effects. They attribute the differences to chemical differentiation due to time-dependent chemical processes in regions with active star formation. One interesting difference between Mon R2 and NGC 2071 is the emission intensity of $C^{18}O\ J = 1-0$ with respect to high density tracers such as $CS\ J = 2-1$, and $HCO^+\ J = 1-0$. In both cases, the strongest peak emission is about 1K, but this appears comparable to, or even stronger than $CS\ J = 2-1$ and $HCO^+\ J = 1-0$ in the case of NGC2071, while the $C^{18}O\ J = 1-0$ intensity is as much as five times weaker than $CS\ J = 2-1$, $HCO^+\ J = 1-0$ and $HCN\ J = 1-0$ in Mon R2, which have comparable peak antenna temperature of ~ 5 K. Goldsmith *et al* (1992) argued that $C^{18}O$ has the least fractional variation affected by the chemical processes and the fractional abundance of CS is enhanced by roughly an order of magnitude in NGC 2071. In the case of Mon R2, the higher
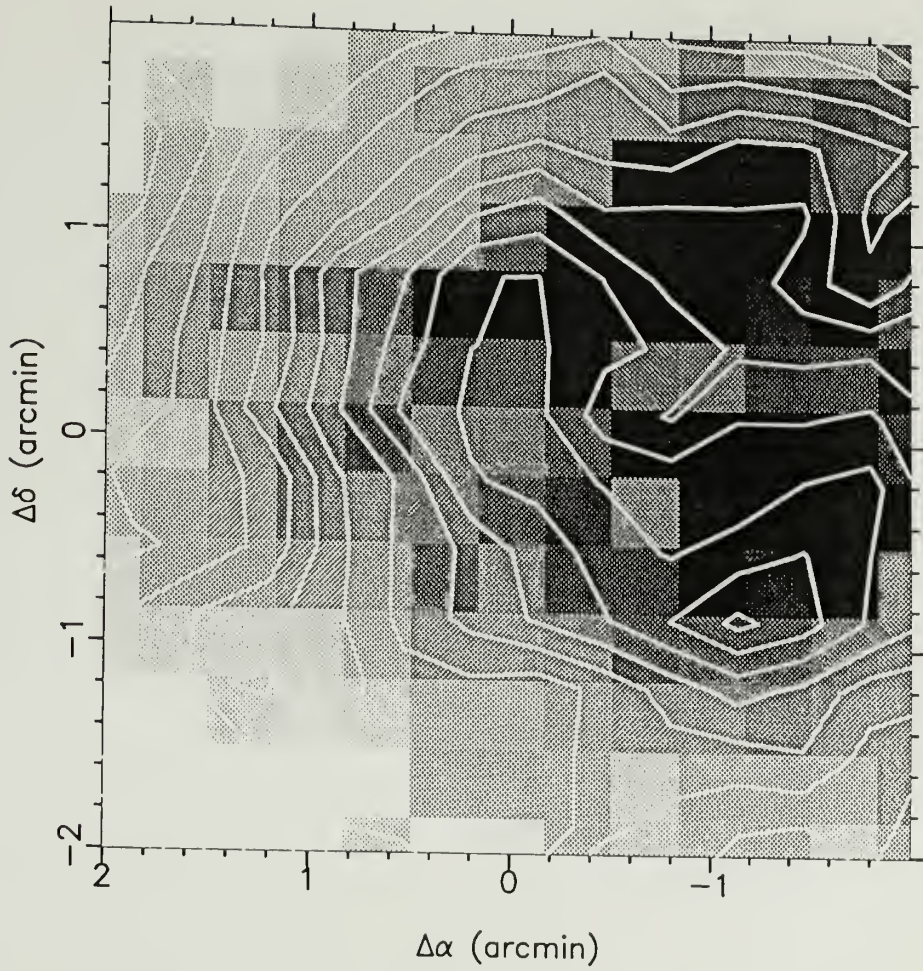
Figure 4.8. An integrated intensity map of HCO^+ $J = 1 - 0$ (halftone) overlayed on that of ^{13}CO $J = 1 - 0$ (contours) for the main core of Mon R2. The gray scale ranges from 3 K km s^{-1} (white) to 16 K km s^{-1} (black). Contour levels are 12, 14, ..., 42 K km s^{-1}.
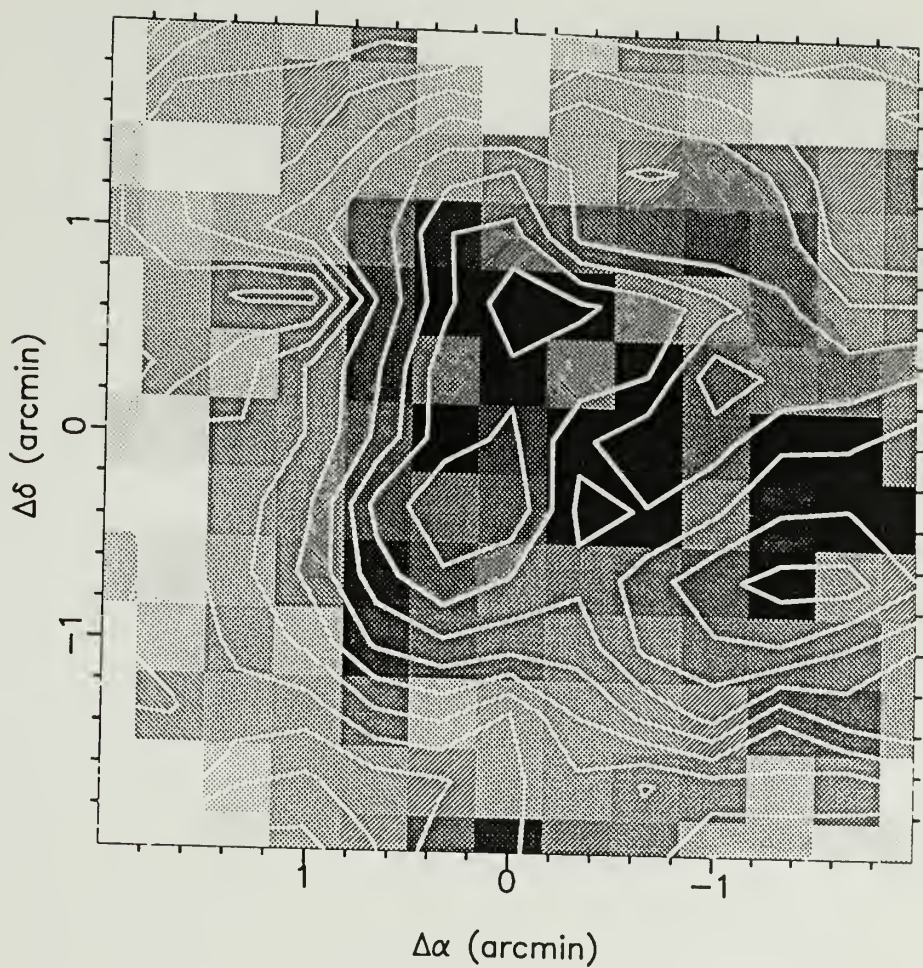
Figure 4.9. An integrated intensity map of $C^{18}O$ $J = 1 - 0$ (halftone) overlayed on that of CS $J = 2 - 1$ (contours) for the main core of Mon R2. The gray scale ranges from 1 K km s^{-1} (white) to 4 K km s^{-1} (black). Contour levels are 4, 5, ..., 15 K km s^{-1}.

intensity of $CS\ J = 2 - 1$ relative to $C^{18}O\ J = 1 - 0$ would definitely mean a significantly greater enhancement of the CS abundance. We also notice that the fact that $CS\ J = 2 - 1$, $^{13}CO\ J = 1 - 0$, and $HCN\ J = 1 - 0$ in the case of Mon R2 reveal rather similar structure is distinctively different from NGC2071, in which case none of these tracers agree so well in their morphology (Goldsmith *et al* 1992). This may suggest drastic differences of physical processes which govern the fractional abundances of various chemical molecules in different sources. As pointed out by Goldsmith *et al* (1992), such a chemical complication strongly cautions us of using one particular tracer to infer physical quantities for star-forming dense cores because the abundance of a particular tracer could be largely affected by the local physical processes.

Despite these complications, the interesting location of the two clumps seen in $CS\ J = 2 - 1$, $^{13}CO\ J = 1 - 0$, and $HCN\ J = 1 - 0$ maps relative to the outflow axis (see Figure 4.7) is strongly suggestive of the way that bipolar outflows are collimated. Figure 4.10 shows the location of the infrared sources with respect to the two clumps. Richardson *et al* (1988) suggested that this elongated structure may be a rotating toroidal disk which collimates the bipolar outflow. This idea can, in fact, be traced back to Torrelles *et al* (1983), who made an ammonia survey of outflow regions searching for these large toroidal disks using single-dish telescope. They found an elongated ammonia structure perpendicular to the outflow axis for Mon R2, which they interpret as evidence for a large disk which collimates the outflow. Torrelles *et al* (1990) made ammonia observations using the VLA and found an interesting arc-like condensation of $\sim 2'$ in size at a position which is 45" to the SW direction of the central compact HII region. This position is roughly coincident with the SW clump identified in our $CS\ J = 2 - 1$, $HCN\ J = 1 - 0$ and $^{13}CO\ J = 1 - 0$ maps. Torrelles *et al* (1990) interpreted the arc-feature as evidence for interaction of the stellar winds with ambient gas.
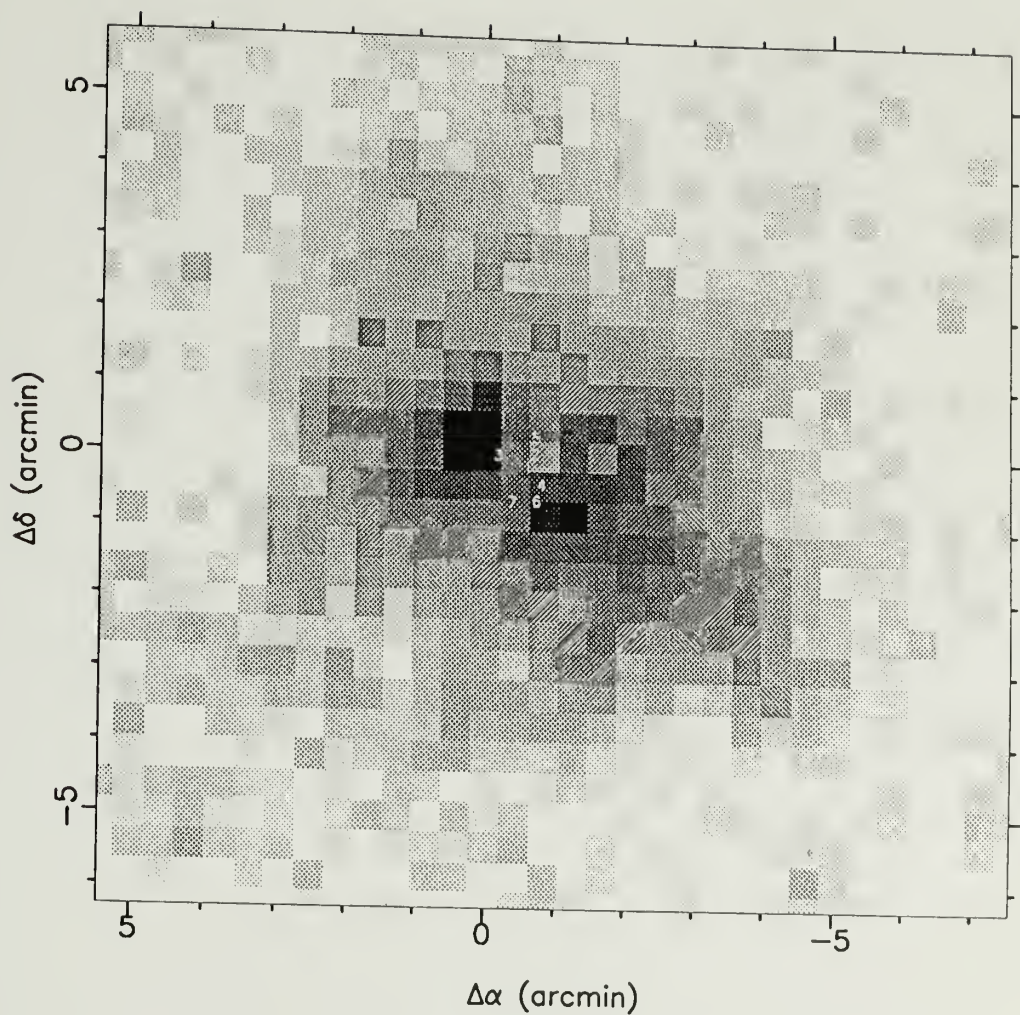
Figure 4.10. The peak antenna temperature map of $CS\ J = 2-1$ emission from the main core. The gray scale ranges from 0.5 K (white) to 4.8 K (black). The Arabic numbers indicate the infrared star cluster, following Beckwith *et al* (1976), Hodapp (1987) and Aspin & Walther (1990).

Do these clumps of gas play a role in collimating the bipolar outflow ? Are they the toroidal collimating disks (Torrelles *et al* 1983; Rodriguez 1987; 1988) ? Figure 4.11 shows a spatial velocity diagram along a cut going through the two clumps in Figure 4.10 using our data obtained with the single beam receiver at FCRAO telescope. The spectral resolution is 0.3 km s^{-1} . It is clear that the NE clump is blue-shifted by 0.5 km s^{-1} . This is consistent with the result of Richardson *et al* (1990). Although this is obviously in accord with the rotational direction expected for a rotating toroidal disk, we feel that the situation may not be so simple. First, different tracers show vastly different morphologies and it is not clear whether the two clumps revealed by CS $J = 2 - 1$, ^{13}CO $J = 1 - 0$ and HCN $J = 1 - 0$ are simply chemical inhomogeneities, along with different structures revealed by ^{12}CO $J = 1 - 0$, HCO^+ $J = 1 - 0$, $C^{18}O$ $J = 1 - 0$ and NH_3 emission. Blake, van Dishoeck & Sargent (1992) studied the circumstellar disk of HL Tauri. They found that CS is depleted at least by a factor of 20-50. Although this may not have much to do with the Mon R2 case, it surely suggests the complexities of chemical processes in circumstellar region. Second, if it is a toroidal disk, then this toroidal disk has an infrared star cluster forming inside and even an ultracompact HII region (Massi, Felli & Simon 1985) and a small shell-like feature (Hodapp 1987; Aspin & Walther 1990). Third, the velocity shift between the two CS clumps could be due to the fact that this core is located on the western side of the large blue-shifted bubble shell of the whole GMC. Figure 4.12 shows an SV cut along the outflow axis in the CS $J = 2 - 1$ emission map. Apparently, it also shows a velocity gradient. The rotational direction implied by this velocity gradient is definitely not that expected for a toroidal disk. This velocity gradient is likely a manifestation of the bipolar outflow.

Figure 4.13 presents a comparison of the dust emission with respect to the outlow shell on a larger scale. One conspicuous feature is that the $IRAS$ point sources on

$T_A^{\bullet}$ (K): 0.3 0.6 0.9 1.2 1.5 1.8 2.1 2.4 2.7 3.0 3.3
A cut from (0.67,   1.00) to (-2.00,   -1.00)
($\Delta\alpha$(arcmin), $\Delta\delta$(arcmin))

16-AUG-92   06:03:30
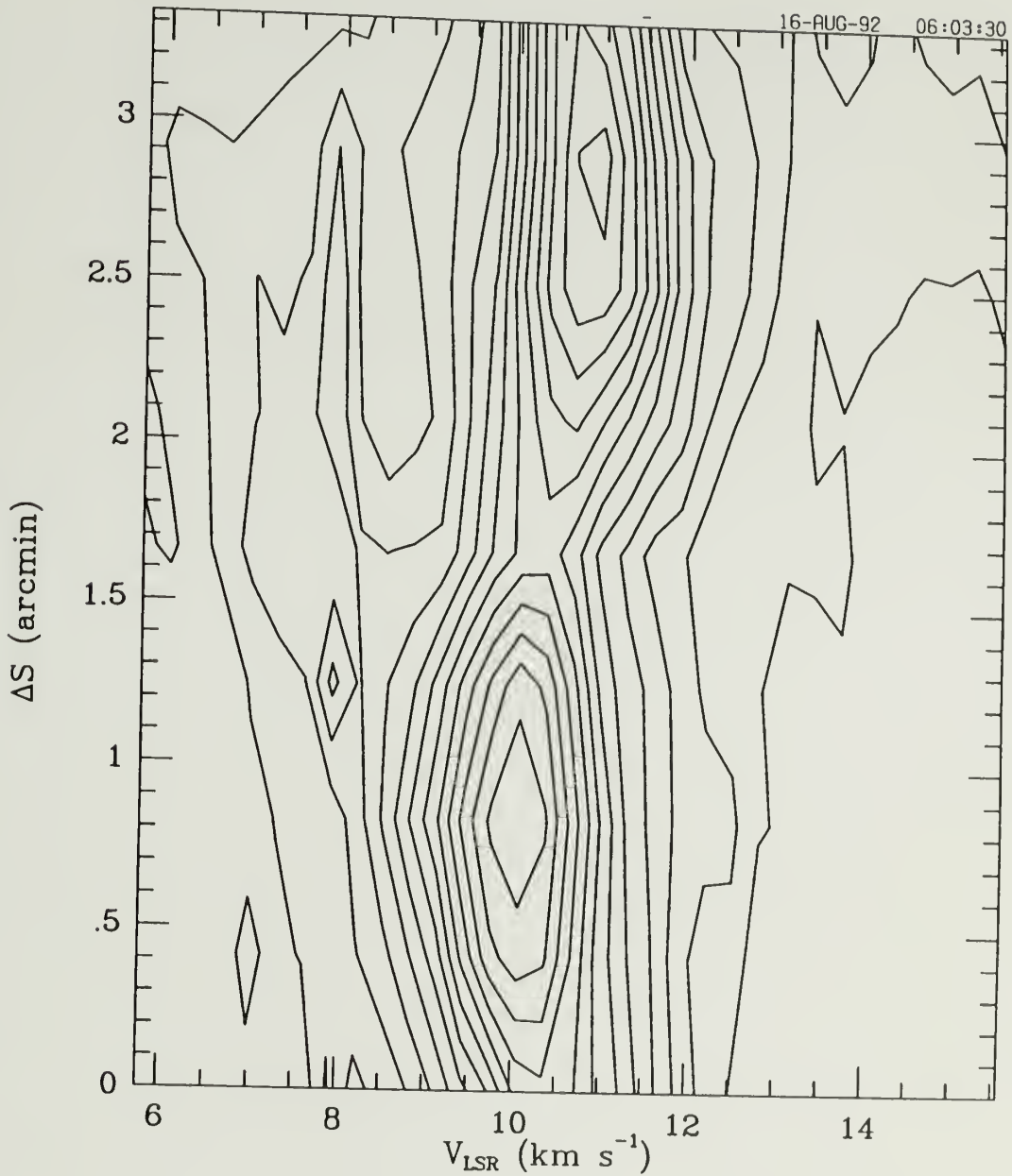
Figure 4.11. An SV diagram of the $CS\ J = 2-1$ emission along a cut going through the two CS clumps. Contours are 0.3, 0.6, ..., 5.1 K
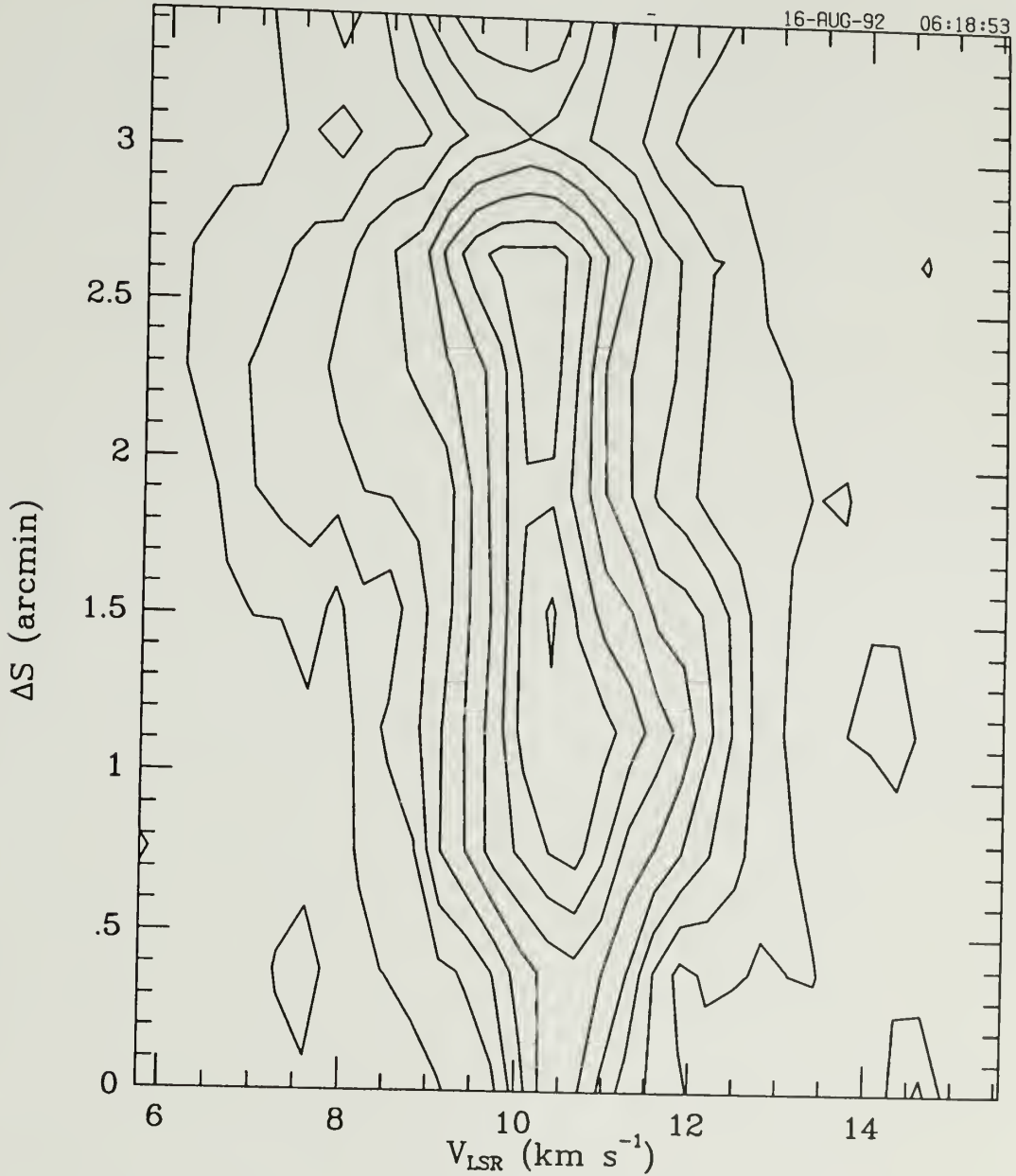
Figure 4.12. A SV diagram of the $CS\ J = 2 - 1$ emission through a cut along the outflow axis. Contours are 0.3, 0.6, ..., 5.1 K.
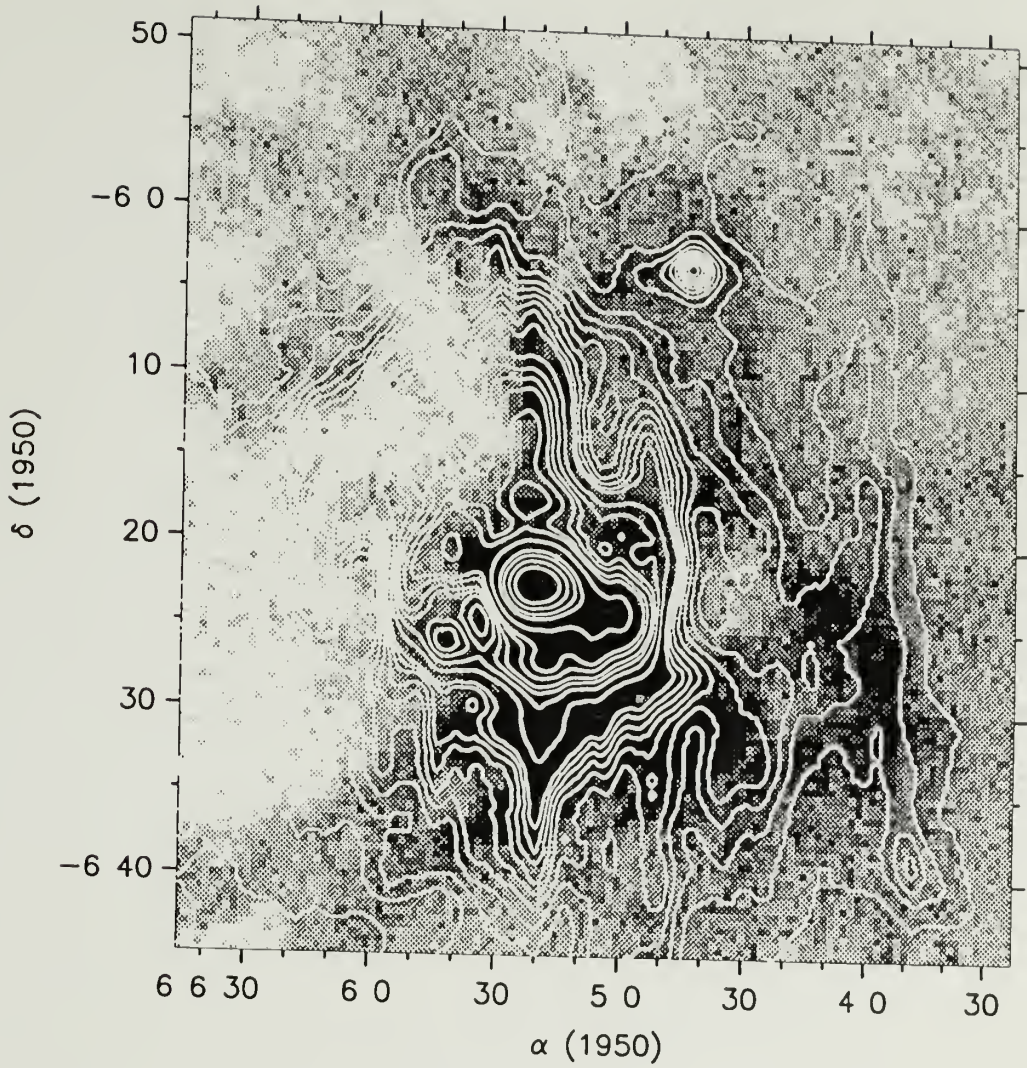
Figure 4.13. HIRES image at 100 microns (contours) overlayed on the ^{12}CO $J = 1 - 0$ emission at $V_{LSR} = 10.88$ km s^{-1} (halftone). The grey scale ranges from 1 to 14 K. The contours are 10, 20, ..., 100, 150, ..., 300, 400, 500, 1000, 3000, 5000, 10000, 20000 MJy/sr.

the right side of the upper ring-like feature in Figure 4.1 are coincident with the locally vertical cavity wall of $^{12}CO\ J = 1 - 0$ emission to the east of the eggplant shaped bipolar outflow shell. A second conspicuous feature is that RN8 (vdB68), which is obviously powering a Strömgren sphere (HR), is located in the shell cavity to the northeast of the main core, and is apparently partly responsible for the locally vertical cavity shell or even the star formation on the wall (see Chapter 6). Presumably, the ionizing photons and possibly stellar winds of this B1 star have cleared out a small cavity near it. This is consistent with the low hydrogen density of $3 - 30\ cm^{-3}$ around this nebulosity, estimated by HR. RN9(vdB69), similar to RN8(vdB68), is also located in the cavity to the east of the dense gas core, but from the shape of the cavity wall close to this star and the spectral type (B2V) of this star, it is perhaps of less importance for the formation of the large bubble shell, although it may have the power to clear out a small cavity. In general, neither RN8(vdB68) nor RN9(vdB69) is likely to be the source responsible for the large cavity shell identified in Chapter 2. Their location in the large cavity is largely the result of another source located somewhat to their east blowing away their ambient gas. This point is supported by the association of RN4 (vdB67) with molecular gas. RN4 is powered by a B2V star. RN4-6 and RN31 are also still embedded in gas. This is consistent with the classification of these sources as Orion population stars (HR). The association of these reflection nebulae with the gas is also seen in Figure 4.14, which presents an overlay of the dust emission with $CS\ J = 2 - 1$ emission. The two CS clumps fall on the strong source IRAS 06052-0622, which is unresolved at 60 and 100 microns, but barely resolved into multiple sources in the 12 and 25 microns bands (Figure 4.1). As reviewed earlier in this section, this infrared source consists of a shell-like feature nebulosity in high resolution NIR observations (Hodapp 1987; Aspin & Walther 1990). But the peculiar thing is that the shell-like feature in the NIR is surrounded by the large ring-like feature in the HIRES images as discussed
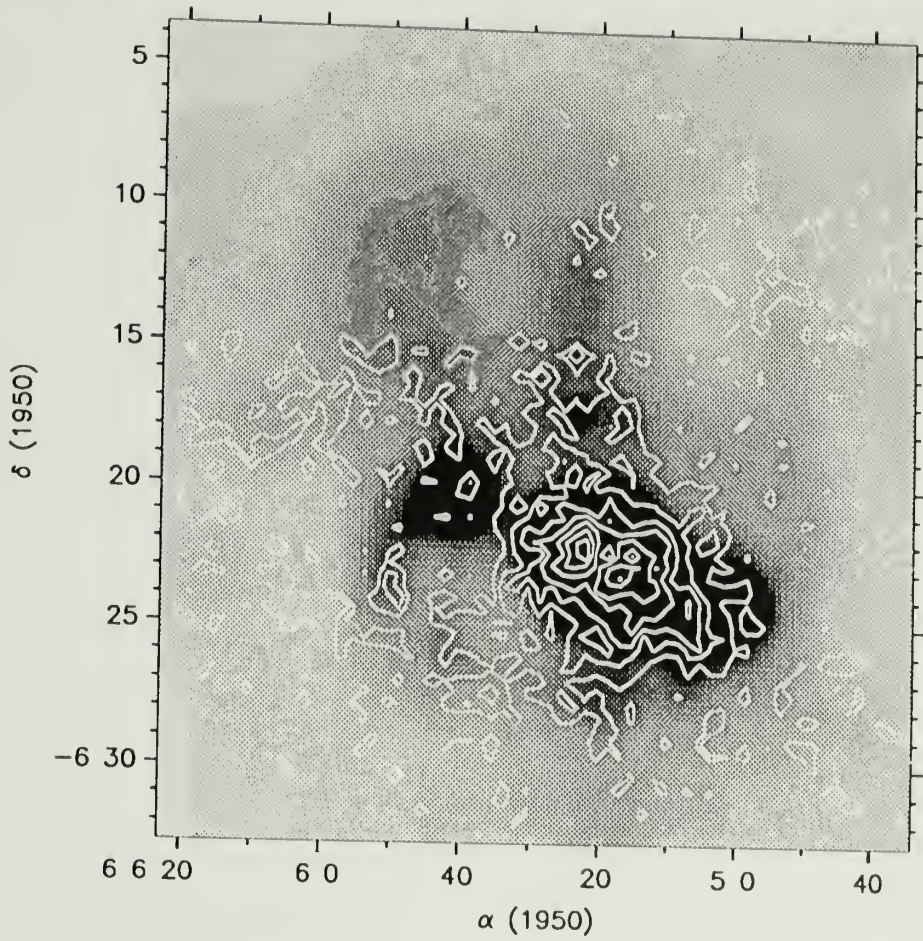
Figure 4.14. $CS\ J = 2 - 1$ peak antenna temperature (contours) compared to the *HIRES* 100 μm image (halftone). Contour levels are 0.5, 1.0, ..., 5.0 K.

above. The question is: what causes these shell or ring features on different scales ? While the internal shell-like feature is probably caused by the IRS2 source (Hodapp 1987; Aspin & Walther 1990), it is not obvious what causes the the large ring-like structure on which a number of reflection nebulae are seen.

An equally puzzling (but perhaps related) question is the existence of the reflection nebula RN 37(DG 092) to the south-east of the core, which is clearly also an emission nebulosity as seen from the POSS red print. This patch of nebulosity has a large area and extends all the way to the core with streaming dark lanes (HR) reminiscent of foreground extinction. The radio map of the low density HII region obtained by Gilmore (1980a,b) seems to show radio emission with a continuous extension towards this nebulosity, but the map does not have large enough coverage to clarify the nature of this nebulosity. We feel that it is possibly an HII region obscured by the foreground material (mostly the blue-shifted shell). We also notice that this object is coincident with a radio source detected at 3.2 GHz with a flux of $180 \pm 50 \ mJy$ (Hughes & Baines 1985). From the estimated upper limit for the flux based on the non-detection of this source at $10.5 \ GHz$, Hughes & Baines (1985) estimated a lower limit for the spectral index of -1.3, based on which they argue that this source maybe a non-thermal source. It is not clear to what extent this result should be trusted. Further study of this region to clarify the nature of this source and the RN 37 region should be very useful.

4.4 GGD 12-15 Region

4.4.1 Review

This core is located roughly 45' to the east of the main core. This region first received attention because several objects in this region were classified as possible Herbig-Haro objects and catalogued by GGD (Gyulbudaghian, Glushkov & Denisyuk 1978), and is thus referred to as GGD 12-15 region (Cohen & Schwartz

1980). Similar to the main core in Mon R2, this core is found to have a compact HII region powered by a B0.5 ZAMS star (Rodriguez *et al* 1980). A bipolar outflow and a water maser are also detected, indicating the youth of this star forming region (Rodriguez *et al* 1982). Cohen & Schwartz (1980) found no emission lines from the core, which led them to conclude that GGD12-15 are reflection nebulae rather than H-H objects. The K-band observations of Cohen & Schwartz (1980) and Reipurth & Wamsteker (1983) reveal a number of nebulosities in the region, corresponding to GGD12-15. GGD12 is the brightest powered by an H_α emission star LkH_α 338 (Herbig & Rao 1972; Cohen & Kuhi 1979), while the compact HII region seems to be associated with GGD14. This region was later studied in the NIR and FIR by Harvey *et al* (1985) and Olofsson & Koornneef (1985). Harvey *et al* (1985) identified 13 infrared objects in a $1' \times 1'$ region. They found a FIR object coincident with the compact HII region with a total luminosity of $\sim 10^4$ $L_\odot$ and a 20 μm peak coincident with the H_2O maser with a total luminosity of $\sim 200 - 1000$ $L_\odot$. They argued that this weaker infrared source possibly has a disk-like structure surrounding the exciting B type star and may be responsible for the bipolar outflow.

Several molecular studies of this region have appeared recently. Güsten & Marcaide (1986) mapped the GGD12-15 region in ammonia, which shows the presence of at least three velocity components at 9.7, 11.2 and 12.2 km s^{-1} , in addition to the presence of the bipolar outflow. Heaton *et al* (1988) and Little, Heaton & Dent (1990) have mapped the region in ^{12}O $2 - 1$, ^{13}CO $J = 1 - 0$ and HCO^+ lines. But their maps have rather limited coverage. Except for their CO $2 - 1$ data, the sampling of their maps is inadequate for understanding the detailed molecular structure of the region.

In this thesis, we have mapped the GGD 12-15 region in a number of molecules at millimeter wavelengths using QUARRY. The *HIRES* images also prove very useful for revealing the dust emission on the scale of interest.

4.4.2 The Structure of GGD 12-15 Core

Figures 4.15 and 4.16 show velocity channel maps for ^{12}CO $J = 1 - 0$ and ^{13}CO $J = 1 - 0$, respectively. Figures 4.17, 4.18, 4.19 and 4.20 show comparisons of the integrated intensity or peak antenna temperature maps of emission of these CO isotopes and several high density tracers. ^{12}CO $J = 1 - 0$ and ^{13}CO $J = 1 - 0$ emission is very extended, while the high density tracers are concentrated close to the infrared star cluster revealed by K-band images (cf. Harvey et al 1985). In this small region, all the high density tracers reveal a rather similar structure. Unlike the main core, the morphologies of this dense core revealed by these tracers, except ^{12}CO $J = 1 - 0$, seems to show better agreement with each other. This may suggest that the main and the GGD 12-15 cores have physical and chemical differences or the star formation activities in them have different ages and properties. Although the bipolar outflow in GGD 12-15 has a velocity of $\sim 30km$ s^{-1} (Rodríguez et al 1982; Little, Heaton & Dent 1990)[5], much higher than the ~ 20 km s^{-1} for the main core outflow, its mass and energy are only ~ 1 $M_\odot$ and $\sim 10^{45}$ ergs (Rodríguez et al 1982; Little, Heaton & Dent 1990), respectively, more than two orders of magnitude smaller than those of the main core (~ 200 $M_\odot$ and $\sim 3 \times 10^{47}$ $ergs$, Wolf, Lada & Bally 1990). Figure 4.21 presents $HIRES$ images in the four $IRAS$ bands for the GGD 12-15 region. Similar to the images for the main core, ring-like features appear conspicuous in the 60 and 100 μm images. Reflection nebulae are labeled by numbers as tabulated in Table 1.1, and $IRAS$ point sources are labeled by solid circles. These $IRAS$ sources are all the sources listed in the $IRAS$ Point Source Catalog falling in this region. Amazingly, similar to the ring-like feature in the main core, reflection nebulae and $IRAS$ point sources are again dominant features of the dust emission ring, and the central strong IRAS point source IRAS 06064-0611 (unresolved in the

---

[5]The spectral coverage of our data obtained using QUARRY system was inadequate for the study of the bipolar outflow. We thus quote the results of previous research in the following.
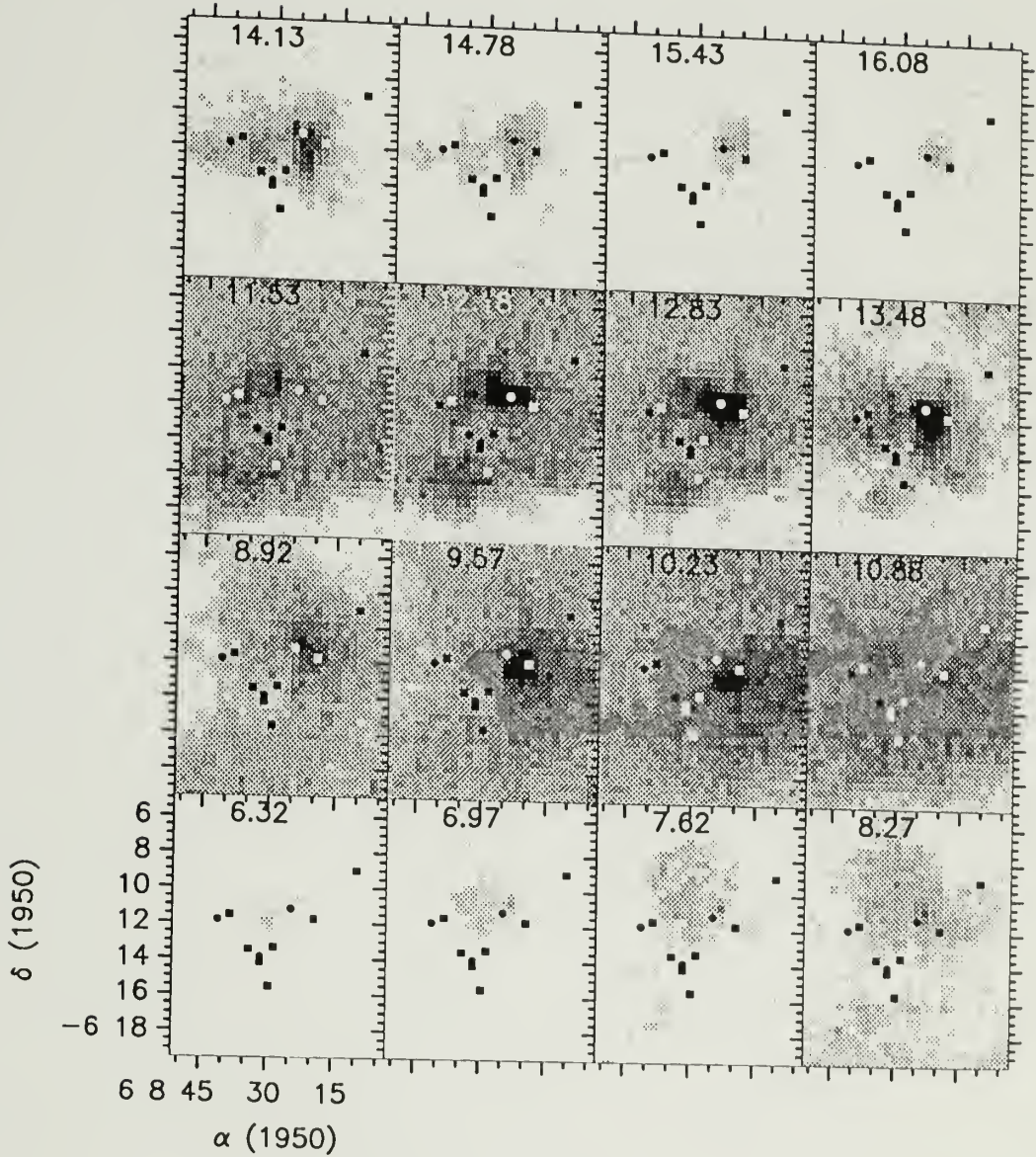
Figure 4.15. ^{12}CO $J = 1-0$ emission from the GGD 12-15 region at different velocity channels. The gray scale ranges from 1 K (white) to 10 K (black). Reflection nebulae are labeled by solid squares, and *IRAS* point sources are indicated by solid circles.
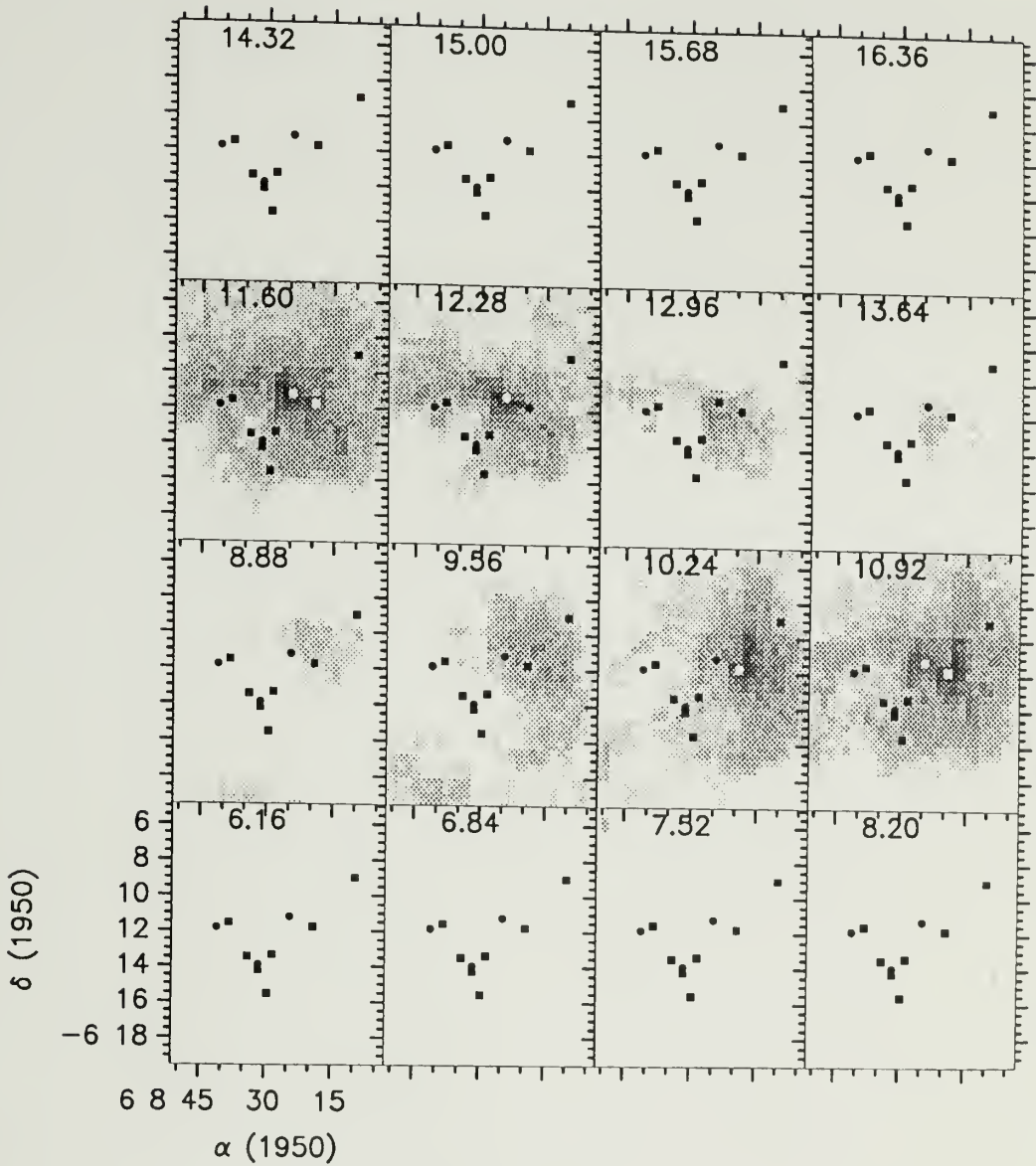
Figure 4.16. ^{13}CO $J = 1-0$ emission from the GGD 12-15 region at different velocity channels. The gray scale ranges from 0.5 K (white) to 7 K (black). Reflection nebulae are labeled by solid squares, and $IRAS$ point sources are indicated by solid circles.

Figure 4.17. Integrated intensity map of $HCN\ J = 1 - 0$ (contours) overlayed on that of $CS\ J = 2 - 1$ (halftone) for the GGD12-15 region. The gray scale ranges from 0.5 (white) to 7 $K\ km\ s^{-1}$ (black). Contour levels are 1.5, 3.0, ..., 20 $K\ km\ s^{-1}$.
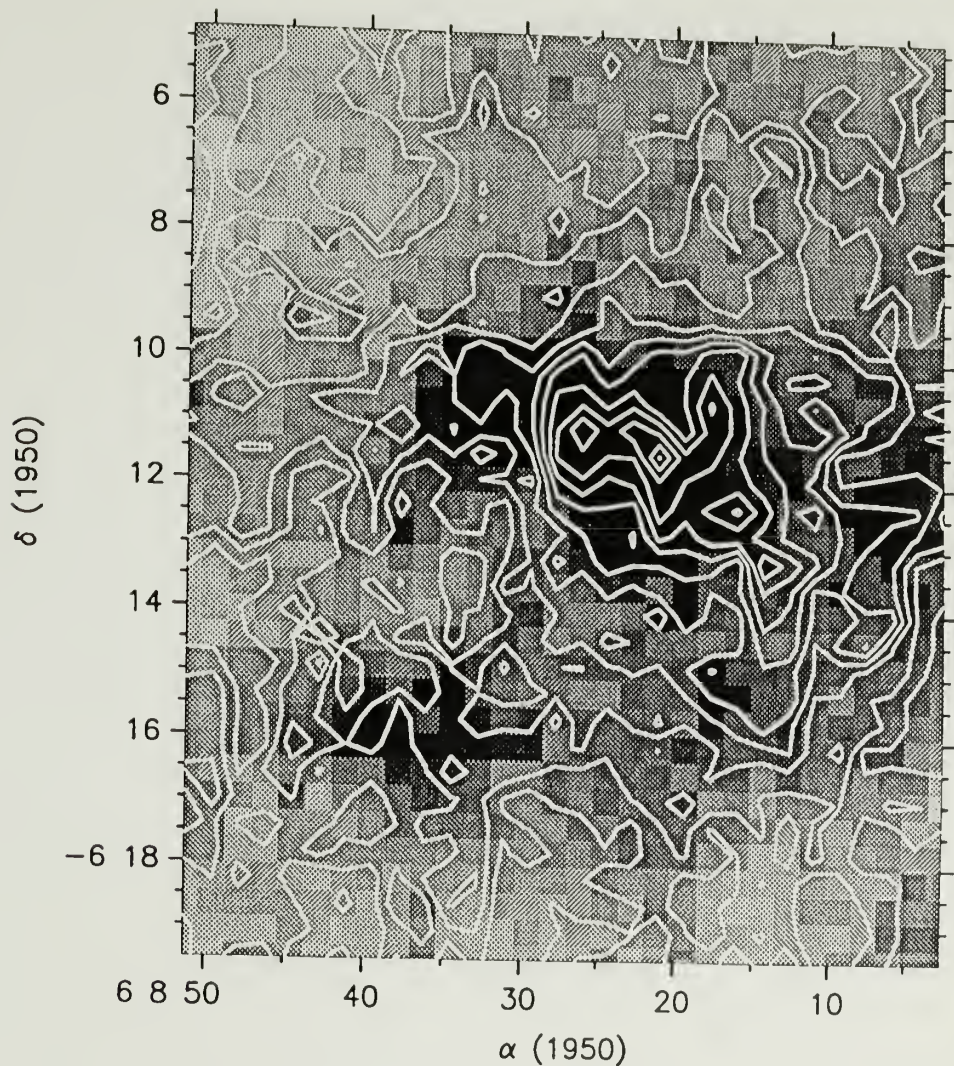
Figure 4.18. Integrated intensity map of ^{13}CO $J = 1 - 0$ (contours) overlayed on the peak antenna temperature of ^{12}CO $J = 1 - 0$ (halftone) in the GGD12-15 region. Contour levels are 2, 4, ..., 24 K km s^{-1}. The gray scale ranges from 1 K (white) to 10 K (black).
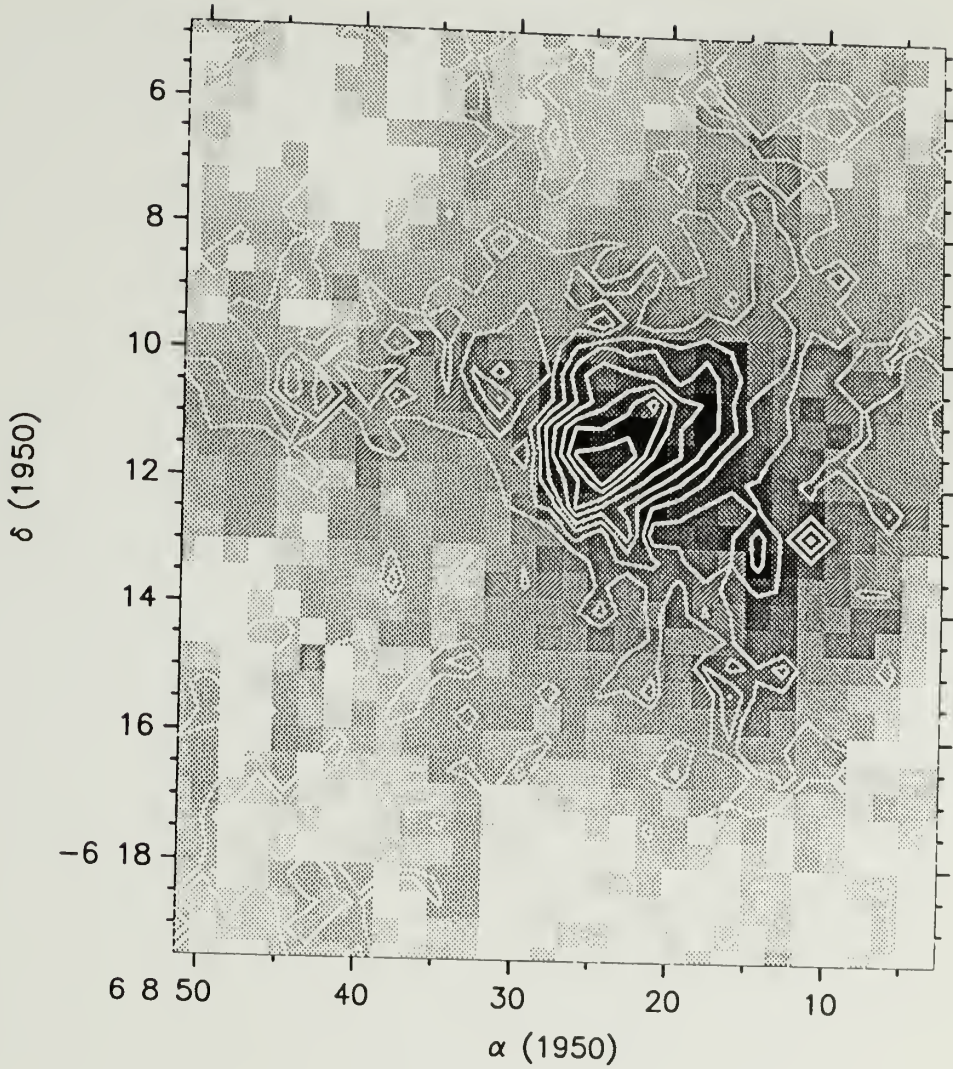
Figure 4.19. The integrated intensity map of CS $J = 2 - 1$ (contours) overlayed on that of ^{13}CO $J = 1 - 0$ (halftone) in the GGD12-15 region. The contour levels are 1, 2, ..., 8 K km s^{-1}. The gray scale ranges from 2 (white) to 20 K km s^{-1} (black).

Figure 4.20. The integrated intensity map of $CS\ J = 2 - 1$ (contours) overlayed on that of $HCO^+\ J = 1 - 0$ (halftone) in the GGD12-15 region. Contour levels are 1, 2, ..., 8 $K\ km\ s^{-1}$. The gray scale ranges from 1 $K\ km\ s^{-1}$ (white) to 9 $K\ km\ s^{-1}$ (black).
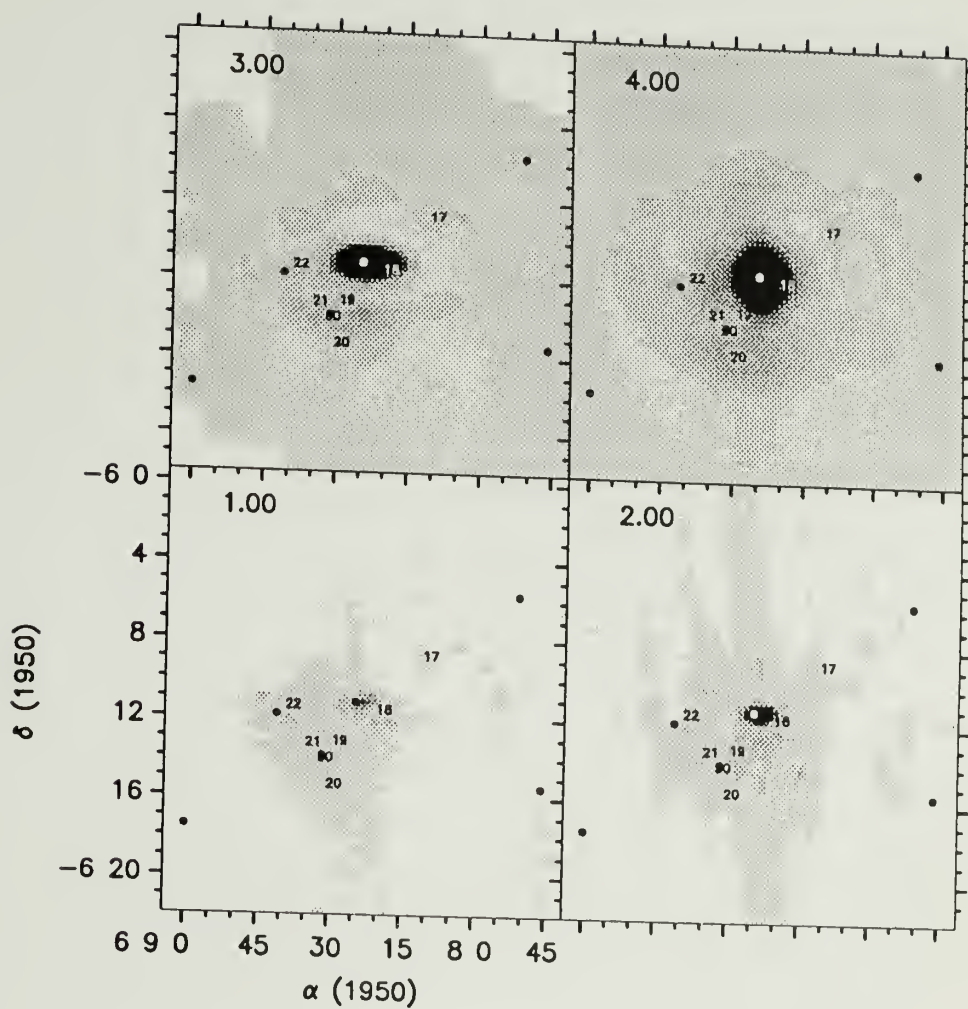
Figure 4.21. HIRES images for the GGD 12-15 region. Reflection nebulae are labeled by numbers, and IRAS point sources are labeled by solid circles.

60 and 100 μm bands) is resolved into two sources in the 12 and 25 μm bands. The lower one is likely RN 18 (NGC 2183), while the infrared star cluster found by K band imaging (Reipurth & Wamsteker 1983; Harvey et al 1985) is centered on the upper one within a $1' \times 1'$ region. Figure 4.22 presents an overlay of the integrated intensity of $CS\ J = 2-1$ emission with the $HIRES$ 100 μm image. The high density gas seems to be confined to the center of the large ring-like feature revealed by the $HIRES$ images, where young stellar objects are emerging.

4.5 $^{12}CO\ J = 1 - 0$ Self-Reversal

Finally, we point out that the red-shifted self-reversal dips of $^{12}CO\ J = 1 - 0$ relative to the $^{13}CO\ J = 1 - 0$ peaks in the main core region, which were taken to be evidence for gravitational collapse (Loren 1976; 1977; Snell & Loren 1977; Leung & Brown 1977), occur on a relatively large scale with an elongation along the outflow axis. Figure 4.23 displays some $^{12}CO\ J = 1 - 0$ and $^{13}CO\ J = 1 - 0$ line profiles in this core region. The linear size of the region which has self-reversal $^{12}CO\ J = 1 - 0$ profiles is as large as 1.5 pc. Although the self-reversal dips of $^{12}CO\ J = 1-0$ are indeed generally red-shifted relative to the $^{13}CO\ J = 1-0$ peaks by up to 1 $km\ s^{-1}$ and the stronger one of the $^{12}CO\ J = 1-0$ double peaks is on the blue-shifted side as expected by the gravitational collapse model (cf. Anglada et al 1991), it seems rather difficult to imagine that gravitational collapse is taking place in such a large scale around a cluster of infrared objects, some of which are perhaps clearing out the ambient gas around them, as evidenced by the ultracompact HII region and shell-like feature in the NIR images on a much smaller scale.

$^{12}CO\ J = 1-0$ line profiles in the GGD12-15 region also have self-reversal dips, which occur in an elongated region of ~ 1.5 pc, roughly along the bipolar outflow axis and centered on the infrared star cluster (also a compact HII region). Figure 4.24 displays a panel of $^{12}CO\ J = 1 - 0$ and $^{13}CO\ J = 1 - 0$ line profiles in the core.
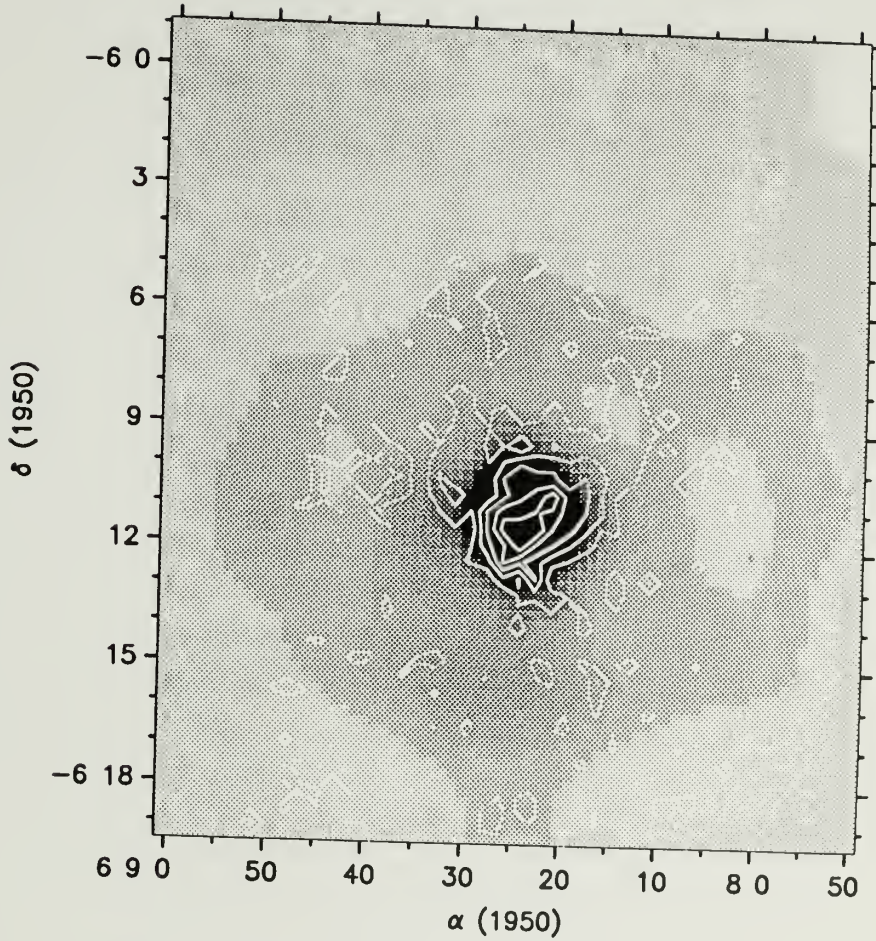
Figure 4.22. Integrated intensity map of the CS $J = 2 - 1$ emission (contours) overlayed on the HIRES 100 μm image for GGD12-15 region. Contour levels are 1.5, 3.0, 4.5, 6.0, 7.5 K km s^{-1}.
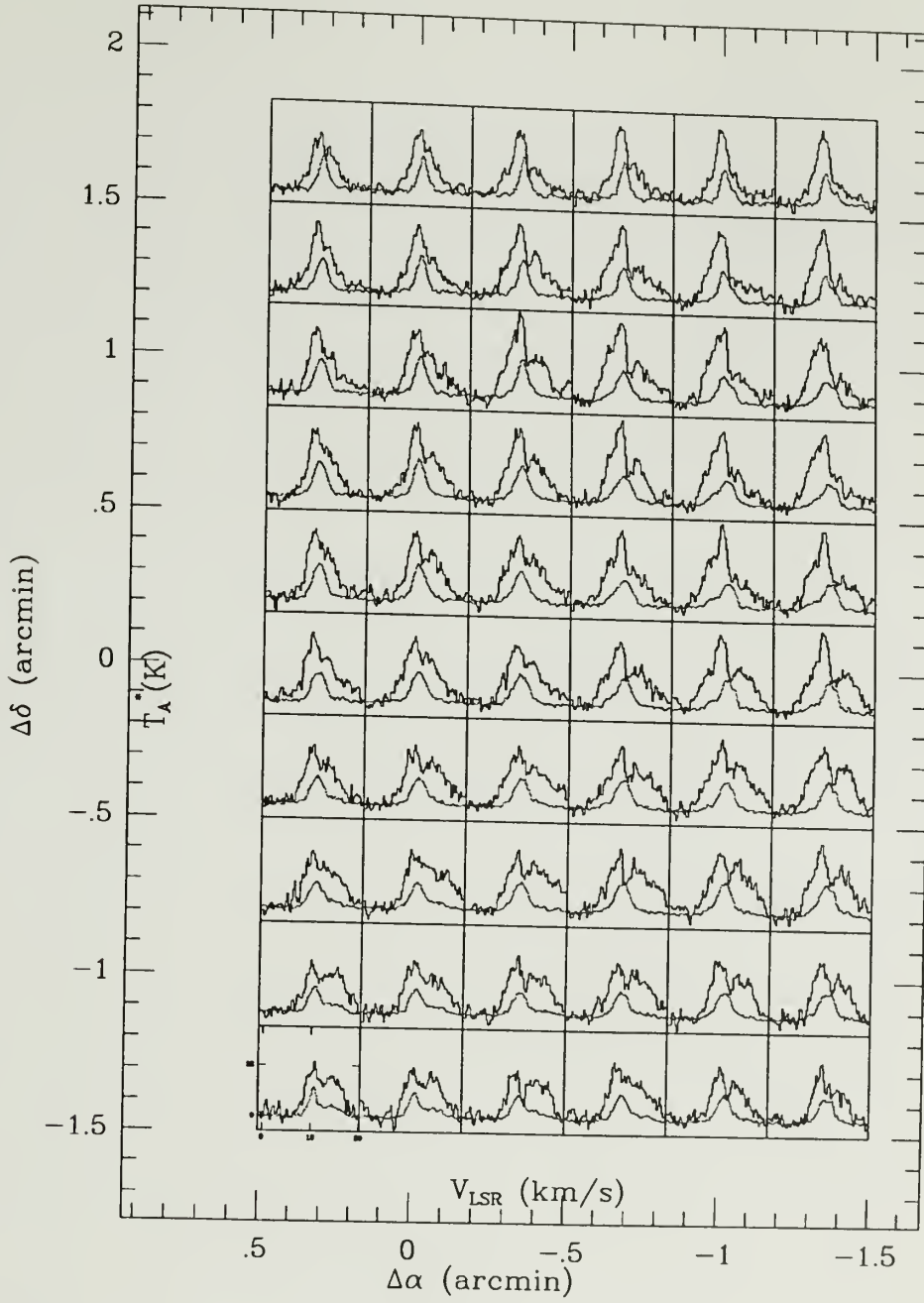
Figure 4.23. $^{12}CO\ J = 1 - 0$ and $^{13}CO\ J = 1 - 0$ line profiles in the main core region of Mon R2.
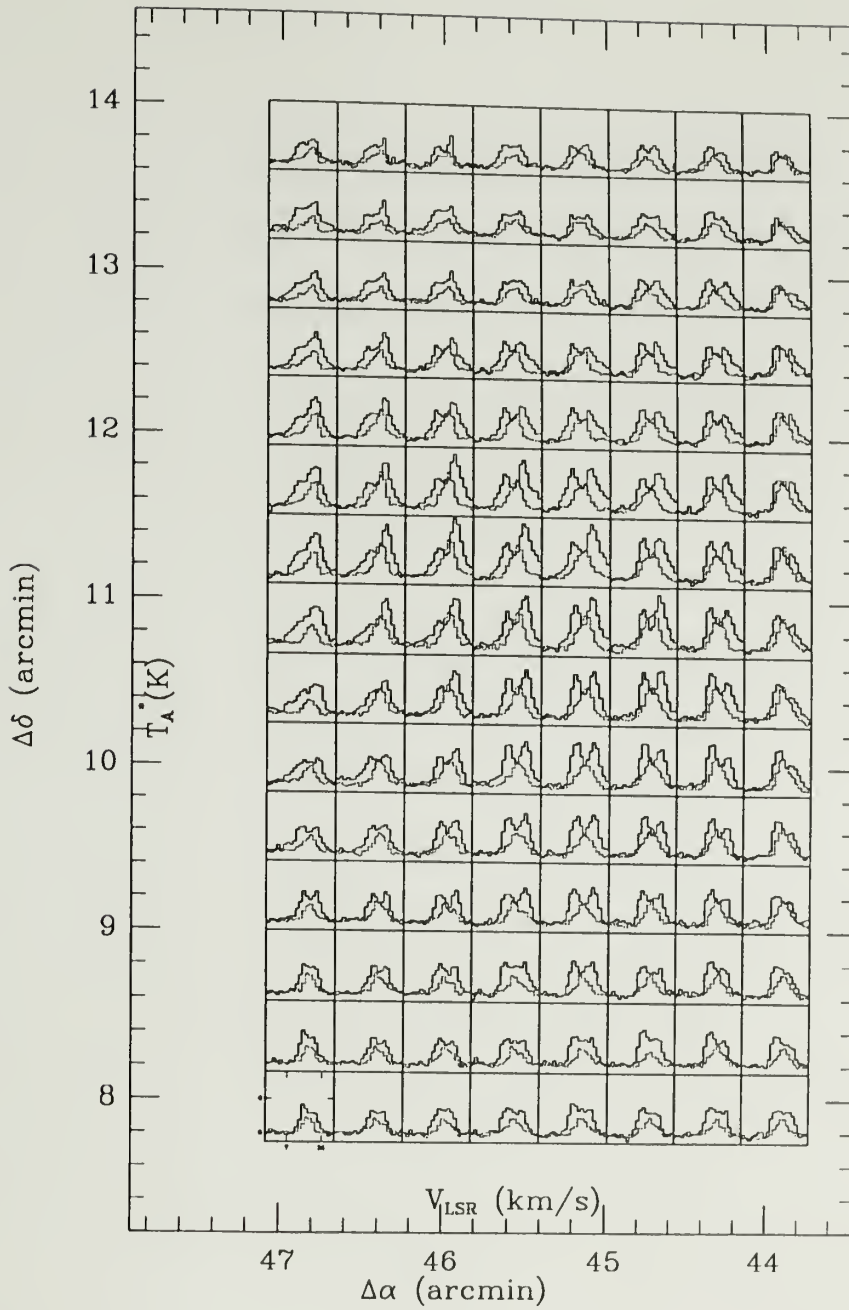
Figure 4.24. $^{12}CO\ J = 1-0$ and $^{13}CO\ J = 1-0$ line profiles in the GGD 12-15 core region of Mon R2.

The self-reversal dips show a somewhat more complex behavior. At some positions, the self-reversal dips are blue-shifted relative to the $^{13}CO\ J = 1 - 0$ peak with the stronger one of the $^{12}CO\ J = 1 - 0$ double peaks on the red-shifted side, while at some other positions they manifest just the opposite behavior. The self-reversal dips of $^{12}CO\ J = 1-0$ are sometimes coincident with the $^{13}CO\ J = 1-0$ peaks. A similar phenomenon is also observed in Rosette molecular cloud (Blitz & Thaddeus 1980; Patel, Xie & Goldsmith 1992). Thus, these cases seem very different from the case of B335, where the $^{12}CO\ J = 1 - 0$ self-reversal occurs in a very small area and can perhaps be interpreted as a manifestation of inside-out collapse (Zhou *et al* 1992).

One simpler alternative explanation consistent with the structure of the cores in Mon R2 is that the far side of a slab of gas is compressed, heated and pushed by shocks to move with a relatively small velocity relative to the cooler pre-shocked gas on the near side, and the stronger emission from the hot shocked gas is absorbed by the cool gas in the foreground. Within this picture, the displacement of the $^{12}CO\ J = 1 - 0$ slef-reversal dips relative to the $^{13}CO\ J = 1 - 0$ peak can be blue-shifted or red-shifted, depending on the relative velocity between the foreground cool gas and the background hot gas. This simple scenario may occur in situations such as expanding bubble shells of HII regions, for example. But self-reversal occurs only under special, restricted conditions. Two of them that we can readily name are the following. First, there must be considerable gas at a comparable velocity so that the optical depth of $^{12}CO\ J = 1 - 0$ at that velocity is large enough. This means that the velocity difference between the cool and hot gas should be small enough that the cool and warm gas overlaps in both spatial and velocity dimensions. Second, in order for self-reversal to be significant there must also exist significant pre-shocked cool gas. These restrictions would seem to rule out ubiquitous $^{12}CO\ J = 1-0$ self-reversal because, for example, most of the shocks that we claim

to be witnessing have probably developed into such an advanced stage that there is not much cool pre-shocked gas overlapping with the background warm gas both spatially and kinematically on the near side.

CHAPTER 5

THE WELL-SHAPED SHELL OF THE CENTRAL
BIPOLAR OUTFLOW

5.1 Introduction

Since the discovery of the first molecular bipolar outflow associated with a young stellar object more than a decade ago (Snell, Loren & Plambeck 1980), extensive observational and theoretical studies have been undertaken. At present, the bipolar outflow phenomenon seems to be one of the most widely observed phenomena associated with star formation (cf. Bally & Lada 1983; Lada 1985; Snell 1987; 1989; Shu, Adams & Lizano 1987; Bally & Lane 1991). However, outflow research is still at a stage where phenomenological models remain useful tools for improving our understanding about this physical process. In particular, geometrical considerations play a critical role for evaluating models in terms of morphology as well as energetics. Several examples are the filled biconical lobe model by Cabrit & Bertout (1986; 1990); the shell model by Moriarty-Schieven (1988) and Moriarty-Schieven & Snell (1988; 1989); the thin paraboloidal shell model by Meyers-Rice & Lada (1991) and the simple yet powerful shell model by Shu *et al* (1991, hereafter referred to as SRLL; see also Masson & Chernin 1992, hereafter referred to as MC). The model presented by SRLL not only has the potential to explain the important characteristics of observed outflows, but also naturally links the bipolar outflow phenomena with star-forming activity. One basic element in the SRLL model is an elongated, thin, closed expanding shell of swept-up ambient gas, driven through momentum conservation by a radially directed stellar wind. However, previous observational studies concentrated on characteristic outflow velocity, overall mass

and energetics as well as the association with young stellar objects. Relatively few observational studies have been published with data providing convincing evidence for the existence of shell structure, while some studies argue for filled, biconical or cylindrical lobes instead of shells (Cabrit & Bertout 1986, 1990; Richer, Hills & Padman 1992). Detection of shells and direct comparison of the spatial shape of an observed shell with that predicted by theoretical models would be helpful for resolving some important issues.

The Mon R2 bipolar outflow (Loren 1981) is by far one of the largest in size and in mass, among the two hundred or so outflows identified (Bally and Lane 1991). Torrelles *et al* (1983) argue that the bipolar outflow in Mon R2 is collimated by a toroid which directs the initially isotropic stellar winds along polar directions. Wolf, Lada & Bally (1990) and Meyers-Rice & Lada (1991) have presented detailed observational studies of the Mon R2 outflow. Although they discuss evidence for the existence of thin shell, they do not find limb-brightened shells in their spatial maps. The outflowing gas appears to have several components, which Meyers-Rice & Lada (1991) explain in terms of the existence of two distinct pairs of bipolar outflow with flow axes almost perpendicular to each other.

In this chapter we report an observational project on the the structure of the Mon R2 bipolar outflow, which focuses on the finding of a well-shaped bipolar outflow shell, and compares its spatial shape and its structure with the SRLL model.

Figure 5.1 and Figure 5.2 present an overlay of the high velocity gas with POSS red print and with the shell seen in velocity channel at $V_{LSR} = 10.88 \ km \ s^{-1}$, respectively. The (0,0) position in these figures is the $\alpha(1950) = 06^h05^m22^s$, $\delta(1950) = -06°22'25"$ position, where a UC HII region and a small cluster of infrared stars are located. Figure 5.3 shows the spatial velocity cut along the outflow axis. Following Meyers-Rice & Lada (1991), we identify four lobe features: the extended blue lobe (EBL), the compact blue lobe (CBL), the compact red lobe (CRL) and the extended
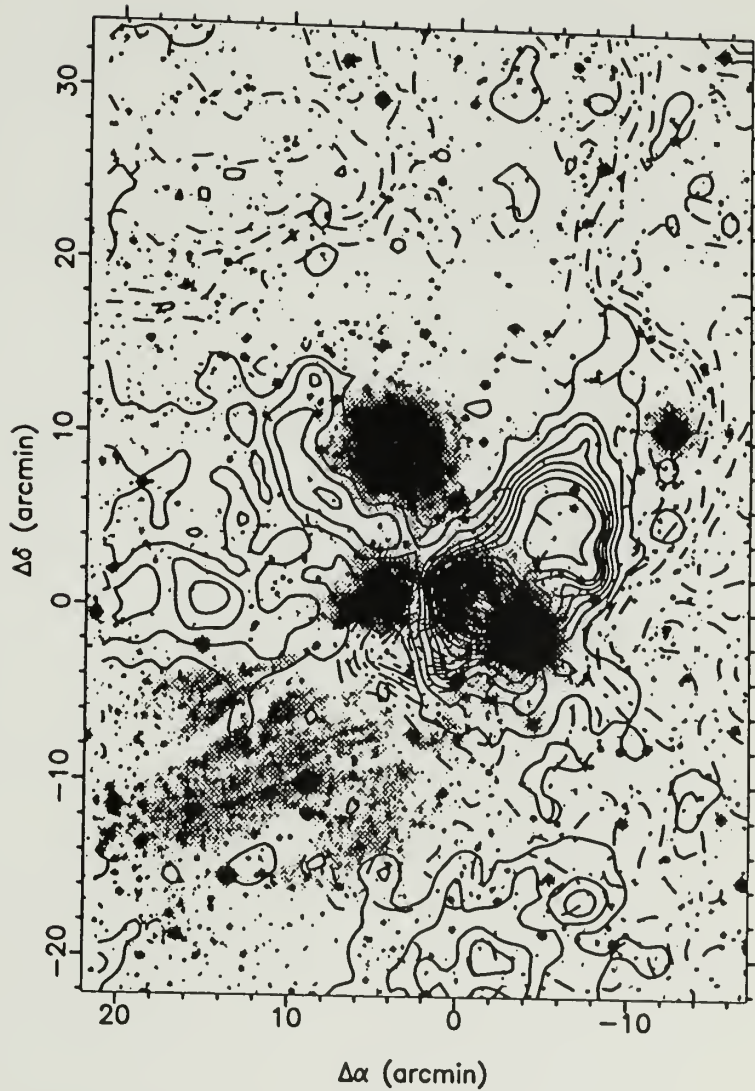
Figure 5.1. An overlay of the high velocity gas emission (contours) on the POSS red print (halftone). Solid contours are for the blue-shifted emission ($V_{LSR} = 2 - 8$ km s^{-1}); contour levels are 1, 2, ..., 35 K km s^{-1}. The dashed contours are for the red-shifted emission ($V_{LSR} = 12 - 18$ km s^{-1}; contour levels are 2, 4, ..., 20 K km s^{-1}.
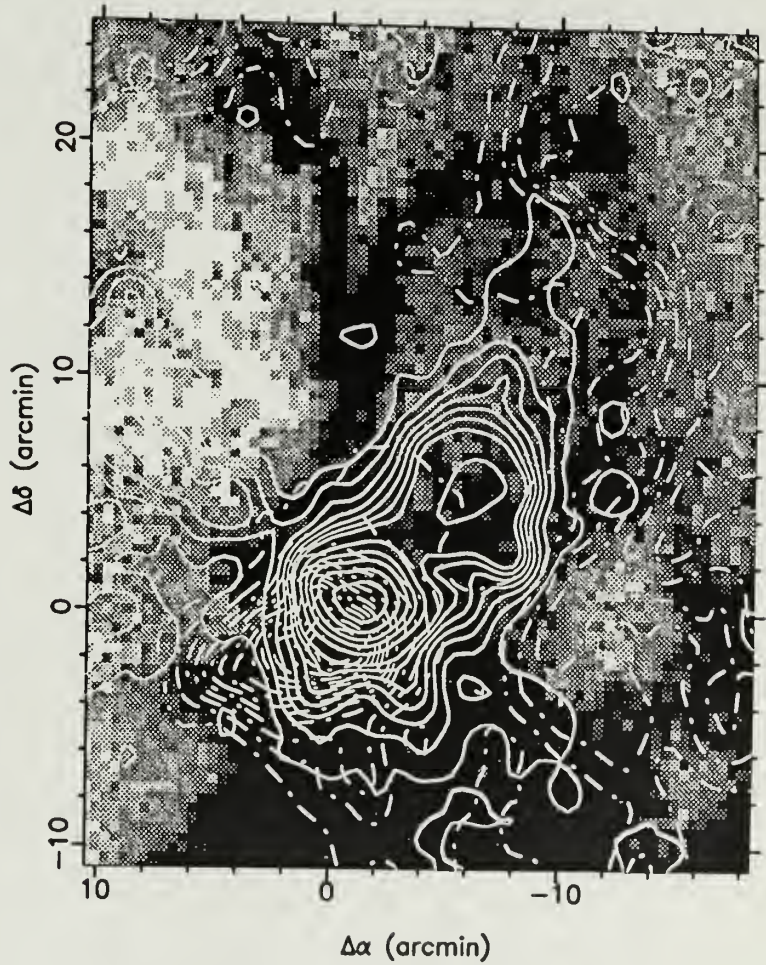
Figure 5.2. High velocity gas emission (contours) compared to the outflow shell at $V_{LSR} = 10.88$ km s^{-1} (halftone). The gray scale ranges from 1 K (white) to 15 K (black). Contours are the same as in Figure 5.1.

red lobe (ERL). While the EBL component is elongated towards the North-West, the ERL component appears short with a "bent" head. One striking feature in Figures 4.2 and 4.3 is the appearance of an eggplant-shaped thin shell feature (conspicuous in several channel maps with velocity close to 10.88 $km\ s^{-1}$, the centroid velocity of the core) extending from the $(0,0)$ position to the North-West for about 22 arcmin.

Figure 5.2 clearly shows that the blue-shifted lobe of the well-known bipolar outflow is located well within the boundary of the shell, suggesting that we are witnessing the limb-brightened thin shell swept up by collimated stellar winds from a central driving source of the bipolar outflow as predicted by outflow models (cf. Snell 1987; SRLL).

5.2 The Outflow Shell

5.2.1 The Model

The SRLL model expresses the shape of the whole, closed outflow shell with an analytical formula, while other models (cf. Moriarty-Schieven & Snell 1989; Meyers-Rice & Lada 1991) have considered only shells with open ends. Figure 5.4 is a schematic of the model (cross-section in the plane containing the outflow axis and the line of sight, i.e., $\phi = \pi/2$). The basic formulae can be summarized as follows (SRLL; MC). In a spherical polar coordinate system (r, θ, ϕ), both the stellar winds from the star and the ambient surrounding medium are assumed to have axial symmetry and reflection symmetry about the equatorial plane ($\theta = \pi/2$). The ram pressure force per steradian, $f(\mu)[g\ cm\ s^{-2}\ sr^{-1}]$, of the wind is assumed to be a function only of $\mu(=cos\theta)$

$$f(\mu) \propto P(\mu), \tag{5.1}$$

and the density of the ambient material $\rho(r,\mu)[g\ cm^{-3}\ sr^{-1}]$ can be expressed

$$\rho(r,\mu) \propto \frac{Q(\mu)}{r^2}, \tag{5.2}$$
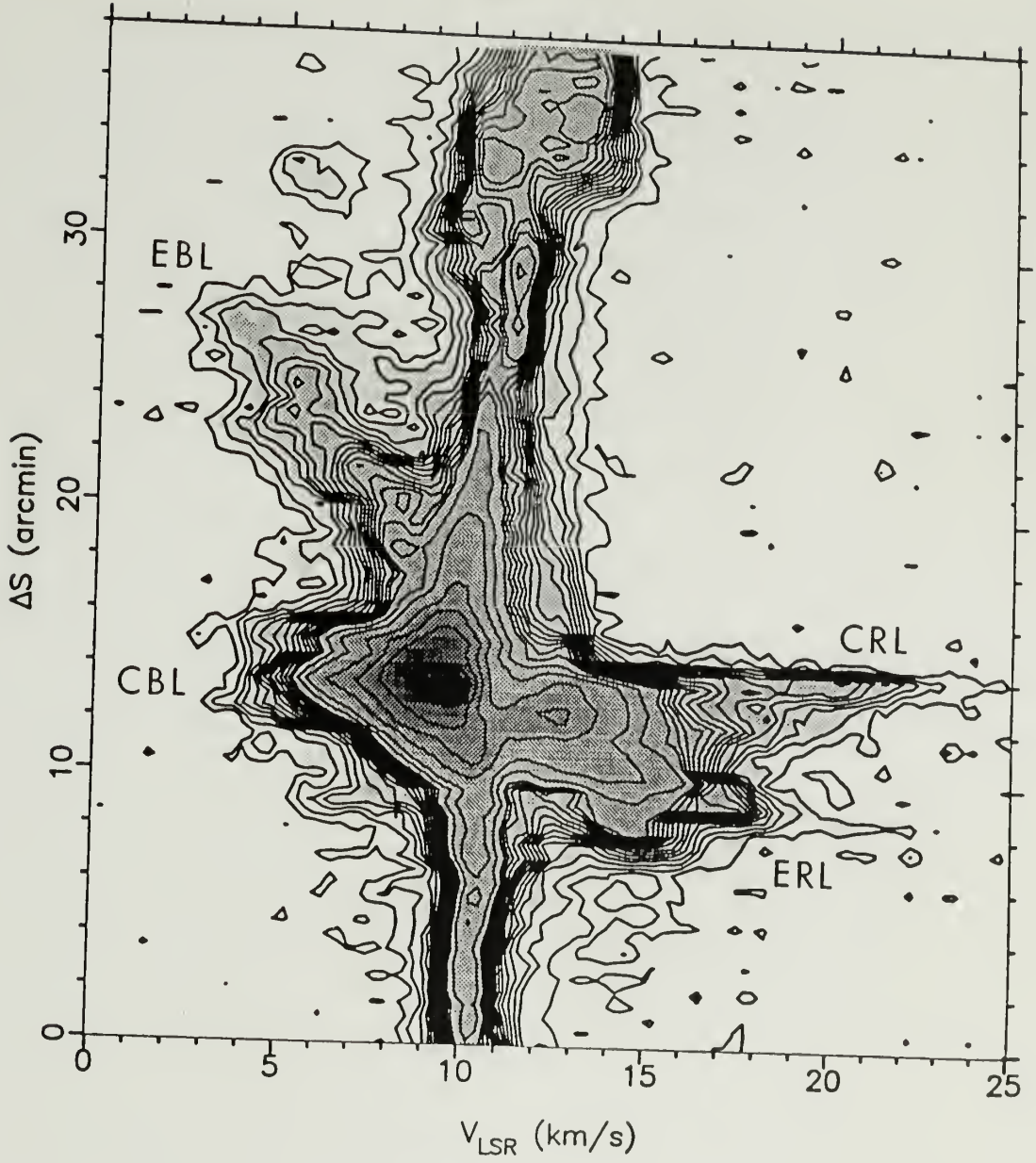
Figure 5.3. The spatial-velocity diagram along the outflow axis, from (7.5, -10) to (-15, 20). Contour levels are 0.3, 0.6, ...,5, 7, ..., 15 K. We follow Meyers-Rice & Lada (1991) in labeling the main features.
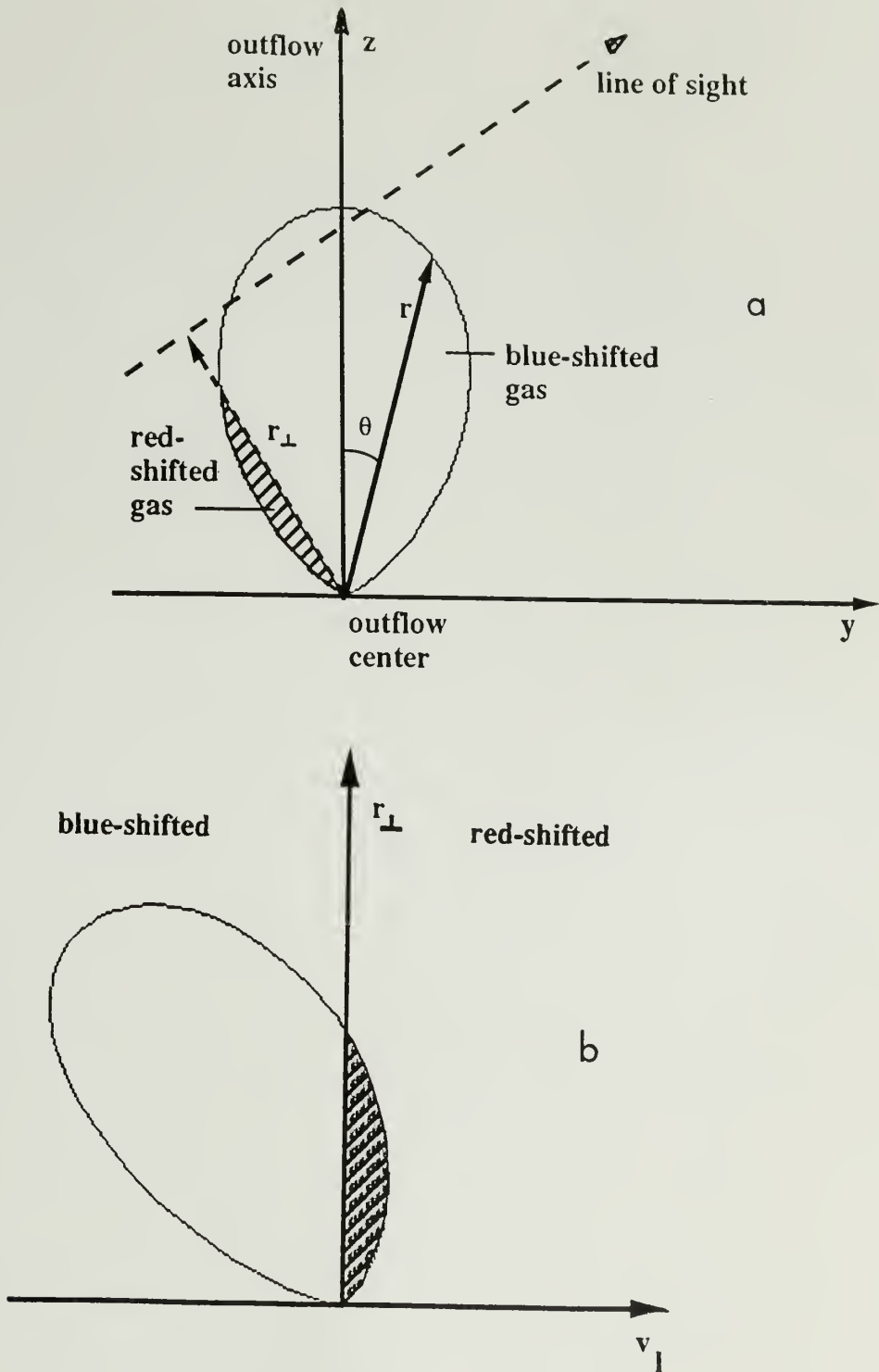
Figure 5.4. (a) Schematic diagram for the outflow shell geometry; (b) Simplified schematic SV diagram along the outflow axis at an inclination angle i, calculated from the model assuming infinitely thin shell without line broadening.

where $P(\mu)$ and $Q(\mu)$ are dimensionless functions not specified by SRLL. One approach is to let $P(\mu)$ and $Q(\mu)$ have a power-law form (MC), $P(\mu) \propto \mu^\alpha$ and $Q(\mu) \propto \mu^{-\beta}$. With these simplifications, and assuming further that the stellar winds move out by sweeping the ambient medium into a thin shell with momentum conservation ("snowplow"), and that the net mass flow along the θ direction in the thin shell is negligible, the shell velocity $v_s(\mu)$ along each radial direction ($\theta = constant$) will be,

$$v_s(\mu) = v_0 \mu^\delta, \tag{5.3}$$

where $\delta = (\alpha + \beta)/2$. Since $v_s(\mu)$ is independent of time, the shell will develop self-similarly, $r_s(\mu) = v_s(\mu)t$. The line of sight velocity of the swept-up gas is

$$v_l = v_s(\mu)(\sin\theta \sin i \sin\phi + \cos\theta \cos i). \tag{5.4}$$

Figure 5.4b shows an SV diagram along the projected outflow axis ($\phi = \pi/2$) with an inclination i, assuming a perfect thin shell without line-broadening.

5.2.2 The Outflow Shell

Can the model account for the observed "eggplant" shaped shell and major characteristics of the high velocity gas ? First, the shell in reality is of finite thickness with velocity broadening as a result of turbulence (SRLL, MC), and the emission from the swept-up gas in the shell is expected to show limb-brightening in velocity channel maps, as can be easily demonstrated by deriving the locus of constant-velocity emission from the swept-up gas. This explains qualitatively why the limb-brightening (outflow shell) only shows up in a few velocity channel maps in Figure 4.2. As for the shape of the shell, it can be shown that the maximum extents of the outflow shell along and perpendicular to the outflow axis projected on the plane of the sky are, respectively,

$$W_s = 2v_0 t \frac{\delta^{\delta/2}}{(\delta + 1)^{(\delta+1)/2}}, \tag{5.5}$$

and

$$L_s = v_0 t (\cos \theta_t)^\delta \sin(i - \theta_t), \tag{5.6}$$

where $\theta_t = \arctan(\frac{(\delta+1)\tan i - ((\delta+1)^2 \tan^2 i + 4\delta)^{1/2}}{2\delta})$. Second, in the plane determined by the line of sight and outflow axis, the blue-shifted line of sight velocity of the swept-up gas in the shell is maximized at the following positional offset from the outflow center along the outflow axis,

$$\Delta s = v_0 t (\cos \theta_v)^\delta \sin(i - \theta_v), \tag{5.7}$$

and achieves a maximum value,

$$v_{max} = v_0 (\cos \theta_v)^\delta \cos(i - \theta_v), \tag{5.8}$$

where $\theta_v = \arctan(\frac{-(\delta+1)+((\delta+1)^2+4\delta \tan^2 i)^{1/2}}{2\delta \tan i})$.

Notice that the quantities W_s, L_s, Δs and v_{max} on the left hand sides in equations 5.5 through 5.8 are all quantities that can be determined observationally. Specifically, the maximum width W_s and maximum length L_s of the Mon R2 outflow shell are found to be 11′ ($\sim 6.2\ pc$) and 22′ ($\sim 3\ pc$) respectively. Δs and v_{max} can be determined to be about 16′ ($\sim 4.3\ pc$) and 8 km/s, respectively, from the S-V diagram along the outflow axis. In obtaining the value for v_{max}, we have taken the centroid velocity of the quiescent gas to be $V_{LSR} = 11.0\ km/s$. This is a bit larger than the V_{LSR} velocity of $10.0 - 10.5\ km/s$ revealed by optically-thin tracers (Wolf, Lada & Bally 1990), but given the velocity gradient on the scale of the outflow (Figure 5.3), 11 km/s seems to be a better reference velocity to use for the EBL component under discussion. Using Equations 5.5 –5.8, the four unknowns v_0, t, δ and i can be obtained numerically, giving $v_0 = 17.0\ km/s$, $\delta = 6.0$, $i = 70°$ and $t = 3.2 \times 10^5$ years. Figure 5.5 presents an overlay of the modeled constant velocity locus with the velocity channel map at 10.8 km/s. We see that the model explains quite well the shape of the observed outflow shell.
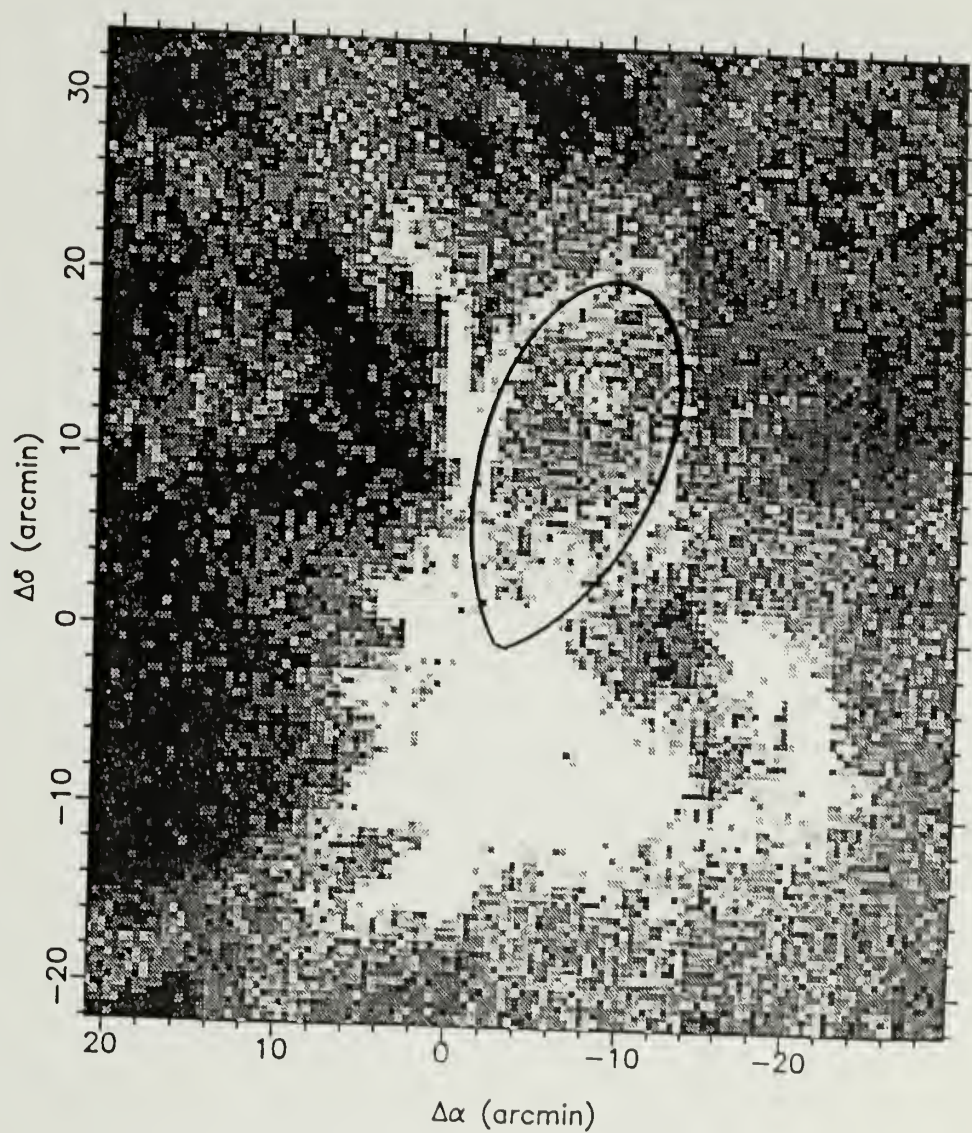
Figure 5.5. An overlay of the modeled constant velocity locus with the velocity channel map at 10.8 km/s. Unlike other grey-scale plots, dark grey scale corresponds to small antenna temperature, while white corresponds to large antenna temperature. The grey scale ranges from 14 K to 1 K.

5.3 Overall Structure of the Mon R2 Outflow

We have so far confined ourselves to the study of the extended blue-shifted emission and the limb-brightened shell caused by the stellar winds directed towards the north-west. An immediate question is: what about the oppositely directed stellar wind from the central source ? Indeed, as mentioned in Section 2, several features are clearly identifiable in the spatial-velocity diagram (Figure 5.3), and we have only explained the EBL component so far. Meyers-Rice & Lada (1991), devising a paraboloidal shell model with an open end for Mon R2, have concluded that the ERL component is the counterpart of the EBL, and attributed CRL and CBL components to the existence of a second bipolar outflow with axis perpendicular to the EBL-ERL bipolar outflow, though they were puzzled by the obvious bending of the ERL component (see Figure 5.2 and Figure 5.3). What is remarkable is that they estimated the inclination angle of the EBL-ERL outflow to be roughly 66°, which is consistent with our results, despite the use of a very different shell model. We interpret this as a manifestation of the fact that inferred outflow properties are highly sensitive to the inclination angle i.

Several facts together seem to be difficult to understand within this double-bipolar-outflow picture. First, the ERL component appears bent spatially; second, all the components, CRL, ERL, CBL and EBL, have comparable velocity extents; third, the two bipolar outflows have the same center and have axes perpendicular to each other. Although it is not impossible for such two outflows to exist, we feel that it may seem too much a coincidence. Such a doubt is enhanced by the finding of the large-scale bubble shell (Chapter 2). In fact, the core appears to have already become a "peninsula" in the cavity presumably because of the slower velocity it achieves relative to the less dense ambient gas, as can be seen in the velocity channel maps presented in Figure 4.2. The reality of this peculiar bubble structure of the region is strengthened by the puzzling "bent" morphology of the

magnetic field in the core (Zaritsky *et al* 1987; Hodapp 1987; Novak *et al* 1989; Jarrett *et al* 1992).

How does a stellar wind affect the gas in this peculiar, initially inhomogeneous environment ? Plausibly, geometry is again the key. Figure 5.6 depicts the picture that we have developed so far of the overall structure of the Mon R2 outflow. We think that the stellar winds directed into the ambient medium to the North-West of the cavity give rise to the EBL component outlined by the limb-brightened shell feature (Figure 4.2), while the oppositely directed stellar winds are flowing largely towards the bubble cavity to the east. The first stream of stellar wind towards the North-West (hereafter referred to as NW wind) sweeps up the ambient gas into an elongated shell roughly in the fashion described by SRLL model. The second stream of the stellar wind moving towards the South-East (hereafter SE wind) gradually finds increasing difficulty in traveling straight ahead along the polar direction. There could be several effects which influence the development of the SW wind. 1) The density of the gas outside of the very dense core may increase in the SW direction because of the shock compression from the large cavity. As a result, the outflow shell swept up by the initially collimated bipolar stellar winds may achieve a larger velocity perpendicular to its axis, and may be forced to develop in the lateral directions. This effect can be seen qualitatively from the "snow-plow" modeling discussed in the previous section; a small or a negative β will reduce the major-minor aspect ratio of the outflow effectively (Equation 5.3); 2) the same effects on the bipolar outflow shell may also be caused by the direct compression from the high pressure of the cavity or the expanding wall of the cavity, as is likely that the bipolar outflow shell driven by the NE wind may be breaking out of the core. Such a compressed outflow shell, if observed with a large inclination angle, would show both red- and blue-shifted lobes with the red-shifted lobe possibly larger in extent; and such a pair of blue- and red-shifted lobes, if interpreted as a second

pair of bipolar outflow, would also have an "axis" perpendicular to the "first" pair of bipolar outflow, as can be seen in Figure 5.6.

5.4   Conclusions

Most outflow models, energy driven or momentum driven, seem to agree on the existence of shell structure (cf. Snell, Loren & Plambeck 1980; Königle 1982; Draine 1983; Dyson 1984; Lada 1985; Moriarty-Schieven & Snell 1988; 1989; Meyers-Rice & Lada 1991; SRLL). The search for outflow shells and detailed studies of their properties are of great importance for understanding the nature of this fascinating phenomenon of star formation.

We have made CO observations of the massive bipolar outflow in the central region of Mon R2. We have found an "eggplant-shaped" bipolar outflow shell outlining the extended blue lobe of the bipolar outflow. The projected lengths of the major and minor axes of the shell are about 5.7 pc and 2.5 pc, respectively, and the average thickness of the shell is estimated to be ~ 0.3 pc. We interpret this shell as "limb-brightening" of the bipolar outflow shell swept up by stellar winds. We have found that the spatial shape of the shell can be satisfactorily accounted for quantitatively within the framework of the Shu *et al* model with radially directed stellar wind. We have determined that the outflow axis is inclined $\sim 70°$ with respect to the line of sight.

Our data confirm the "bent" morphology of the red-shifted lobe, the overlapping of blue- and red-shifted emission in the center of the outflow. We suggest that these are the results of the red-shifted lobe of the bipolar outflow being axially compressed. The likelihood of a highly asymmetric development of the red-shifted lobe rests on the finding that the massive core, including the bipolar outflow itself, is located on a large-scale expanding bubble shell in the giant molecular cloud.

While there seems to be the tendency to seek shell features from high velocity gas, we point out that "limb-brightening" of shells may also reveal themselves in
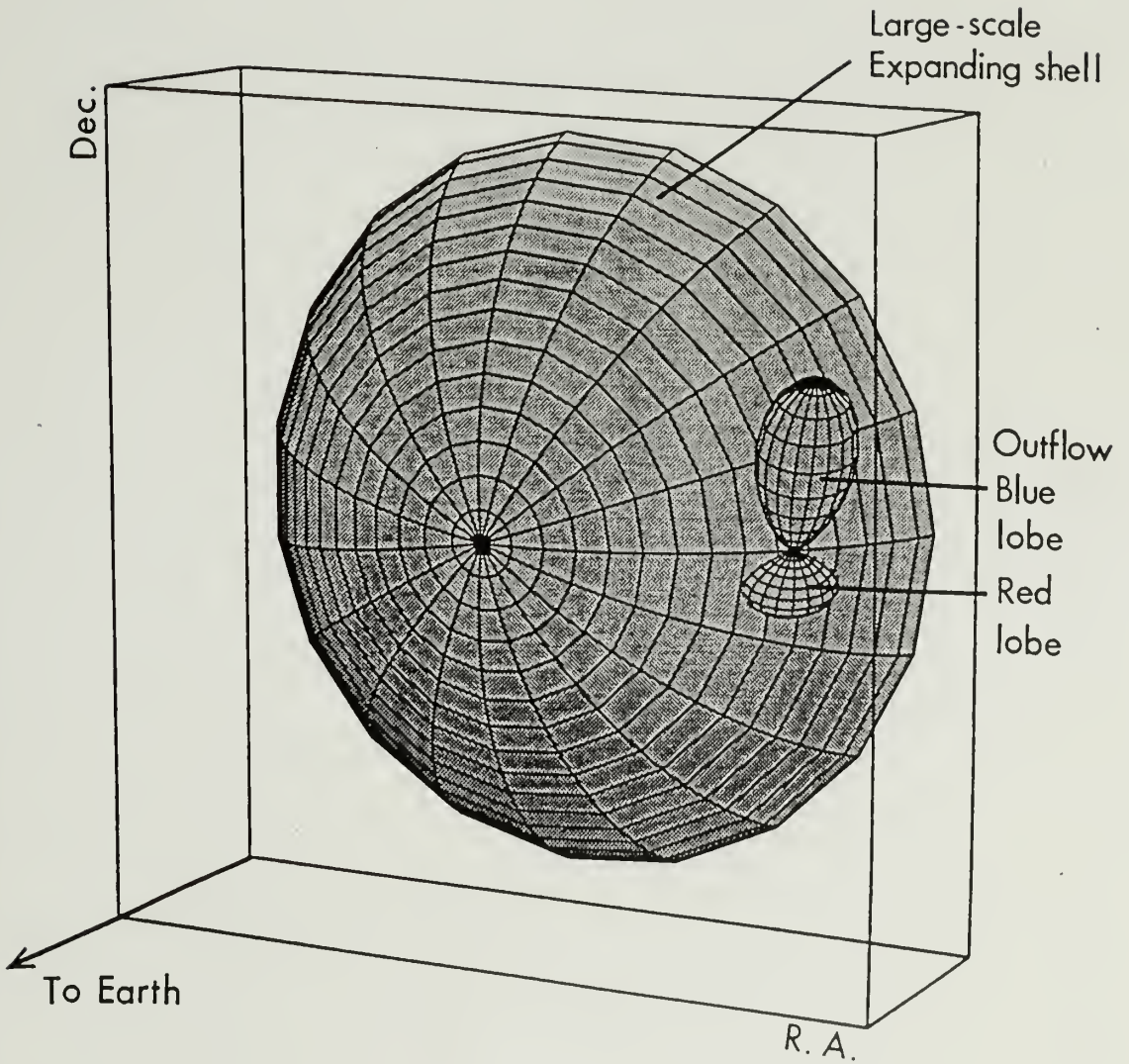
Figure 5.6. A cartoon depicting the physical picture of the overall structure of the Mon R2 outflow.

moderate and even low velocity gas, depending largely on the inclination angle of the outflow axis with respect to the line of sight.

CHAPTER 6

THE ORIGIN OF BUBBLE SHELLS AND TRIGGERED
STAR FORMATION

6.1   Review

Shell structures in the interstellar medium are observed in gas and dust tracers
such as HI (cf. Heiles 1979; 1984; Hu 1981) and *IRAS* (Schwartz 1987; Van Buren &
McCray 1988) on linear scales ranging from hundreds of parsecs or more to tenths
of parsecs. Stars are believed to be responsible for almost all of these bubble shells;
some are manifestations of star formation, some others evolution or even death
(supernovae) of stars. In general, birth, advanced evolution or death of a single star
can generate small to moderately-sized bubbles from tenths to tens of parsecs in size,
while the death or birth of a group of stars (supernova) may produce supershells (cf.
McCray & Kafatos 1987; Mac Low & McCray 1988). But there do not seem to be any
examples of a group of evolved late type stars working together to produce a large
bubble shell. While supernovae do occur, in or near molecular clouds (cf. Herbst
& Assousa 1978; Wheeler, Mazurek & Sivaramakrishnan 1980), the most frequent
events that create bubble shells in molecular clouds are surely star formation. Young
stellar objects have at least two major means to significantly affect their maternal
cloud. One is by their Lyman photons which create hot, ionized bubbles (Terzian
1968; Terzian & Balick 1974; Panagia 1973, 1991; Spitzer 1978; Tenorio-Tagle 1982;
Churchwell 1991). But only massive young stars have significant ionizing flux. The
other means is mass loss effects or stellar winds (Castor, McCray & Weaver 1975;
Falle 1975; Dyson 1977; 1989; Weaver *et al* 1977; Shull 1980, 1982; Koo & McKee
1992a,b) which are now believed to accompany the birth of almost every young
stellar object (Panagia 1991; Shu 1991).

Besides the bubble cavities that they make, one other consequence of these events is that a new generation of stars may form in the shock-compressed bubble shells with a higher efficiency and probably also with a tendency to form higher mass stars (Lada, Elmegreen & Blitz 1978). Bubble shells with triggered star formation could be the result of ionizing fluxes (cf. Elmegreen & Lada 1977; Sargent 1985; Elmegreen 1992), supernovae explosions (Herbst & Assousa 1978; McCray & Kafatos 1987; Elmegreen 1992) or stellar winds (Weaver *et al* 1977; Elmegreen 1992). This concept of triggered star formation can be traced back at least to Blaauw (1964), who first considered the linear age sequence of subgroups in OB associations as a manifestation for sequential star formation. But the reshaping of clouds in interstellar medium by high pressure events received earlier attention (Bok & Reilly 1947; Öpik 1953; Oort 1954; Dibai 1958). With the available large amount of observational data about star formation in molecular clouds in the last 15 years or so, it has become clear that star formation processes are widely associated with shock processes, which are known to cause severe compression of gas in molecular clouds. As a result, since the theoretical modeling of triggered star formation in molecular clouds associated with OB associations by Elmegreen & Lada (1977), triggered star formation has almost become the dominant mechanism used for the explanation of star formation on various scales, and one finds less and less reliance on the Jeans instability in recent papers for star formation on a large scale. The recent articles by Blaauw (1991) and Elmegreen (1992) serve as a rather complete review of the present research status in this field. Elmegreen (1992) places triggered star formation in three different categories according to the strength of the triggering; strong, moderate and weak. Strong triggering refers to the star formation purely caused by high pressure events; no star formation would have occurred but for the influence of shocks. Moderate triggering is referred to the star forming processes sped up by external high pressure events. Finally, weak triggering is

used for gathering or rearrangement of star forming cloudlets by external processes. According to the physical scale on which triggered star formation occurs, Elmegreen (1992) further divided triggering into three classes; small scale, intermediate scale and large scale. Although these efforts obviously can not avoid ambiguity and subjectiveness, they definitely provide useful conceptual grounds for the discussion of this type of problems.

In Chapter 2, we have seen that the gas distribution in Mon R2 demonstrates sharp emission ridges (Figures 2.3 to 2.18) in some velocity channels along with many other features, which can be interpreted as a very large bubble shell (diameter ~ 30 pc). But, why are they there, how are they formed, and what are their properties ? In this Chapter, we will address these questions. We first show evidence for shock compression of sharp emission ridges in section 6.2. Then we discuss the origin of these bubble shells in Section 6.3. In Section 6.4, we examine star formation related to these bubble shells and the properties of the sharp emission ridges. Finally, in Section 6.5, we summarize this chapter.

6.2 The N-S Emission Ridge

The sharp emission ridges in Figures 2.3 to 2.18 are one of the conspicuous features in Mon R2. Take N-S ridge as an example, from left to right, the emission of all tracers increases from a minimum value (essentially zero) to a maximum within a few arcminutes, and then decreases slowly to zero again. The sharpness of the intensity jumps across the edge in $^{13}CO\ J = 1 - 0$ emission can be seen in Figures 6.1, which displays emission intensity cut for $^{13}CO\ J = 1 - 0$ emission at different velocities along right ascension at $\delta(1950) = -05°32'$.

We pointed out in chapter 2 that $^{12}CO\ J = 1 - 0$ is optically thick almost everywhere in Mon R2, while the $^{13}CO\ J = 1 - 0$ peak optical depth is lower than 1 except in the dense cores and some positions along the sharp emission ridges where

A cut from (8.00 , 50.00) to (−27.00 , 53.00)
(Δα(arcmin), Δδ(arcmin))

Δα (arcmin)
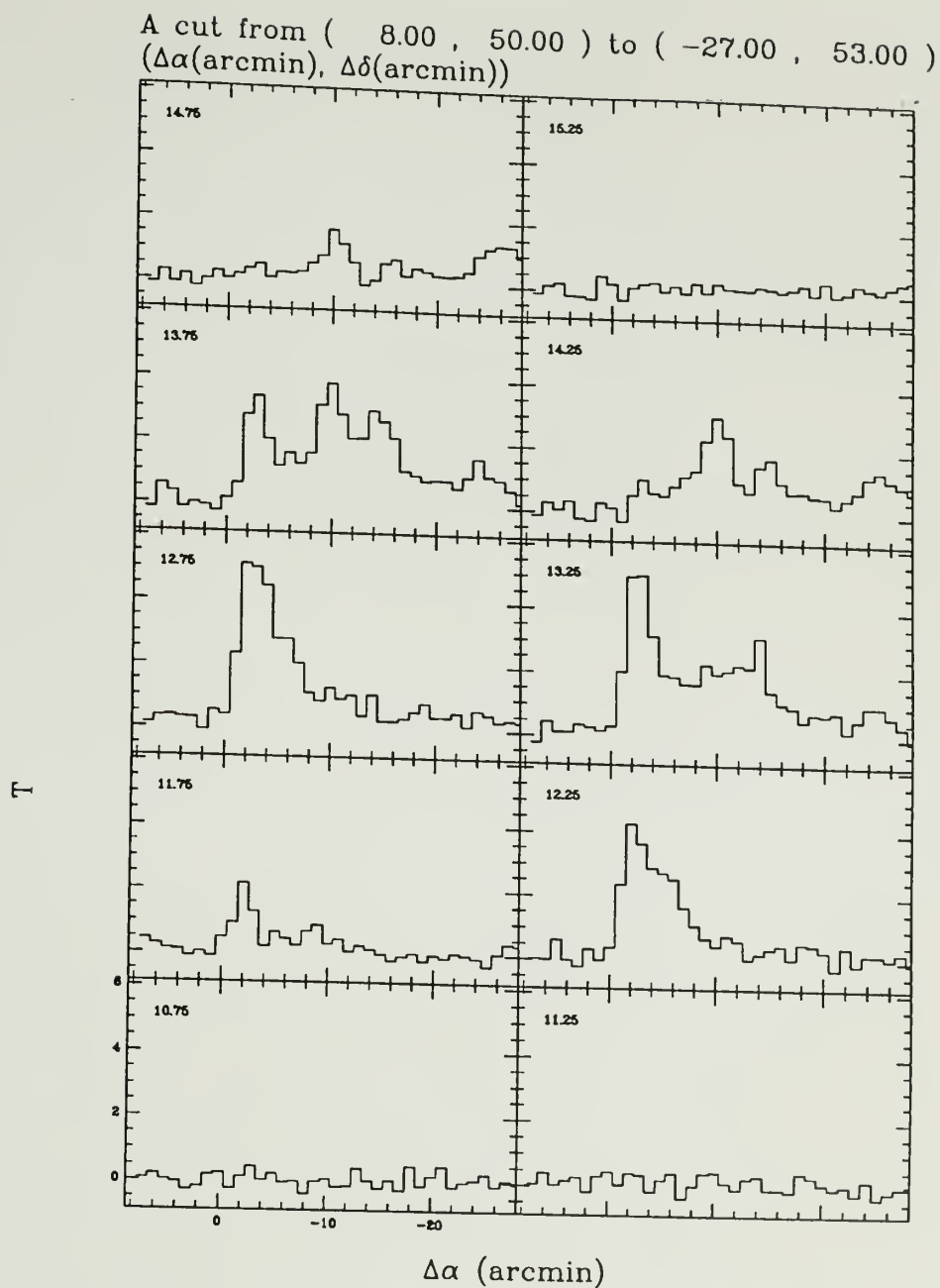
Figure 6.1. A cut along right ascension at $\delta(1950) = -05°32'$ showing the intensity variations of $^{13}CO\ J = 1-0$ emission at different velocities as a function of position.

even $^{13}CO\ J = 1 - 0$ is marginally thick. If we interpret $^{12}CO\ J = 1 - 0$ as tracing the kinetic temperature and $^{13}CO\ J = 1 - 0$ as tracing the column density, then the sharp emission ridges revealed by both $^{12}CO\ J = 1 - 0$ and $^{13}CO\ J = 1 - 0$ emission should be interpreted as an enhancement of both excitation temperature and column density. But what about the density of the ridges ? To answer this question, we have attempted to obtain some data for high density tracers including $CS\ J = 2 - 1$, $HCN\ J = 1 - 0$ and $HCO^+\ J = 1 - 0$ across the northern portion of the N-S ridge using the QUARRY system at FCRAO. Unfortunately, bad weather conditions devastatingly affected our plan, and we ended up obtaining only a map of $HCO^+\ J = 1 - 0$ for an area of $12' \times 5'$ across the N-S ridge. Fortunately enough, the detection of $HCO^+\ J = 1 - 0$ alone seems to be sufficient to show that the sharp emission ridge consists of material with H_2 densities of $\geq 10^4\ cm^{-3}$, not merely an enhancement of column density or excitation temperature. Figure 6.2 displays some $HCO^+\ J = 1 - 0$ line profiles.

Before we conclude this section, we point out again that the velocity dispersion of $^{12}CO\ J = 1 - 0$ and $^{13}CO\ J = 1 - 0$ lines is relatively small at the emission rim, while it gets considerably larger when the emission intensity decreases in the puffy emission area to the right of the rim. This point can be seen in Figures 2.25, 2.27 and 2.28, which show SV cuts of $^{12}CO\ J = 1 - 0$ across the N-S emission ridge along right ascension.

6.3   The Origin of the Large-Scale Bubble Shell

6.3.1   IRAS point sources

Besides the reflection nebulae association, the best existing survey of young stellar objects in the whole Mon R2 region is the *IRAS* PSC catalogue. To reduce the chance superposition of *IRAS* point sources which are not associated with Mon R2, we selected them based on the criteria outlined by Beichman *et al* (1986).
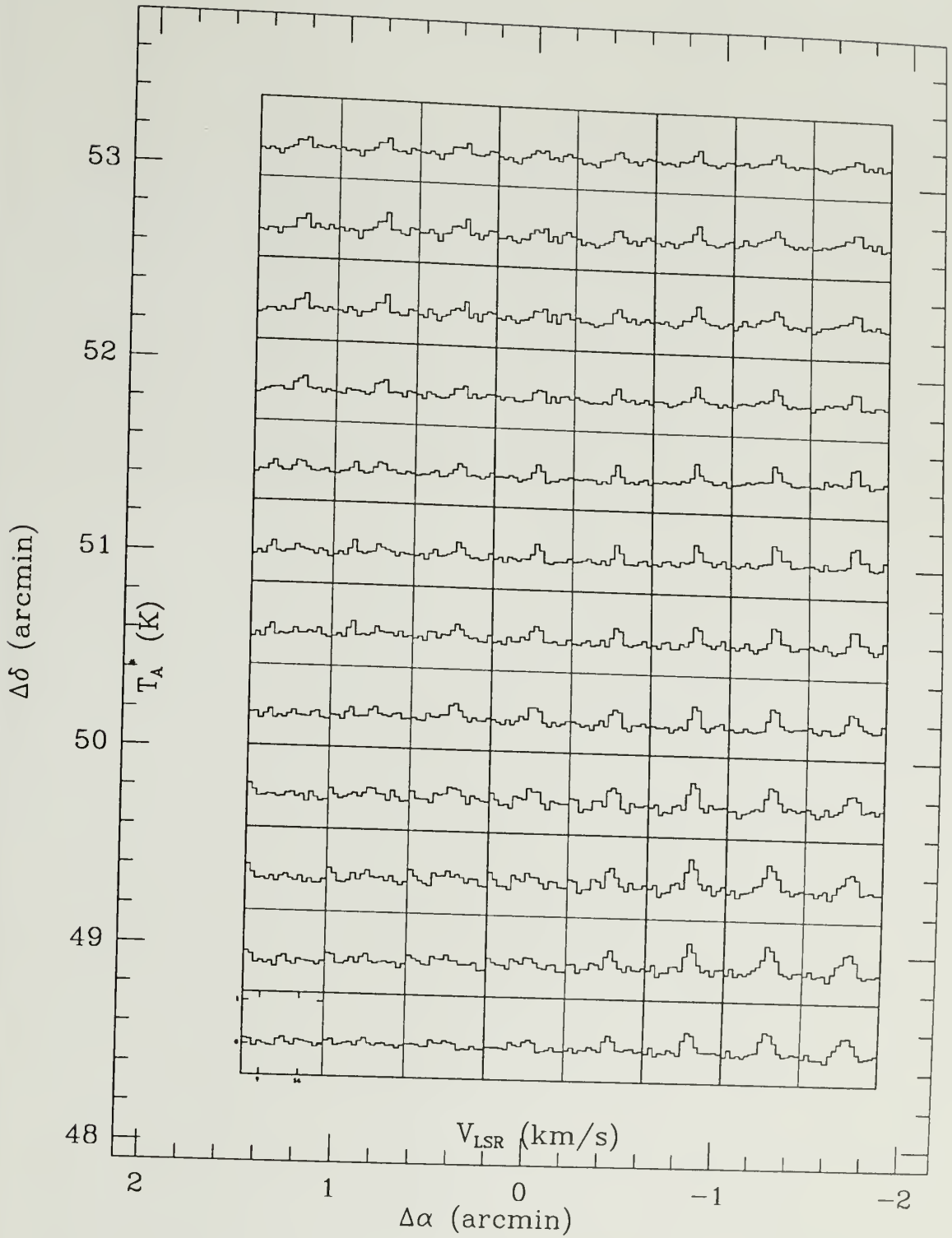
Figure 6.2. Line profiles of HCO^+ $J = 1 - 0$ across the sharp emission ridge. The coordinates are offsets in arcminutes relative to the center of the main core, which has coordinates of $\alpha(1950) = 06^h05^m22^s$, $\delta(1950) = -06°22'25"$.

Specifically, we required either firm detection at 25 or at both 60 and 100 μm. These criteria help eliminate infrared sources identified with faint visible stars (usually detected only at 12 μm) and sources only detected at 100 μm which could be infrared cirrus (Low $et\ al$ 1984), from condensations in the interstellar dust. To further reduce the possibility of including those stars which are not related with the cloud, we also required $F25 \geq F12$. These criteria that we adopted are not as stringent as those required for "dense cores" in the literature (Emerson 1987; Parker 1991). But we find that the more stringent criteria we use, the more favorable are the results to the conclusions that we are to draw. Since all the selection criteria in the current literature are purely empirical, we decided to use the most conservative selection criteria which are most likely to be correct. Table 6.1 tabulates the properties of these selected $IRAS$ point sources which fall in the Mon R2 region mapped in $^{12}CO\ J = 1 - 0$. We adopt a convenient formula (Casoli $et\ al$ 1986; Parker 1991), $L_{IR}(L_{\odot}) = 4.7 \times 10^{-6} D^2 (\frac{S_{12}}{0.79} + \frac{S_{25}}{2.0} + \frac{S_{60}}{3.9} + \frac{S_{100}}{9.9})$, to estimate the $IRAS$ luminosity of these sources. Because some sources have only upper limit estimates for some bands, we have calculated two luminosities for all the sources, lower and upper limits. The results are included in Table 6.1. While some of these sources have luminosities comparable to low mass stars, some of them are undoubtedly suggestive of embedded high mass stars.

Figures 2.3 to 2.10 in Chapter 2 presented an overlay of $^{12}CO\ J = 1-0$ emission at a velocity of 10.88 $km\ s^{-1}$ with the $IRAS$ point sources and reflection nebulae. It is clear that neither the $IRAS$ point sources nor the reflection nebulae are uniformly distributed across the whole area. Instead, we find that the regions with significant gas emission are the preferred sites of these objects. Specifically, we notice that the N-S oriented sharp emission ridge in the western portion of the cloud contains a large proportion of the $IRAS$ point sources, while the E-W oriented emission ridge in the eastern portion of the cloud harbors most of the reflection nebulae. Masers

Table 6.1. IRAS point sources in Mon R2.

IRAS sources	F12 (Jy)	F25 (Jy)	F60 (Jy)	F100 (Jy)	$L_1(L_\odot)$	$L_2(L_\odot)$
06027-0714	-0.25	0.96	4.93	6.35	2.39	2.70
06045-0554	0.76	0.99	0.98	4.96	2.21	2.21
06046-0536	-0.25	0.25	3.42	-9.49	1.00	2.28
06046-0603	-0.25	2.24	15.32	28.32	7.91	8.23
06047-0546	-0.25	1.66	4.83	3.96	2.47	2.78
06049-0541	0.36	1.84	4.47	-9.49	2.52	3.48
06049-0504	-0.29	0.36	1.16	-10.26	0.48	1.88
06050-0623	11.82	118.60	-441.60	-20190.00	74.26	2226.89
06050-0509	-0.39	1.48	4.18	10.26	2.85	3.34
06051-0653	-0.25	0.25	2.18	-5.21	0.68	1.53
06052-0533	-0.25	0.60	13.10	22.30	5.91	6.23
06052-0512	-0.25	0.68	2.50	-15.94	0.98	2.91
06053-0622	469.50	4095.00	13070.00	20190.00	8032.48	8032.48
06053-0614	0.78	1.07	-6.05	-81.76	1.52	11.33
06054-0515	0.84	1.37	-2.41	-33.97	1.75	5.80
06055-0524	-0.45	0.44	4.80	-10.40	1.45	3.07
06055-0653	0.52	2.11	3.85	4.76	3.18	3.18
06056-0621	7.07	29.28	-13070.00	-20190.00	23.59	5414.27
06056-0700	-0.26	0.69	2.24	-11.19	0.92	2.38
06058-0615	0.71	0.83	18.38	-154.50	6.03	21.63
06059-0632	0.38	4.42	9.64	6.52	5.82	5.82
06060-0657	0.92	1.57	-3.59	-9.74	1.95	3.85
06060-0617	0.28	1.23	-18.38	38.98	4.91	9.62
06068-0643	0.73	1.35	1.91	-8.47	2.09	2.94
06068-0641	0.98	2.00	-1.91	-8.47	2.24	3.59
06070-0619	2.95	15.25	177.50	314.40	88.63	88.63
06084-0611	27.13	603.50	3613.00	4876.00	1755.03	1755.03
06085-0613	2.99	3.27	-3613.00	-4876.00	5.42	1424.36
06086-0611	2.38	2.57	-3613.00	-4876.00	4.30	1423.23
06093-0608	6.60	12.34	140.50	249.40	75.74	75.74
06094-0628	-0.25	0.32	7.03	25.17	4.50	4.82
06103-0612	4.02	20.77	70.31	122.80	45.91	45.91
06111-0624	0.44	0.48	0.69	-11.24	0.97	2.11
06123-0619	0.36	0.42	-1.87	21.17	2.80	3.28
06124-0621	1.82	2.07	15.64	53.84	12.79	12.79
06125-0658	-0.25	0.19	-0.51	4.12	0.51	0.96

and GGD objects are mostly located in dense cores, maybe partially a result of biased observations.

To partially check whether these *IRAS* sources are really dust condensations heated by embedded real young stellar objects rather than dust condensations heated by external sources such as shocks, we show in Figures 6.3 to 6.6 K-band images for IRAS 06045-0554, IRAS 06046-0536, IRAS 06046-0603 and IRAS 06049-0541, which are typical sources located on the N-S sharp emission ridge. The data were kindly obtained for us by Michael Skrutskie and Michael Meyer using their infrared camera at the UNAM 2.1 m telescope in September 1991. Except IRAS 06046-0536, for which the K-band image shows a faint feature of questionable reality, all the *IRAS* point sources have at least one counterpart at K-band. Given the color selction criteria that we used, we feel that these *IRAS* point sources are possibly real stellar objects. Since the K-band images have a 3σ sensitivity of 15^m, which is not very deep, and IRAS 06046-0536 is indeed the faintest one as seen from the estimated *IRAS* luminosities in Table 6.1, it is possible that even this source is a real low mass stellar object embedded in the cloud. Of course, the possibility that these objects are background and foreground stars cannot be ruled out. To further clarify this problem, intensive NIR photometry of the *IRAS* point sources located on the sharp emission ridges is planned and will be carried out in 1993.

6.3.2 The Formation of The Mon R2 Bubble Cavity

6.3.2.1 Possible Powering Sources

Mon R2 is clearly not associated with any known OB associations. But one important aspect of the star formation in Mon R2 seems to be the existence of at least two generations of stars. The first generation is represented by some of the reflection nebulae powered by B and A type ZAMS stars (HR; Table 1.1 in this thesis), whose ages range from 6 million to 10 million years (HR). The
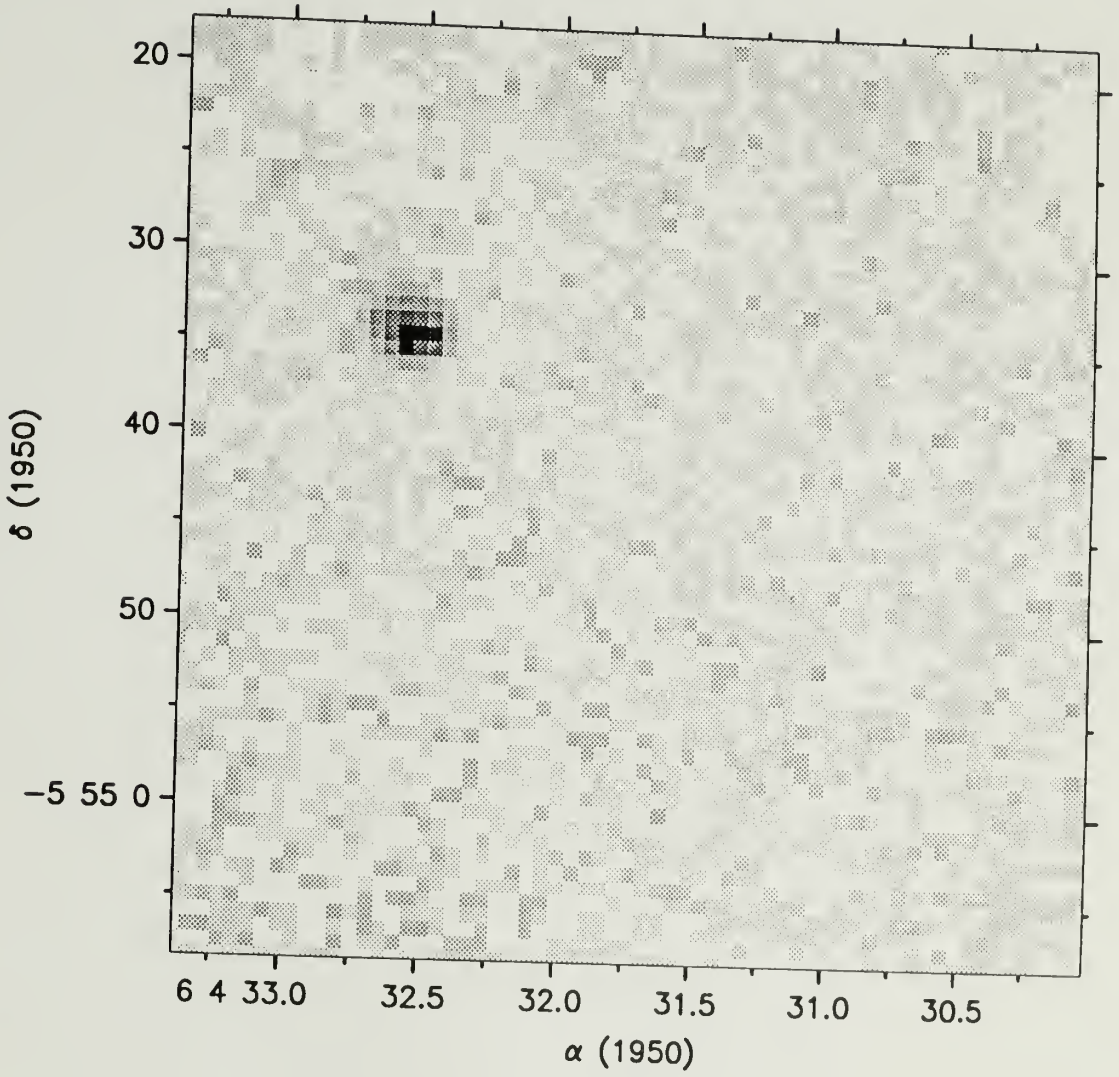
Figure 6.3. K-band image for IRAS 06045-0554.
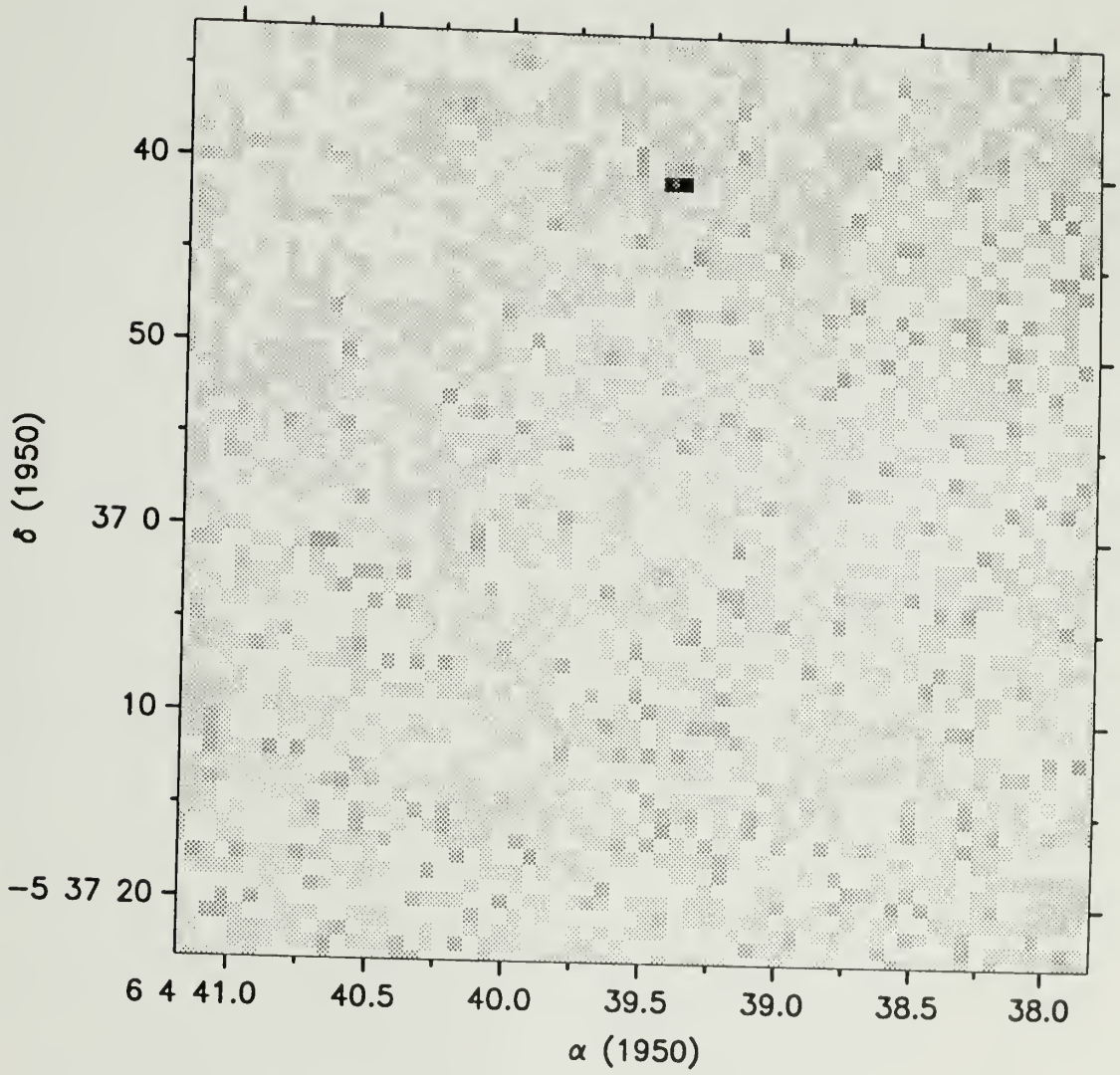
Figure 6.4. K-band images for IRAS 06046-0536.
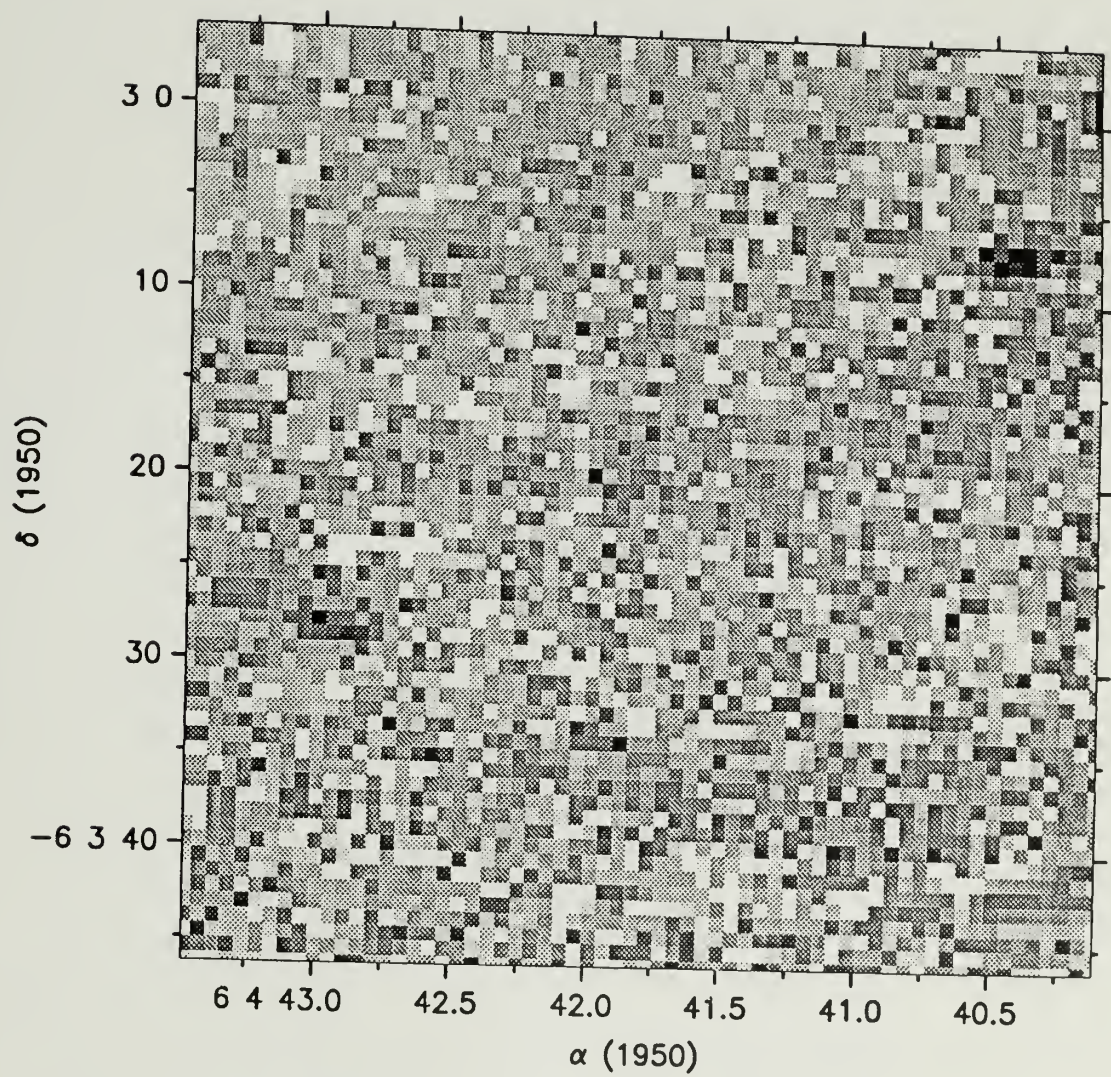
Figure 6.5. K-band images for IRAS 06046-0603.
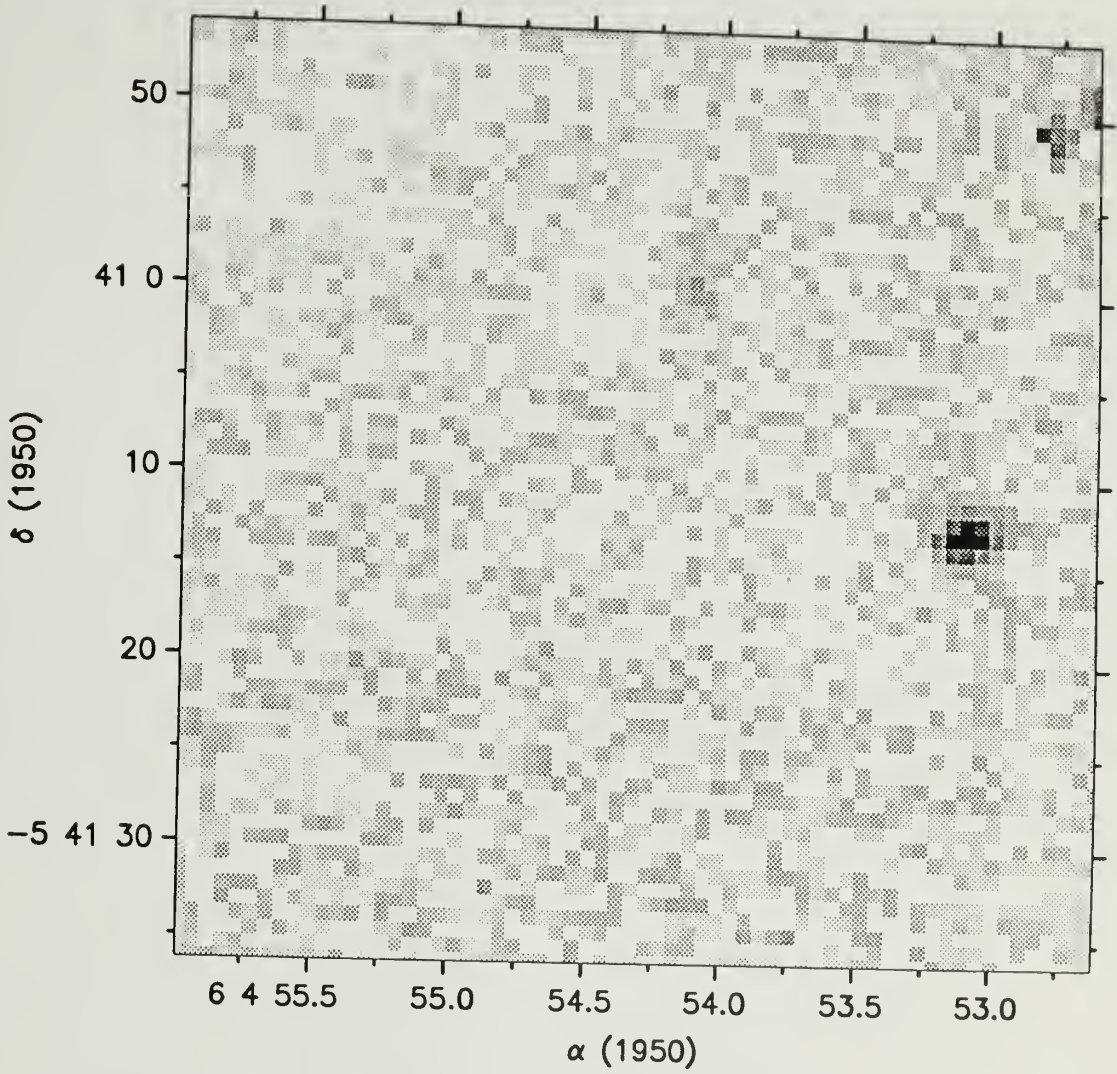
Figure 6.6. K-band images for IRAS 06049-0541.

second generation of young stellar objects are represented by the ultracompact HII regions, some reflection nebulae illuminated by H_α emission stars (Be stars) or Orion population stars (HR), *IRAS* point sources in the cores and sharp emission ridges, whose ages may be on the order of 10^4 to 10^5 yrs as suggested by the ages of the bipolar outflows (Wolf, Lada & Bally 1990; Meyers-Rice & Lada 1991; Chapter 5 in this thesis). It is worth emphasizing that not all of the reflection nebulae tabulated in Table 1.1 belong to the first generation (a classification wherever possible is given in Table 1.1), and not all IRAS point sources tabulated in Table 6.1 belong to second generation. In fact, the poor spatial resolution of the *IRAS* in many cases could not resolve single stars, and sometimes each point source could be the result of a cluster of infrared objects, as we have seen in Chapter 4 for the main core and GGD 12-15 core.

What is the origin of the bubble shells in Mon R2 ? These known young stellar objects are surely good candidates. In a sense, almost all young stellar objects could be "bubble blowers", because all of them are believed to go through the mass loss stage. But not every one could produce the large expanding bubble shell in Mon R2. First, the second generation of stars taking place in the sharp emission ridges can be excluded immediately simply because of their unfavorable locations. The location of the main core, the GGD12-15 core, and several other cores in the eastern portion of Mon R2 on the large bubble shells attests that they are the "victims" of the violent events, and thus young stellar objects inside them can also be excluded from our consideration. This judgement is supported by the fact that all these cores seem to have been re-shaped by the events responsible for the large bubble shells, as discussed in Chapters 2 and 4. Also, the extent of the eggplant-shaped outflow bubble shell from the main core, which is the most energetic one among these cores, clearly defines the main core's influence on the GMC. In fact, all these aforementioned objects do not seem to satisfy the following age requirement: given

the dynamical crossing time scale of the large bubble shells, the high pressures must have occurred at least $\sim 5 \times 10^6$ *years* ago. Second, sources which are responsible for the large molecular cavity should not have much molecular material with it. Specifically, since we realize from the analysis in Chapter 2 that the original cloud gas should have a LSR velocity of $\sim 11 - 13$ *km* s^{-1} , we should not expect much gas at this velocity to be associated with the suspected powering sources.

With these simple filtering steps, what remain among the known young stellar objects would be a few reflection nebulae, some of which are associated with *IRAS* point sources, namely, RN8-9, RN11-16 and RN36-37. Although RN8-9 (B1V and B2V types, respectively) have cleared small molecular cavities around them locally, their proximity to the cavity walls does not seem to suggest that they are solely responsible for the large cavity in Mon R2 as discussed in Chapter 4. RN 10 (vdB70) has a Strömgren sphere surrounding it visible on the POSS prints and the corresponding spectral type is B1V (HR). Its *IRAS* counterpart is 06059-0519 with an *IRAS* luminosity between 1 to 10 $L_\odot$. From Figures 2.3 to 2.10, it is clear that this star has cleared out a molecular cavity around it and its stellar winds and ionized photons are still eating the N-S ridge to its west. It is likely that this star is responsible for the open northern end of the large bubble cavity (see Chapter 2) as well as the northern part of the N-S ridge, although other possibilities, such as magnetic field, further discussed in the next section may also play a role. Its location relative to the molecular gas is fully consistent with the fact that the Strömgren sphere has a larger extent and smaller surface brightness to the east with an estimated density of ~ 10 cm^{-3} (HR). The radial velocity of the star is 13 km s^{-1} , which is in perfect accord with the velocity of the ^{12}CO $J = 1 - 0$ emission on the ridge.

RN36 is a reflection nebula associated with IRAS 06094-0628 with an estimated *IRAS* luminosity between 4.5 and 4.8 $L_\odot$ (see Table 6.1). This star also seems

to be associated with ^{12}CO $J = 1 - 0$ emission at $V_{LSR} \sim 7 - 9$ km s^{-1} , in consistency with the fact that it emits considerably in $IRAS$. Thus it is possible that this star is embedded and heating up the dust. The peculiar thing is that the patch of associated ^{12}CO $J = 1 - 0$ emission is considerably blue-shifted relative to the majority of the gas. The nature of the source is not known, but its $IRAS$ luminosity suggests that it is a massive young stellar object. It is not clear whether it is a second generation star born on the gas shell moving towards us, or it is a first generation star participated in the making of the bubble cavity.

RN 37 (DG 092) is the mysterious large sized, low surface brightness reflection/emission nebula discussed in Chapter 4. It is possible that it is an obscured HII region. Its large size and location in the cavity strongly suggest that it may be related to the formation of the cavity. Further observational efforts to reveal its nature would be very interesting and rewarding.

RN11-16 are also very interesting objects in several respects. First, they are located close to the projected center of the large bubble cavity. Second, $IRAS$ 0607-0619 is coincident with RN13 (NGC 2182, vdB 72), which has a spectral type of B3V (HR) and a visual magnitude of 7.9^m. The $IRAS$ luminosity of this source is estimated to be 88.6 $L_\odot$, not in conflict with the known spectral type of the star. What is special about this source is that it has an $IRAS$ color characteristic of an HII region (Wood & Churchwell 1989; 1991). In the radio survey of Mon R2 at 3.2 and 10.5 GHz, Hughes and Baines (1985) found a thermal radio source G213.8-12.1, corresponding to a B0.5V to B1V star. But the reported location of this radio source is at $\alpha(1950) = 06^h07m13 \pm 2^s$, $\delta(1950) = -06°14'30" \pm 30"$, which is as much as 4' to 5' away from the $IRAS$ source. Since it is difficult to attribute this difference to positional uncertainties, we feel that either they are two distinct sources or there is a relatively large extended HII region there, obscured by the large bubble shell moving towards us. Given the significant diffuse $IRAS$ emission around this position

and the lack of significant $^{12}CO \ J = 1 - 0$ and $^{13}CO \ J = 1 - 0$ emission, as we discussed in Chapter 3, we suggest that there is a moderately sized, obscured HII region on the far side of the cloud, with heated dust particles emitting in the $IRAS$ bands. Further studies to identify the nature of this region is perhaps the most important step towards a full understanding of the origin of the large bubble cavity. But except RN 13, none of RN11-12 and RN14-16 have $IRAS$ sources associated with them, probably an indication that they have dispersed most of the material in their immediate surroundings. This seems to be consistent with the known spectral types B5V and B8V for RN14 and 15, respectively. The spectral types of RN11-12 and RN16 are not known. But from the large reddening of these objects, and the fact that they have essentially the same distance (Racine 1968; HR) but are not associated with $IRAS$ point sources, it is reasonable to expect that they are stars located in the cavity behind the large bubble shell moving towards us. The only two other early type stars that we know of close to the projected center of the bubble cavity are SAO 132894 (B9V) and SAO 132895 (B5V). The latter star is coincident with RN 13. But it is useful to notice that none of these stars located close to the kinematic center of the large bubble shell have known spectral types early enough to provide sufficient energy ($\sim 5 - 10 \times 10^{48}$ $ergs$, see Chapter 2) to have blown out the large scale bubble shell.

6.3.2.2 A Qualitative Model

After the above examinations of the young stellar objects, we see three possibilities. **1**). There are O stars in the back side of the cloud, which are obscured by the foreground material. **2**). There were O stars formed in the back side of the cloud, which left main sequence, and even exploded as supernovae. For these two possibilities, the energy requirement of $\sim 5 - 10 \times 10^{48}$ $ergs$ does not seem to be a problem, because O stars are well known to deposit significant mechanical energy

to gas within the main sequence life time. An O6.5 star, for example, is estimated to transfer as much as 5×10^{50} $ergs$ into mechanical energy (Tenorio-Tagle 1982) during its main sequence life time of 3×10^6 years (Lang 1974). This energy, in fact, will be added to by the stellar winds of these and other stars (e.g., those known A and B stars powering reflection nebulae), or by additional energy from supernova explosions (Elmegreen 1992). 3). Although the cluster of stars with known spectral types which are associated with the reflection nebulae have too little ionizing flux to be responsible for the large bubble cavity and gas shells in Mon R2, it is possible that these B stars have or have had strong enough stellar winds to have blown out the large bubble cavity and filled it with hot shocked gas (cf. Castor et al 1975; Weaver et al 1977; Dyson 1984; Koo & McKee 1992a,b). Assuming that the stellar winds of these stars have lasted $\sim 10^6$ years, then the mechanical luminosity required is $\sim 10^2$ $L_\odot$. Since the known ZAMS stars located in the cavity alone add up to a bolometric luminosity of $\sim 10^4$ $L_\odot$, a mechanical to bolometric luminosity ratio of $\sim 1\%$ is implied. Given the statistical study of the bipolar outflows (Bally & Lane 1991), this percentage appears a little high, but can not be ruled out. We discuss the three possibilities in the following. We start with discussing the possible existence of O stars.

At the time this research project was started, violent large-scale gas motions in Mon R2 were not known, and the cloud had been regarded as a relatively "quiescent" one. It was believed that the star formation in Mon R2 had not significantly dissipated the gas in a global manner (HR; Hughes & Baines 1985). Indeed, besides a couple of compact HII regions in the cores which are possibly the second generation of star formation and are not causing much effect on the gas on the large scale of the cloud, most of the young stellar objects are B type stars associated with the reflection nebulae. Given the cloud mass of $\sim 5 \times 10^4$ $M_\odot$, which is comparable to Orion B, the fact that no O type stars are seen in Mon R2 is in some sense disquieting

(Karen Strom, private communication). HR were also somewhat puzzled, and wrote "This cloud has (as yet ?) not given birth to O stars capable of dissipating a major portion of the dark cloud material, although perhaps this process has started in the core".

We can ask two questions. First, given the age of the B type stars associated with the reflection nebulae of $6 - 10 \times 10^6$ years (HR), what happens if there were indeed O stars formed simultaneously with the stars powering the reflection nebulae as the first generation of star formation ? The answer is that it is possible that they would have left the main sequence and their ionizing flux would now be reduced significantly[1](Manfroid 1976; Beltrametti, Tenorio-Tagle & Yorke 1982). This is because the more massive the star is, the sooner it consumes its hydrogen fuel. An O6.5 ZAMS star ($L = 1.5 \times 10^5 \ L_\odot$, Panagia 1973), for example, has a main sequence lifetime of $\sim 3.6 \times 10^6$ years (Lang 1974). A B0 ZAMS star ($L = 2.5 \times 10^4 \ L_\odot$) has a main sequence lifetime of $\sim 1 \times 10^7$ years. After that, the star's effective surface temperature drops and the number of Lyman photons is significantly reduced. In the case of Mon R2, the age determination of $6 - 10 \times 10^6$ years by HR seems to be a rather reliable result. They based this on two main aspects. 1). The color-magnitude diagram of the star cluster powering up the reflection nebulae is well behaved with little scatter and shows no sign of "turnup", which sets a conservative lower limit of 6×10^6 years. 2). The B1 stars are still on the main sequence, which sets a conservative upper limit of 10^7 years.[2] Therefore, even if there were O stars which formed simultaneously with the cluster of B stars powering up the reflection

---

[1] I acknowledge initial discussions of the problem with Bob Dickman and Bruce Elmegreen.

[2] From the luminosities tabulated by Panagia (1973) and the age estimate formula given by Lang (1974), we estimate a main sequence lifetime of 3×10^7 years. Here we want to be conservative about the age and follow HR in adopting $\sim 10^7$ years as the upper limit for the age of the Mon R2 reflection nebulae. Given the lack of knowledge about the conversion efficiency from the star luminosity to mechanical luminosity of the gas, we have to treat the type and number of O stars in Mon R2 as a free parameter in this hypothesis. A small difference in age estimate for the star cluster does not affect our general consideration.

nebulae, it is possible that they would have already left main sequence and become untraceable (Manfroid 1976; Beltrametti, Tenorio-Tagle & Yorke 1982). The second question is: can an O star be optically hidden by the foreground material moving towards us ? Given the column density of gas and dust determined in Chapter 2, we feel that the possibility can not be ruled out.

The interesting point is that we may be fortunate enough to be witnessing obscured O stars, or the remnant or "fossil" HII regions. First, the existence of the large scale molecular cavity, systematic gas motions mimicing bubble shell motions and the sharp emission ridges in a sense provide evidence for violent processes which occurred $\sim 5 \times 10^6$ years ago. Second, the radio continuum maps of the region (Haslam, Quigley & Salter 1970; Reich 1978; Haslam et al 1982; Sofue & Nakai 1983) reveal an emission loop. Third, the mysterious RN37 (DG 092), which is also located in the cavity, seems also to give one additional reason for suspecting the existence of one or even more undetected or unrecognized O stars or their fossil HII regions obscured by foreground cloud material. Fourth, the mysterious radio source G213.8-12.1 is located close to the projected kinematic center of the bubble shell. We notice that a B0.5 type determined by Hughes & Baines (1985) for this source based on classical method could be a lower limit. The reason is that this HII region may be an evolved one, and non-spherical development of the HII region, such as a "blister" and "champagne" flow, may significantly reduce the amount of detectable radio emission. In fact, it is also important to appreciate the fact that we see mostly blue-shifted gas emission and little red-shifted emission from Mon R2. The most natural explanation of this is that the first generation of star formation occurred close to the far side of the cloud, and the molecular material is being dispersed and pushed in the fashion of "blister" or "champagne" flow model (cf. Israel 1978; Tenorio-Tagle 1982). Indeed, we find that if one or more O stars formed simultaneously with the first generation of stars, but just recently left the main

sequence [3] and reduced the amount of Lyman photons, then all the issues discussed above can be in principle explained in a natural and consistent way. Specifically, one or more hypothetical O stars could have been located close to the far side of the cloud and their HII regions have developed as a "champagne" flow (cf. Tenorio-Tagle 1982), and caused the back side of the cloud to be evaporated or dissipated, and the front side being pushed towards the earth forming the observed blue-shifted shell structure. When this occurs, Bodenheimer, Tenorio-Tagle & Yorke (1979) showed that the total energy can be more effectively transferred into mechanical energy, compared to the case of spherical expansion. They estimated that an O6.5 star can deposit as much as 5×10^{50} $ergs$ to the ionized gas during its lifetime of 3×10^6 years. Although it is not clear how much energy the neutral gas obtains during the its interaction with the ionized gas, it is reasonable to expect that the neutral gas ends up with a few percent of the energy carried by the ionized gas, giving $10^{49} ergs$, comparable to our rough estimate for the kinetic energy for the Mon R2 bubble shells[4].

Within this scenario, the mysterious RN 37 could be interpreted as leakage of the ionized gas on the inner layer of the dense shell; IRAS 06070-0619 could be interpreted as due to ionized HII on the high density portion of the shell or resulting from emission close to the obscured O type stars; and the radio thermal source G213.8-12.1 could be an obscured HII region on the inner layer of the bubble shell or even close to the obscured O stars.

Moreover, this hypothesis also provides a natural explanation to some other puzzles related to the structure of the cloud. **1.** As reviewed in Chapter 4, radio

---

[3] Given the well-shaped, sharp emission ridges, which show no signs of serious gas dispersion towards the cavity side, the high pressure must either be still present or has disappeared only very recently.

[4] We will further discuss this issue in the next section from a different perspective using the Elmegreen & Lada (1977) theory when we discuss the properties of the sharp emission ridges.

observations reveal that the HII region in the main core consists of at least two components — a diffuse one and a compact one (cf. Downes *et al* 1975; Gilmore 1980a,b). While it was later clarified that the compact component is due to a B0 star embedded in the main core (Massi, Felli & Simon 1985), the diffuse component has remained a puzzle. In our hypothesis, this diffuse component is naturally interpreted as the ionized gas on the inner side of the large neutral bubble shell where the main core is located in the front (see Figure 6.7). This physical picture for the main core is similar to what Gilmore (1980b) adopted in his modeling of the inner few arcminutes region of the core. **2.** The radio continuum maps of the region (Haslem, Quigley & Salter 1970; Reich 1978; Haslam *et al* 1982; Sofue & Nakai 1983) reveal an emission loop, the nature of which can not be easily determined because of the weakness of the emission (Reich 1978). In the O-star hypothesis, this enhanced emission is naturally understood. **3.** The enhancement of background red light in a rather roundish region (Figure 1.2) as discussed in Chapter 1 is simply due to the H_α emission of the HII region. Figure 6.7 depicts the physical picture for Mon R2 GMC, which integrates the major features and physical processes as summarized in the above.

It is worth pointing out again that in this physical hypothesis, we do not exclude the possible effects of stellar winds from the hypothetical O stars and all the known early type stars. We find that stellar winds from a few stars such as RN8-10 could be locally important and cause serious deformations and add complexities to the kinematics of the large bubble shell feature caused by the hypothetical O star(s). As indicated in Figure 6.7, stellar winds from RN 10 could be responsible for the open end of the major large bubble cavity in Mon R2, as discussed in the previous section. But the problem is that, in comparison with the physical picture provided above, the possibility that the large scale bubble shells in Mon R2 are PURELY due to stellar winds of the cluster of the first generation stars is somewhat less
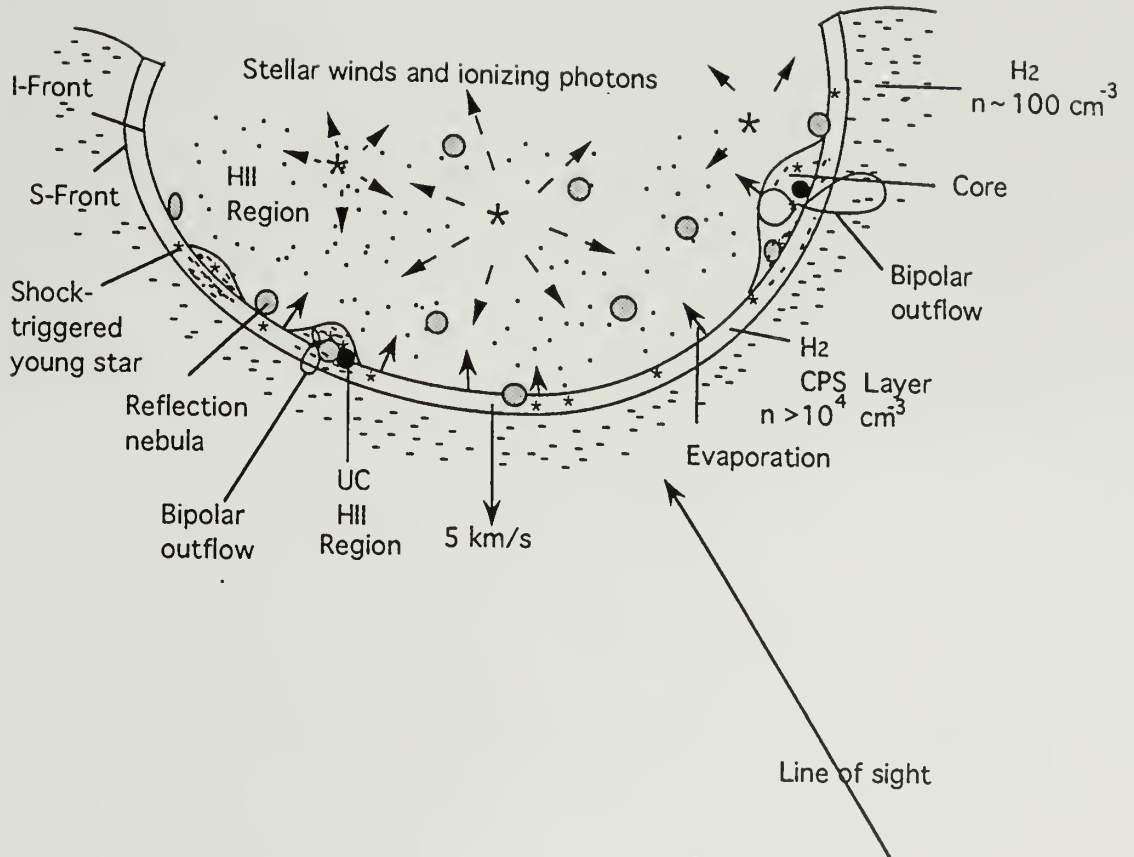
Figure 6.7. A cartoon depicting the physical structure of Mon R2.

attractive, although the possibility can not be ruled out. First, it is not clear how the stellar winds cause the enhancement of background red light (Figure 1.2) and radio continuum in a rather roundish region. Also, unless additional earlier type stars are proposed, the stellar wind picture does not naturally explain the presence of the several mysterious regions including RN 37, G213.8-12.1, IRAS 06070-0619 and the diffuse component of the HII region detected in the main core region. Second, this picture still leaves the question why there were no O stars formed in this region.

In the construction of the physical picture for Mon R2, we have not emphasized the possibility that the O stars may have become supernovae. There are several reasons for this. First, the line widths as well as the centroid velocity of $^{12}CO\ J = 1 - 0$ are only a few $km\ s^{-1}$ all over the whole cloud, and the kinetic energy is $\sim 5 - 10 \times 10^{48}$ ergs. All these do not seem to suggest the presence of any major "super-violent" events such as supernova explosion, although the supernova explosions can not be ruled out. Second, one may argue that the hypothetical O stars may not had enough time to become SNs[5]. Third, there are no known supernovae remnants associated with Mon R2. Although there is a known pulsar, PSR 0559-05 ($\alpha(1950) = 05^h59^m31^s.62$, $\delta(1950) = -05°27'46.4"$) (Manchester & Taylor 1981) in the N-W portion of Mon R2, its distance implied by its dispersion measure is 3.3 kpc (Lyne & Graham-Smith 1990). This large distance, its location and the morphology of the gas distribution in Mon R2 suggest that it is perhaps purely a positional coincidence. Fourth, even if a supernova did occur in this "champagne" flow case, because of its short lifetime, it may not play a major role in reshaping the molecular cloud (Yorke *et al* 1989; Elmegreen 1992) compared to the long lasting effects of OB stars' ionizing flux on the main sequence.

Finally, we point out that the elongation of the cloud (Maddalena *et al* 1986)

---

[5]The separation between the time that the O star leaves main sequence and the time that it becomes an SN is typically a few million years (Weaver, Zimmerman & Woosley 1978; Beltrametti, Tenorio-Tagle & Yorke 1982).

and the large-scale bubble shell, and velocity gradient along SE-NW direction are consistent with the general direction of the magnetic field (Dyck & Lonsdale 1979). It is not clear what role the magnetic field plays in the formation of the bubble shell in Mon R2. However, it is a reasonable speculation that the elongation of the bubble shell together with the velocity gradient may be caused by the presence of the magnetic field in the sense that gas motion occurred preferably along the magnetic field direction because of the difficulty of gas flow across the magnetic field lines. We have carried out CCD imaging polarimetry of selected regions (Jarrett *et al* 1992), and preliminary results of this study reveal that the magnetic field vectors are aligned along the N-S ridge, while to the east of this ridge magnetic field direction appears entangled. This suggests that magnetic field may be "frozen" in the shell material, and dynamically important.

6.4 Triggered Star Formation in Mon R2

Figures 2.3 to 2.10 clearly shows that young stellar objects, *IRAS* point sources in particular, are preferably found along the sharp emission ridges. A natural question is: are these *IRAS* point sources triggered star formation or merely a manifestation of the common knowledge that stars are born in molecular clouds ? The key to the answer seems to lie in the fact that there seems to have been two generations of star formation in Mon R2, as discussed in the previous section. Given the fact that the second generation of stars mostly represented by the *IRAS* point sources with ages on the order of 10^5 *years* tend to be concentrated in a few dense cores and sharp emission ridges in the outer part of the cloud, in contrast to the first generation of stars represented by most of the reflection nebulae (ages on the order of 10^7 *years*), we feel that there is little doubt that the formation of the second generation of stars is triggered by the influence of the first generation of star formation, at least in the sense of moderate triggering (Elmegreen 1992). In

other words, we feel that the second generation of star formation found in the sharp emission rims and dense cores is either enhanced by the shock compression due to the first generation of star formation or is a direct result of the shock compression. According to the classification scheme of Elmegreen (1992), Mon R2 case would be triggered star formation on an intermediate scale.

Also, the first and second generations of stars in Mon R2 have an age difference of $6 - 10 \times 10^6 yrs$ and a spatial separation (At least between the IRAS point sources on the N-S emission ridge and the majority of the B star clusters) on the order of 10-20 pc. This is characteristic of the other cases of triggered star formation on intermediate scales (Elmegreen & Wang 1988). Given the shock-crossing time in this region of $\sim 2.5 \times 10^6$ yrs, this shows good consistency with the expected age separation if the second generation of star formation is induced by the first generation (Elmegreen & Lada 1977).

Before we end this section, we wish to call attention to one IRAS source. Among the $IRAS$ point sources on the sharp emission ridges, a particularly interesting one is IRAS 06046-0603. This source is located right on the tip of the eggplant-shaped bipolar outflow shell (see the ^{12}CO $J = 1 - 0$ emission at $V_{LSR} = 10.88$ km s^{-1} in Figure 2.7). Curiously enough, this source is one of the only four $IRAS$ point sources in Mon R2 which were reported by Wood & Churchwell (1989) to have $IRAS$ colors characteristic of compact HII regions. The other three sources are 06053-0622, 06070-0619 and 06084-0611. 06053-0622 and 06084-0611 are known compact HII regions in the main core and GGD 12-15 core, respectively, and 06070-0619 is possibly associated with a radio thermal source as discussed in the previous section. The questions are: is $IRAS$ 06046-0603 a result of triggered star formation ? Is it associated with an HII region ? And is it related to the eggplant-shaped bipolar outflow shell ? Further observations designed to answer these questions are planned.

6.5   Discussion

Triggered star formation is not a new idea. Systematic observational studies on this issue have been going on since the 1970's, and more than ten molecular clouds in the Galaxy are reported to be undergoing triggered star formation on intermediate scales (Elmegreen 1985). While most of the known examples have two spatially well-separated star clusters with ages on the order of a few million years, the formation of the second generation of stars in Mon R2 is obviously just actively taking place with stars having ages on the order of 10^5 years or less, and being still deeply embedded in gas. The two generations of stars are completely separated neither spatially nor kinematically. In fact, some of the first generation stars are still trying to clear out their ambient gas. This is probably an indication that the gas density before shock compression was reasonably large and triggered star formation took place within a reasonably short time (Elmegreen 1992).

Up to date, the only systematic theory treating triggered star formation is the one proposed by Elmegreen & Lada (1977)[6], who considered the expansion stage of an HII region in a giant molecular cloud caused by the ionizing photons of OB stars. A shock front (hereafter S-front) travels ahead of the ionization front (hereafter I-front), and heats up and compresses the neutral cloud material before it becomes ionized by the I-front (Kahn 1954; Oort & Spitzer 1955; Pottash 1958; Elmegreen 1976). Elmegreen & Lada (1977) concentrated on the properties of this layer of gas between the I and S fronts, which they referred to as cooled, post-shock (CPS) layer because the radiative cooling of the layer is believed to be relatively rapid. Assuming a D-critical I-front, slab geometry, a cloud density of $n_3 \times 10^3$ hydrogen

[6]Although the gravitational instabilities of the cooled post-shock shells were later refined by Elmegreen & Elmegreen (1978) and Elmegreen (1989), we find that for our qualitative discussion in the following, the comprehensive discussions in Elmegreen & Lada (1977) are sufficient and even more relevant.

atoms and N_0 O6.5V stars in a region of 10 pc^2, they show that the shock velocity can be written as

$$v_s(r)(km\ s^{-1}) = 9.4r^{-1/4}N_0^{1/4}n_3^{-1/2}, \qquad (6.1)$$

where r(pc) is the distance of the shock from the stars. They also give a simplified expression for r after $t_6 \times 10^6$ years,

$$r(t) = 7.3N_0^{1/5}n_3^{-2/5}t_6^{4/5}, \qquad (6.2)$$

an expression for the column density N of the layer,

$$N(cm^{-2}) = 3.09 \times 10^{21}rn_3(1 - 0.18r_0/r - 0.82(r_0/r)^{1/4}) \qquad (6.3)$$

where $r_0(pc) = 0.10N_0n_3^{-2}$ is the thickness of a hypothetical layer of ionized hydrogen which can be maintained by the ionizing flux. When the CPS layer is not yet self-gravitating, they also show that the thickness of the CPS layer is

$$L(pc) = 4.8 \times 10^{-3}r^{3/2}N_0^{-1/2}n_3T_2, \qquad (6.4)$$

where T_2 is the neutral gas kinetic temperature in unit of 100 K. For $N_0n_3^{-2} \ll 1$, Elmegreen & Lada (1977) also derived the distance r and time t when gravitational instability occurs,

$$r_I(pc) = 14.4N_0^{1/5}n_3^{-4/5}, \qquad (6.5)$$

and

$$t_I(10^6\ years) = 2.3n_3^{-1/2}. \qquad (6.6)$$

If the large bubble shell in Mon R2 is mainly the result of O stars which are obscured or left main sequence or even exploded as a supernova, as discussed in the previous section, then it is reasonable to proceed in the following with a qualitative comparison between the theory and our observations. We integrate hypothesis for the origin of the large-scale shell and the triggered star formation scenario in the following.

1. O stars formed in Mon R2 at positions close to the back side of the cloud (as seen from the earth) $5 - 10 \times 10^6$ years ago. Soon afterwards, the HII region broke out of the back side in the fashion described by the "Champagne flow" model and formed a semi-spherical I-front bounded dense shell, which expands with decreasing velocity.

2. The sharp emission ridges could be the I-front bounded CPS layers viewed roughly edge on, where the S-front has passed and compressed the original cloud gas into the present high density layer.

3. From the fact that front side of the cloud having a velocity of $4 - 5$ km s^{-1} , a radius of ~ 15 pc and a column density on the order of 10×10^{21} H_2 , N_0, n_3 and t_6 can be solved using Equations 6.1 and 6.2, giving $t_6 = 2.9$, $n_3 = 0.4$ and $N_0 = 0.02$. i.e., the original average cloud H_2 density is on the order of 200 cm^{-3} and the age of the O stars is about 3 million years. Given the Mon R2 area of ~ 700 pc^2, the above N_0 implies 1.4 O6.5 stars. All these derived quantities seem to be reasonable.

4. From Equations 6.6 and 6.5, we obtain 3.6×10^6 years and 14 pc, respectively, for the time and radius at which the gravitational instability sets in. Given the size and estimated age for Mon R2 and the various possible errors in making the estimates, we conclude that these values are in good agreement with the fact that star formation is actively going on in the CPS layers in Mon R2, as evidenced by the $IRAS$ point sources.

5. Equation 6.4 gives a thickness of ~ 0.1 pc for non-strongly self-gravitating layer, which is far smaller than the separation between the the rim of the N-S emission ridge and many $IRAS$ point sources. It is not clear whether it is purely because the theory breaks down for the gravitationally-unstable layer or because new generation of stars emerged ahead of the CPS layer as a result

of the deceleration of the CPS layer (Elmegreen & Lada 1977) or due to some other reasons such as viewing angle.

6. The broader and weaker line profiles to the west of the N-S emission ridge could be an indication of the passing shock front disturbing the pre-shock cloud gas or due to the stellar winds or ionizing flux from a new generation of stars evidenced by the *IRAS* point sources disussed earlier in this chapter. The CPS layer itself might even be in the process being broken apart by the ongoing star formation triggered by the first generation of stars (Elmegreen & Lada 1977).

7. The cloud seems to be clumpy originally, and some large clumps had spontaneous star formation occurring at the time the O stars formed. At least two of these clumps, now seen as GGD12-15 and the main core, have been shock-compressed and bounded by ionizing flux and stellar winds, moving away from the O stars due to the rocket effects (cf. Kahn 1954; Oort & Spitzer 1955; Bertoldi & McKee 1990). This interaction can be seen from the cometary shape of GGD 12-15; we are seeing this object with a large viewing angle with respect to the symmetry axis of this interaction. The main core may also be suffering from the same effects, but because the symmetry axis has a large angle with respect to the plane of the sky, we are looking at this cometary object roughly tail-on. This point is supported by the blue-shifted velocity of the core (Chapter 4). In both of these cores, a new generation of stars have been triggered by the shocks which have passed, and coexist with the old generation of stars, which are still on the main sequence. Some of the newly formed stars are going through the mass loss phase and are seen to be powering bipolar outflows. These cores are being gradually dissipated by the ionizing photons and stellar winds from both generations of stars.

CLUMPINESS IN MON R2

7.1 Review

As mentioned in Chapter 1, an important development in quantitative study of clump properties as well as turbulence in molecular clouds has been the discovery of Larson's laws (Larson 1979; 1981; Snell 1981). The sample of "clumps" used in Larson (1981) includes dense cores, globules, dark clouds, and GMCs[1] These laws were later confirmed with different samples of "clumps" with slightly different power-law exponents (Leung, Kutner & Mead 1982; Myers and Benson 1983; Myers 1983; Solomon *et al* 1987). Solomon *et al* (1987) used the Massachusetts-Stony Brook CO survey data and identified 273 individual GMCs by applying a fixed thresholding temperature to a data cube (L-B-V). They obtained the size-linewidth relation first, and then used it together with the virial theorem to obtain clouds' masses. Besides confirming Larson's laws, they further argued that the CO J=1-0 luminosity is correlated with cloud mass in the galaxy. But research in this direction has encountered remarkable challenges in recent years (Issa, MacLaren & Wolfendale 1990; Adler & Roberts 1991; Scalo 1991). Issa, MacLaren & Wolfendale (1990) carried out a study of Larson's laws based on the same data set that Solomon *et al* (1987) used for their research, but found that serious uncertainties are involved in defining a cloud by using a single thresholding temperature, and clouds at vastly

---

[1]Indeed, "clouds" and "clumps" can be regarded as synonyms. "Clouds" are often used for more or less isolated molecular structures, while "clumps" are often used for sub-structures within individual molecular clouds. But this difference is small and sometimes ambiguous. For example, any cloud is a clump of a larger scale structure, and even giant molecular clouds can be regarded as clumps on the scale of galactic disks. We feel that for the sake of studying Larson's laws at least, we refer all sub-structures within Mon R2 as clumps in this thesis.

different distances may be mistakenly treated as a single GMC. Their conclusion is that the size-linewidth relationship in Solomon *et al* (1987) is "not a genuine reflection of the dynamical state of Giant Molecular Clouds (GMCs)". Since this uncertainty in cloud definition leads to an overestimate of masses of GMCs, they further question the presence of large GMCs claimed to be in or close to virial equilibrium by Solomon *et al* (1987). The results of Issa, MacLaren and Wolfendale (1991) received strong support from the independent theoretical investigation by Scalo (1991) and Adler and Roberts (1991). Adler & Roberts (1991) generated model galactic disks by N-body cloud-particle simulations. They found that clouds identified using longitude-velocity diagrams are often chance superpositions of clouds spread out along the line of sight in the model galactic disk, and that the size-linewidth relationship is not a reliable indicator of the physical nature of the cloud complexes.

Although the defending article written by Solomon and Barrett (1991) is also convincing, it is clear that both of the two schools of thought cannot be correct. In this situation, a close examination of Larson's laws based on high-quality data sets for an individual GMC will help resolve the controversy. One important point that has been recognized is that Larson's laws should also apply to sub-concentrations within individual GMCs if they indeed represent a real physical characteristic of molecular clouds (cf. Larson 1979; 1981; Carr 1987; Stutzki & Güsten 1991). One great advantage of studying clumps within individual GMCs is that the distance ambiguity problem is greatly relieved, and thus the physical quantities dependent on distance can be better determined provided clumps are properly identified. But efforts to study Larson's laws based on data sets for individual GMCs remain rare. A few examples include Orion (Bally *et al* 1987), Rosette (Blitz 1987; 1991), Cep OB3 (Carr 1987) and M17SW (Stutzki & Güsten 1991).

7.2 Definition and Identification of Clumps

The concept of clouds or clumps is intrinsic to our way of perceiving spatial structures. It is by classifying and defining individual smaller features that we gradually build the basis on which to recognize complex structures, from smaller, simple features to large, complex features. This suggestive tendency in defining features provides the background for our communication. The definition of clouds and clumps has been our major way of studying the structure of interstellar medium, but definitions of these features have also been the root of confusion (cf. Scalo 1991).

The practical way of defining molecular clouds or clumps in observational astronomy is to identify "contour islands" in spatial maps or spatial-velocity (SV) maps of spectral line emission from molecular tracers (Blitz 1980). While this can be done by using our "eyes" (hereafter referred to as the "eye method"), which definitely gives us the most intuitive identification, it is not practical for large amount of data which contains many clouds or clumps. In this case, the only way is to automate the identification using a computer and a given definition algorithm. The most common algorithm is perhaps the one used for identifying molecular clouds from galactic $^{12}CO\ J = 1-0$ survey data (Clemens 1985; Scoville $et\ al$ 1987; Solomon $et\ al$ 1987), which can be briefly summarized as follows. For a data cube $T(nx, ny, nz)$ whose elements are antenna temperatures of $^{12}CO\ J = 1-0$ and whose dimensions are positions and velocity, a thresholding temperature (typically a few times larger than the rms noise) is chosen and the whole data cube is searched for elements with values larger than this thresholding temperature. Then, a cloud is defined as the ensemble of those pixels satisfying this selection criterion and also simply connected ($\Delta nx = \pm 1$, $\Delta ny = \pm 1$, $\Delta nz = \pm 1$). Hereafter we will refer to this method as the "traditional method".

This "traditional method" of identifying clouds is undoubtedly consistent with the intuitive "eye method" of defining clouds; the difference is only that the new

method combines the spatial maps and SV maps, and draws "3D contours"; the "enclosures" of the 3D contours are defined as molecular clouds. In a way, this is certainly better than defining molecular clouds as "contour islands" based on spatial maps or SV maps with eyes, because the latter cannot easily integrate the information from spatial and SV maps. But this new method is not as good as the "eye method" in that it defines separable structures at one specific contour value as "clouds", while our eyes actually pick up features at various contour levels. This weakness is presumably very obvious, but few attempts to approach the problem based on 3D data can be found in the literature.

Stutzki & Güsten (1991) developed a "Gaussian clump" method for analyzing their $C^{18}O\ J = 2 - 1$ data cube for the giant molecular cloud M17. This algorithm can be briefly described as follows. Assuming a clump has a Gaussian intensity distribution, the peak of the map is fitted by this intensity distribution until it converges, then the fitted clump is subtracted from the map, and the fitting is repeated iteratively until no more clumps satisfying some criteria can be identified. One striking point of the work is that they identified as many as 179 clumps from their $C^{18}O\ J = 2 - 1$ data consisting merely 280 spectra; implying that each clump averages less than 2 map points (spectra). Despite the multiple peaks manifest in the line profiles from M17, we feel that caution should be taken in interpreting the results of this Gaussian clump program. Logically, given a single clump of an irregular shape, fitting it to a Gaussian intensity distribution would leave a residual map which can be further decomposed into smaller Gaussian clumps. This could be in a sense similar to the attempt to decompose a rectangle into circles of maximum size by iteration; the number of resulted circles is only limited by the lower size limit for the circles imposed on the program. From this consideration, we feel this algorithm, which assumes smooth morphology for clumps, could give rise to "fictitious" clumps because clumps are generally corrugated and fractal

(cf. Dickman, Horvath & Margulis 1991; Scalo 1991; see also next section in this Chapter).

A more intuitive way of identifying clumps is perhaps to improve the "traditional method" so that the computer program also picks out features at different contour levels, in a fashion similar to the "eye method". Such a method actually exists for 2D data (Houlahan 1989; Scalo 1991; Dickman, Horvath & Margulis 1991; Cernicharo 1991; Houlahan & Scalo 1992). While Dickman, Horvath & Margulis (1991) concentrated on the fractal nature of clump boundaries, Houlahan (1989), Scalo (1991), Cernicharo (1991) and Houlahan & Scalo (1992) intended to characterize the complex structure of interstellar molecular clouds, and developed the "structure tree analysis" technique to characterize the complex, hierarchical structure. But it is clear that this algorithm can be easily used for studying clump quantities. The basic physical idea associated with this algorithm is in accord with a very important observational fact; molecular clouds are found to show hierarchical structure in the sense that large features can always be resolved into smaller sub-structures down to the resolution limit (cf. Wilson & Walmsley 1989).

In this chapter, we implement this clump identification method with multiple thresholding temperatures for analyzing our 3D data. Our algorithm is in general similar to that of Houlahan & Scalo (1992) in identification of clumps, except that we are dealing with 3D data here and necessarily have some special problems. Our main concern in this chapter is to investigate the correlations of clump quantities, and we do not analyze the "structure tree" in any statistical method as Houlahan & Scalo (1992) attempted. We present our computer algorithm and its technical as well as physical limitations in the next section. Section 7.3 presents the results, and Section 7.4 is a discussion of the results.

7.3 Computer Algorithm

7.3.1 Clump Identification

While $^{12}CO\ J = 1 - 0$ might trace column density on a large scale (see the reasonably good correlation between $^{12}CO\ J = 1 - 0$ and $^{13}CO\ J = 1 - 0$ emission on a large scale in Chapter 2), $^{13}CO\ J = 1 - 0$ is surely preferable mass tracer to $^{12}CO\ J = 1 - 0$ on small as well as large scales because of its moderately small optical depth relative to that of $^{12}CO\ J = 1 - 0$. We use our $^{13}CO\ J = 1 - 0$ data obtained using Bell Labs 7m telescope for the clumpiness analysis, supplemented by our $^{12}CO\ J = 1 - 0$ data for determination of related physical quantities. We assume that $^{13}CO\ J = 1 - 0$ is optically thin.

Starting with $^{13}CO\ J = 1-0$ data in the format of 3D data cube with dimensions being Velocity, RA and DEC, our computer algorithm to identify and analyze clumpiness consists of four technical steps, which are detailed in the following.

1. The data cube is successively thresholded at increasing intensity levels from zero to the maximum intensity G_{max} of the cube with a preassumed increment ΔG. At each grey level G, "clumps" are identified using the "traditional method" (cf. Clemens 1985; Scoville *et al* 1987; Solomon *et al* 1987; Lee, Snell & Dickman 1990), in which a "clump" is defined as an ensemble of simply connected pixels with intensities not less than G. When these clumps are identified, important information such as boundary pixels and centroid positions are retained.

2. The second step of this algorithm is to compare the clumps identified at a thresholding level with those identified at a previous, low thresholding level for containment test. This test is similar to that described by Houlahan (1989), Scalo (1991) and Houlahan & Scalo (1992), except it is performed in three dimensions, with information of containment (lineage) being recorded. At the end of this process, the containment information is further analyzed in

filtering out structures which are essentially the same as clumps identified at previous low thresholding levels. The very important concept in the algorithm is the principle of "containment and splitting", i.e., only those clumps which share with at least one other clump a "parental clump" identified at a previous lower thresholding intensity level are counted as real clumps, while any clump which is a unique "child" of a clump identified at previous lower thresholding temperatures is regarded as a repetition of the same clump. Besides this important physical restriction, we find that a few more restrictions must be applied in practice to relieve the adverse effects of noise and data defects. With sufficient tests of the program with authentic data, we find that two filters are effective in filtering out the effects of noise. One is requiring a minimum spatial area or perimeter of clumps. The other is requiring a minimum velocity dispersion of a clump. Both these criteria are based on the fact that data pixels should have un-correlated noise, so that requiring a sufficiently large spatial or velocity size for a clump should effectively eliminate the adverse effects of noise.

3. When these real clumps are identified, a number of physical quantities such as the centroid velocity, velocity dispersion, centroid spatial position, area, perimeter, peak intensity, LTE mass and virial mass are calculated for each clump and catalogued along with lineage information and levels at which the clump has been identified.

4. The last step of the algorithm includes a managing program which plots structure trees, correlates relevant quantities, and performs curve fitting and other data analysis tasks.

7.3.2 Determination of Physical Quantities

Step 3 of the computer algorithm presented above includes computation of physical quantities of clumps. We briefly discuss a few obvious as well as subtle

quantities from observations is a very difficult and even highly controversial problem. We briefly discuss a few obvious as well as subtle problems in the following.

1. The rms noise of our ^{13}CO $J = 1 - 0$ data is about 0.3 K within a 0.5 $km\ s^{-1}$ channel, and the peak antenna temperature of the data cube is about 10K. While it is ideal to have an essentially infinite number of thresholding temperatures from 0 to the peak antenna temperature for the purpose of building structure trees, we find that an increment significantly smaller than the rms noise begins to lose physical sense. This is similar to making contour maps. Tests show that intensity increments significantly smaller than the rms noise produce basically the same physical results as far as the study of the clump physical quantities is concerned, with the help of noise control means discussed above. Although the program imposes no restriction on the intensity increment, we chose $\Delta G = 0.3K$ for this study.

2. When the data cube is thresholded or truncated by the finite number of thresholding intensities (temperatures), the emission of a single clump identified at a previous low intensity is partitioned into more than one individual clumps. There is in fact another very important emission component left out: the emission which is weaker than the present grey level, yet stronger than the previous grey level. In a hierarchical picture of the molecular cloud, which is a basic assumption of identifying clumps with multiple thresholding temperatures, this emission component can be naturally interpreted as "interclump medium" consistent with the definition of the clumps. This concept is in fact an operational need in the the way that "clouds" or "clumps" are identified traditionally in the literature. This is so because identifying clumps from an emission map would necessarily leave the weaker component as "interclump medium", at least in an operational sense. Now the problem is, how do we

take into account of this component in computing physical quantities for the clumps? Conceivably, this component should also exist along a line of sight and thus make an additional contribution on the order of the intensity level at which the interclump medium is defined, and thus its total integrated emission should be subtracted from the lines of sight consisting the clumps in estimating the clump quantities such as mass. But the problem is that the velocity dispersion of the interclump medium, which is needed to perform such a subtraction, is difficult to assess along each line of sight. As a zero order of approximation, we decide to approximate this linewidth by the real velocity dispersion along each line of sight. Then, assuming that ^{12}CO $J = 1 - 0$ peak antenna temperature can be taken as the excitation temperature of ^{13}CO $J = 1 - 0$, the mass of a clump can be estimated under the LTE assumption as described in Dickman (1978b).

It is important to realize that the velocity dispersion along each line of sight for the identified clumps must be based only on the pixels with intensity larger than the grey levels at which clumps are identified, because pixels with lower emission intensities could belong to other clumps or interclump medium. First, the velocity dispersion of the upper portion of a line profile at spatial position (i, j) with intensity larger than the grey level G can be estimated by the rms standard deviation (Dickman & Kleiner 1985)

$$\sigma_{top}^{i,j} = (\Sigma_k T_k^{i,j}(v_k^{i,j} - v_c^{i,j})^2 / \Sigma_k T_k^{i,j})^{1/2}, \tag{7.1}$$

where $v_c^{i,j}$ is the intensity weighted centroid velocity. Assuming the line profiles of the clump to be Gaussian shaped, the real velocity dispersion of the line profile can be obtained by applying a simple correction factor to Eq. 7.1 [2]

---

[2]The parabolic extrapolation adopted by Lee, Snell & Dickman (1990) tends to underestimate the correction factor for a Gaussian, presumably because Gaussian has a more extended wing than a parabola (Lee, private communication).

$$\sigma_{los}^{i,j} = \sigma_{top}^{i,j}(\log \frac{2.72T_A^*}{T_A^* + 1.72G})^{-1/2}, \tag{7.2}$$

where T_A^* is the peak antenna temperature along each line of sight.

3. With this estimated velocity dispersion along each line of sight for a clump, we calculate the mass of a clump by using the LTE method described by Dickman (1978b). To do this, we have smoothed, and resampled our ^{12}CO $J = 1-0$ data to the 1.5' resolution and the 1' spacing of the ^{13}CO $J = 1 - 0$ data. The computer program reads in the ^{12}CO $J = 1 - 0$ data and finds the peak antenna temperatures at corresponding lines of sight for the clumps identified in the ^{13}CO $J = 1-0$ data. These ^{12}CO $J = 1-0$ peak antenna temperatures are used as the excitation temperature (Dickman 1978b).

4. To estimate the total velocity dispersion of clumps, we consider both the velocity dispersion observed along lines of sight and spatial velocity variations, using the formulae of Dickman & Kleiner (1985). Specifically, the average velocity dispersion along lines of sight for a clump is

$$\sigma_{los} = (\Sigma_{i,j}(\sigma_{los}^{i,j})^2/N)^{1/2}, \tag{7.3}$$

where N is the number of lines of sight. The spatial velocity variation is characterized by the centroid velocity dispersion given by

$$\sigma_c = (\Sigma_{i,j}(v_c^{i,j} - v_c)^2/N)^{1/2}, \tag{7.4}$$

where v_c is the average centroid velocity of a clump. The total velocity dispersion of a clump is given by

$$\sigma = (\sigma_c^2 + \sigma_{los}^2)^{1/2}. \tag{7.5}$$

The often used FWHM velocity dispersion is $\Delta V = 2.35\sigma$.

5. It is clear that clumps identified using the above algorithm can be of arbitrary shape, and their boundaries are fractal in nature (Dickman, Horvath & Margulis 1991; Scalo 1991), as we will discuss in the next section. But the characteristic radius of a clump can be defined as $R = 1/2(A/\pi)^{1/2}$. If we assume the clumps have a roughly roundish shape and uniform density [3], then the often discussed virial mass can be shown to be (Langer *et al* 1989)

$$M_{VIR}(M_\odot) = f180R(pc)(\Delta V)^2(km\ s^{-1}),\tag{7.6}$$

where f is a numerical factor accounting for the neglected terms such as magnetic field, external pressure etc. In this study, we take $f = 1$.

7.3.3 A Few Obvious Limitations

Despite the care that we have taken in implementing the above algorithm, serious limitations still exist. Most of these are due to the data itself and lack of understanding about the "clumpiness". We analyze several major problems in the following.

First, the definition of "clumps" is meaningful only in relative terms. While the existence of clumps seems a necessity, as reviewed in Chapter 1, the size of clumps is not well known and perhaps much smaller than both the spatial and spectral resolution of our data (Tauber 1989; Tauber, Goldsmith & Dickman 1991). Kwan & Sanders (1986) have devised a clumpy model for molecular clouds in which small clumps with thermal linewidths and masses as little as 1 $M_\odot$ are coherently organized in space and velocity into bigger units. They showed that this model, with a sufficiently small volume filling factor, can provide a satisfactory explanation to the

---

[3]Unfortunately, we know that this is not the case. I believe that this assumption itself leads to terribly large errors which make it almost impossible to assess whether clumps are in virial equilibrium, not mentioning the possible effects of interclump pressure, as we will discuss in the next section.

generally observed Gaussian line profiles of optically thick lines such as $^{12}CO\ J = 1 - 0$. Obviously, the clumps that we identify using our $^{13}CO\ J = 1 - 0$ data for Mon R2 and our clump finding program illustrated above are not the small clumps in Kwan & Sanders' model. However, it seems rather reasonable that the clumps that we identify are still meaningful even in this type of models if we understand them as hierarchies of coherent structures of the small clumps.

Second, clump "blending" could still be a serious problem. Structures that have spatial and velocity separations larger than the observational resolution limits can in principle be decomposed by the above algorithm, but definitely not those that overlap both spatially and kinematically.

Third, while the spatial dynamical range of our data (~ 200) is reasonably large, its limited value still casts some effects to our result. e.g., the incomplete coverage of the low intensity emission close to map borders is bound to cause an error in determination of clump quantities. Fortunately, this effect only occurs at low thresholding temperatures, and does not seriously affect our general results. The intensity dynamical range, however, is relatively small (e.g., compared to that of infrared emission maps). This causes the identification of clumps to have some dependence on the thresholding temperatures. But tests show that the error caused by this effect is typically small provided the intensity increment of thresholding is small, and can be controlled by filtering out small clumps which could be affected by small intensity fluctuations.

7.4   Results

7.4.1   Fractal Nature of the Clump Morphology

Figure 7.1 presents a plot of log (Perimeter) versus log (Area). The area and perimeter are well correlated with relatively small scatter, and the data is well fit by a single power law of slope 0.80, giving a Hausdorff dimension of $D_H = 1.60 \pm 0.02$.
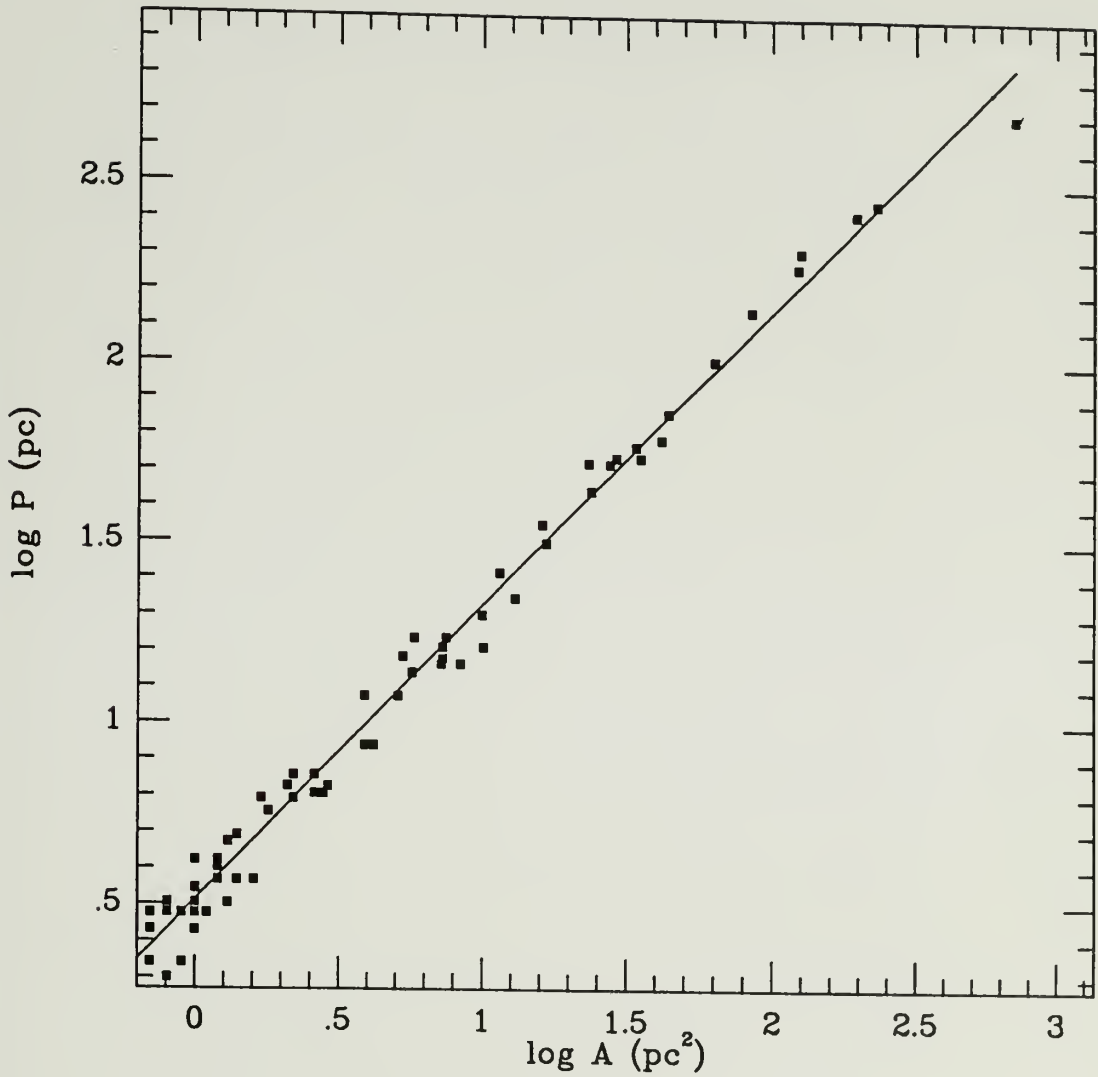
Figure 7.1. A plot of log (Perimeter) versus log (Area) for the clumps identified in Mon R2. The solid line is the least square fit, which implies a Hausdorff dimension of $D_H = 1.60$.

This value is bigger than that determined by studies of other molecular clouds based on $IRAS$ images (Bazell & Désert 1988; Dickman, Horvath & Margulis 1990; Scalo 1991), which give values of $D_H \sim 1.1 - 1.4$. Some unpublished results of analyses based on CO data for various molecular clouds, as summarized by Scalo (1991), also give values of $D_H \sim 1.34 - 1.46$. The physical point is that our results are consistent with all these studies in revealing that the shapes of clumps are fractal rather than smooth, possibly a strong indication that the clumps suffer a lot of complex physical processes which determine their boundary shapes (Dickman, Horvath & Margulis 1990).

7.4.2 Correlations of Clump Quantities

Figure 7.2 presents a plot of log (ΔV) versus log (Area). Despite the relatively large scatter of the data in both axes, the correlation of the two quantities is obvious and is best fit by

$$\Delta V = (1.17 \pm 0.10)R^{0.42\pm0.04}, \tag{7.7}$$

where ΔV is in $km\ s^{-1}$ and R in pc. It is noticeable that the power-law exponent of 0.42 ± 0.04 is larger than the value of 0.25 ± 0.06 determined for clumps in Cep OB3 (Carr 1987), yet consistent with the value of 0.5 determined for clumps within M17 (Stutzki & Güsten 1990). But our value is in general consistent with the values of $0.4 - 0.6$ derived for molecular clouds of various sizes in outer as well as inner Galaxy (cf. Larson 1981; Leung, Kutner & Mead 1982; Myers & Benson 1983; Myers 1983; Sanders, Scoville & Solomon 1985; Scoville et al 1987; Solomon et al 1987; Lee, Snell & Dickman 1990).

Figure 7.3 plots log M_{LTE} versus log ΔV. Again the correlation trend is apparent and can be fitted by

$$M_{LTE}(M_\odot) = (50.1 \pm 0.2)\Delta V^{4.0\pm0.3}(km\ s^{-1}). \tag{7.8}$$
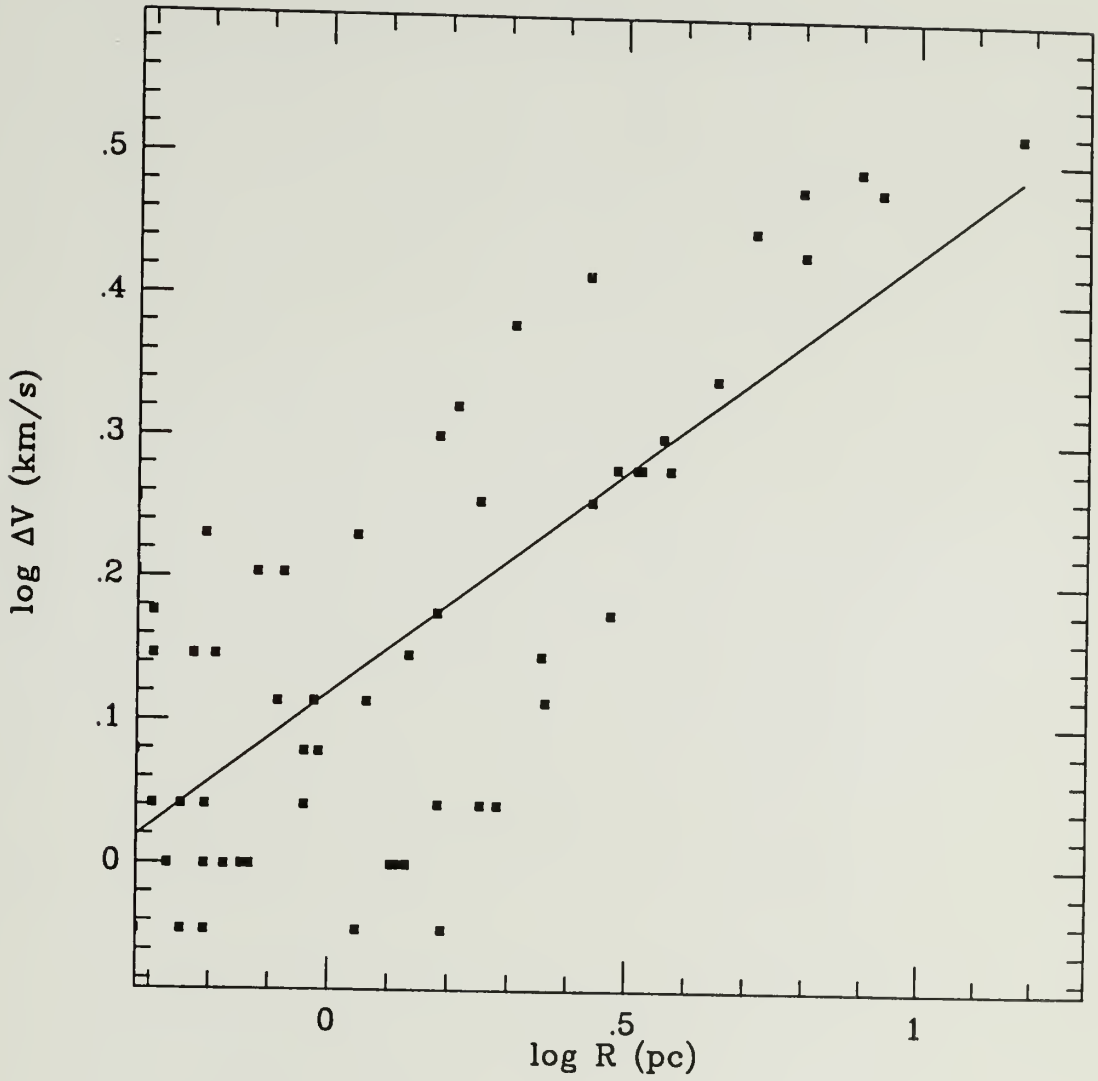
Figure 7.2. log (ΔV) versus log (Area). The solid line is the least square fit.
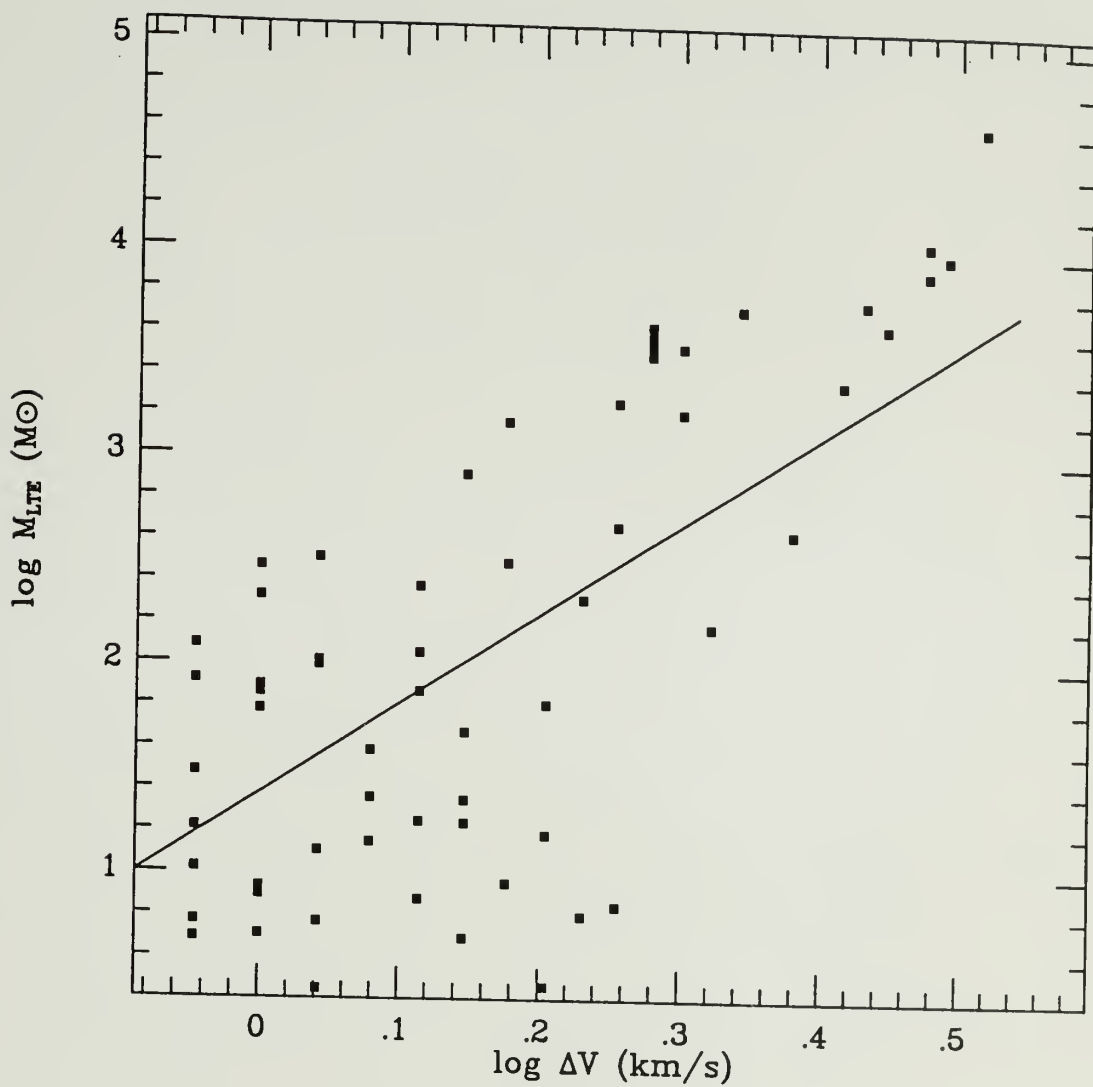
Figure 7.3. A plot of log (M_{LTE}) versus log (ΔV) for clumps in Mon R2. The solid line is the least square fit.

The power-law exponent of 4 is in remarkable consistency with that reported by Leung, Kutner & Mead (1982) for a sample of globules, by Bally *et al* (1987) for the clumps in Orion A and by Stutzki & Güsten (1990) for M17SW, yet significantly different from the value of ~ 10, implied by the results of Carr (1987) for the clumps within Cep OB3.

Finally, Figure 7.4 plots log M_{LTE} versus log M_{VIR}. The correlation between the two quantities is clear and can be fitted by

$$M_{LTE}(M_\odot) = (0.11 \pm 0.03)M_{VIR}^{1.28\pm0.07}(M_\odot). \tag{7.9}$$

This correlation between the two masses has been previously reported for other samples of "clumps", and has been interpreted as evidence for clouds being in or close to gravitational virial equilibrium (Scoville *et al* 1987; Solomon *et al* 1987; Carpenter, Snell & Schloerb 1990; Lee, Snell & Dickman 1990).

7.4.3 Clump Spectra

Figure 7.5 presents a histogram of the distribution of clumps with their LTE masses. The fluctuations are large. The solid line is a least-squares fit represented by $N = (37 \pm 13)M^{0.31\pm0.07}(M_\odot)$. We excluded the first bin at the low mass end because it obviously suffers from serious bias (incomplete sampling). This fit implies $dN/dM \propto M^{-1.3}$. The absolute value of the exponent is 1.3, compared to 1.1 for clumps in ρ Oph (Loren 1989), 1.4 for clumps in Cep OB3 (Carr 1987), 1.5 for clumps in Rosette (Blitz 1991), 1.6 for clumps in Orion B (Lada, Bally & Stark 1991) and 1.7 for M17SW (Stutzki & Güsten 1990).

7.5 Discussion

Our results in the previous section seem to support the existence of a size-linewith relationship. Despite the fact that a large scatter exists in the log ΔV
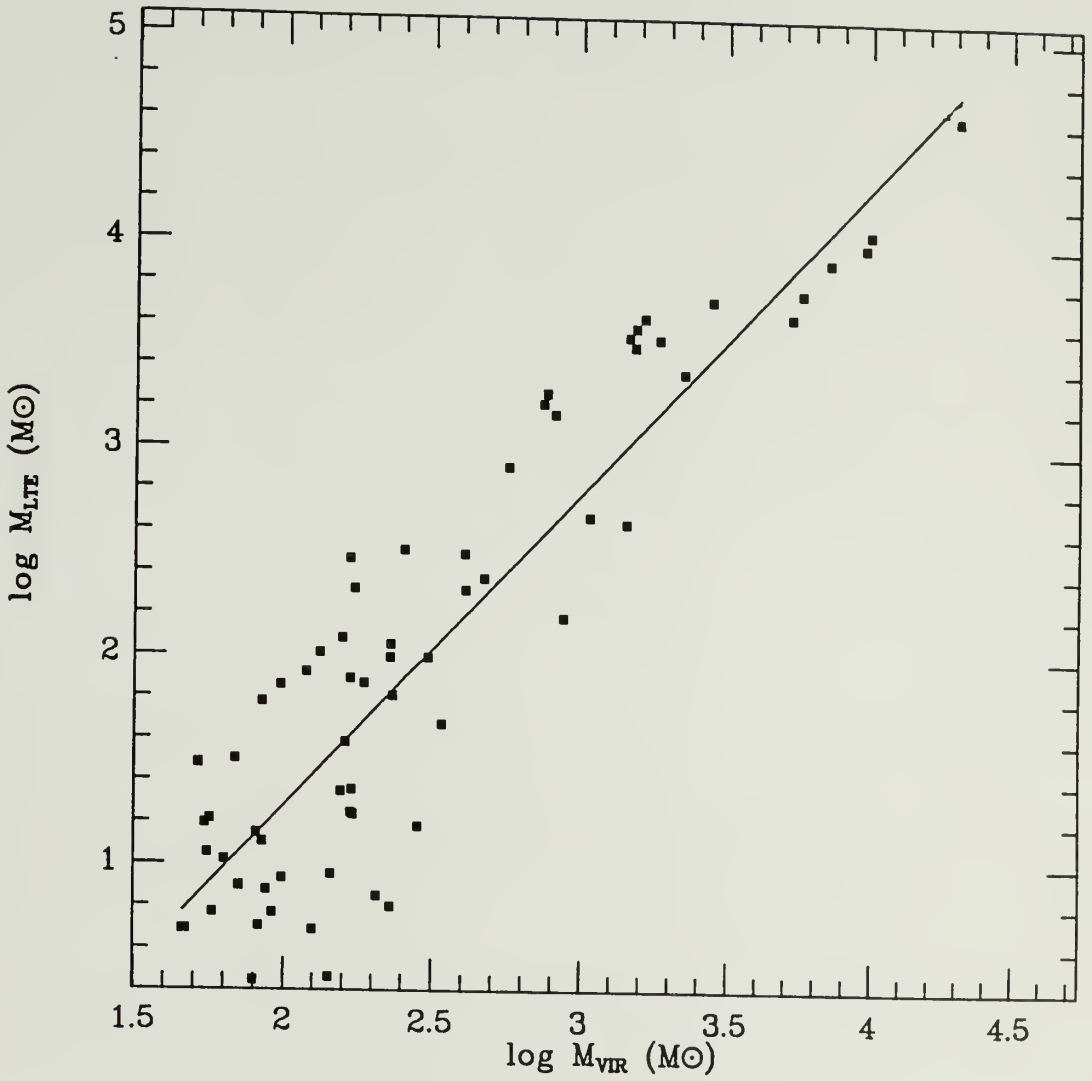
Figure 7.4. Plot of log M_{LTE} versus M_{VIR}. The solid line is the least square fit.
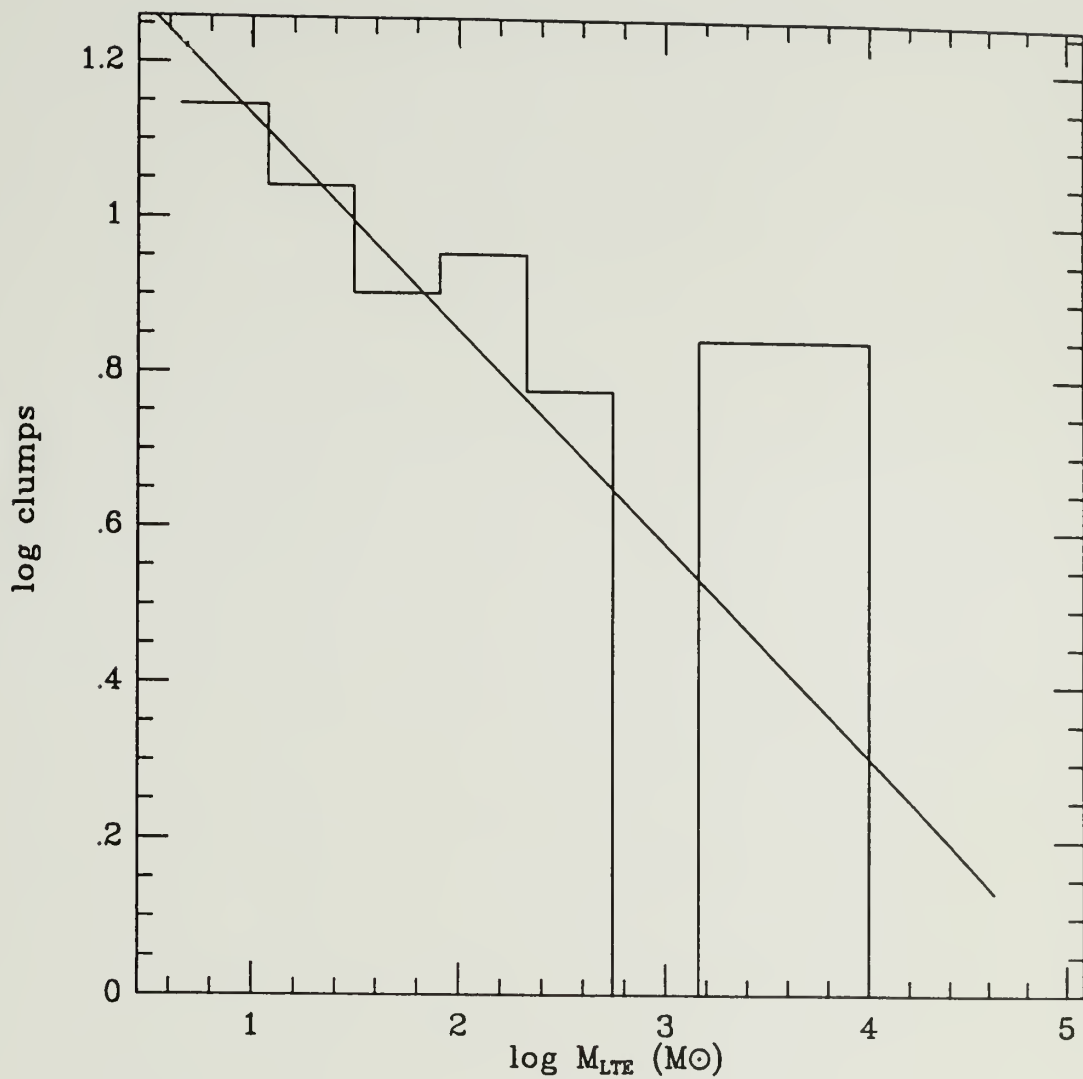
Figure 7.5. Mass spectrum of the clumps in Mon R2; the fluctuations are large. The solid line is a least-squares fit $N = (37 \pm 13)M^{0.31\pm0.07}(M_\odot)$. The first bin at the low mass end has been excluded in the fitting.

versus log R plot (Figure 7.2), we feel that the clear trend of correlation is difficult to attribute to inadequate cloud identification. An important point is that this size-linewidth relationship is found based on the way that clouds or clumps are usually defined. Thus if our traditional concept of clouds or clumps (as discussed earlier in this Chapter) is retained, then we must consider the size-linewidth relationship as a genuine property of clumps or clouds, which deserves serious explanation. However, it seems that the question raised by Issa, MacLaren & Wolfendale (1990) whether this size-linewidth relation is "a genuine reflection of the DYNAMICAL state" of molecular clouds is a good one, and should not be neglected.

Now how is dynamical state of clumps usually assessed ? The mass of clumps is an important physical quantity related to dynamics. There are generally two masses which can be estimated observationally. One is the gas mass determined from $^{12}CO\ J = 1 - 0$ or $^{13}CO\ J = 1 - 0$ by using LTE or empirical extinction-integrated intensity relationship (Dickman 1978a; Liszt 1982; Dickman & Herbst 1989), and the other is the virial mass defined by Eq. 7.6. The common way of evaluating the the dynamical state of a cloud has been to compare the two masses; if the two are comparable, then it is believed that the clumps are in virial equilibrium or gravitationally bound. But in practice, it is generally realized that estimates for both masses are subject to significant systematic errors. As a result of this realization, the requirement for clumps or clouds to be in or near virial equilibrium is reduced to requiring a clear correlation between the two mass estimates (cf. Larson 1981; Solomon *et al* 1987; Scoville *et al* 1987).

According to this, the clumps in Mon R2 would be in or close to gravitational virial equilibrium, given the excellent correlation between the two masses for the clumps in Mon R2 (Figure 7.4). But if this were true, then should we not expect to have clumps with much smoother morphology than that revealed by the log (Perimeter) versus log (Area) relation ? Also, we have seen in Chapter 2 that both

$^{12}CO\ J = 1 - 0$ and $^{13}CO\ J = 1 - 0$ images show extremely filamentary structure, which is clearly difficult to attribute to clumps which are gravitationally-bound, because gravitationally bound clumps would show a more or less roundish shape. Given the violent processes that we have shown to be taking place in Mon R2, we feel that it is unlikely that the clumps in Mon R2 should have a roundish shape.

This point can also be seen as follows. The average density of a clump calculated from its total mass is one of the physical quantities which is most sensitive to geometrical shape. If we assume that clumps have a roundish shape, while in reality they are highly asymmetric, then a density-linewidth plot would be expected to have a much larger scatter than the mass-linewidth relation. Figure 7.6 proves this point; in contrast to the well-defined mass-linewidth correlation (Figure 7.3), the density-linewidth plot has such a large scatter that no correlation is obvious.

One easy exit from this difficulty seems to be the realization that given a size-linewidth relation, the two masses are not independent physical quantities (Maloney 1990). First, we notice that given a size-linewidth relation, Eq. 7.8 can be a natural result if the average optical depth of $^{13}CO\ J = 1 - 0$ and average peak antenna temperature of the clumps do not vary greatly. This is so because the formula for calculating the mass of clumps scales with several relevant quantities in the following fashion (Dickman 1978b),

$$M_{LTE} \propto \frac{R^2 \Delta V \tau^{13} T_x}{1 - e^{(5.29/T_x)}} \tag{7.10}$$

where τ^{13} is the peak optical depth of $^{13}CO\ J = 1 - 0$ emission. The term $R^2 \Delta V$ alone can give rise to a $\Delta V^{\frac{2+\beta}{\beta}}$ dependence, where β is the power-law exponent of the size-linewidth relation, and is likely to dominate the final dependence of M_{LTE} on ΔV. Thus, a correlation between M_{LTE} and ΔV is not surprising if a size-linewidth relation holds.

Second, it is clear that virial mass is expected to be a function of ΔV

$$M_{VIR} \propto \Delta V^{\frac{1+2\beta}{\beta}}, \tag{7.11}$$
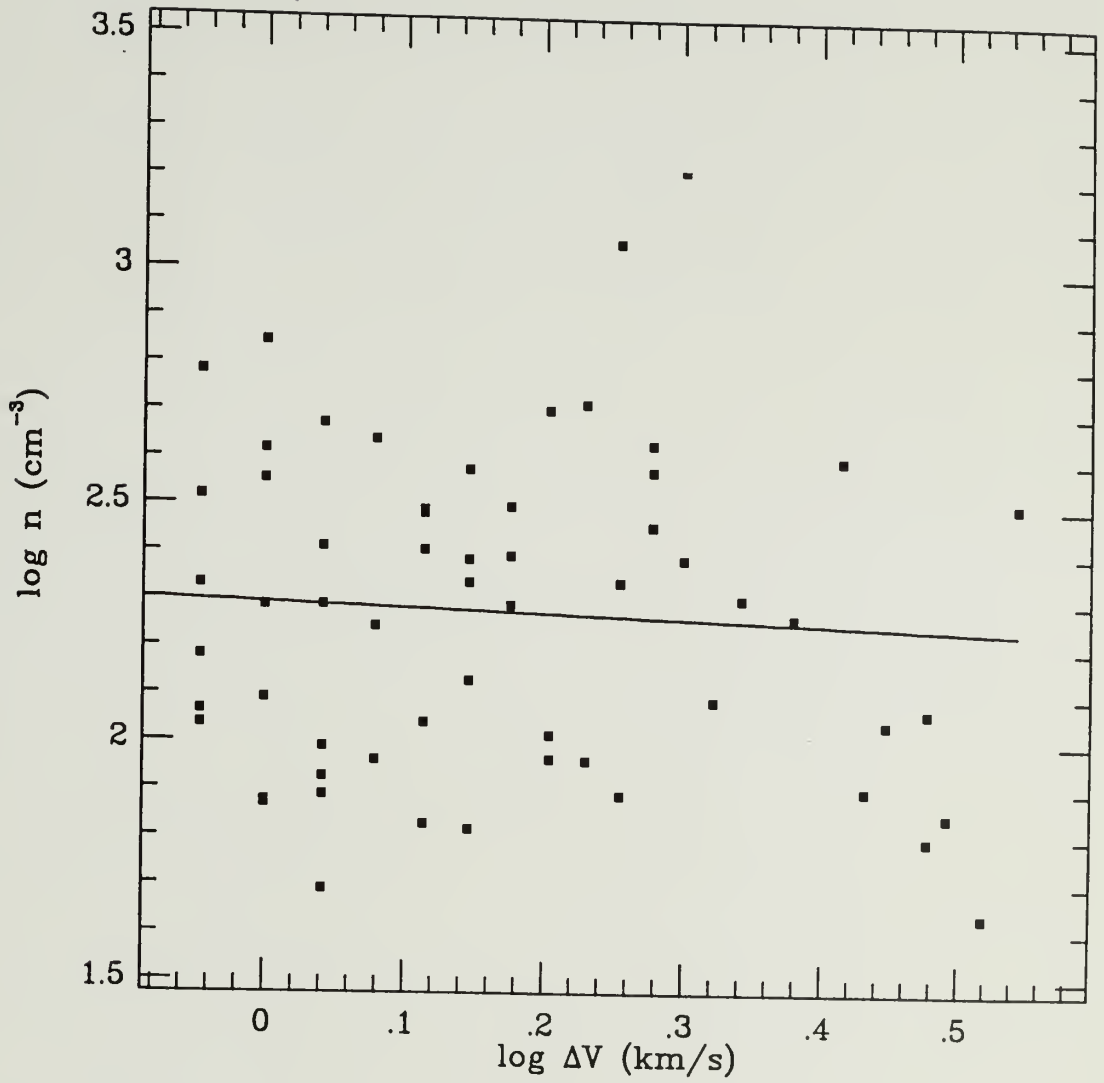
Figure 7.6. A plot of log n versus log ΔV. No obvious correlation is found.

Given the observed power-law relation (exponent α) between the LTE mass and the velocity dispersion of clumps (Equation 7.8), it is readily seen that the two masses should be related by $M_{LTE} \propto M_{VIR}^{\gamma}$, where $\gamma = \frac{\alpha\beta}{1+2\beta}$. Given the β and α values with errors, the resultant γ value is consistent with Equation 7.9.

Given these results, we feel that a size-linewidth relation is likely to be an authentic result under the conventional definition of clouds or clumps based molecular emission maps. It is the existence of this relation that gives rise to the empirical correlation between the virial mass and the LTE or empirical mass determined using $^{12}CO \ J = 1 - 0$ or $^{13}CO \ J = 1 - 0$ emission intensity, as well as the correlation between the LTE masses and linewidths (Maloney 1990). Although this seems to invalidate the simple argument that clouds or clumps are in or close to virial equilibrium based on simple correlation of the two mass estimates, the possibility that the size-linewidth is a manifestation of physical processes related to dynamical state of clumps or clouds cannot be ruled out. But it is important to realize that there could be many mechanisms which give rise to this size-linewidth relation (cf. Larson 1981; Fleck 1983; Henriksen & Turner 1984; Chièze 1987; Falgarone & Puget 1986; Myers & Goodman 1988a, b; Henriksen 1991).

C H A P T E R   8

SUMMARY

In a way, this thesis work has been destructive; the abundant data that we collected and analyzed clearly indicate that some previous speculations are either wrong or incomplete. But this thesis is also constructive; we achieved a relatively simple physical picture of Mon R2, which can essentially account for the major observational results. We showed that many previous research results do stand up to our abundant data sets, and some of the existing models for star formation and cloud structure make amazingly good sense in confronting our new data. Besides, we also made attempts to develop new ways to attack old problems. We summarize main conclusions of this study in Section 8.1. Unfortunately, I have the feeling that this thesis has created more questions and problems than it has solved. We list some of the questions in Section 8.2, which hopefully can serve as guidance for future work. My hope is that these new questions and problems are closer to the truth.

8.1   Conclusions

Monoceros R2 is a nearby ($D = 830 \pm 50 \ pc$) giant molecular cloud associated with an association of reflection nebulae. This cloud has a size of $\sim 40 \ pc \times 60 \ pc$ and a mass of $\sim 5 \times 10^4 \ M_\odot$, comparable to its more famous neighbors Orion A and Orion B. Yet the Mon R2 region appears to have much less bright emission nebulosities in optical images than Orion A or Orion B, and is not known to be associated with any early O type stars. Given their comparable large masses and sizes, this contrast is somewhat puzzling. Aimed at improving our understanding about this GMC

with the hope of shedding light on this type of GMC related to R-associations, we mapped Mon R2 in $CO\ J = 1-0$ transition with 25" spacing using the FCRAO 14 m telescope with QUARRY. This data set, consisting of $\sim 167,000$ spectra covering $\sim 40 \times 40$ pc region, is supplemented by a $40,000$ spectra map for $^{13}CO\ J = 1-0$ obtained using the Bell Laboratory 7m telescope with 1' spacing, *IRAS BIGMAP* images as well as maps of high density molecular tracers for the dense cores obtained with QUARRY. The major results of this study are summarized in the following.

1. We found that $^{12}CO\ J = 1-0$ and $^{13}CO\ J = 1-0$ intensities of Mon R2 are well correlated on a large scale, which validates $^{12}CO\ J = 1-0$ as reliable kinematic tracer on a sufficiently large scale. The scatter of the data in this correlation is large enough to preclude $^{12}CO\ J = 1-0$ as a reliable column density tracer on small scales.

2. The dominant morphological features in Mon R2 revealed by our $^{12}CO\ J = 1-0$ and $^{13}CO\ J = 1-0$ images are two sharp emission ridges, and diffuse, low intensity emission in the South-East corner of the map, forming a ring-like emission feature. One ridge runs across the whole extent of the cloud from North to South in the western portion of the cloud, passing through the main core. The other ridge is oriented horizontally from East to West in the eastern portion of the cloud, silhouetting a chain of dense cores including GGD 12-15, which has a spectacular cometary shape.

3. One important realization developed during the course of this thesis is that there are at least two generations of star formation in Mon R2. The first (older) generation is represented mainly by the known reflection nebulae powered mostly by B and A type stars on main sequence, distributed preferably along a narrow band in the East to West direction. The age of this first generation of stars is estimated to be at least $6 - 10 \times 10^6$ years. The second (younger)

generation of stars is represented mainly by numerous $IRAS$ point sources, preferably located in the dense cores and sharp emission ridges. In particular, the N-S oriented sharp emission ridge harbors tens of $IRAS$ point sources lined up nicely along the ridge. From the age of bipolar outflows and UC HII regions in the main core and GGD 12-15 core, we estimate that the second generation of stars have an age on the order of $\sim 10^5$ $years$, an order of magnitude younger than the first generation.

4. We found that the large scale structure of Mon R2 is dominated by the existence of a bubble shell (Diameter ~ 32 pc) with its front side moving towards us at a radial velocity of $\sim 4 - 5$ km s^{-1} . We found no evidence for the red-shifted far side of the bubble shell. The characteristic crossing time-scale is $\sim 5 \times 10^6$ years, and the kinetic energy of the systematic motion is estimated to be $5 - 10 \sim 10^{48}$ ergs.

5. A detailed examination of all the available data sets has convinced us that this large sized bubble shell is very likely a result of the combined effects of ionizing power and stellar winds originating from the formation of first generation of young stellar objects. Given the age of this first generation of stars and the large mass of the cloud, we feel that it is reasonable to adopt the hypothesis that there are even O type stars which are obscured by the foreground extinction or left main sequence. It is possible that it is these O type stars on the far side of the cloud which blew out the cavity in the fashion of "champagne" flow and formed the large scale semi-spherical bubble shell. This leads to the suggestion that Mon R2 might look more like Orion B (whose HII regions are believed to be on the front side of the neutral molecular material) were we to look at Mon R2 from the other side.

6. The existence of the two generations of star formation and their locations with respect to the large scale bubble shells strongly suggest that the younger generation of stars could have been triggered by the violent compression forces generated by the ionizing photons and stellar winds of the older generation of stars. With the hypothesis that there are hidden O type stars on the far side of the cloud, we went further in comparing the main observational characteristics of the shell structure and star formation with the theoretical model of Elmegreen & Lada (1977). Although some key physical questions can only be addressed on order-of-magnitude analysis, we find that Elmegreen & Lada theory provides a rather remarkable qualitative account of major observational results. While the star formation in the N-S oriented sharp emission ridge can be explained as the result of gravitational collapse or fragmentation of post-shock layers of the gas shell, we argued that the coexistence of two generations of star formation in the cores can be interpreted only if these cores were pre-existing clumps before the formation of the large bubble shells.

7. We found that the central main core, including the well-known powerful bipolar outflow, is part of the large blue-shifted bubble shell moving towards us. We further suggest that the core was a pre-existing clump with first generation of star formation going on before being overtaken, shock-compressed and reshaped by the ionizing photons and stellar winds from other more massive stars of the first generation which blew out the large scale blue-shifted bubble shell. We suggest that this core has a cometary shape with its head pointing into the large cavity and symmetry axis having a small inclination angle with respect to the line of sight. In other words, the core is a "peninsula", immersed in the high pressure cavity. Two generations of star formation coexist in this core. The earlier generation of star formation is represented by a few bright reflection nebulae with powering stars on the main sequence with age of $\sim 1 \times 10^7$ years,

while the younger generation is represented by the embedded infrared star cluster and the UC HII region, the bipolar outflow and the presence of water masers. This second generation could well have been triggered by the shock compression of the first generation. We also find that the velocity gradient across the shell is consistent with what is expected. Thus, we suggest that this picture is preferable to the previous physical model of cloud rotation.

8. We found that the GGD 12-15 core, including the bipolar outflow in it, is also located on the large scale expanding shell. The location and morphology as well as the kinematics of the GGD 12-15 dense core region in the eastern portion of the cloud are best explained if it is a pre-existing clump being shock-compressed by the ionizing photons and stellar winds which blew out the large bubble shell. Its clear cometary shape in some velocity channel maps indicates that the symmetry axis of impinging shock front has a large inclination angle with respect to the line of sight. Similar to the situation in the main core, two generations of star formation coexist in this core. It is proposed that the second generation of star formation could have been triggered by the first generation of stars.

9. We found a well-shaped limb-brightened bipolar outflow shell outlining the blue-shifted emission of the central bipolar outflow. We modeled the outflow within the framework of Shu et al (1991) and found that the shape of the shell can be well accounted for with radially directed winds sweeping up ambient material with momentum conservation. The outflow axis is determined to be inclined $\sim 70°$ relative to the line of sight. The blue-shifted lobe is directed away from the large scale cavity and thus develops roughly in the fashion described by Shu *et al* (1991). The red-shifted lobe of the bipolar outflow, however, is directed towards the high pressure cavity, and is being significantly axially

compressed. This compression causes the stellar wind from the central star develops in lateral direction. We believe that this abnormal development of the red-shifted lobe has given rise to the observational results that red- and blue-shifted emission overlaps significantly close to the center. In this picture, we do not need a second pair of bipolar outflow as has previously been proposed by other investigators.

10. *IRAS HIRES* images reveal in the main core and the GGD 12-15 core spectacularly fragmented ring-like features ($\sim 2 - 3$ *pc*) with reflection nebulae and *IRAS* point sources on them. The ring-like feature in the main core contains in its center a much smaller ring-like feature (~ 0.1 *pc*) previously revealed by NIR images.

11. We discussed difficulties with the use of single- or multi-temperature dust models in deriving dust temperature and column density. We implemented an inversion method to analyze dust emission spectra at FIR wavelengths in terms of a continuous dust temperature distribution, and applied this method to *IRAS BIGMAP* images of Mon R2. Although it is impossible to constrain the amount of very cold dust using *IRAS* data alone, we suggest that the column density image obtained with proper care serves as a good tracer of the variation of the dust column density. We derived a modified Wien's displacement law to constrain the interpretation of the results concerning the range of dust temperature that the *IRAS* sensitively samples. We found that dust column density image derived using the inversion method has a much better correlation with the gas column density image than does any *IRAS* image alone. Even so, the quantitative correlation between the dust and gas column densities is poor. We interpreted this poor correlation in terms of the existence of substantially ionized gas, and the insufficient heating of the large dust grains in weak emission

regions not associated with active star forming activity.

12. We discussed difficulties related to the identification of clumps and the determination of their physical properties. We implemented computer programs to identify clumps and determine their physical properties by "simulating" the traditional way that identifies clumps as "contour islands" from spatial and spatial-velocity maps. Specifically, we threshold our $^{13}CO \ J = 1-0$ data cube with increasing intensity levels, and identify clumps as simply connected pixels in 3D space. Then, the clumps identified at different levels are merged based on the principle of "containment & splitting". The log Perimeter - log Area plot gives a Hausdorff fractal dimension of $D_H = 1.6$ for the clumps. The data confirms the size-linewidth and mass-linewidth relations of Larson's laws as well as the correlation between virial mass and mass determined using LTE or empirical relations. But we argue against interpreting the mass-linewidth or mass-mass correlation as evidence for gravitational boundedness of clumps or clouds because we showed that these two relations can be natural consequences of a size-linewidth relation. We suggest that the size-linewidth relation is perhaps the basic relation of Larson's laws, yet it is an open question whether this relation is a manifestation of the intrinsic dynamic properties of clumps or clouds.

13. Given the existence of the two generations of stars generating ionizing photons and stellar winds, which necessarily ionize, dissociate and dissipate ambient molecular material, Mon R2 is at a stage of being largely re-shaped and even dispersed. There is abundant evidence for the existence of holes and shells of various sizes surrounding these young stellar objects. We showed evidence for "nested" bubble shells. We suggest that the "nesting" of bubble features is a mechanism which can potentially give rise to hierarchical structure.

8.2   Future Work

1. There are at least two generations of star formation in Mon R2; the younger generation was triggered by the older generation. Detailed observations of both generations will be interesting. While optical photometric studies have been carried out for some stars of the first generation, determination of the spectral type for those remaining members would provide very useful information concerning the properties of this old generation of stars, and would also shed light on the origin of the large scale expanding shell. An investigation of the proper motions of these stars in comparison with the gas and dust distribution will also be useful for understanding the kinematics and the formation of this generation of stars as well as the fashion that the second generation of stars are triggered.

2. NIR photometric studies of the second generation of stars (mostly $IRAS$ point sources) will be very important for understanding the properties of this generation of triggered star formation. NIR observations of a group of the $IRAS$ point sources on the N-S emission ridge are planned and will be carried out in the winter of 1992. But it should be equally interesting to carry out NIR photometric studies of the chain of dense cores silhouetting the sharp emission ridge in the eastern portion of the cloud, where triggered star formation may also be taking place as evidenced by numerous $IRAS$ point sources and reflection nebulae.

3. It is unfortunate that we were not able to obtain sufficient observing time on QUARRY for mapping interesting regions such as the N-S emission ridges, dense cores in the eastern portion of the cloud using density tracers including $CS\ J = 2-1$,$HCN\ J = 1-0$ and $HCO^+\ J = 1-0$. These observations would serve as a perfect project to combine with the aforementioned NIR observations

for revealing the details of triggered star formation in the cooled post shock gas layers and testing the existing theory of fragmentation of thin gas layers and triggered star formation.

4. Infrared and radio observations of the central region in Mon R2 may provide direct clues and evidence for or against the O-star hypothesis proposed in this thesis for the origin of the expanding bubble shell.

5. The "jumps" of column density and density, the gradual broadening of line profiles of ^{12}CO $J = 1 - 0$ and ^{13}CO $J = 1 - 0$ across the sharp emission ridges from the cavity side to the other side appear very impressive. These layers may serve ideal observational targets for chemical studies of shocked gas and detailed multi-transitional studies of the physical conditions of shocked gas. Interferometric millimeter observations of strips across these sharp emission ridges may help to reveal their structure, the small-scale fragmentation and to assess the relationship of small-scale fragmentation and star formation.

6. We developed an inversion technique for analyzing dust emission spectra in terms of a continuous dust temperature distribution. We applied this method to *IRAS* images by forcing the carriers of 12 μm emission to take power-law emissivity, while in reality the carriers of 12 μm and even 25 μm emission may have complex properties. The current version of the inversion method cannot easily deal with this problem. A numerical version of the inversion method is being developed as a step forward toward this direction.

7. The bipolar outflow in the main core that we analyzed should be a good target of further research. One particularly interesting thing is to see if the mass distribution of the high velocity blue-shifted gas obeys Shu *et al* model. Observations with better resolution (e.g., interferometric millimeter observations) would be useful for revealing the shell structure on a smaller scale. Questions concerning

the origin, collimation, the detailed structure of the eggplant-shaped shell, its relation with the dense gas clumps, ring-like feature revealed by *HIRES*, and the exact nature of its interaction with the ambient medium as well as the large expanding shell in Mon R2 are all very interesting observational topics. Also, the origin and properties of the star forming ring-like feature revealed by *HIRES* with respect to that of its internal, much smaller ring-like feature revealed by NIR observations seem to be an extremely interesting future research project.

8. Finally, we wish to point out again the existence of "nested" bubble shells and the potential importance of this peculiar geometrical aspect of star formation in relating to hierarchical structure of molecular clouds. Further observational efforts in this direction should be of considerable interest to future theoretical modeling of molecular clouds and star formation.

9. Goodbye. I appreciate your fighting your way to the end of this thesis.

BIBLIOGRAPHY

Adams, F.C., Lada, C.J., & Shu, F.H. 1987, *ApJ, 312*, 788.

Adler, D.S., & Roberts, W.W., Jr. 1991, preprint.

Anglada, G., Estalella, R., Rodríguez, L.F., Cantó, J., & López, R. 1991, *A&A, 252*, 1639.

Aspin, C., & Walther, D.M., 1990, Astron. Astrophys., 235, 387.

Bachiller, R., Cernicharo, J., Martín-Pintado, J., Tafalla, M. & Lazareff, B. 1990, *A&A, 231*, 174.

Bally, J. & Lada, C.J. 1983, *ApJ, 265*, 824.

Bally, J. & Lane, A.P. 1991, in *The Physics of Star Formation and Early Stellar Evolution*, ed. C.J. Lada & N.D. Kylafis (Dordrecht:Kluwer), p.471.

Bally, J., Langer, W.D., & Liu, W. 1991, *ApJ, 383*, 645.

Bally, J., Langer, W.D., Stark, A.A., & Wilson, R.W., 1987, *ApJ, 312*, L45.

Bally, J., Langer, W.D., Wilson, R.W., Stark, A.A, & Pound, M.W. 1991, in *Fragmentation of Molecular Clouds and Star Formation*, ed. E. Falgarone, F. Boulanger & Duvert (Dordrecht: Kluwer), 11.

Bazell, D., & Désert, F.X. 1988, *ApJ, 333*, 353.

Beckwith, S., Evans II, N.J., Becklin, E.E., & Neugebauer, G. 1976, *ApJ, 208*, 390.

Beichman, C.A. 1987, *ARA&A, 25*, 521.

Beichman, C.A., Myers, P.C., Emerson, J.P., Harris, S., Mathieu, R., Benson, P.J., & Jennings, R.E. 1986, *ApJ, 307*, 337.

Beichman, C.A., Wilson, R.W., Langer, W.D., & Goldsmith, P.F. 1988, *ApJ, 332*, L81.

Beltrametti, M., Tenorio-Tagle, G., & Yorke, H.W. 1982, *A&A, 112*,1.

Benson, B.J., & Myers, P.C. 1983, *ApJ, 270*, 589.

Bertoldi, F., & McKee, C.F. 1990, *ApJ, 354*, 529.

Blaauw, A. 1964, *ARA&A, 2*, 213.

Blaauw, A. 1991, *The Physics of Star Formation and Early Stellar Evolution*, ed. C.J. Lada & N.D. Kylafis (Dordrecht:Kluwer), 125.

Blake, G.A., van Dishoeck, E.F., & Sargent, A.I. 1992, *ApJ, 391*, L99.

Blitz, L., 1980, in *Giant Molecular Clouds in the Galaxy*, eds. P.M. Solomon and M.S. Matthews (Tucson: University of Arizona Press), 201.

Blitz, L., 1987, in *Physical Processes in Interstellar Clouds*, eds. G.E. Morfill and M. Scholer (Dordrecht: Reidel), 35.

Blitz, L., & Thaddeus, P. 1980, *ApJ, 241*, 676.

Blitz, L. 1991, *The Physics of Star Formation and Early Stellar Evolution*, ed. C.J. Lada & N.D. Kylafis (Dordrecht:Kluwer), 3.

Bodenheimer, P. 1972, *Rep. Prog. Phys., 35*, 1.

Bodenheimer, P., Tenorio-Tagle, G., & Yorke, H.W. 1979, *ApJ, 233*, 85.

Bok, B.J., & Reilly, E.F. 1947, *ApJ, 105*, 255.

Boissé, P., 1990, *A&A, 228*, 483.

Boulanger, F., Falgarone, E., Puget, J.L., & Helou, G. 1990, *ApJ, 364*, 136.

Cabrit, S., & Bertout, C. 1986, *ApJ, 307*, 313.

Cabrit, S., & Bertout, C. 1990, *ApJ, 348*, 530.

Carpenter, J.M., Snell, R.L., & Schloerb, F.P. 1990, *ApJ, 362*, 147.

Carr, J.S., 1987, *ApJ, 323*, 170.

Casey, S.C. 1991, *ApJ, 371*, 183.

Casoli, F., Dupraz, C., Gerin, M., Combes, F., & Boulanger, F. 1986, *A&A, 169*, 281.

Castor, J., McCray, R., & Weaver, R. 1975, *ApJ, 200*, L107.

Cernicharo, J. 1991, *The Physics of Star Formation and Early Stellar Evolution*, ed. C.J. Lada & N.D. Kylafis (Dordrecht:Kluwer), 287.

Chen, N.X. 1990, *Phys. Rev. Lett., 64*, 1193.

Chevalier, R.A., & Theys, J.C. 1975, *ApJ, 195*, 53.

Churchwell, E. 1991, *The Physics of Star Formation and Early Stellar Evolution*, ed. C.J. Lada & N.D. Kylafis (Dordrecht:Kluwer), 221.

Chièze, J.P. 1987, *A&A, 171*, 225.

Clemens, D.P. 1985, PhD thesis, University of Massachusetts, Amherst.

Cohen, J.G., & Frogel, J.A. 1977, *ApJ, 211*, 178.

Cohen, M., & Kuhi, L.V. 1979, *ApJS, 41*, 743.

Cohen, M., & Schwartz, R.D. 1980, *MNRAS, 191*, 165.

de Muizon, M., & Rouan, D. 1985, *A&A, 143*, 160.

Dent, W.R.F. 1988, *ApJ, 325*, 252.

Désert, F.-X., Boulanger, F., & Puget, J.L. 1990, *A&A, 237*, 215.

Dibai, E.A. 1958, *Sov. AJ, 2*, 429.

Dibai, E.A. 1960, *Sov. AJ, 4*, 13.

Dickman, R.L. 1975, *ApJ, 202*, 50.

Dickman, R.L. 1978a, *AJ, 83*, 363.

Dickman, R.L. 1978b, *ApJS, 37*, 407.

Dickman, R.L. 1985, in *Protostars and Planets II*, ed. D.C. Black & M.S. Matthews (Tucson: University of Arizona Press), 150.

Dickman, R.L. 1988, in *Molecular Clouds in the Milky Way and External galaxies*, eds. R.L. Dickman, R.L. Snell & J.S. Young, (Berlin: Springer-Verlag), 55.

Dickman, R.L., & Herbst, W., 1990, *ApJ, 357*, 531.

Dickman, R.L., Horvath, M.A., & Margulis, M. 1990, *ApJ, 365*, 586.

Dickman, R.L., & Kleiner, S.C. 1985, *ApJ, 295*, 479.

Dickman, R.L., Snell, R.L., & Schloerb, F.P. 1986, *ApJ, 306*, 326.

Disney, M.J., McNally, D., & Wright, A.E. 1969, *MNRAS, 146*, 123.

Dixon, R.S., & Sonneborn, G. 1980, *Master List of Nonstellar Optical Objects*, Ohio State University Press.

Dorschner, V.J., & Gütler, J.J. 1964, *Astron. Nachr., 287*, 257.

Dorschner, V.J., & Gütler, J.J. 1965, *Astron. Nachr., 289*, 57.

Downes, D., Winnberg, A., Goss, W.M., & Johansson, L.E.B. 1975, *A&A, 44*, 243.

Draine, B.T. 1983, *ApJ, 270*, 519.

Draine, B.T. 1990, in *The Interstellar Medium in Galaxies*, ed. II.A. Thronson, Jr. & Shull, J.M. (Netherlands: Kluwer Academic Publishers), p. 483.

Draine, B.T., & Anderson, N. 1985, *ApJ, 292*, 494.

Draine, B.T., & Lee, H.M. 1984, *ApJ, 285*, 89.

Dwek, E. 1986, *ApJ, 302*, 363.

Dyck, H.M., & Lonsdale, C.J. 1979, *AJ, 84*, 1339.

Dyson, J.E. 1977, *A&A, 59*, 161.

Dyson, J.E. 1984, *Ap&SS, 106*, 181.

Dyson, J.E. 1989, *Structure and Dynamics of Interstellar Medium*, ed. G. Tenorio-Tagle, M. Moles & J. Melnick (Heidelberg: Springer-Verlag).

Egan, M.P., Leung, C.M., & Spagna, G.F. 1988, *Computer Phys. Comm., 48*, 271.

Elmegreen, B.G. 1976, *ApJ, 205*, 405.

Elmegreen, B.G. 1985, *Birth & Evolution of Massive Stars & Stellar Groups*, ed. W. Boland & H. van Woerden (Dordrecht:Reidel), 227.

Elmegreen, B.G. 1989, *ApJ, 340*, 786.

Elmegreen, B.G. 1991, *Evolution of Interstellar Matter and Dynamics of Galaxies*, ed. B.W. Burton, P.O. Lindblad & J. Palous (Cambridge: Cambridge University Press).

Elmegreen, B.G. 1992, preprint, *III Canary Islands Winter School*, to be published by Cambridge University Press.

Elmegreen, B.G., & Elmegreen, D.M. 1978, *ApJ, 220*, 1051.

Elmegreen, B.G., & Lada, C.J. 1977, *ApJ, 214*, 725.

Elmegreen, B.G., & Wang, M. 1988, in *Molecular Clouds in the Milky Way and External galaxies*, eds. R.L. Dickman, R.L. Snell & J.S. Young (Berlin: Springer-Verlag), 240.

Emerson, J.P. 1987, in *Star Forming Regions*, ed. M.Peimbert & J.Jugaku (Dordrecht:Reidel), 19.

Erickson, E.F., Caroff, L.J., Simpson, J.P., Strecker, D.W., & Goorvitch, D. 1977, *ApJ, 216*, 404.

Erickson, N.R., Goldsmith, P.F., Novak, G., Grosslein, R.M., Viscuso, P.J., Erickson, R.B., & Predmore, C.R. 1992, *IEEE Trans. on Microwave Theory and Techniques, 40*, 1.

Evans II, N.J. 1978, *Protostars and Planets*, ed. T. Gehrels & M.S. Matthews (Tucson: University of Arizona Press), 153.

Evans II, N.J. 1985, *Protostars and Planets II*, ed. D.C. Black & M.S. Matthews (Tucson: University of Arizona Press), 175.

Falgarone, E., & Puget, J.L. 1986, *A&A, 162*, 235.

Falle, S.A.E.G. 1975, *A&A, 43*, 323.

Fleck, R.C., Jr. 1983, *ApJ, 272*, L45.

Fleck, R.C., Jr. 1988, *ApJ, 333*, 840.

Frerking, M.A., Langer, W.D., & Wilson, R.W. 1982, *ApJ, 262*, 590.

Fuller, G.A., & Myers, P.C. 1992, *ApJ, 387*, 523.

Geiss, J. 1988, in *Rev. Mod. Ast., 1*, ed. G. Klare (Heidelberg:Springer-Verlag), 1.

Genzel, R., & Downes, D. 1977, *A&ASS, 30*, 145.

Genzel, R. 1991, in *The Physics of Star Formation and Early Stellar Evolution*, ed. C.J. Lada and N.D. Kylafis (Dordrecht:Kluwer), 155.

Gilmore, W. 1980a, *AJ, 85*, 894.

Gilmore, W. 1980b, *AJ, 85*, 936.

Gilmore, W., Brown, R.L., & Zuckerman, B. 1975, *Bull. AAS, 7*, 260.

Goldreich, P., & Kwan, J. 1974, *ApJ, 189*, 441.

Goldsmith, P.F., 1987, in *Interstellar Processes*, eds. D.J. Hollenbach & H.A. Thronson,Jr. (Dordrecht:Reidel), p51.

Goldsmith, P.F., 1988, in *Molecular Clouds in the Milky Way and External galaxies*, eds. R.L. Dickman, R.L. Snell & J.S. Young (Berlin: Springer-Verlag), 1.

Goldsmith, P.F., & Langer, W.D. 1978, *ApJ, 222*, 881.

Goldsmith, P.F., & Linke, R.A. 1981, *ApJ, 245*, 482.

Goldsmith, P.F., Lis, D.C., Hills, R., & Lasenby, J. 1990, *ApJ, 350*, 186.

Goldsmith, P.F., Lis, D.C., Lester, D.F., & Harvey, P.M. 1992, ApJ, 389, 338.

Goldsmith, P.F., Margulis, M., Snell, R.L., & Fukui, Y. 1992, *ApJ, 385*, 522.

Goldsmith, P.F., Plambeck, R.L., & Chiao, R.Y., 1975, ApJ, 196, L39.

Goldsmith, P.F., Snell, R.L., Hasegawa, T., & Ukita, N. 1987, *ApJ, 314*, 525.

Goldsmith, P.F., Snell, R.L., Hemeon-Heyer, M., & Langer, W.D. 1984, *ApJ, 286,* 599.

Goldsmith, P.F., Snell, R.L., & Lis, D.C. 1987, *ApJ, 313,* L5.

Gordon, M.A. 1987, *ApJ, 316,* 258.

Gordon, M.A. 1988, *ApJ, 331,* 509.

Goudis, C. 1982, *The Orion Complex: A Case Study of Interstellar Matter,* (Dordrecht: Reidel).

Guhathakurta, P., & Draine, B.T. 1989, *ApJ, 345,* 230.

Güsten, R., & Marcaide, J.M. 1986, *A&A, 164,* 342.

Gyul'budagyan, A.L. 1982, *Sov. Astron. Lett., 8,* 123.

Gyulbudaghian, A.L., Glushkov, Yu.I., & Denisyuk, E.K. 19i78, *ApJ, 224,* L137.

Hackwell, J.A., Grasdalen, G.L., & Gehrz, R.D. 1982, *ApJ, 252,* 250.

Harvey, P.M., Campbell, M.F., & Hoffmann, W.F. 1977, ApJ, 211, 786.

Harvey, P.M., Wilking, B.A., Joy, M. & Lester, D.F. 1985, *ApJ, 288,* 725.

Haslam, C.G.T., Quigley, M.J.S., & Salter, C.J. 1970, *MNRAS, 147,* 405.

Haslam, C.G.T., Salter, C.J., Stoffel, H., & Wilson, W.E. 1982, *A&ASS, 47,* 1.

Hayashi, C. 1966, *ARA&A, 4,* 171.

Heaton, B.D., Anderson, M., Dent, W.R.F., & Little, L.T. 1988, *A&A, 203,* 99.

Heiles, C. 1979, *ApJ, 229,* 533.

Heiles, C. 1984, *ApJSS, 55,* 585.

Henriksen, R.N. 1991, *ApJ, 377,* 500.

Henriksen, R.N., & Turner, B.E. 1984, *ApJ, 287,* 200.

Henry, P.S. 1976, *Rev. Sci. Instr., 47,* 1020.

Herbig, G.H., & Rao, N.K. 1972, *ApJ, 174,* 401.

Herbst, W., & Assousa, G.E. 1978, in *Protostars and Planets,* ed. T. Gehrels & M.S. Matthews (Tucson: University of Arizona Press), 368.

Herbst, W., & Racine, R. 1976, *AJ, 81,* 840 (HR).

Heyer, M.K., Snell, R.L., Goldsmith, P.F., Strom, S.E., & Strom, K.M., 1986, ApJ, 308, 134.

Heyer, M.H., Snell, R.L., Morgan, J., & Schloerb, F.P. 1989, *ApJ, 346*, 220.

Hildebrand, R.H. 1983, *QJRAS, 24*, 267.

Hirano, N., Kameya, O., Nakayama, M., & Takakubo, K. 1988, *ApJ, 327*, L69.

Ho, P.T.P., & Townes, C.H. 1983, *ARA&A, 21*, 239.

Hodapp, K.-W. 1987, *A&A, 172*, 304.

Houlahan, P. 1989, PhD thesis, University of Texas at Austin.

Houlahan, P., & Scalo, J. 1992, preprint.

Hu, E.M. 1981, *ApJ, 248*, 119.

Hubble, E.P 1922, *ApJ, 56*, 400.

Hudson, H.S., & Soifer, B.T. 1976, *ApJ, 206*, 100.

Hughes, V.A., & Baines, J.G.N. 1985, *ApJ, 289*, 238.

Hunter, C. 1962, *ApJ, 136*, 594.

Hunter, J.H., Jr., Sandford, M.T., II, Whitaker, R.W., & Klein, R.I. 1986, *ApJ, 305*, 309.

Irvine, W.M., Goldsmith, P.F., & Hjalmarson, Å1987, in *Interstellar Processes*, eds. D.J. Hollenbach & H.A. Thronson, Jr. (Dordrecht:Reidel), 561.

Israel, F.P. 1978, *A&A, 70*, 769.

Issa, M., MacLaren, I. & Wolfendale, A.W. 1990, *ApJ, 352*, 132.

Jarrett, T.H., Dickman, R.L., & Herbst, W. 1989, *ApJ, 345*, 881.

Jarrett, T.H., Novak, G., Xie, T., & Goldsmith, P.F. 1992, in preparation.

Jenniskens, P.M.M., & Wouterloot, J.G.A. 1990, *A&A, 227*, 553.

Jenniskens, P.M.M., Habing, H.J., Wouterloot, J.G.A., Lintel-Hekkert, P.te., & Blaauw, A. 1986, in *Light on Dark Matter*, ed. F.P. Israel (Dordrecht:Reidel), 325.

Kahn, F.D. 1954, *Bull.Inst.Netherlands, 12*, 187.

Kimura, T., & Tosa, M. 1988, *MNRAS, 234*, 51.

Klein, R.I., Whitaker, R.W., & Sandford, M.T. 1985, in *Protostars and Planets II*, ed. D. Black & M.S. Matthews (Tucson:University of Arizona Press), 340.

Knapp, G.R., & Brown, R.L. 1976, *ApJ, 204*, 21.

Koo, B.-C., & McKee, C.F. 1992a, *ApJ, 388*, 93.

Koo, B.-C., & McKee, C.F. 1992b, *ApJ, 388*, 103.

Königle, A. 1982, *ApJ, 261*, 115.

Kutner, M.L., & Tucker, K.D. 1975, *ApJ, 199*, 79.

Kuiper, T.B.H., Whiteoak, J.B., Fowler, J.W., & Rice, W. 1987, *MNRAS, 227*, 1013.

Kwan, J., & Sanders, D.B., 1986, ApJ, 309, 783.

Lada, C.J. 1985, *ARAA, 23*, 267.

Lada, C.J., Blitz, L., & Elmegreen, B.G. 1978, in *Protostars and Planets*, ed. T. Gehrels & M.S. Matthews (Tucson: University of Arizona Press), 341.

Lada, C.J., Thronson, H.A., Jr., Smith, H.A., Schwartz, P.R., & Glaccum, W. 1984, *ApJ, 286*, 302.

Lada, E.A., Bally, J., & Stark, A.A. 1991, *ApJ, 368*, 432.

Lang, K.R. 1974, *Astrophysical Formulae*, (Berlin: Springer-Verlag).

Langer, W.D. 1985, in *Birth and Infancy of Stars*, eds. R. Lucas, A. Omont & R. Stora (Amsterdam:North Horland), 279.

Langer, W.D. 1992, private communication.

Langer, W.D., & Penzias, A.A. 1990, *ApJ, 357*, 477.

Langer, W.D., Frerking, M.A., & Wilson, R.W. 1986, *ApJ, 306*, L29.

Langer, W.D., Wilson, R.W., Goldsmith, P.F., & Beichman, C.A. 1989, *ApJ, 337*, 355.

Larson, R.B. 1972, *MNRAS, 157*, 121.

Larson, R.B. 1973, *ARA&A, 11*, 219.

Larson, R.B. 1979, *MNRAS, 186*, 479.

Larson, R.B., 1981, MNRAS, 194, 809.

Laureijs, R.J., Chlewicki, G., & Clark, F.O. 1988, *A&A, 192*, L13.

Laureijs, R.J., Chlewicki, G., Clark, F.O., & Wesselius, P.R. 1989, A&A, 220, 226.

Laureijs, R.J., Clark, F.O., & Prusti, T. 1991, *ApJ, 372*, 185.

Laureijs, R.J., Mattila, K., & Schnur, G. 1987, *A& A, 184*, 269.

Layzer, D. 1964, *ARA&A, 2*, 341.

Lee, Y., Snell, R.L., & Dickman, R.L. 1990, *ApJ, 355*, 536.

Leene, A. 1986, *A&A, 154*, 295.

Léger, A., & Puget, J.L. 1984, *A&A, 137*, L5.

Leung, C.M. 1975, *ApJ, 199*, 340.

Leung, C.M. 1976, *ApJ, 209*, 75.

Leung, C.M. 1985, in *Protostars and Planets II*, eds. D.C. Black & M.S. Matthews (Tucson: University of Arizona Press), 104.

Leung, C.M., & Brown, R.L. 1977, *ApJ, 214*, L73.

Leung, C.M., Kutner, M.L., & Mead, K., 1982, *ApJ, 262*, 583.

Linke, R.A., & Goldsmith, P.F. 1980, *ApJ, 235*, 437.

Lis, D.C., & Goldsmith, P.F. 1990, *ApJ, 356*, 195.

Lis, D.C., & Leung, C.M. 1990, *Icarus, 91*, 7.

Liszt, H.S. 1982, *ApH, 262*, 198.

Little, L.T., Heaton, B.D., Dent, W.R.F. 1990, *A&A, 232*, 173.

Loren, R.B. 1976, *ApJ, 209*, 466.

Loren, R.B. 1977, *ApJ, 215*, 129.

Loren, R.B. 1981, *ApJ, 249*, 550.

Loren, R.B. 1989, *ApJ, 338*, 902.

Loren, R.B., Peters, W.L., III, & Vanden Bout, P.A. 1974, *ApJ, 194*, L103.

Low, F.J. *et al* 1984, *ApJ, 278*, L19.

Lynds, B.T. 1962, *ApJS, 7*, 1.

Lyne, A.G., & Graham-Smith, F. 1990, *Pulsar Astronomy* (Cambridge: Cambridge University Press), 246.

MacLow, M.-M., & McCray, R. 1988, *ApJ*, *324*, 776.

Maddalena, R.J., Morris, M., Moscowitz, J., & Thaddeus, P. 1986, *ApJ*, *303*, 375.

Maloney, P. 1990, *ApJ*, *348*, L9.

Manchester, R.N., & Taylor, J.H. 1981, *AJ*, *86*, 1953.

Manfroid, J. 1976, *A&A*, *46*, 31.

Martin, R.N., & Barrett, A.H. 1978, *ApJS*, *36*, 1.

Massi, M., Felli, M, & Simon, M., 1985, A&A, 152, 387.

Masson, C.R., & Chernin, L.M. 1992, *ApJ*, *387*, L47 (MC).

Mathis, J.S. 1990, *ARA&A*, *28*, 37.

Mathis, J.S., Rumpl, W., & Nordsieck, K.H., 1977, *ApJ*, *217*, 425.

Mathis, J.S., & Whiffen, G. 1989, *ApJ*, *341*, 808.

Mazurek, T.J. 1982, in *Regions of Star Formation* eds. R.S.Roger & Dewdney (Dordrecht:Reidel), 61.

McCray, R., & Kafatos, M. 1987, *ApJ*, *317*, 190.

Mcdonald, G.H., Little, L.T., Brown, A.T., Riley, P.W., Matteson, D.J., & Felli, M. 1981, *MNRAS, 195*, 387.

McNally, D. 1971, *Rep. Prog. Phys.*, *34*, 71.

McVitter, G.C. 1956, *AJ, 61*, 451.

Meyers-Rice, B.A., & Lada, C.J. 1991, *ApJ*, *368*, 445.

Mezger, P.G., Wink, J.E., & Zylka, R. 1990, *A&A*, *228*, 95.

Montalbán, J., Bachiller, R., Martin-Pintado, J., Tafalla, M., & Gómez-González, J. 1990, *A&A, 233*, 527.

Moriarty-Schieven, G.H., & Snell, R.L. 1988, *ApJ*, *333*, 316.

Moriarty-Schieven, G.H., & Snell, R.L. 1989, *ApJ*, *338*, 952.

Moriarty-Schieven, G.H., Snell, R.L., Strom, S.E., & Grasdalen, G.L. 1987, *ApJ*, *317*, L95.

Moriarty-Schieven, G.H., Snell, R.L., Strom, S.E., Schloerb, F.P., Strom, K.M., & Grasdalen, G.L. 1987, *ApJ*, *319*, 742.

Morris, M., & Knapp, G.R. 1976, *ApJ*, *204*, 415.

Morris, M., Montani, J., & Thaddeus, P. 1980, *Interstellar Molecules* ed. B.H. Andrew (Dordrecht:Reidel), 197.

Mouschovias, T.ch. 1991, in *The Physics of Star Formation and Early Stellar Evolution*, ed. C.J. Lada & N.D. Kylafis (Dordrecht:Kluwer), 449.

Mundy, L., Wilking, B.A., & Myers, S.T. 1986, *ApJ, 311*, L75.

Myers, P.C. 1983, *ApJ, 270*, 105.

Myers, P.C., 1987, in *Interstellar Processes*, eds. D.J. Hollenbach & H.A. Thronson, Jr. (Dordrecht:Reidel), p71.

Myers, P.C., & Benson, P.J., 1983, *ApJ, 266*, 309.

Myers, P.C., Fuller, G.A., Goodman, A.A., & Benson, P.J. 1991, *ApJ, 376*, 561.

Myers, P.C., & Goodman, A.A. 1988a, *ApJ, 326*, L27.

Myers, P.C., & Goodman, A.A. 1988b, *ApJ, 329*, 392.

Norman, C., & Silk, J. 1980, *ApJ, 238*, 158.

Novak, G., 1988, PhD Thesis, University of Chicago.

Novak, G., Gonatas, D.P., Hildebrand, R.H., Platt, S.R., & Dragovan, M. 1989, *ApJ, 345*, 802.

Olofsson, G., & Koornneef, J. 1985, *A&A, 146*, 337.

Oort, J.H. 1954, *Bull.Astr.Inst.Netherlands, 12*, 177.

Oort, J.H., & Spitzer, L. 1955, *ApJ, 121*, 6.

Öpik, E.J. 1953, *Irish AJ, 2*, 219.

Pajot, F., Boissé, P., Gispert, R., Lamarre, J.M., Puget, J.L., & Serra, G. 1986, *A&A, 157*, 393.

Panagia, N. 1973, *AJ, 78*, 929.

Panagia, N. 1975, *A&A, 42*, 139.

Panagia, N. 1991, in *The Physics of Star Formation and Early Stellar Evolution*, ed. C.J. Lada & N.D. Kylafis (Dordrecht:Kluwer), 565.

Parker, N.D. 1991, *MNRAS, 251*, 63.

Patel, N. 1992, FCRAO memo.

Patel, N., Xie, T., & Goldsmith, P.F. 1992, in preparation.

Penston, M.V. 1969, *MNRAS, 145*, 457.

Penzias, A.A. 1975, in *Atomic and Molecular Physics and the Interstellar Matter* ed. P. Balian *et al* (Amsterdam:North-Holland), 403.

Phillips, J.P., White, G.J., Ade, P.A.R., Cunningham, C.T., Richardson, K.J., Robson, E.T., & Watt, G.D. 1982, *A&A, 116*, 130.

Pikel'ner, S.B. 1973, *CoASP, 6*, 151.

Pottasch, S. 1958, *Rev. of Mod. Phys., 30*, 1053.

Puget, J.L., & Léger, A. 1989, *ARA&A, 27*, 161.

Puget, J.L., Léger, A., Boulanger, F. 1985, *A& A, 142*, L19.

Racine, R. 1968, *AJ, 73*, 233.

Racine, R., & van den Bergh, S. 1970, in *The Spiral Structure of Our Galaxy* ed. Becker & Cantopoulos, 219.

Reich, W. 1978, *A&A, 64*, 407.

Reipurth, Bo., Wamsteker, W. 1983, *A&A, 119*, 14.

Richardson, K.J., White, G.J., Monteiro, T.S., Hayashi, S.S. 1988, *A&A, 198*, 237.

Richer, J.S., Hills, R.E., & Padman, R. 1992, *MNRAS, 254*, 525.

Righini, G., Simon, M., & Joyce, R.R. 1976, *ApJ, 207*, 119.

Rodríguez, L.F. 1987, in *Star Forming Regions*, ed. M. Peimbert & J. Jugaku (Dordrecht:Reidel), 239.

Rodríguez, L.F. 1988, in *Galactic and Extragalactic Star Formation*, eds. R.E. Pudritz and M. Fich (Dordrecht:Kluwer), 97.

Rodríguez, L.F., Carral, P., Ho, P.T.P., & Moran, J.M. 1982, *ApJ, 260*, 635.

Rodríguez, L.F., & Cantó, J. 1983, *Rev. Mex. A&A, 8*, 163.

Rodríguez, L.F., Moran, J.M., Ho, P.T.P., & Gottlieb, E.W., 1980, *ApJ, 235*, 845.

Rowan-Robinson, M. 1979, *ApJ, 234*, 111.

Rowan-Robinson, M. 1980, *ApJS, 44*, 403.

Rowan-Robinson, M. 1986, *MNRAS, 219*, 737.

Salas, L. 1992, *ApJ, 385*, 288.

Sanders, D.B., Scoville, N.Z., & Solomon, P.M. 1985, *ApJ, 289*, 373.

Sanders, D.B., Solomon, P.M., & Scoville, N.Z. 1984, *ApJ, 276*, 182.

Sargent, A.I. 1977, *ApJ, 218*, 736.

Sargent, A.I. 1979, *ApJ, 233*, 163.

Sargent, A.I. 1985, in *Birth and Evolution of Massive Stars and Stellar Groups* ed. W. Boland & H.V. Woerden (Dordrecht:Reidel), 5.

Sargent, A.I., van Duinen, R.J., Fridlund, C.V.M., Nordh, H.L., & Aalders, J.W.G. 1981, *ApJ, 249*, 607.

Scalo, J.M. 1985, in *Protostars and Planets II*, ed. D.C. Black & M.S. Matthews (Tucson: University of Arizona Press), 201.

Scalo, J.M., 1987, in *Interstellar Processes*, eds. D.J. Hollenbach & H.A. Thronson, Jr. (Dordrecht:Reidel), 349.

Scalo, J.M., 1988, in *Molecular Clouds in the Milky Way and External galaxies*, eds. R.L. Dickman, R.L. Snell & J.S. Young (Berlin: Springer-Verlag), 201.

Scalo, J.M. 1991, in *Physical Processes in Fragmentation and Star Formation* eds. R. Capuzzo-Dolcetta, C. Chiosi & A.Di Fazio (Dordrecht:Kluwer).

Schwartz, P.R. 1980, *ApJ, 238*, 823.

Schwartz, P.R. 1987, *ApJ, 320*, 258.

Schwartz, P.R., & Spencer, J.H. 1977, *MNRAS, 180*, 297.

Scoville, N.Z. 1985, in *Protostars and Planets II*, ed. D.C. Black & M.S. Matthews (Tucson: University of Arizona Press), 188.

Scoville, N.Z., & Kwan, J. 1976, *ApJ, 206*, 718.

Scoville, N.Z., & Sanders, D.B. 1987, in *Interstellar Processes*, eds. D.J. Hollenbach & H.A. Thronson, Jr. (Dordrecht:Reidel), 21.

Scoville, N.Z., Solomon, P.M., & Penzias, A.A. 1975, *ApJ, 201*, 352.

Scoville, N.Z., Yun, M.-S., Clemens, D.P., Sanders, D.B., & Waller, W.H. 1987, *ApJS, 63*, 821.

Seares, F.H., & Hubble, E.P. 1920, *ApJ, 52*, 8.

Sellgren, K. 1984, *ApJ, 277*, 623.

Shimmins, A.J., Clarke, M.E., & Ekers, R.D. 1966, *Australian J. Phys., 19*, 649.

Shimmins, A.J., Day, G.A., Ekers, R.D., & Cole, D.J. 1966, *Australian J. Phys., 19*, 837.

Shu, F.H., Adams, F.C., & Lizano, S. 1987, *ARAA, 25*, 23.

Shu, F.H., Lizano, S., Ruden, S., & Najita, J. 1988, *ApJ, 328*, L19.

Shu, F.H., Ruden, S.P., Lada, C.J. & Lizano, S. 1991, *ApJ, 370*, L31 (SRLL).

Shull, J.M. 1980, *ApJ, 238*, 860.

Shull, J.M. 1982, in *Regions of Recent Formation*, ed. R.S. Roger & P.E. Dewdney (Dordrecht:Reidel), 91.

Shull, J.M., & Draine, B.T. 1987, in *Interstellar Processes*, eds. D.J.Hollenbach & H.A. Thronson, Jr. (Dordrecht:Reidel), 285.

Silk, J. 1978, in *Protostars and Planets*, ed. T. Gehrels & M.S. Matthews (Tucson: University of Arizona Press), 172.

Simon, M., Righini-Cohen, G., Felli, M., & Fischer, J. 1981, *ApJ, 245*, 552.

Snell, R.L., 1981, *ApJS, 45*, 121.

Snell, R.L. 1987, in IAU Symposium 115, *Star Forming Regions*, ed. M.Peimbert & J.Jugaku (Dordrecht:Reidel), p.213.

Snell, R.L. 1989, in *Structure and Dynamics of Interstellar Medium* ed. G. Tenorio-Tagle, M. Moles & J. Melnick (Heidelberg: Springer-Verlag), 231.

Snell, R.L., Heyer, M.H., & Schloerb, F.P. 1989, *ApJ, 337*, 739.

Snell, R.L., & Loren, R.B. 1977, *ApJ, 211*, 122.

Snell, R.L., Loren, R.B., & Plambeck, R.L. 1980, *ApJ, 239*, L17.

Sodroski, T.J., Dwek, E., Hauser, M.G., & Kerr, F.J. 1987, *ApJ, 322*, 101.

Sofue, Y., & Nakai, N. 1983, *A&ASS, 53*, 57.

Solomon, P.M., & Barrett, J.W. 1991, in *Dynamics of Galaxies and Molecular Cloud Distribution* eds. F. Combes & F. Casoli (Dordrecht:Kluwer).

Solomon, P.M., Rivolo, A.R., Barrett, J., & Yahil, A., 1987, *ApJ, 319*, 730.

Solomon, P.M., & Sanders, D.B. 1985, in *Protostars and Planets II*, ed. D.C. Black & M.S. Matthews (Tucson: University of Arizona Press), 59.

Spitzer, L. 1978, *Physical Processes in the Interstellar Medium*, John Wiley & Sons, Inc.

Stenholm, L.G. 1987, in *Physical Processes in Interstellar Clouds*, eds. G.E. Morfill and M. Scholer (Dordrecht: Reidel), 195.

Strom, S.E. 1985, in *Protostars and Planets II*, ed. D.C. Black & M.S. Matthews (Tucson: University of Arizona Press), 17.

Strom, K.M., Strom, S.E., & Vrba, F.J. 1976, *AJ, 81*, 320.

Stutzki, J., & Güsten, R. 1990, *ApJ, 356*, 513.

Sume, S.D., & Irvine, W.M. 1977, *A&A, 60*, 345.

Tauber, J. 1990, PhD Thesis, University of Massachusetts at Amherst.

Tauber, J., Goldsmith, P.F., & Dickman, R.L. 1991, *ApJ, 375*, 635.

Tayler, R.J. 1968, *Rep. Prog. Phys., 31*, 167.

Tenorio-Tagle, G. 1979, *A&A, 71*, 59.

Tenorio-Tagle, G. 1982, in *Regions of Recent Formation*, ed. R.S. Roger & P.E. Dewdney (Dordrecht:Reidel), 1.

Tenorio-Tagle, G., & Bodenheimer, P. 1988, *ARA&A, 26*, 146.

Terzian, Y. 1968, *Interstellar Ionized Hydrogen*, (New York: W.A. Benjamin Inc.).

Terzian, Y., & Balick, B. 1974, *Fund. of Cosmic Phys., 1*, 301.

Thronson, H.A., Gatley, I., Harvey, P.M., Sellgren, K., & Werner, M.W. 1980, *ApJ, 237*, 66.

Thronson, H.A., Lada, C.J., & Hewagawa, T. 1985, *ApJ, 297*, 662.

Thronson, H.A., & Harper, D.A. 1986, *ApJ, 300*, 396.

Tomita, Y., 1990, submitted to Publ. Astron. Soc. Japan.

Tomita, Y., 1987, in IAU Symposium 115, *Star Forming Regions*, ed. M.Peimbert & J.Jugaku (Dordrecht:Reidel), 51.

Torrelles, J.M., Ho, P.T.P., Rodríguez, L.F., & Cantó, J., 1990, *ApJ, 349*, 529.

Torrelles, J.M., Rodríguez, L.F., Cantó, J., Carral, P., Marcaide, J., Moran, J.M., & Ho, P.T.P. 1983, *ApJ, 274*, 214.

Valée, J.P., Viner, M.R., & Hughes, V.A. 1979, *AJ, 84*, 1581.

Van Buren, D., & McCray, R. 1988, *ApJ, 329*, L93.

van den Bergh, S. 1966, *AJ, 71*, 990 (vdB).

van den Bergh, S. 1968, *Ap. Letters, 2*, 71.

Vishniac, E.T. 1983, *ApJ, 274*, 152.

Walker, C.K., Adams, F.C., & Lada, C.J. 1990, *ApJ, 349*, 515.

Weaver, R., McCray, R., Castor, J., Shapiro, P., & Moore, R. 1977, *ApJ, 218*, 377.

Weaver, T.A., Zimmerman, G.B., & Woosley, S.E. 1978, *ApJ, 225*, 1021.

Weiland, J.L., Blitz, L., Dwek, E., Hauser, M.G., Magnani, L., & Rickard, L.J. 1986, *ApJ, 306*, L101.

Werner, M.W., Gatley, I., Harper, D.A., Becklin, E.E., Loewenstein, R.F., Telesco, C.M., & Thronson, H.A., Jr. 1976, *ApJ, 204*, 420.

Westbrook, W.E., Werner, M.W., Elias, J.H., Gezari, D.Y., Hauser, M.G., Lo, K.Y., & Neugebauer, G. 1976, *ApJ, 209*, 94.

Wheeler, J.C., Mazurek, T.J., & Sivaramakrishnan, A. 1980, *ApJ, 237*, 781.

Wilking, B.A., Harvey, P.M., Lada, C.J., Joy, M., & Doering, C.R. 1984, *ApJ, 279*, 291.

Willson, R.F., & Folch-Pi, F.J. 1981, *AJ, 86*, 1084.

Wilson, R.F., Jefferts, K.B., & Penzias, A.A. 1970, *ApJ, 161*, L43.

Wilson, T.L., & Walmsley, C.M. 1989, *AAR, 1*, 141.

Wolf, G.A., Lada, C.J., & Bally, J. 1990, *AJ, 100*, 1892.

Wood, D.O., & Churchwell, E. 1989, *ApJ, 340*, 265.

Wood, D.O., & Churchwell, E. 1991, *ApJ, 372*, L99.

Wynn-Williams, C.G., Becklin, E.E., Forster, J.R., Matthews, K., Neugebauer, G., Welch, W.J., & Wright, M.C.A. 1977, *ApJ, 211*, L89.

Xie, T., & Goldsmith, P.F. 1990, *ApJ, 359*, 378.

Xie, T., Goldsmith, P.F., & Nimesh, P. 1992, submitted to *ApJ Letters*.

Xie, T., Goldsmith, P.F., Snell, R.L., & Zhou, W. 1993, *ApJ*, January 1.

Xie, T., Goldsmith, P.F., & Zhou, W. 1991, *ApJ, 371*, L81.

Yorke, H.W., Tenorio-Tagle, G., Bodenheimer, P., & Rózyczka, M. 1989, *A&A, 216*, 207.

Zaritsky, D., Shaya, E.J., Scoville, N.Z., Sargent, A.I., & Tytler, D. 1987, *AJ*, *93*, 1514.

Zhou, S., Wu, Y., Evans II, N.J., Fuller, G.A., & Myers, P.C. 1989, *ApJ*, *346*, 168.

Zhou, S., Evans II, N.J., Kömpe, C., & Walmsley, M. 1992, *submitted to ApJ*.